Western Graduate&PostdoctoralStudies

Western University
Scholarship@Western

Electronic Thesis and Dissertation Repository

4-18-2018 2:30 PM

Development of Nanostructures by Atomic and Molecular Layer Deposition

Andrew P. Lushington, *The University of Western Ontario*

Supervisor: Sun, Xueliang, *The University of Western Ontario*

A thesis submitted in partial fulfillment of the requirements for the Doctor of Philosophy degree in Mechanical and Materials Engineering

© Andrew P. Lushington 2018

Follow this and additional works at: https://ir.lib.uwo.ca/etd

 Part of the Other Materials Science and Engineering Commons

Recommended Citation

Lushington, Andrew P., "Development of Nanostructures by Atomic and Molecular Layer Deposition" (2018). *Electronic Thesis and Dissertation Repository*. 5354.
https://ir.lib.uwo.ca/etd/5354

This Dissertation/Thesis is brought to you for free and open access by Scholarship@Western. It has been accepted for inclusion in Electronic Thesis and Dissertation Repository by an authorized administrator of Scholarship@Western. For more information, please contact wlswadmin@uwo.ca.

Abstract

Atomic layer deposition (ALD) is a thin film deposition technique that has a rich history of being an enabling technique. This vapor phase deposition process can produce a variety of thin films and nanostructures. ALD is based on sequential, self-limiting reactions and provides angstrom level control over film growth. Furthermore, ALD allows for conformal deposition on high-aspect ratio structures and can provide tunable film composition. As nanotechnology marches forward, the development of nanomaterials has significantly advanced. Additional functionality can be imparted to nanomaterials by using surface modification techniques. Given the advantages of ALD, this technique has become a powerful tool for modifying the surface of materials and increasing the functionality and application of nanomaterials. The toolkit of available materials for surface modification is further augmented by including molecular layer deposition (MLD), a technique used to grow organic polymer-like materials. By combining ALD and MLD together, novel inorganic-organic hybrid materials can be produced with specifically tailored properties.

The first part in the thesis investigates the effect of ozone on nitrogen doped carbon nanotubes (NCNTs) and pristine carbon nanotubes (PCNTs). The deleterious effects of ozone were found to occur only for NCNTs, while little to or no damage occurs for PCNTs. Furthermore, this work highlights the importance of understanding precursor-substrate interaction, especially when dealing with nanomaterials.

The second and third part of this thesis outline the synthesis of novel thin films made by ALD and MLD. First, an aluminum alkoxide film with tunable conductivity was made using trimethylaluminium (TMA), ethylene glycol (EG), and terephthaloyl chloride in various subcycle configurations to control the ratio of aluminum to carbon in the film. The films were then pyrolyzed in a reducing atmosphere to yield a conductive aluminum oxide/carbon composite. Depending on the ratio of aluminum to carbon in the grown film, post-pyrolyzed films displayed varying levels of electronic conductivity. Synchrotron based XPS was then used to elucidate the origin of conductivity within the film. The second novel film is a mixed inorganic-organic polyurea film. For the first time, polarization-dependent x-ray absorption spectroscopy was used to determine the difference in orientation and ordering between pure organic polyurea films and inorganic-organic polyurea films. In-depth analysis of this data revealed that the hybrid inorganic-

organic films possessed a high degree of ordering compared to their organic counterpart. Both studies present the possibility of combining ALD and MLD in tuning various film properties such as electronic conductivity and oligomer packing density.

The fourth part of this thesis investigates the formation of single-atom and ultra-small clusters of platinum produced by ALD. The self-limiting characteristics of trimethyl(methylcyclopentadienyl)-platinum on NCNTs and PCNTs was investigated by varying precursor exposure time and determining the influence of reactor temperature. This study determined that a 1 minute exposure of the Pt precursor at 250°C yielded primarily single atoms and ultra-small clusters on NCNTs, but not PCNTs. Extended x-ray fine structure analysis was conducted to determine the bonding characteristics of Pt to NCNTs and PCNTs. This study outlines the necessary conditions to deposit single atom and ultra-small clusters of Pt on carbon nanotube substrates and the parameters that influence this process.

The final experimental investigation of this thesis is the protection of metallic lithium (Li) by ALD and MLD. Fifty cycles of either TMA-H_2O, TMA-EG or TMA-glycerol (GLY) were used to coat the surface of Li metal. Galvanostatic cycling of Li symmetric cells was then conducted to determine the protective capabilities of these films. The results revealed that electrodes coated with TMA-GLY provided prolonged cyclability of metallic Li electrodes. For the first-time gravimetric intermission titration technique was then conducted on coated electrodes to unravel the effects of lithium electrodissolution and electroplating. This study demonstrated that the longevity of TMA-GLY coated electrodes originates from the relatively low overpotential required to plate and strip Li from the MLD film. Finally, scanning electron microscopy and Rutherford backscattering spectometry was used to determine composition and morphology of the formed solid electrolyte interphase on coated electrodes following electrochemical cycling.

Keywords

Atomic layer deposition, molecular layer deposition, surface modification, nanomaterials, nitrogen doped carbon nanotubes, inorganic-organic thin films, single-atom catalysts, lithium-based batteries, metallic lithium electrodes, solid electrolyte interphase, carbonate-based electrolyte, synchrotron radiation, XPS, XANES, EXAFS, Rutherford backscattering spectroscopy.

Co-Authorship Statement

1.

Title: Surface Modification of Nitrogen Doped Carbon Nanotubes by Ozone via Atomic Layer Deposition

Authors: Andrew Lushington, Jian Liu, Yongji Tang, Ruying Li, and Xueliang Sun

The final version of this manuscript has been published in the Journal of Vacuum Science & Technology A, 2014, 32, 01A124. Jian Liu helped with ALD experiments and production of nitrogen doped carbon nanotubes. Yongji Tang conducted Raman spectroscopy measurements. Ruying Li provided access to all equipment. All authors contributed editorial comments on the manuscript.

2.

Title: A Novel Approach in Controlling the Conductivity of Thin Films Using Molecular Layer Deposition

Authors: Andrew Lushington, Jian Liu, Mohammad N. Banis, Biwei Xiao, Stephen Lawes, Ruying Li, Xueliang Sun.

The final version of this manuscript has been published in Applied Surface Science, 2015, 357, 1319. Jian Liu provided assistance with manuscript writing, figure design and ALD/MLD experiment design. Mohammad N. Banis conducted synchrotron based X-ray tests. Biwei Xiao conducted Raman spectroscopy measurements. Stephen Lawes aided in construction of four-point probe and analysis of conductivity measurements. Ruying Li provided access to the equipment. All authors contributed editorial comments on the manuscript.

3.

Title: Orientation and Ordering of Organic and Hybrid Inorganic-Organic Polyurea Films Using Molecular Layer Deposition

Authors: Andrew Lushington, Craig Langford, Jian Liu, Kaiqi Nie, Ruying Li, Xuhui Sun, Jinghua Guo, and Xueliang Sun.

The final version of this manuscript has been published in the Journal of Physical Chemistry C, 2017, 121 (21), 11757. Craig Langford conducted MATLAB calculations. Jian Liu provided experimental insight. Kaiqi Nie helped with conducting synchrotron radiation experiments. Ruying Li and Jinghua Guo provided access to the equipment. All authors contributed editorial comments on the manuscript.

4.

Title: Single-Atom and Clusters to Nanoparticles: Controlling the Nucleation of Pt Through Regulated Gas Phase Chemisorption.

Authors: Andrew Lushington, Samantha Stambula, Mohammad N. Banis, Niancai Cheng, Yang Zhou, Ruying Li, Tsun-Kong Sham, Gianluigi A. Botton, and Xueliang Sun

This manuscript is currently in preparation for submission. Both Andrew Lushington and Samantha Stambula contributed equally to this work. Samantha conducted TEM analysis and data acquisition. Mohammad N. Banis performed synchrotron experiments at CLS. Niancai Cheng helped with experimental design. Yang Zhou conducted ICP experiments and provided analysis of ICP data. Ruying Li provided access to all equipment. Tsun-Kong sham helped with analysis of synchrotron data. All authors contributed editorial comments on the manuscript

5.

Title: Deconvoluting the Effects of Stripping and Plating of Lithium Coated using ALD and MLD.

Authors: Andrew Lushington, Yang Zhao, Lyudmila V. Goncharova, Qian Sun, Ruying Li, and Xueliang Sun.

This manuscript is currently under preparation for submission. Yang Zhao and Qian Sun provided experimental help. Lyudmila V. Goncharova conducted RBS experiments as well as analysis of RBS data. Ruying Li provided access to instruments. All authors contributed manuscript editorial comments.

To failure, the greatest of life's teachers

Acknowledgments

This Ph.D. work was carried on in Professor Andy Xueliang Sun's Nanomaterials and Energy Group at the University of Western Ontario (UWO). Here, it is with my pleasure that I acknowledge every individual who has accompanied with me and contributed to my work in the past five years.

I would like to give my sincerest gratitude to Professor Xueliang Sun. He has provided me with an incredible platform to launch my professional carrier from. His dedication, guidance, passion, kind-hearted nature, and genuine scientific curiosity will forever serve as a guiding star for me. Never have I witnessed such a delicate balance between ambition, time management, and earnestness. His character will always stand as a central pillar in my life and I am truly grateful to have been under his guidance these past 5 years.

I would also like to personally thank Mrs. Ruying (Kathy) Li. Her kind hearted and loving nature are really sold short by such simple adjectives. In the past 5 years she has demonstrated what it means to show unconditional love to all attributes of life. Whether it be a scientific inquiry or facing a tough life decision, Kathy is always there to listen and provide the sincerest of responses. Thank you so much for your help over the years, your gratitude and sincerity will not be forgotten.

I am grateful to Prof. Jian Liu for providing me with an excellent introduction into Prof. Sun's group. I will never forget how enthusiastic we would get talking about ALD and the long days spent fixing vacuum pumps and cleaning oil. I would also like to thank all past and current group members. There are many times where I felt very proud to be part of such an ambitious group of researchers. Especially, I would like to thank Dr. Qian Sun, Dr. Xifei Li, Dr. Hossein Yadegari, Dr. Niancai Cheng, and Dr. Mohammad N. Banis. These individuals were an invaluable source of information and our interactions will always be remembered. The amount of information I have learned from these individuals is irreplaceable. I will especially like to mention Dr. Biqiong Wang, Dr. Biwei Xiao, Dr. Xia Li. We all started this academic journey around the same time and watching each of our careers expand has been nothing short of fascinating. I am very grateful to have shared this experience with you guys and I hope our paths cross again in the future. I would also like to thank Mr. Yang Zhao for showing me what determination really looks like. Never have

I met an individual, apart from Prof.Sun, with such ambition and determination. His guidance and discussion will forever be remembered.

I am grateful to Dr. Tsun-Kong Sham in the Department of Chemistry at Western University and Dr. Jinghua Guo at the Advanced Light Source at Lawrence Berkeley National Laboratory, for their help on synchrotron based X-ray studies and analysis. Both of you provided an excellent platform for me to quench my thirst for fundamental knowledge.

I am also grateful to my advisory committee members, Prof. Robert Klassen and Prof Jun Yang for their advice, support, and concern during my PhD.

I would like to thank Mr. Stephen Lawes, Mr. Craig Langford, Ms. Mudi Kadu, Mr. Adam Riese, Ms. Anastasia Pasche, Mr. Benjamin Steen, Mr. Zachary Linder, and Mr. Spencer Yim. I am incredible luckily that our paths crossed here in London, ON. I learned so much of what friendship means from you guys and I will forever be grateful for that. I can't even imagine what this journey would look like without your support and quirky natures. From late night chess games to unforgettable nights at BETA and CODA, your friendship will always be remembered.

I would also like to give the sincerest thanks to the Ottawa/Toronto crew, Mr. Alec (the fetus) Murphy, Ms. Kaitlyn Young, Mr. Vlad Tohaneau, Ms. Indra Calu, Ms. Aretha Heenan and Mr. Jeremy St. Onge. Without you guys in Toronto I don't know what I would have done. The countless nights of escape and mental support you guys provided will never be forgotten. You guys were an invaluable part of this journey and I give you all the thanks and love. To Mr. Christopher Demelo, Mr. Phil Zelkie, Mr. Ryan Riddle and Mrs. Monica Nuyens, thank you for filling in the nerdy hole in my heart with your SnargeCo brand products. I am also grateful to the whole Easby family for providing such a warm and loving home. Your family dynamic will never be forgotten and will forever serve as a reminder to what a loving family really means.

I would also like to give my sincerest thanks to the members of MF DOOM. You are an incredible group people who I am truly glad to call friends. Your support and friendship during those especially difficult times will be cherished. You guys have shown me that regardless of geographic location, true friendships can still be forged, especially in the salt mines of the crucible. You guys have really been a crucial aspect of this process and for that I am truly grateful. Thank you.

Finally, I would like to thank my Mom and Dad. Your unconditional love and support over the years is incalculable. Saying that I love you just doesn't cut it or even come close to how much you both mean to me. Your encouragement, motivation, and support over the past few years are incalculable. You guys are the source of my happiness and motivation and have taught me to successfully walk a fine line between confidence and doubt. I would also like my thank my brother and sister-in law, Joy and Jolene Lushington. The love and admiration you both demonstrate to each other is simply amazing. There is no doubt in my mind that Aliyah will growth up to be as kind hearted, honest, and loving as your two are.

Thank you all for your love and support. There is no way I could have gotten to where I am without you all of you.

Andrew Lushington

December 19, 2017

Table of Contents

Abstract i
Co-Authorship Statement iii
Acknowledgments vi
Table of Contents ix
List of Tables xiii
List of Figures xiv
List of Appendices xx
List of Abbreviations xxi

Chapter 1 - Introduction and Literature Review **1**

1.1 Introduction to this Thesis 1
1.1.1 Energy Storage and Conversion 1
1.1.2 Atomic and Molecular Layer Deposition 2
1.2 Thesis Objectives 3
1.3 Thesis Organization 4
1.4 Introduction to Fundamentals 6
1.4.1 Gas Phase Deposition Techniques 6
1.4.2 Physical Vapor Deposition 7
1.4.3 Chemical Vapor Deposition 8
1.4.4 Atomic Layer Deposition 12
1.4.5 Molecular Layer Deposition 17
1.5 Literature Review 20
1.5.1 Unique Capabilities of ALD 20
1.5.2 Unique Capabilities of MLD 24
1.5.3 Use of ALD and MLD for Lithium-based Batteries 26
1.5.4 ALD and MLD for Lithium-ion Batteries 27
1.5.5 ALD and MLD for Lithium-Sulfur Batteries 31
1.5.6 Application of ALD and MLD for Fuel Cells 33
1.6 References 37

Chapter 2 - Experimental Apparatus and Characterization Techniques……..**45**

2.1 Experimental Apparatus..... 45

2.1.1 Savannah 100 (Cambridge Nanotech, USA)..... 45

2.1.2 Gemstar-8 (Arradiance, USA)..... 48

2.2 Characterization Techniques..... 50

2.2.1 Scanning Electron Microscopy..... 50

2.2.2 Fourier Transform Infrared Spectroscopy..... 52

2.2.3 Raman Spectroscopy..... 54

2.2.4 Quartz Crystal Microbalance..... 55

2.2.5 X-ray Reflectivity..... 57

2.2.6 Synchrotron Based Characterization Techniques..... 58

2.2.6.1 Near Edge X-ray Absorption Fine Structure Spectroscopy..... 59

2.2.6.2 Extended X-ray Absorption Fine Structure Spectroscopy..... 60

2.3 References..... 63

Chapter 3 - Surface Modification of Nitrogen Doped Carbon Nanotubes by Ozone via Atomic Layer Deposition…..……..**64**

3.1 Introduction..... 65

3.2 Experimental Details..... 67

3.3 Results and Discussion..... 68

3.4 Conclusions..... 78

3.5 Supporting Information..... 79

3.6 References..... 81

Chapter 4 - Controlling the Conductivity of Thin Films using Molecular Layer Deposition..... **85**

4.1 Introduction..... 86

4.2 Experimental Details..... 87

4.3 Results and Discussion..... 88

4.4 Conclusions..... 95

4.5 References..... 97

Chapter 5 - Orientation and Ordering of Organic and Hybrid Inorganic-Organic Polyurea Films using Molecular Layer Deposition **100**

5.1 Introduction 101

5.2 Experimental Details 103

5.3 Results and Discussion 104

5.4 Conclusions 114

5.5 References 115

Chapter 6 - Single-Atom and Clusters to Nanoparticles: Controlling the Nucleation of Pt Through Regulated Gas Phase Chemisorption **119**

6.1 Introduction 120

6.2 Experimental Details 122

6.3 Results and Discussion 124

6.4 Conclusion 133

6.5 Supporting Information 135

6.5.1 Data Processing 135

6.5.2 Elemental Quantification 140

6.5.3 Additional Histograms 142

6.6 References. 143

Chapter 7 - Deconvoluting the Effects of Stripping and Plating of Lithium Coated using ALD and MLD **147**

7.1 Introduction 148

7.2 Experimental 151

7.3 Results and Discussion 152

7.3.1 Galvanostatic cycling of Li-Li symmetric cells 152

7.3.2 Galvanostatic Intermission Titration Technique 156

7.3.3 Morphology Analysis by Scanning Electron Microscopy 161

7.3.4 Rutherford Backscattering Spectroscopy 163

7.4 Conclusions 164

7.5 Supporting Information 166

7.6 References 169

Chapter 8 - Conclusion and Future Prospective **174**

8.1 Conclusions 175

8.2 Thesis Novelties 178

8.3 Future Perspective 179

Appendices **183**

Appendix A: Permission from AIP for Published Article 183

Appendix B: Permission from Elsevier for Published Article 184

Appendix C: Permission from ACS for Published Article 185

Curriculum Vitae **186**

List of Tables

Table 1.1. Overview of various ALD coatings applied to different Li-ion battery cathode materials……..……28

Table 3.1. XPS survey analysis comparison between untreated NCNTs and 300°C ozone treated NCNTs……...…75

Table 6.1. Comparison of density and diameter data obtained from HAADF-STEM for NCNTs and PCNTs exposed to $MeCpPtMe_3$ at different temperatures and dosing times. ICP analysis was performed to determine the atomic weight percent of Pt on each sample analyzed in HAADF-STEM……...…128

Table S6.1 Number of images analyzed, and the number of Pt entities counted per image……...139

Table S6.2. Auger Spectroscopy elemental quantification of NCNTs. Reported at. % were acquired from the average value of nine measurements with the error calculated by the sample standard deviation……....140

List of Figures

Figure 1.1. Family tree diagram of common thin film deposition techniques [4]. Processes central to this thesis are highlighted in red……7

Figure 1.2. Schematic diagram demonstrating film deposition using PVD on a structured substrate……...8

Figure 1.3. Schematic diagram demonstrating film deposition using CVD on a structured substrate……...9

Figure 1.4. Schematic diagram demonstrating film deposition using CVD on a structured substrate……..……...10

Figure 1.5. Arrhenius plot outlining the influence of temperature on growth rate of CVD films [17]…….……....12

Figure 1.6. a) Flow process of ALD cycle consisting of two half steps with alternating cycles of precursor and reactant dosing separated by a purge step. b) Practical growth conditions for ALD of particles and thin films. c) Saturating pulse conditions to achieve self-limiting growth…...…13

Figure 1.7. Temperature dependence for the growth of ALD films……..……..14

Figure 1.8. Demonstration of substrate effect on growth rate…….……15

Figure 1.9. Schematic diagram demonstrating film deposition using ALD on a structured substrate…….16

Figure 1.10. Table summarizing materials grown by ALD [21]…….……16

Figure 1.11. Schematic of MLD using bifunctional monomers with “triangular” or “square” functional groups [23]……18

Figure 1.12. Ideally, organic precursor molecules should react with only one surface site with film growth occurring vertically. However, molecules may react twice and polymer chain may have tilt perpendicular to the surface [32]……19

Figure 1.13. Borosilicate glass microcapillary array functionalized using ALD. Film resistance can be tailored to suit the application. Materials with high stable secondary emission properties can be used since they are decoupled from the substrate [45]……..….22

Figure 1.14. Diagram demonstrating the various opportunities that ALD provides for the deposition of nanoparticles. ALD can be used to control (1) the size of particles, and (2), (3), (4) particle composition. The highly uniform nature of ALD can be used to deposit particles over A) high aspect ratio trenches and holes, B) on powders and microspheres and C) on nanostructures substrates such as nanowires [52]……...23

Figure 1.15. (a) – (e) TEM images of 50 cycles of Pt ALD using progressively longer exposures of oxygen. (f) Influence of oxygen exposure partial pressure on Pt nanoparticle size [53]……...24

Figure 1.16. (a) Electron density and (b) refractive index measurements for Al_2O_3: alucone film alloys. (c)Elastic modulus and (d) hardness measurements for Al_2O_3: alucone alloy films [30]….25

Figure 1.17. Various interfacial reactions that can occur at the electrode/electrolyte interface that can be detrimental to battery performance [70]……..……..……..27

Figure 1.18. Schematic for the controlled layer chemistry of aluminum glycerol (AlGL) films used to coat Si nanocomposite electrodes [87]…….……...30

Figure 1.19. a), c) TEM micrograph and b) HAADF-STEM of nano-Si coated with aluminum organic thin film. d) EELS elemental mapping of aluminum organic thin film. e) comparison of cycling capacity of coated and un coated nano silicon and f) rate test of coated nano silicon [88]……...……..31

Figure 1.20. MLD alucone coating for safe high temperature Li-S batteries in carbonate based electrolytes [101] …….…....33

Figure 1.21. Schematic diagram of platinum encapsulated in zirconia nanocages produced using area-selective ALD [108] …….…….35

Figure 2.1. Outline of various components of an ALD S100 Cambridge Savannah tool starting with precursor distribution manifold assembly followed by reactor and exhaust assembly….....46

Figure 2.2. a) Birds eye view of the Gemstar-8 system with labels. b) and c) Interior of ALD reaction chamber demonstrating precursor inlet, outlet, and pressure sensor location. d) Inert gas vapor pressure assist line attached to the organometallic manifold……...……....49

Figure 2.3. a) Schematic drawing of a conventional SEM. b) Outline of electron beam interaction with sample and the various signals that can be produced by this interaction [1]……....51

Figure 2.4. a) Schematic outline for the working principle of FTIR. b) Photo of the Thermo Scientific Nicolet 380 FTIR system used……53

Figure 2.5. a) Schematic outline of various types of light scatter that can occur following sample irradiation with a laser source [4]. b) Photo of the HORIBA Scientific LabRAM HR Raman spectrometer used……...…55

Figure 2.6. a) Schematic outline of Phoenix QCM crystal head assay provided by Colnatec [7]. b) Use of QCM in Gemstar-8 ALD system……..……...57

Figure 2.7**.** a) Schematic outline of operational setup to perform XRR. b) Typical XRR curve outlining the importance of curve features. c) Photo of the Bruker D8 Advance used for XRR….58

Figure 2.8. a) Schematic outline of core-hole excitation by X-rays to higher energy levels and b) generation of Auger electrons via Auger decay to fill empty core-hole states [11]. Measurements of X-ray absorption by c) transmission based techniques and d) electron yield techniques. E) depiction of TEY cascade effect caused by Auger electron emission [12]…….….60

Figure 3.1. SEM images of a) PCNTs and e) NCNTs before ozone treatment; b-d) PCNTs and f-h) NCNTs after ozone treatment at different temperatures for 500 cycles……..68

Figure 3.2. SEM images of NCNTs treated with (a-c) 2s of ozone pulse and (d-f) 4s of ozone pulse using different cycles at 250°C……...…70

Figure 3.3. TEM images a) untreated NCNTs, ozone treated NCNTs at b) 150°C, c) 250°C for 500 cycles…….…….71

Figure 3.4. Raman spectra of a) NCNTs and before and after ozone treatment at different temperatures; b) Comparison of I_D/I_G ratio for NCNTs at different temperatures, ALD cycles, and ozone pulse time…….....72

Figure 3.5. HRTEM image a) untreated NCNTs, and ozone treated NCNTs at b) 150°C, c), d) 250°C. Scale bar in white represents 10 nm……73

Figure 3.6. a) N_2 adsorption-desorption isotherms at 77K and b) pore size distribution of as produced NCNTs and 300°C ozone treated carbon NCNTs…….….74

Figure 3.7. N 1s spectra for NCNTs a) before ozone treatment and b) after ozone treatment at 300°C for 500 cycles…….…….…….....76

Figure S3.1. XPS survey spectrum a) before ozone treatment and b) after 300°C ozone treatment……79

Figure S3.2. High resolution XPS of C 1s spectrum a) before ozone treatment and b) after 300°C ozone treatment……..79

Figure S3.3. Raman spectra of a) PCNTs and before and after ozone treatment at different temperatures; b) Comparison of I_D/I_G ratio for PCNTs at different temperatures, ALD cycles, and ozone pulse time…….80

Figure 4.1. Mechanism of MLD reaction between TMA, EG and TC……89

Figure 4.2. SEM cross section view of MLD films deposited using a sequence of 1:1 with increasing cycling number. Scale bar represents 50 nm……..89

Figure 4.3. Thickness of 1:1, 1:3 and TMA-EG MLD films verses number of deposition cycles at 150°C…….…90

Figure 4.4. FTIR spectra for 100nm thick TMA-EG, 1:1 and 1:3 MLD films deposited on double polished Si at 150°C……..…….91

Figure 4.5. Raman spectra for a) 1:1 and b) 1:3 MLD films with initial thickness of 200nm annealed with 5% H_2/Ar at 600, 700, 800 and 900°C for 1 hour……...…..92

Figure 4.6. Sheet resistance measurements for 100nm thick TMA-EG, 1:1, and 1:3 MLD films pyrolyzed at various temperatures……..……94

Figure 4.7. Synchrotron based XPS of a) as deposited and b) 800°C pyrolyzed TMA-EG and 1:3 MLD films……..95

Scheme 5.1. Schematic representation for preparation of hybrid inorganic-organic polyurea MLD films using trimethylaluminum (TMA), ethylene diamine (ED) and 1,4 phenylene diisocyonate (PDIC)…….….105

Figure 5.1. a) Growth rate comparison between PDIC-ED (triangle) and TMA-ED-PDIC (circle) and b) QCM data for one cycle of TMA-ED-PDIC. Saturation conditions for c) PDIC, d) ED, e) TMA…….106

Figure 5.2. FTIR spectra of PDIC-ED (black) and TMA-ED-PDIC (red) films grown on double polished Si. Characteristic polyurea bonds are outlined……...…107

Figure 5.3. a) C 1s and b) N1s NEXAFS spectra of 25 nm TMA-ED-PDIC and PDIC-ED polymers grown at 50°C acquired using total electron yield……...…….108

Figure 5.4. Polarization dependent NEXAFS data taken at for a) PDIC-ED b) TMA-ED-PDIC..110

Figure 5.5. Interpretation of NEXAFS orientation signatures for disordered films. (a) Polarization dependence of the π* bond with fits using the model with fixed tilt angle. Using a model assuming that π* orbitals have random azimuthal orientation and Gaussian distribution of tilt angles with an average tilt τ. The width of this distribution, serves as an orientation disorder parameter. The smaller δ is the more ordered the system is. (b) Solutions to τ and δ using A_π values for TMA-ED-PDIC and ED-PDIC. (c) Schematic diagram outlining the significance of τ and δ values…...….112

Figure 5.6. Depiction of structural morphology of (a) hybrid inorganic-organic polyurea films and (b) pure organic polyurea films…….……113

Figure 6.1. HAADF-STEM images of ALD Pt deposition on NCNTs at 250°C using a dosing time of (a) 1 minute, (b) 30 minutes, and (c) 60 minutes. Experimental (d) PSD histograms were acquired from six different NCNTs for each sample. Image quantification steps and raw/processed images can be found in the supporting information……..…126

Figure 6.2. PSD comparison for (a) a 1 minute exposure of Pt to NCNTs at a temperature of 100°C, 175°C, and 250°C, and (b) a 30 minute exposure of Pt to NCNTs at a temperature of 100°C and 250°C……...128

Figure 6.3. HAADF-STEM images of single pulsed Pt deposited at 250°C on a (a) NCNT and (b) PCNT for a 1 minute exposure. PSD comparison of (c) a 1 minute exposure on NCNTs and PCNTs and (d) a 1 minute and 30 minute exposure on PCNTs……..129

Scheme 6.1. Representation of the chemisorption of $MeCpPtMe_3$ species on defective graphene and graphene oxide……...……130

Figure 6.4. (a) Pt L_3-edge XANES of samples prepared using varying dosing times of $MeCpPtMe_3$ on NCNTs and PCNTs at 250°C along with standard Pt and PtO_2. (b) Pt L_3 edge k^2-weighted FT-EXAFS spectra of samples presented in (a) in solid lines and their corresponding best fits as dotted lines……..…133

Figure S6.1. Experimental steps used for the quantification of the Pt equivalent diameter. 60 minute Pt dosing time at 250°C (a) calibrated raw HAADF image. ImageJ was used to subtract the (b) background from (a), thus forming the (c) background subtracted image. Pt was then (d) manually removed using the polygon selection tool in ImageJ. Digital Micrograph software was used to subtract image (d) from (a) to produce image (e), wherein the (f) threshold was adjusted, and the image was (g) analyzed with ImageJ……..…..136

Figure S6.2 Error analysis for the Pt quantification process. Histogram showing the (a) total counts for the Pt entities as a function of the number of pixels, summed from a five day data analysis of a single image. (b) Fitted Gaussian model and parameters from the low range peak in (a)……..138

Figure S6.3 Error analysis results from a five day study of a single HAADF image with bins showing the experimental error. Data analysis from a single image showing (a) each individual analysis over five days and (b) the mean and standard deviation for each bin from the five day measurement. The errors in (b) represent the error introduced into the measurement from the manual process…….....138

Figure S6.4 High energy EELS analysis of Pt deposited on NCNTs for 60 minutes at a temperature of 250°C was imaged using ADF (a) before and (b) after the EELS acquisition. The (c) ADF image corresponding to the (d) spectrum image shows that the bright spots correlate to a Pt-L edge, as shown in the (e) extracted spectra from the areas outlined in (c) and (d)……...142

Figure S6.5. PSD histograms from (a) NCNTs at 100°C using a dosing time of 1 minute, and 30 minutes, and (b) NCNTs and PCNTs at 250°C using a dosing time 30 minutes……....142

Figure 7.1. Galvanostatic cycling of Li-Li symmetric cells at a current density of 1 mA cm^{-2} until a capacity of 1 mAh cm^{-2} is reached. Cells are cycled in EC/DEC/DMC electrolyte with 1M $LiPF_6$……153

Figure 7.2. Galvanostatic cycling of Li-Li symmetric cells at a current density of 3 mA cm^{-2} until a capacity of 2 mAh cm^{-2} is reached. Cells are cycled in EC/DEC/DMC electrolyte with 1M $LiPF_6$……155

Figure 7.3. a) First few cycles of GITT data for bare Li outlining an envelope voltage pattern. b) Cells are cycled using a 15s current pulse at a density of 5 mA cm^{-2} followed by a rest period of 3 minutes until a capacity of 5 mAh cm^{-2} is attained. c) 10 GITT cycles for bare Li cell…….158

Figure 7.4. GITT experiments for half-cell configurations of TMA-GLY or TMA-H2O as either anode and cathode against bare Li. Schematic outline for configuration employed can be found at the top right corner of each graph…….……159

Figure 7.5. Cross section SEM images of lithium surface following 1st half cycle (0-a) using GITT (top row) and top view SEM images of the same electrodes after 5 galvanostatic cycles. Scale bar in white represents 100 μm……...……161

Figure 7.6. RBS spectra and calculated depth profile for bare Li (a, d), TMA-H2O coated Li (b, e), and TMA-GLY coated Li (c, f) following 60 cycles of plating and stripping at 3 mA cm^{-2} using a capacity of 2 mAh cm^{-2}……..163

Figure S7.1. Galvanostatic cycling of Li-Li symmetric cells at a current density of 3mA cm^{-2} until a capacity of 1mAh cm^{-2} is reached……..164

Figure S7.2. Galvanostatic cycling of Li-Li symmetric cells at a current density of 5mA cm^{-2} until a capacity of 1mAh cm^{-2} is reached……..……164

Figure S7.3. GITT experiments for half-cell configurations of TMA-GLY anode and cathode against bare Li. Schematic outline for configuration employed can be found at the top right corner of each graph……165

Figure S7.4. GITT experiments for half-cell configurations of TMA-H2O anode and cathode against bare Li. Schematic outline for configuration employed can be found at the top right corner of each graph……169

List of Appendices

Appendix A: Permission from AIP for Published Article……..……...179

Appendix B: Permission from Elsevier for Published Article……..180

Appendix C: Permission from ACS for Published Article……....181

List of Abbreviations

AEY	Auger electron yield
ALD	Atomic layer deposition
BET	Brunauer-Emmett-Teller
BJH	Barrett-Joyner-Halenda
BN	Boron nitride
CFM	Cubic feet per minute
CLS	Canadian light source
CNTs	Carbon nanotubes
CVD	Chemical vapor deposition
DEC	Diethyl carbonate
DMC	Dimethyl carbonate
EC	Ethylene carbonate
ED	Ethylenediamine
EELS	Energy electron loss spectroscopy
EFSTEM	Energy filtered scanning tunneling electron microscopy
EG	Ethylene glycol
EHMO	Extended Huckle molecular orbital
EMC	Ethyl methyl carbonate
EXAFS	Extended X-ray absorption fine structure
FTIR	Fourier transform infrared spectroscopy

GITT	Gravimetric intermission titration technique
GLY	Glycerol
GPC	Growth per cycle
HAADF	High angle annular dark field scanning
HER	Hydrogen evolution reaction
HOPG	Highly oriented pyrolytic graphite
HOR	Hydrogen oxidation reaction
HRTEM	High resolution transmission microscopy
ICP-AES	Inductively coupled plasma optical emission spectroscopy
IR	Infrared
LIB	Lithium-ion battery
Li-S	Lithium sulfur battery
MCP	Microchannel plate
$MeCpPtMe_3$	trimethyl(methylcyclopentadienyl)-platinum (IV)
MFC	Mass flow controller
MLD	Molecular layer deposition
MOCVD	Metal-organic chemical vapor deposition
NCNT	Nitrogen doped carbon nanotube
NEXAFS	Near-edge X-ray absorption find structure
NP	Nanoparticle
OER	Oxygen evolution reaction
ORR	Oxygen reduction reaction

PCNT	Pristine carbon nanotubes
PDIC	1,4 phenylene diisocyonate
PSD	Particle size distribution
PVD	Physical vapor deposition
QCM	Quartz crystal microbalance
RBS	Rutherford backscattering spectroscopy
ROI	Region of interest
RT	Room temperature
S100	Savannah 100 ALD system
SEI	Solid electrolyte interphase
SEM	Scanning electron microscope
STEM	Scanning transmission electron microscopy
TC	Terephthaloyl chloride
TEM	Transmission electron microscopy
TEY	Total electron yield
TFEL	Thin film electroluminescent
TMA	Trimethylaluminum
VLS-PGM	Variable line spacing plane grating monochromator
XAFS	X-ray absorption fine structure
XANES	X-ray absorption near edge spectroscopy
XPS	X-ray photoelectron spectroscopy
XRR	X-ray reflectivity

1

Introduction and Literature Review

1.1 Introduction to This Thesis

1.1.1 Energy Storage and Conversion

It is often said that necessity is the mother of innovation. This statement holds true for global warming, As it becomes an increasingly pertinent issue certain technological fields have experienced rapid advancement. and this certainly is the case for global warming. One avenue toward curbing the progression of global warming, is shifting away from the use of fossil fuels. Unfortunately, 85% of the worlds energy use is currently derived from fossil fuel sources [1]. This rate of consumption is not sustainable and maintaining our present course will lead to irreversible and unanticipated consequences to our complex climate system. Although fossil fuels will continue remain a significant source of energy in the next few decades, a path toward a more sustainable means of energy production use can be envisioned. This path would involve transitioning to clean and renewable energy sources such as solar and wind. Transmission and distribution of electricity would also need to be accurately controlled to allow for efficient use of energy. Additionally, major disruptions within the chemical industry need to occur so that CO_2 and H_2O can be economically converted to produce fuels and chemicals to serve our desired needs rather than relying on oil and gas feedstocks.

For this path to be attainable, significant advancements in the field of energy storage and conversion are required. Electricity produced from intermittent sources, such as solar and wind, need to be stored in energy storage devices so that it may be distributed and transmitted efficiently. Numerous energy storage systems are currently available such as pumped hydro storage, flywheel energy storage, and compressed air energy storage [2]. However, electrochemical energy storage systems are uniquely positioned to address future energy storage needs. Lithium-based batteries have dominated the rechargeable battery market due to their high gravimetric energy density.

Furthermore, as we move toward a more design-oriented world, a need for energy storage devices with high volumetric energy density is required. Lithium-based batteries, especially all-solid-state batteries, can address this need. These distinct characteristic makes them ideal for use in electric vehicles. Electrification of the transportation sector would result in significant reduction in the production of environmental pollutants caused combustion of fossil fuels.

Currently the successful use of hydrogen as a fuel source is a scientific and technological challenge and remains elusive. However, if addressed appropriately this technological achievement would significantly change our use of fossil fuels and provide an opportunity toward achieving energy sustainability. One method toward achieving a sustainable hydrogen economy is accurate control over the water splitting reaction, $2H_2O \rightarrow 2H_2 + O_2$. This reaction can be broken down into four half reactions: hydrogen evolution reaction (HER), oxygen evolution reaction (OER), hydrogen oxidation reaction (HOR), and oxygen reduction reaction (ORR). Both the HOR and ORR reaction can be utilized in fuel cell devices that convert hydrogen or some other fuel source into water while the HER and OER reaction are used for hydrogen fuel production. For these reactions to occur in the economically efficient manner the use of precious metal catalysts are required. Developing effective catalysts that can easily facility bond-making and bond breaking reaction at the electrode-electrolyte interface remains a key priority for materials scientists working in this field [3].

For this envisioned sustainable energy economy to be successful, several scientific and technological challenges first need be addressed. Many of these challenges are materials related and require innovative solutions by materials scientists.

1.1.2 Atomic and Molecular Layer Deposition

Atomic layer deposition (ALD) is a vapor phase technique used to deposit thin films and nanostructures. It is a technique that has pushed the advancement of semiconductor technology and hold promise for application in the field of energy storage and conversion. As materials become increasingly complex and move toward the nanoscale regime, coating techniques that can provide accurate control of growth and material composition becoming increasingly necessary. ALD can provide both these advantages due to its cyclic, self-saturating nature. This advantage results in ALD being the technique of choice for coating nanomaterials compared to other deposition techniques such as chemical vapor deposition and physical vapor deposition. In general,

the ALD process consists of introducing gaseous chemical precursors that can react to the substrate. Additionally, a purge step separates precursor introduction ensuring that gas-surface reactions occur as half-reactions. This allows for each dose of the precursor to completely react with the substrate through a self-limiting process. As a result, ALD is a non-line-of-sight technique that can conformally coat complex, nanostructure substrates in a pin-hole free manner. Although ALD can be used to grow thin films, careful selection of substrate and chemical precursor can allow for the growth of nanoparticles. This imparts ALD with the ability to grow particles with angstrom level control. Furthermore, particles can be grown in a non-line-of-sight fashion on nanomaterials, providing an optimal route in taking advantage of high surface area to volume materials.

While ALD is typically used to grow inorganic materials, molecular layer deposition (MLD) can be used to grow organic polymeric materials. MLD is based on the same fundamental principles as ALD and involves the use of self-limiting surface reactions. However, MLD introduces a molecular fragment being deposited during each ALD cycle rather than an inorganic one that is either oxidized or reduced. Furthermore, ALD and MLD can be combined to create hybrid inorganic-organic materials and provides many exciting opportunities for materials scientists. By combining the properties of inorganic materials with that of organic ones, unique coating materials and nanostructures can be produced by ALD and MLD with tunable properties. Furthermore, nanolaminate materials can be produced with these two techniques to create novel properties.

ALD and MLD are two powerful techniques that can be used to address challenges faced by materials scientists. These techniques provide an avenue toward engineering material properties and allow scientists to expand the capabilities of currently available materials.

1.2 Thesis Objectives

This thesis focuses on understanding material surface properties and developing novel thin films and nanostructures. This understanding is then applied to enhance materials with potential use in lithium-based batteries and fuel cells. The main research objects are listed below:

Part 1. Understanding surface properties and development of novel nanomaterials and thin films

1. To understand the influence of ozone based ALD techniques on carbon nanotubes and nitrogen doped carbon nanotubes.
2. Development of thin films with tunable conductivity by combining the techniques of ALD and MLD.
3. To develop a polyurea based films by ALD and MLD that have a high degree of hydrogen bonding. Further, understanding the influence of these techniques on polymer properties such as orientation and packing order is explored. Synchrotron based radiation is used to determine film properties.

Part 2. Application of ALD and MLD to energy storage and conversion

1. To understand the deposition characteristics of Pt on nanomaterial substrates. Different deposition parameters are explored in order to try and develop a process that can accurately control the growth of Pt from single atoms to clusters.
2. Apply techniques of ALD and MLD to metallic lithium electrodes. To control reactions at the electrolyte/electrode interface, various ALD and MLD coatings with different properties are applied to Li foil. The effects of lithium electroplating and electrodissolution on these coatings are explored and discussed.

1.3 Thesis Organization

This thesis consists of eight chapters, an introductory chapter, an experimental chapter, five articles and one conclusion chapter. It is organized according to the requirements outlined by the Thesis Regulation Guide provided by the School of Graduate and Postdoctoral Studies at the University of Western Ontario in the form of an "integrated-article". The following parts are included

Chapter 1 introduces various gas phase deposition techniques to provide background fundamental knowledge. This platform is then used to describe the techniques of atomic layer deposition (ALD) and molecular layer deposition (MLD). A literature review is provided as to the use of these two techniques in modifying and engineering surface material properties. This is expanded upon by examining the potential use of ALD and MLD in the field of energy story and conversion.

Chapter 2 describes and explores the various tools used in this thesis to perform ALD and MLD. An outline of the different characterization techniques is also provided along with their background knowledge and theory.

Chapter 3 presents a study on the effect of ozone on carbon nanotubes and nitrogen doped carbon nanotubes. The influence of ozone on these two substrates is systematically explored. Control of ozone exposure is conducted by using an ALD tool and various material properties are examined.

Chapter 4 outlines the development of a novel aluminum alkoxide film with tunable composition between aluminum and carbon. Post-treatment annealing of this film allowed for a control over electronic conductivity. Synchrotron radiation and Raman spectroscopy is used to determine film properties before and after annealing and is used to establish the origin of electronic conduction.

Chapter 5 reports a novel inorganic-organic polyurea film by ALD and MLD. Polarization dependent near-edge x-ray absorption spectroscopy is used to determine film properties of organic polyurea polymers and the newly developed inorganic-organic polyurea polymer.

Chapter 6 outlines the processes that influence the deposition of single atoms and ultra-small clusters on Pt on nitrogen-doped carbon nanotubes and pristine carbon nanotubes. Varying exposures of trimethyl(methylcyclopentadienyl)-platinum without the use of an oxidizing pulse at various temperatures are used to determine the self-limiting characteristics of this Pt precursor. High-angle annular dark field scanning transmission electron microscopy and synchrotron radiation are used characterize Pt nanostructures produced by ALD.

Chapter 7 explores the use of three different ALD and MLD films for protecting the surface of metallic Li for use as an anode in lithium-based batteries. The stripping and plating behavior of Li coated with 50 cycles of either trimethylaluminum (TMA)-water, TMA-ethylene glycol, TMA-glycerol are examined using galvanostatic cycling and gravimetric intermission titration technique. Using Rutherford backscattering spectroscopy, the composition of the solid electrolyte interphase is examined and discussed.

Chapter 8 summarizes the results and contribution of this thesis. Additionally, the author states future perspectives of the use of ALD and MLD in energy storage and conversion and the unique future capabilities that these techniques can provide.

1.4 Introduction to Fundamentals

This section will introduce the primary theoretical and practical concepts central to this thesis. The overarching theme of this section is to explore the underlying principles that allow for the practical application of nanostructures produced by atomic and molecular layer deposition. First, fundamentals of physical vapor deposition (PVD) and chemical vapor deposition (CVD) will be discussed followed by an introduction to atomic layer deposition (ALD) and it's analogue, molecular layer deposition (MLD). Factors that influence the growth of thin films and nanostructures will also be explored. The aim of this section is to demonstrate how the fundamental physical properties of gas phase deposition techniques can be used to accurately control the growth of thin films and nanostructures.

1.4.1 Gas Phase Deposition Techniques

Many scientific and technological achievements have been made possible by advancements in the field of thin film deposition. Gas, vapor, liquid, or solid phase methods can produce a wide range of thin film materials. Thin film deposition technologies typically fall into two main categories: Gas phase processes and liquid phase processes. Gas phase processes include physical vapor deposition (PVD), chemical vapor deposition (CVD), and atomic layer deposition

(ALD). Figure 1.1 presents an outline of the various deposition techniques than can be used to produce thin films.



Figure 1.1. *Family tree diagram of common thin film deposition techniques* [4]. *Processes central to this thesis are highlighted in red.*

1.4.2 Physical Vapor Deposition

Physical vapor deposition (PVD) involves the evaporation of a target material to produce a vapor that is transferred through the gas phase and deposited on a substrate. PVD is used to deposit films with a thickness in the range of a few nanometers to microns [5]. Sputtering is one type of PVD process that involves bombarding a target material with ions or accelerated charged under high vacuum. Due to the large amount of kinetic energy imparted by the incident particle, atoms are dislodged from the surface and transported to a substrate to form a thin film [6]. Using

this process many different types of materials can be deposited including metals and metal oxides. For example an aluminum target can be sputtered in the presence of oxygen to form a layer of aluminum oxide [7]. The deposition rate of sputtering can be as low as 1 nm/s and scales with power. Another type of PVD process is evaporation. Rather than bombarding a surface with high energy particles, evaporation relies on heating a target metal in a crucible and transporting the evaporated atoms to a substrate. This low temperature vacuum technique allows evaporated atoms to travel to a surface with minimal interference and is ideally suited for creating films of pure metals [8]. Evaporation PVD is ideally done for elements with low melting points, such as gold. The growth rate for evaporation PVD is low and ranges between 0.1 – 1.0 nm/s. Although PVD allow for a high degree of control over material composition, it is referred to as a "line of sight" technique and is not well suited for coating substrates with complex geometry. Because the reactive species is transported in a vacuum, there is little chance for collision and the vapor tends to travel in a straight-line, resulting in low deposition on trench walls, as highlighted in Figure 1.2 Furthermore, films produced by PVD are not chemically bonded to the surface and have relatively low surface adhesion properties [9].

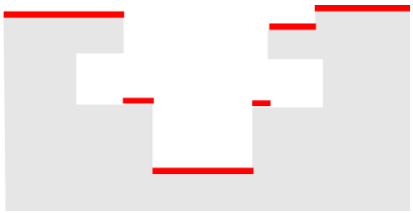


Figure 1.2. *Schematic diagram demonstrating film deposition using PVD on a structured substrate where deposition only occurs on surfaces in the line of sight of the target.*

1.4.3 Chemical Vapor Deposition

Chemical vapor deposition (CVD) is a gas-phase thin film deposition technique involving the introduction of a continuous flow of chemical precursor over a substrate. Precursor reaction may occur both in the gas phase and/or on the substrate. CVD processes are quite complicated and may involve several reactions occurring simultaneously and include hydrolysis, reduction, disproportionation, oxidation, carburization, nitridation and thermal decomposition [10]. There are many ways to initiate the chemical reaction including thermal energy (thermal CVD)[11], ultraviolet light (photo-assisted CVD) [12] or plasma (plasma-enhanced CVD) [13]. The most

relevant type of CVD to the scope of this thesis is metal-organic CVD (MOCVD) and involves the use of a metal-organic compound, containing a direct metal-carbon bond being introduced into the reaction chamber. However, the definition of MOCVD can be extended to precursors that have metal-nitrogen bonds (metal alkylamides), metal-oxygen bonds (metal-alkoxides) and metal hydrides [14]. Pressure plays an important role in CVD reactions and can be evaluated by the Damköhler number (D_a).

$$D_a = \frac{Reaction\ rate}{mass - transfer\ rate}$$

The Damköhler number can be used to help distinguish whether the rate-limiting step for film deposition is due to mass-transfer effects or reaction rate [15]. For $D_a \gg 1$, mass-transfer is the rate limiting step while for $D_a \ll 1$, mass-transfer occurs more rapidly than the reaction and the CVD process is said to be kinetically controlled. By employing a vacuum during the CVD process, a lower D_a number can be achieved. This means that the rate of mass transport increases at lower pressures thereby allowing the substrate to approach a phase closely related to the bulk gas phase, making deposition less dependent on mass transport and more dependent on reaction kinetics. This increases film uniformity and conformality, but comes with a penalty to deposition rate if reaction rates are slow. Because CVD is done at moderate pressures, the mean free path of precursor molecules is reduced, increasing the scattering in all direction [15]. This results in both surface and gas phase reactions and therefore increased conformality compared with PVD, as shown in Figure 1.3.

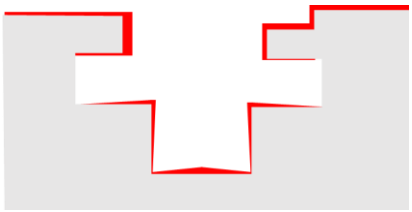


Figure 1.3. *Schematic diagram demonstrating film deposition using CVD on a structured substrate where deposition is limited to certain areas.*

The sequence for CVD reaction involves several steps, beginning with vapor phase deliver to the reaction chamber, proceeded by a series of quasi steady-state processes occurring at the substrate surface. An important feature of the CVD process is the presence of a hot layer of gas just above

the substrate called the “boundary layer” [15]. This sequence is schematically illustrated in Figure 1.4.

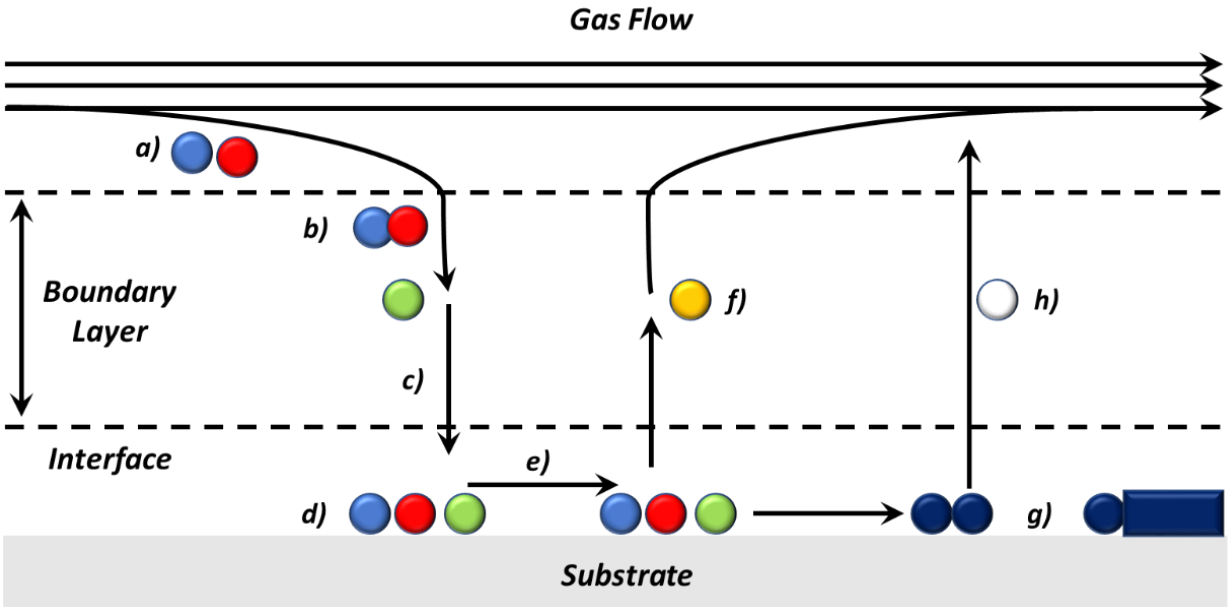


Figure 1.4. *Schematic outline of a MOCVD process.*

a) *Precursor introduction:* Precursor is introduced into the reaction chamber by an inert gas as a vapor.

b) *Gas phase reactions:* Depending on the precursor employed, reactions may occur in the gas phase, resulting in non-uniform nucleation and formation of powder on the surface. The occurrence of this process should be reduced as much as possible to maintain film uniformity.

c) *Transfer of precursor to substrate:* As the precursor crosses the boundary layer, the carrier gas transfers precursor vapor to the substrate surface. The gaseous layer between the substrate and the position where the gas flow velocity is maximum, is called the boundary layer. The rate of diffusion here depends on the total reactor pressure, temperature, and concentration of precursor molecules in the gas phase present above the boundary layer.

d) *Reaction of precursor to substrate:* Following diffusion through the boundary layer, precursor molecules are absorbed on the substrate.

e) *Surface diffusion:* Adsorbed precursor particles do not necessarily have to be static on the surface and have been shown to be mobile on the substrate surface. This is a factor that may contribute to the growth of islands and particles during CVD.

f) *Desorption of Precursor:* Desorption and mass transport of decomposed precursor may occur on the surface and is dependent on surface functionality as well as precursor reactivity.

g) *Nucleation, island growth, and film growth:* Surface chemical reaction leading to growth of islands and particles or film depending on surface reaction sites. Precursors either react with neighboring molecules, with the substrate or with molecules in the gas phase to form a film.

h) *Desorption of volatile surface reaction products:* Volatile reaction by-products and unreacted precursor molecules are pushed out from the reactor by carrier gas.

Growth of films by thermal CVD is determined by several different parameters including, substrate temperature, reactor pressure, and gas-phase chemistry. The growth rate of films produced using CVD can be limited by either surface reaction kinetics, or mass transport of precursor to the substrate. Figure 1.5 presents an Arrhenius plot outlining the influence of temperature on growth rate. Three different regions can describe this reaction process. The first region is characterized by low temperatures and low pressures and is known as the precursor depletion region and film growth is determined by surface reaction kinetics. With a lower reactor pressure, a thin boundary layer is formed, and reactants can easily reach the surface. As temperature increases film growth enters a diffusion controlled region where almost all precursor molecules react to the substrate to form a film. This region is said to be independent of substrate temperature and is a key component to achieving highly uniform and conformal films. Further increasing the temperature results in a region controlled by reaction kinetics. As temperature and pressure increases, a thicker boundary layer is formed and precursor diffusion to the surface becomes difficult. Furthermore, diffusion of by-products produced at the surface becomes difficult due to increased thickness of the boundary layer. Therefore, the rate of film growth is limited by kinetic processes such as precursor adsorption, surface reactions and desorption of reaction by-products [16].

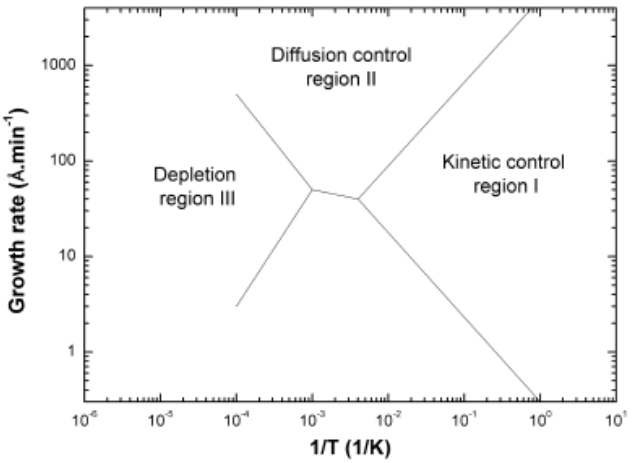


Figure 1.5. *Arrhenius plot outlining the influence of temperature on growth rate of CVD films* [17].

1.4.4 Atomic Layer Deposition

Atomic layer deposition is an analogue of CVD but allows for increased control over film thickness and provides enhanced film conformality over high aspect-ratio surfaces. In CVD, two or more precursors are introduced simultaneously into a reaction chamber. ALD separates introduction of precursor so each can react as two half reactions. By sequentially introducing precursors into the reaction chamber, each precursor can chemisorb onto the substrate surface until all reaction sites are consumed in a self-saturation process. Once all surface sites are saturated, excess precursor and reaction by-products are removed with an inert gas using a purge step. This is followed by introduction of a second reactant which can react to the chemisorbed precursor initially introduced. This process continues until all reaction sites are consumed and self-saturation is achieved. Another purge step is then performed to remove excess reactant and reaction by-products, thus completing one ALD cycle. This pulse-purge-pulse-purge process, coupled with self-saturating behavior, allows ALD to deposit thin film with angstrom level control. However, in practicality, it is unlikely that a fully formed monolayer is deposited with each half cycle. For this to happen several conditions need to be fulfilled, including ensuring precursor stability throughout its introduction to the substrate and complete homogeneity of surface functionality. A more accurate description of film morphology would be the deposition and nucleation of nanoparticles or a partial coating which eventually stitches together over subsequent cycles [18]. Growth rate for ALD is typically calculated by measuring film thickness and dividing by the

number of ALD cycles employed. This is commonly referred to as growth per cycle (GPC). Figure 1.6 provides a schematic outline of a typical ALD process.

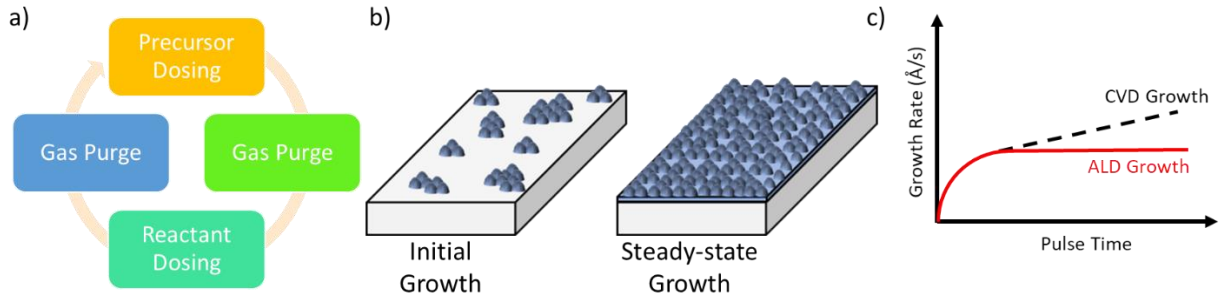


***Figure 1.6**. a) Flow process of ALD cycle consisting of two half steps with alternating cycles of precursor and reactant dosing separated by a purge step. b) Practical growth conditions for ALD of particles and thin films. c) Saturating pulse conditions to achieve self-limiting growth.*

The reaction scheme outlined above is dependent on several physical properties including precursor stability, reactivity, volatility, and reactor temperature. Precursor chemistry is crucial to achieving good ALD of thin films and several precursor requirements need to be met. ALD precursors must be thermally stable in the gas phase and not react with surrounding precursor molecules, but still be reactive enough to undergo chemisorption on the surface. The precursor must also be volatile and have a low melting point to allow for sufficient vapor to be drawn by the vacuum during a pulse step. This can be achieved by choosing compounds that have a low molecular weight and ligands with branching asymmetry that are coordinatively saturated to the central atom. Another important for achieving a self-limiting monolayer by an ALD precursor is steric protection of the central atom. This reduces chances for reaction to occur with other precursor molecules in the gas phase [19]. The range of temperatures for which these properties are favorable is known as the ALD window, as shown in Figure 1.7. If these stringent requirements are not met decomposition of precursor in the gas phase may occur and result in higher than expected growth rates and CVD type film formation.

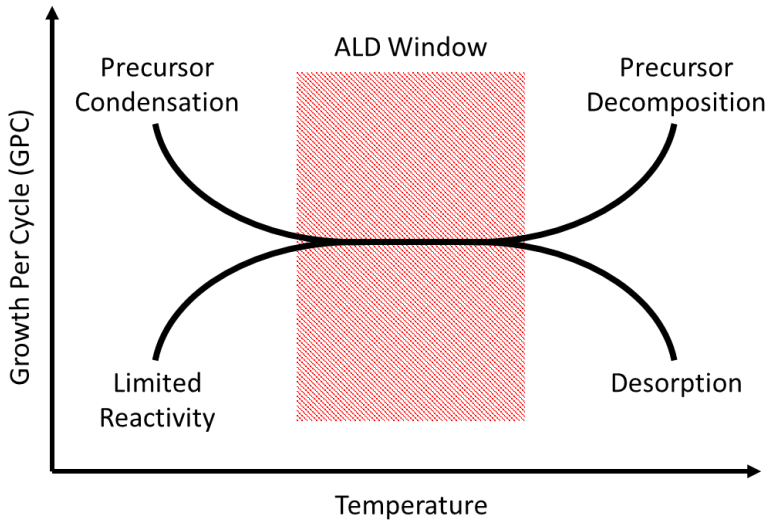


Figure 1.7. *Temperature dependence for the growth of ALD films.*

The linear growth observed for ALD processes stem from self-limiting characteristics. However, as mentioned earlier, the initial stages of ALD film growth is likely to occur in a non-linear fashion. This is dependent on surface adsorption and reaction of precursor to the substrate and is related to surface chemistry. With continued deposition, the effect of the original substrate is lost and steady state growth can be achieved [20]. If GPC is higher for the first few cycles, this growth is referred to as substrate-enhanced growth. If growth is initially impeded the GPC is referred to as being substrate-inhibited. Finally, if the substrate has an insignificant effect on GPC, then ALD proceeds in a linear fashion [21]. Nucleation of ALD is important for the deposition of continuous pin-hole free films. A lack of uniform nucleation sites results in island like growth and results in the deposition of nanoparticles (NPs) that follow a Volmer-Weber growth pattern [22]. This can be advantages for the deposition of NPs by ALD and fine tuning of this feature can allow for NP growth on high aspect ratio structures. This is especially useful for the deposition of noble metal catalysts.

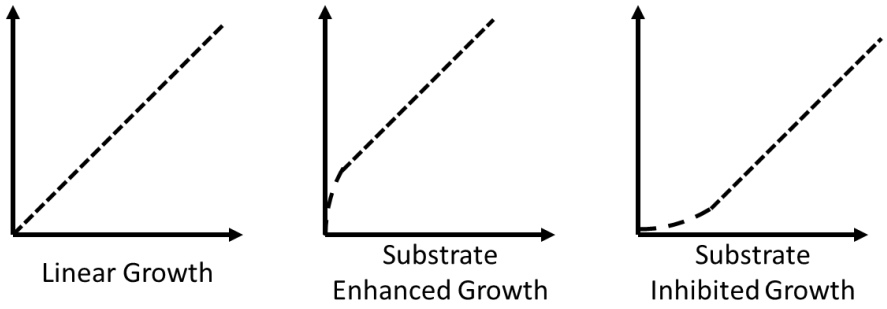


Figure 1.8. *Demonstration of substrate effect on growth rate.*

Three chemisorption mechanisms can occur in an ALD reaction to achieve self-limiting characteristics. This first is a ligand exchange reaction mechanism where the precursor molecules (ML_n) splits on the surface. The ligand (L) combines with a surface group ||-a to form a volatile compound that can be purged away as by-product, aL. The remaining part of the molecule then chemisorbs to the surface as a ML_{n-1} species. Ligand-exchange reactions can proceed for more than one ligand and can also occur for adsorbed ML_z species and surface groups. These reactions release ligands as aL and consume additional ||-a groups, thereby reducing available sites for metals to bond. The second type of self-limiting reaction is a dissociation reaction. This involves a splitting of the reactant molecule between two reaction sites on the surface. Similar to the ligand exchange reaction, dissociation may continue on the surface, but it does not affect the number of bonded M atoms and the number of bonded ligands. The third type of reaction mechanism that can occur is the association reaction. This reaction proceeds by forming coordinate bonds with reactive surface sites. In association reactions there is no release of ligands [21].

Ligand Exchange: ||-a + ML_n (g) ---> ||-ML_{n-1} + aL (g)

Dissociation Reaction: ||-a + ||-b + ML_n (g) ---> ||-a- ML_{n-1} + ||-b- L

Association Reaction: ||-a + ML_n (g) ---> ||-a-ML_n

The growth mechanism in ALD is unique and different from both CVD and PVD. By splitting the introduction of precursor into two separate self-saturating half reactions, film conformality is greatly improved. Compared to PVD and CVD, which are considered line-of-sight techniques, ALD is a non-line of sight technique that can conformally coat high aspect ratio structures. Conformal step coverage occurs when reactants migrate rapidly after adsorption on step surfaces. However, this comes with a penalty to deposition time. ALD deposition can range from 0.01nm/cycle to 1 nm/cycle, with cycle time being up to 2 min/cycle depending on ALD reactor, substrate, and precursor used. ALD processes are typically used for the deposition of solid inorganic materials. Materials by ALD are grown as oxides, nitrides, sulphides, selenides, tellurides, pure elements, and others. Figure 1.10 presents an overview of all the inorganic materials deposited using ALD.

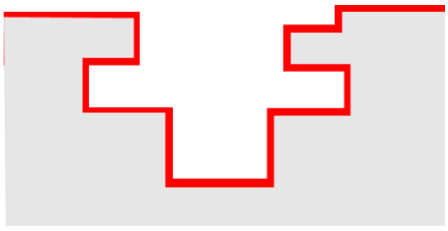


Figure 1.9. *Schematic diagram demonstrating film deposition using ALD on a structured substrate where deposition occurs uniformly across the surface.*

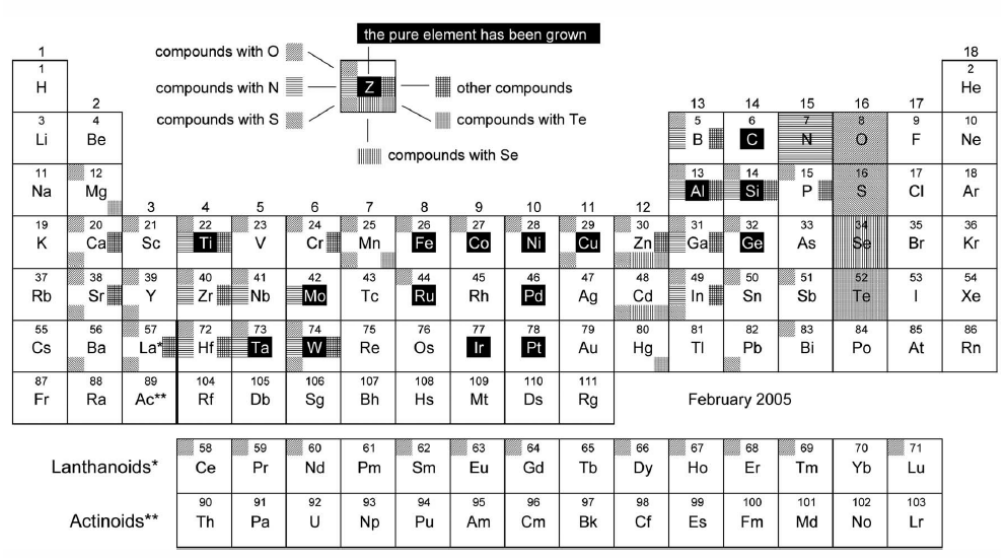


Figure 1.10. *Table summarizing materials grown by ALD [21].*

1.4.5 Molecular Layer Deposition

Molecular layer deposition (MLD) is an extension of ALD and is used to deposit organic materials. Similar to ALD, an MLD cycle is comprised of two precursor doses separated by purge/evacuation step between each dose to remove excess precursor molecules as well as reaction by-products. During each dose, a bifunctional precursor molecule reacts with the appropriate surface groups. A key difference between ALD and MLD is the linking chemistry used. During ALD, a metal precursor is reacted with another compound to remove ligands and regenerate surface functionality. MLD utilizes various linking chemistries and is dependent on precursor bifunctionality, which can be represented in an A-L-A and B-M-B format. In these precursors, "A" and "B" are chemical functional groups, such as chlorides, amines, hydroxyls, carboxylic acids, and/or acid chlorides, while "L" and "M" are organic carbon-based fragments. Some of the first organic MLD processes involved condensation polymerization reactions to form surface bonded polymeric materials [23]. This versatile chemistry can be used to deposit thin conformal organic polymers such as polyamides[24], polyimides[25], and polyureas[26]. Furthermore, some of these organic precursors can also be mixed with the inorganic precursors from ALD to define a new class of hybrid organic-inorganic material. For example, a metal alkyl, such as trimethylaluminum (TMA), can react with a diol, such as ethylene glycol to produce an aluminum alkoxide species. The metal alkyl molecule is described as MR_x, while the diol is represented as HOR'OH. The general MLD reaction can be written as, with * denoting a surface species [27]:

$$MR^* + HOR'OH \rightarrow M\text{-}OR'OH^* + RH$$
$$R'OH^* + MR_x \rightarrow R'O\text{-}MR_{x-1}^* + RH$$

Hybrid organic-inorganic materials can provide precisely turned mechanical, optical, chemical and electrical properties [28]. Development of new hybrid organic-inorganic materials is dependent on the methods used to prepare these materials. Relatively simple inorganic-organic composite materials may be used to create complex hybrid frameworks such as superlattices and nanolaminates from alternating inorganic and organic layers [29]. Furthermore, these hybrid organic-inorganic films have properties that range between pure organic and inorganic films and allow for control over density [30], refractive index, elastic modulus, and hardness [31] .

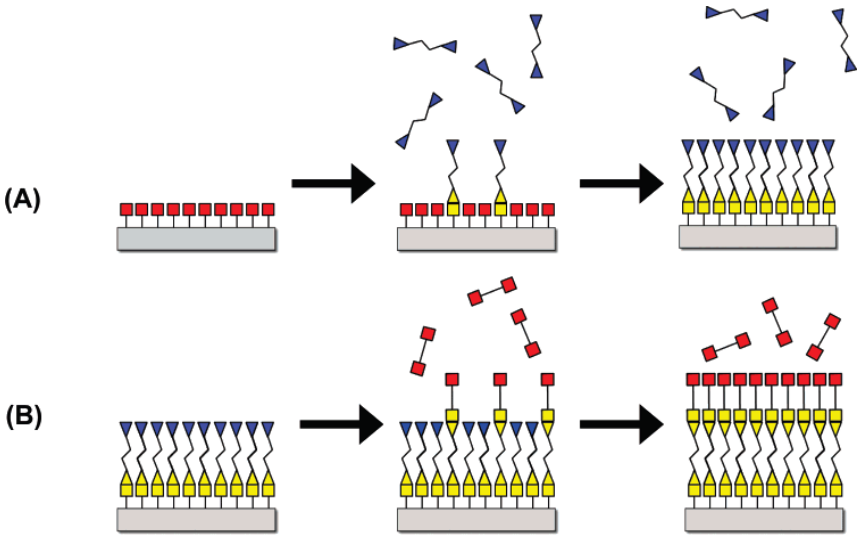


Figure 1.11. *Schematic of MLD using bifunctional monomers with "triangular" or "square" functional groups* [23].

Although the reaction schematic above presents the growth of MLD films as occurring linearly, this is highly unlikely to be the case. The ideal growth rate of MLD films should then be equal to the combined length of each organic precursor molecule. One reason for deviation from this behavior is that organic precursor molecules with long chains are likely to tilt, resulting in film growth that is not ideally perpendicular to the surface. Furthermore, steric hindrance of large organic molecules results in decreased packing density and blocking of surface nucleation sites [32]. Bifunctional precursor molecules, such as ethylene glycol, may bend and react twice with the surface, reducing the number of reactive sites and resulting in decreased growth rate. Figure 1.12 outlines the effect of these three processes in reducing the growth rate of MLD films.

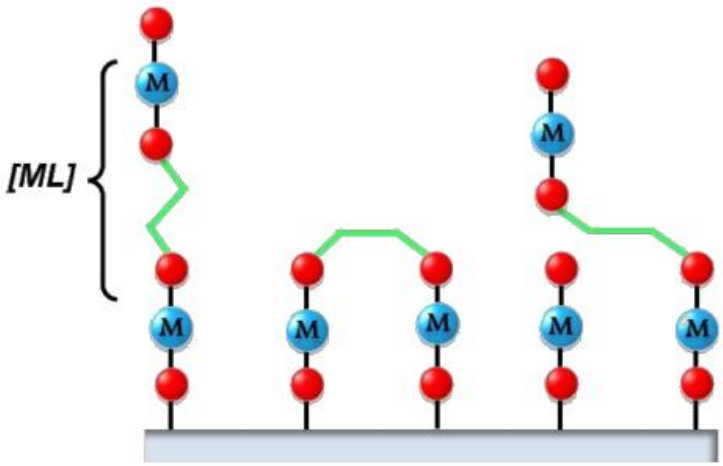


Figure 1.12. *Ideally, organic precursor molecules should react with only one surface site with film growth occurring vertically. However, molecules may react twice and polymer chain may have tilt perpendicular to the surface [32].*

MLD reactions have also been shown to have decreasing growth rate with increasing temperature [33]–[35]. This temperature dependent behavior is attributed to the sticking coefficient (S_0) of precursors adsorbed on the surface. Additionally, diffusion out of the film is enhanced at higher temperatures, resulting in a lower growth rate. The following equation can be used to describe this phenomenon [36]:

$$S_0 = \frac{a}{\left[1 + \frac{k_d}{k_r}\left\{\exp\left(\frac{E_d - E_r}{kT}\right)\right\}\right]}$$

a =Trapping coefficient of the precursor

k_d = Rate of desorption of precursor

k_r =Rate of reaction of precursor to substrate

E_d = Activation energy for desorption

E_r = Activation energy for reaction

1.5 Literature Review

Surface engineering plays an important role in many scientific and industrial applications. ALD and MLD are important and unique techniques that can be used to engineer surfaces with precise physical and chemical properties. Due to gas-phase nature of ALD, it is one of the few techniques that can provide these properties in a conformal and uniform manner over high aspect ratio structures. As materials become more complicated and move into the nano-realm, these properties become increasingly demanding. As a result, ALD has attracted the attention of researchers in the field of nanotechnology. The precise nature of control over film thickness allows for new strategies in modifying the surface of nanoscaled materials. Furthermore, ALD provides an avenue toward designing novel nanostructures. This section is aimed at providing a literature review of the unique properties that ALD and MLD films can provide. A highlight of this section is to demonstrate the ability of ALD in functionalizing surfaces as well as the high degree surface engineering enabled by both ALD and MLD. The application of these capabilities in the field of lithium-based batteries and fuel cells will be explored.

1.5.1 Unique capabilities of ALD

ALD was originally developed in the 1970s by Suntola and Anston as a tool for producing thin film electroluminescent (TFEL) displays [37]. These multi and full color displays required precise control over film thickness and film doping. The processing of TFEL displays by ALD highlights the advantages of this technique compared to CVD or PVD. The uniformity and facile doping capabilities of ALD over a large area, as well as its straightforward scale-up capabilities of this technique, provided an opportunity for the industrial processing of TFEL displays. However, ALD did not find its largest user until the early 2000s, the microelectronics industry. A central component to any semiconductor, or transistor, is a high-k gate oxide. These gate oxides need to be uniform and pinhole-free to prevent current leakage. Typically, SiO_2 was used as a gate dielectric, but this material suffers from seriously current tunneling when downsized to below 1 nm [38]. To address the challenges surrounding oxide thickness and conformality, Intel adopted HfO_2 deposited by ALD in 2007 for mass production of their 45 nm node transistor [39]. Since then ALD has been adopted by many other industrial semiconductor manufacturers to deposited high-k dielectrics [40]–[42]. Furthermore, as electronics move to materials with decreased dimensionality such as graphene, nanowires, and carbon nanotubes, conformal deposition of high-

k gate oxides becomes increasingly important. This necessity makes ALD a critical tool for the microelectronics industry and is probably the only viable technique that can provide these capabilities.

ALD has long been considered as an enabling tool. It provides an avenue toward enhancing material surface properties and for precisely engineering surface functionality. An example of this is the use of ALD for functionalizing the surface of glass capillary arrays of microchannel plates (MCPs). These two-dimensional arrays of microscopic channel electron multipliers are used in a wide variety of detector applications including, photo-detection, astronomy, electron microscopy, field emission displays, and fluorescence imaging in biotechnology [43]. MCP detectors allow for high gain, high spatial resolution, high timing resolution with very low background signal rates. Conventional MCP fabrication requires an additional thermo-chemical processing step in order to activate channel walls for electron multiplication. However, using this process does not allow for the electrical conductivity and the secondary electron emission properties of the MCP to be decoupled. The linking of these two properties severely limits the specialization and application of these detectors. With the advent of ALD-MCPs, tremendous improvements to the operational parameters of MCPs can be realized. ALD is used to functionalize the surface of borosilicate glass tubes with an electrode layer, a resistive layer, and a high secondary emissive layer. By taking advantage of the high degree of compositional control imparted by ALD, the resistivity of the glass capillary array can be decoupled from its base chemistry. Characteristics of the resistive and secondary emissive layer can be tuned by adjusting ALD process parameters such as temperature, composition, and precursor chemistry [44]. This allows for the final operational parameters of MCPs to be highly specified and tailored for a specific application. This example demonstrates how ALD is ideally suited for providing a means toward engineering surface functionality and its use as an enabling technique.

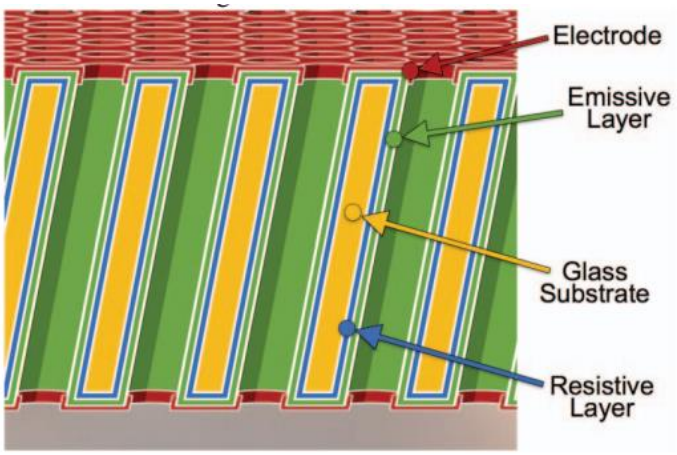


Figure 1.13. *Borosilicate glass microcapillary array functionalized using ALD. Film resistance can be tailored to suit the application. Materials with high stable secondary emission properties can be used since they are decoupled from the substrate [45].*

By carefully choosing precursor, substrate, and deposition conditions, ALD can also be used to deposit NPs. This is especially important for the deposition of noble metal catalysts. On most substrates, deposition of metals is difficult due to slow nucleation kinetics, resulting in the growth of islands [46]–[48]. Furthermore, metal particles have a tendency to agglomerate and can lead to the deposition of larger nanoparticles [49]. This growth mode is commonly referred to as Volmer-Weber growth and can be exploited to deposit metallic nanoparticles on various supports for catalysis applications [50]. ALD provides the advantage of providing control over particle size and composition. Since the catalytic activity of many chemical reactions is dependent on particle size, synthesis of particles with a narrow size distribution is imperative. By taking advantage of the cyclical nature of ALD, particle size can be accurately controlled. Furthermore, catalyst activity can be improved by tuning nanoparticle composition and structure, both of which can be done by ALD. By tailoring the interaction of metal precursors with their substrates, and surface metal deposits, ALD allows for core shell metal nanoparticles to be produced with a high degree of composition control [22], [51]. Another advantage of ALD is its ability to coat nanostructured surfaces uniformly. Similarly, the deposition of metallic nanoparticles by ALD allows for narrow particle size distribution in a uniform manner over large surfaces. Figure 1.14 provides a schematic outline for the various opportunities that ALD offers for the synthesis of nanoparticle catalysts.

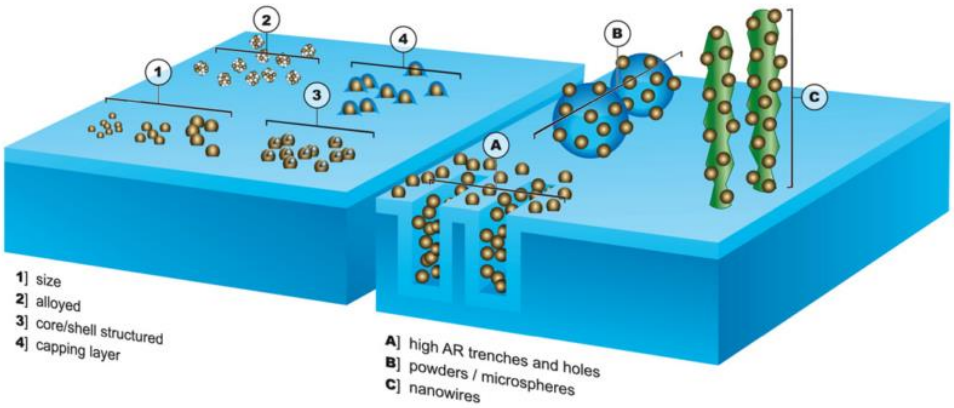


Figure 1.14. *Diagram demonstrating the various opportunities that ALD provides for the deposition of nanoparticles. ALD can be used to control (1) the size of particles, and (2), (3), (4) particle composition. The highly uniform nature of ALD can be used to deposit particles over A) high aspect ratio trenches and holes, B) on powders and microspheres and C) on nanostructures substrates such as nanowires* [52].

One example that highlights the importance of ALD deposition parameters in controlling the size of nanoparticles is a study conducted by Mackus et al [53]. This investigation examined the influence of oxygen exposure on the deposition of Pt nanoparticles. By increasing the exposure of oxygen, particle ripening was found to occur rapidly and enhance Pt ALD growth, resulting in rapid film formation. Interestingly, oxygen partial pressure was also found to influence the nucleation of Pt. By using a lower partial pressure of oxygen, a narrow particle size distribution was observed. Increasing the partial pressure of oxygen causes a broad range of particles to be deposited due to oxygen promoting the diffusion of Pt atoms across the surface. Using a sufficiently high O_2 exposure, Pt atoms begin to aggregate and coalesce into small islands. Furthermore, the surface produced islands can subsequently catalyze surface reactions by dissociating molecular oxygen and contribute to combustion of precursor ligands.

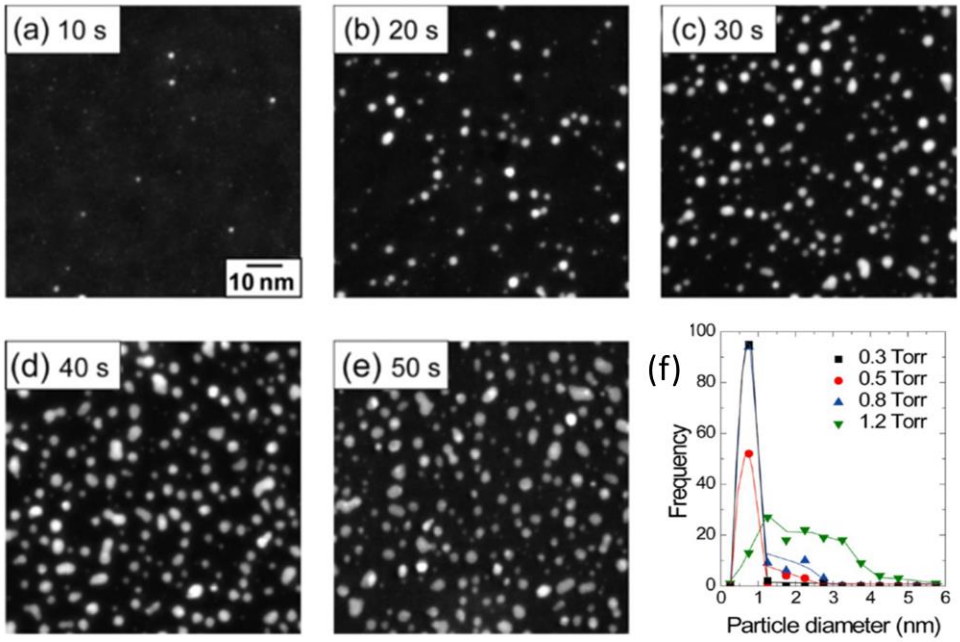


Figure 1.15. *(a) – (e) TEM images of 50 cycles of Pt ALD using progressively longer exposures of oxygen. (f) Influence of oxygen exposure partial pressure on Pt nanoparticle size [53].*

This oxygen exposure dependent behavior for the growth of Pt can be used to achieve area-selective deposition and allows for the development of novel nanopatterning [22], [54], [55]. Additionally, selective growth conditions can be applied for the deposition of core shell particles [52].

1.5.2 Unique capabilities of MLD

Due to the wide application of ALD and its ability to provide atomic layer control over film thickness, there has been an expansion in developing films that are inspired by the ALD process. This led to the introduction of organic precursors in a similar self-limiting sequential manner and allows for the deposition of polymeric like thin films. This process, known as molecular layer deposition (MLD), extends the available materials that can be deposited using gas phase chemistry. Further development of this technique by mixing inorganic precursor from ALD with organic ones creates new class of hybrid inorganic-organic materials. These hybrid inorganic-organic films are commonly referred to as metalcones. In a report first published by Dameron et al., aluminum alkoxide films, known as alucone, were deposited using trimethylaluminum (TMA) and ethylene glycol (EG) [27]. Following this several other metalcone films have been deposited

including zincones [56]–[59], zircones [60], [61], titanicones [62]–[65], hafnicones [66], vanadicones [62] and mangancone [62]. These hybrid materials expand the capabilities MLD and increases the functionality and uniqueness of thin films produced using this technique. Furthermore, by introducing the atomic scale control of inorganic films provided by ALD, inorganic-organic materials with tunable composition can be produced. This strategy paves an avenue toward developing nanolaminate materials with highly tunable properties. An excellent example of this is the deposition of alucone-Al_2O_3 alloy films to control film density, refractive index, elastic modulus, and hardness. By adjusting the relative number of TMA/H_2O cycles to TMA/EG cycles, alloy film composition can be accurately controlled [30]. Figure 1.16 demonstrates the various properties displayed by Al_2O_3: alucone films produced using ALD and MLD.

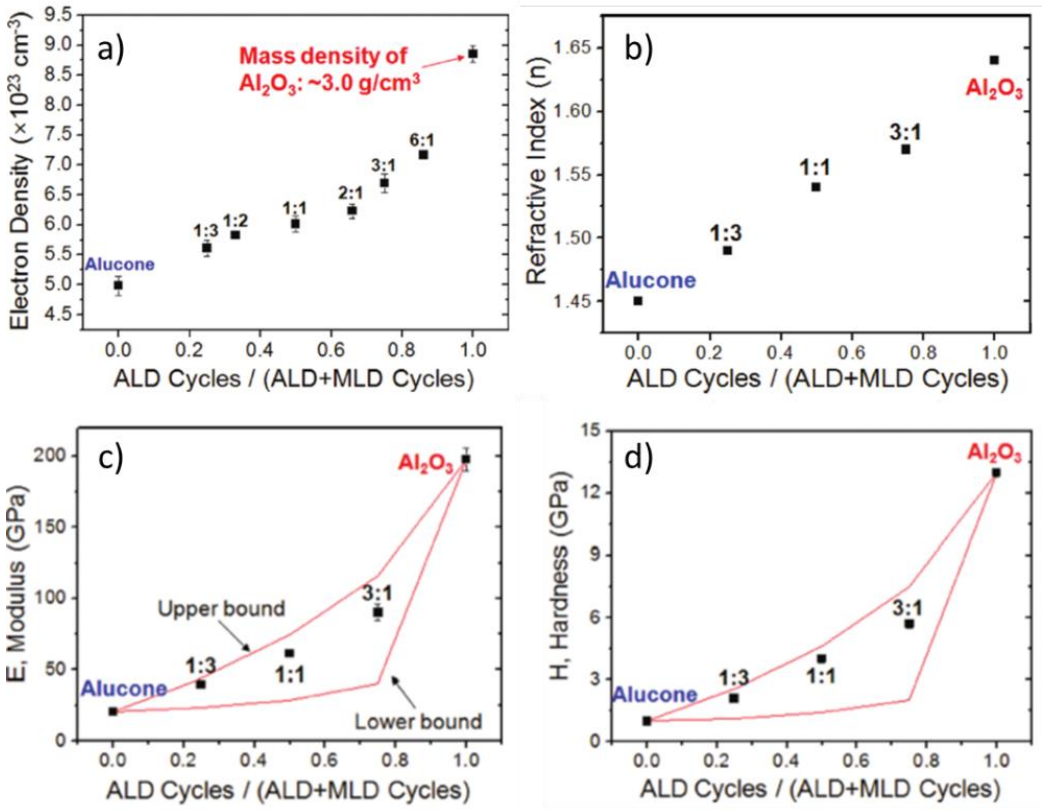


Figure 1.16. *(a) Electron density and (b) refractive index measurements for Al_2O_3:alucone film alloys. (c)Elastic modulus and (d) hardness measurements for Al_2O_3: alucone alloy films* [30].

Given the unique capabilities of ALD and MLD films, the application of these techniques has been widespread. For this thesis, a review ALD and MLD use in the field of lithium-based

batteries and fuel cells is provided. The aim of the next section is to demonstrate the unique advantages that ALD and MLD can provide for these two fields. It will highlight the use of these techniques as an enabling tool.

1.5.3 Use of ALD and MLD for Lithium-based Batteries

Due to a growing concern over climate change and attempts to limit the use of fossil fuels, a move toward renewable energy forms, such as solar and wind, has recently taken hold. However, these renewable energy sources are intermittent and require energy storage devices for them to be used effectively. These environmental concerns have also led to a rise in the production of hybrid and all-electric vehicles. Lithium-based batteries are considered as one of the best energy storage systems due to their light weight as well as high energy density [67]. Depending on use, various lithium-based battery chemistries can be applied to provide either high gravimetric energy density or high volumetric energy density. However, there are several issues that are common encountered across various lithium-based battery chemistries. Many of these are related to reactions occurring at the interface between the electrode and electrolyte. Interfacial reactions during charge/discharge processing play a critical role in determine the performance of electrochemical cells [68], [69]. The types of reaction occurring at the interface is dependent on battery chemistry as well as electrode design. An overview of various detrimental reactions that can occur at the electrode/electrolyte interface is presented in Figure 1.17. For this purpose, surface modification of electrode materials with coatings has been conducted to improve battery performance. By protecting the surface of the electrode from harmful, unwanted side reactions battery performance can be enhanced. However, the success of this strategy hinges on employing a deposition technique that can provide a high degree of uniformity and conformality. Currently, battery electrodes are predominantly made using coating technologies, lamination, and calendaring. Therefore, any type of coating technique used to increase the longevity of battery electrodes must be easily incorporated into this manufacturing process. Furthermore, electrodes employed in lithium-based batteries are often highly porous and quite complicated. ALD and MLD are two techniques that are well situated as a coating strategy for electrode materials given its ability to deposit thin films in a conformal and uniform manner. Furthermore, it is a non-line of sight technique and allows for deposition to occur in geometrically complicated structures, like those found for lithium-based electrodes. In addition to this, films produced by ALD tend to be processed at lower temperatures compared to CVD to PVD. This is important as many materials in the

electrode, such as the binder and current collector, may undergo decomposition or chemical changes at elevated temperatures. In this section we will explore the use of ALD protective coatings in lithium-ion batteries (LIB) and lithium-sulfur batteries (Li-S).

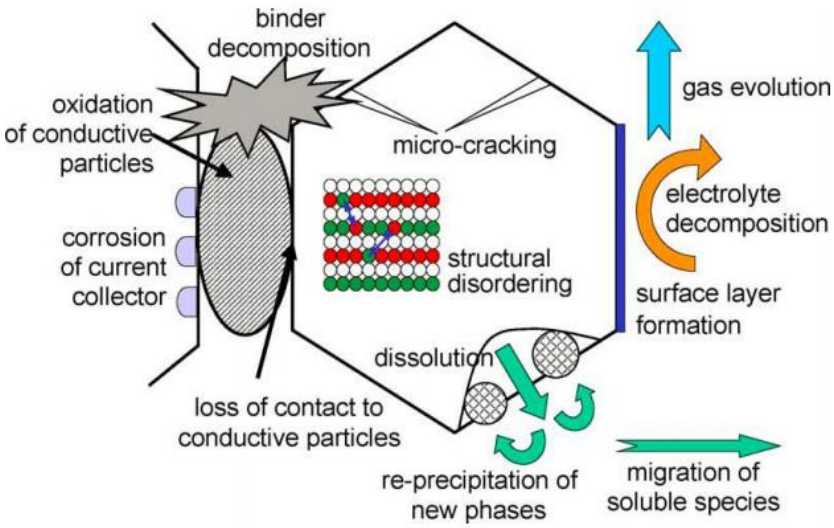


Figure 1.17. *Various interfacial reactions that can occur at the electrode/electrolyte interface that can be detrimental to battery performance* [70].

1.5.4 ALD and MLD for Lithium-ion Batteries

Rechargeable LIBs have been considered as the most promising energy storage system for a wide variety of applications. Their advantages include long cycle life, low self-discharge, high operating voltage, and wide temperature window [71]. The charge/discharge mechanism of LIBs is based on a rocking-chair concept where lithium ions swing between the negative electrode and the positive electrode through an organic liquid electrolyte. Typically, the positive electrode (cathode) is a thin layer of powdered metal oxide cast onto an aluminum foil. The negative electrode (anode) also consists of a thin film of a powdered material, typically graphite, cast on a copper foil. An organic solvent and polymer separator is then used between the electrodes and allows for the migration of lithium ions. The cathode of LIBs suffers from many detrimental side reactions due to the high voltage present at the interface between the electrode and electrolyte. This can result in elemental dissolution, structural disordering and generation of gas/etchants from the electrolyte, such as HF [72]. One of the most commonly employed cathode materials in LIBs that suffers from many of these issues is $LiCoO_2$. To effectively mitigate the issues mentioned earlier, ALD of Al_2O_3, TiO_2 and ZrO_2 have been employed to on $LiCoO_2$ electrodes. In particular,

two cycles of Al_2O_3 was found to improve the electrochemical performance of nano-sized $LiCoO_2$ by 250% compared to uncoated $LiCoO_2$ [73]. This drastic improvement originates from ALD Al_2O_3 preventing the dissolution of Co^{4+} into the electrolyte. This allows $LiCoO_2$ to maintain its structural integrity throughout the electrochemical cycling process. Interestingly, when comparing the performance of Al_2O_3 and ZrO_2 coated $LiCoO_2$, Al_2O_3 was found to provide better cycling stability while ZrO_2 was better suited toward retaining rate capability at high current densities [74]. This demonstrates that the coating material employed provides specific functionality when enhancing performance. Table 1.1 provides an outline of some of the various coating materials that have been applied to some LIB cathode materials.

Table 1.1. *Overview of various ALD coatings applied to different Li-ion battery cathode materials.*

Cathode material	ALD coating	Reference
$LiCoO_2$	Al_2O_3	[67]–[72]
	TiO_2	[68], [71], [72]
	ZnO	[69]
	ZrO_2	[68]
	AlW_xF_y	[73]
$LiNi_{0.33}Mn_{0.33}Co_{0.33}O_2$	Al_2O_3	[74], [75]
	LiTaOx	[76]
$LiMn_2O_4$	Al_2O_3	[77]
	ZrO_2	[78]
$LiNi_{0.5}Mn_{1.4}O_4$	$AlPO_4$	[79]
	Al_2O_3	[80], [81]
	$LiAlO_2$	[81]

For LIB anode materials the formation of a solid electrolyte interphase (SEI) significantly influences electrochemical performance. The SEI formed on the surface of the anode passivates the electrode surface and prevents uncontrolled reduction of electrolyte and serves as an important interface for maintaining safe operation of a battery [75]–[78]. However, the SEI has been shown

to consume Li, thereby reducing the specific capacity of the cell, resulting in low columbic efficiency. The problem of SEI formation becomes even more problematic for anode materials that undergo large volume changes during electrochemical cycling, such as Si, Li, Sn and SnO_2. As the volume of the material increases during cycling, fresh electrode surface is exposed to the electrolyte, causing new SEI formation. This consumes electrolyte, as well as Li, and eventually contributes to degradation of cell performance. By using an ALD surface coating, an artificial SEI layer is produced and can improve the specific capacity, rate capacity, columbic efficiency and thermal stability of a cell [69]. Graphite is widely used anode material in LIBs due to its low cost and ease of manufacturing. However, due to rapid uncontrolled SEI formation, graphite undergoes significant capacity decay [76]. ALD of Al_2O_3 and TiO_2 on the surface of graphite has been shown to improve SEI formation and decrease electrolyte decomposition [79]–[81]. Graphite electrodes modified using ALD coating present improved cycling performance as well as increased coulombic efficiency during the first charge-discharge cycle, suggesting a decrease in the number of side reactions. Post mortem analysis of the graphite electrodes reveal that a thinner SEI is produced for ALD-coated electrodes. A decrease in the formation of both LiF and Li_2O was identified as one reason ALD coated graphite displayed better performance.

MLD has also been applied as coating to suppress SEI formation in carbon anode materials for LIBs [82]. However, this investigation determined that MLD alucone (TMA-EG) coatings are worse than ALD Al_2O_3 coating. Furthermore, MLD coated carbon anodes demonstrated even worse performance compared to bare carbon anodes. This behavior was believed to stem from the poor ionic transport properties of alucone MLD. Although MLD was shown to decrease the performance of carbon based anode LIB materials, it has shown promising results for Si-based anode materials. Silicon is considered as a potential substitute for graphite as an anode material due to its exceptional specific capacity, low charge/discharge potential as well as extraordinary theoretical capacity (4200 mAh/g) [83]. However, application of Si is hindered by its large volume change, resulting in mechanical failure, loss of electrical contact and poor cyclability [84]. Nanostructured Si materials, however, experience less structural damage and pulverization compared to bulk Si due to nanostructures effectively releasing strain. ALD of metal oxides have previously been utilized to reduce the effect of parasitic side reactions occurring between the liquid electrolyte and the electrode surface. However, metal oxides by ALD are often dense and brittle not lack the structural stability required to provide support during large volume expansion for

materials Si, which may undergo volumetric expansions of up to 300% [85]. To accommodate the large volume expansion of nano-Si, Piper et al [86] utilized hybrid inorganic-organic films. The hybrid inorganic-organic film was produced by reacting TMA with glycerol, as shown in Figure 1.18. The chemical nature of glycerol results in more than one other hydroxyl group available for reaction with TMA. This provides a large degree of crosslinking to occur between polymer chains and strengthens the alucone film, leading to films with increased fracture toughness [23]. This increased robustness is ideal for accommodating large volumetric changes typically seen for nano-Si composite electrodes.

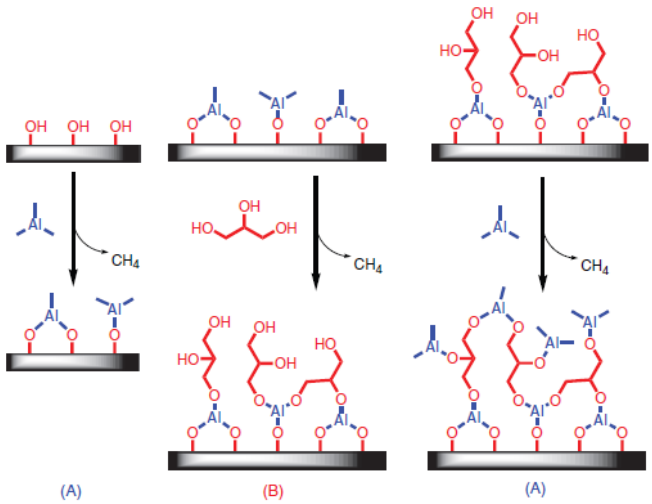


Figure 1.18. *Schematic for chemistry of aluminum glycerol (AlGL) films* [87].

The coated nano-Si was characterized by transmission electron microscopy (TEM), and high angle annular dark field scanning (HAADF) scanning transmission electron microscopy (STEM). This technique is highly sensitive to atomic number and provides an accurate representation of the conformity of AlGL coating on the nano-Si, as shown in figure 19. The cyclic stability of the AlGL coated nano-Si is shown in figure 4e and demonstrates superior stability compared to bare nano-Si, which fails after the 30^{th} cycle. The coated nano-Si demonstrates a capacity of nearly 900 mAh/g with a columbic efficiency in excess of 99%.

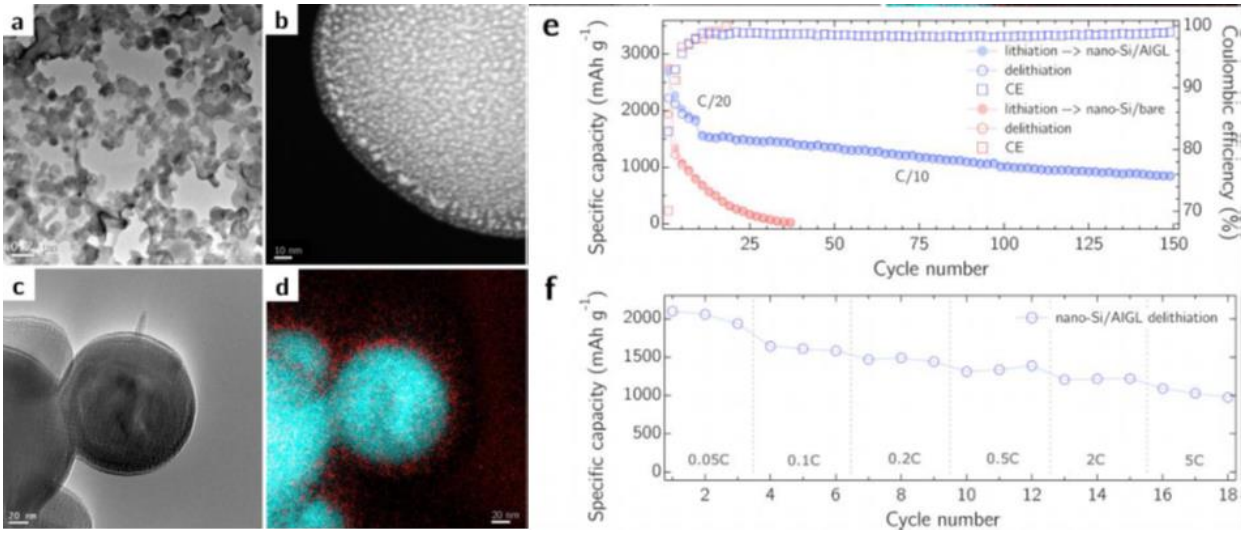


Figure 1.19. *a),c) TEM micrograph and b) HAADF-STEM of nano-Si coated with aluminum organic thin film. d) EELS elemental mapping of aluminum organic thin film. e) comparison of cycling capacity of coated and un coated nano silicon and f) rate test of coated nano silicon*[88].

Clearly, MLD coatings can aid in providing mechanical stability for electrochemical materials that undergo large volume expansions. However, the paper also introduces another interesting aspect to MLD films. In a double-edged sword fashion, the advantages offered by nanomaterials in providing shorter diffusion paths for lithium ions, are also associated with major drawbacks such as their high surface area and high surface energy which unfortunately increase the number of undesirable surface reactions. Thick solid electrolyte interphase (SEI) films form on the surface of nanosized anodes, which end up consuming lithium ions supplied by the cathode [89]. The SEI is composed of decomposition products because of electrolyte reduction following the initial charge transfer at the anode surface. Lithium ions participating in the formation of SEI is irreversibly lost and is an important consideration in the material balance for commercial cells [90].

1.5.5 ALD and MLD for Lithium-Sulfur Batteries

Another type of lithium-based battery chemistry that is currently being investigated are lithium-sulfur batteries (Li-S). This next-generation energy storage system provides a high theoretical energy density of 2600 Wh/kg [91]. Like LIBs, Li-S batteries are composed of an anode, cathode, and electrolyte. The cathode is typically comprised of sulfur encapsulated in a conductive host, usually carbon, while the anode is a metallic lithium electrode. Given that sulfur

has a lower molar weight than most metal oxide materials employed in LIBs, Li-S batteries have a high theoretical specific capacity and are used in applications that required high gravimetric energy density. Furthermore, sulfur can undergo multi-electron reactions with Li metal, providing it with more energy density than many LIB systems [92]. However, the electrochemical reaction between sulfur and Li is significantly more complicated than the rocking chair mechanism observed in LIBs. A typical discharge process for sulfur cathodes involves a multi-step electrochemical reaction in which solid S_8 molecules combine to form long chain soluble polysulfides. This long chain is then further reduced to solid Li_2S_2 and then again reduced to a final discharge product of Li_2S [93]. This complicated solid-liquid dual-phase electrochemical reaction imposes several challenges for the commercialization of Li-S battery technology. Firstly, dissolved long chain polysulfides migrate across the cell to the anode and directly react with lithium metal to form short chain polysulfides or solid Li_2S_2/Li_2S, resulting in corrosion of lithium metal as well as loss of active sulfur. This phenomenon is commonly known as the "shuttle effect" and is a serious problem for Li-S batteries [91]. Furthermore, volume expansion of the sulfur cathode during lithium insertion results in delamination of active material from the current collected, as well as breaks in the conductive network and results in rapid battery failure [94].

One strategy to retain sulfur and maintain good electrochemical performance, is to prevent the dissolution of polysulfide species. This can be achieved by introducing an interlayer between the sulfur cathode and the electrolyte and can be accomplished using surface coating techniques [95]–[97]. ALD and MLD one avenue for depositing ultrathin films that can maintain the high energy density of sulfur while the uniformity of the coating can help to protect sulfur cathode materials. Furthermore, the low temperature employed with these techniques prevent evaporation of sulfur from occurring during the deposition process. ALD of Al_2O_3 on carbon-sulfur electrodes is one simple and effective strategy in preventing sulfur dissolution [98], [99]. Studies have revealed that formation of AlF_3 and $LiAlO_2$ during electrochemical cycling results in the formation of a SEI layer that can improve lithium-ion transportation kinetics at the sulfur cathode [99].

MLD has also been shown to enhance the performance of Li-S cells. MLD alucone-coated sulfur cathodes have been shown to double cell capacity compared to uncoated carbon-sulfur cathodes. Furthermore, the coulombic efficiency of MLD coated sulfur electrodes was found to be better than their uncoated counterparts [100]. This study was further advanced by applying MLD

alucone coating to Li-S batteries cycled in carbonate-based electrolytes [101]. Typically, carbonate electrolyte systems cannot be used in Li-S cells due to uncontrolled reactions occurring between dissolved polysulfides and carbonate compounds in the electrolyte [92], [102], [103]. Therefore, ether-based electrolytes are traditionally used for Li-S cells. However, ether based solvents have a very low flash point and pose significant safety issues for Li-S batteries operating at elevated temperatures. This landmark study demonstrates the prolonged cyclability of Li-S cells in carbonate electrolytes and reveals the unique opportunities that surface modification by MLD can provide in diversifying the application of Li-S batteries.

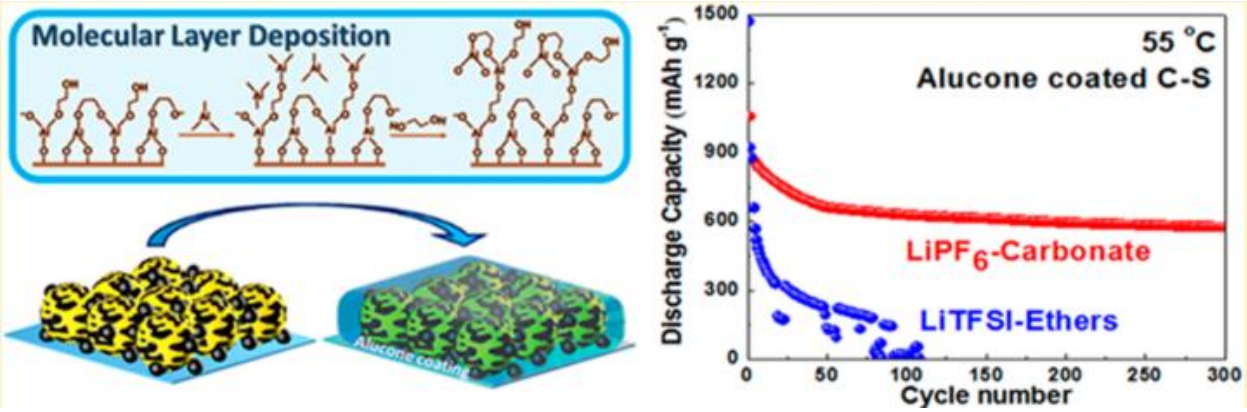


Figure 1.20. *MLD alucone coating for safe high temperature Li-S batteries in carbonate based electrolytes* [101].

1.5.6 Application of ALD and MLD for Fuel Cells

Metallic nanoparticles are often used in catalytic applications due their ability to enhance catalytic activity as well as their intrinsic high surface area to volume ratio. Since the catalytic activity of particles is strongly dependent on particle size, synthesis of nanoparticles with a narrow size distribution and high density is of paramount importance. Emphasis has recently been placed on the development of advanced catalysts and electrode materials for fuel cells through the incorporation of noble metal nanoparticles on high surface area carbon supports [47]. However, a challenge associated with the design of these electrode materials is the development of methods that can reduce the overall loading of costly noble metal catalysts while retaining their high activity. As an example, for direct methanol fuel cells to become economically viable, Pt catalyst loading must be below 1 mg/cm^2 [104]. Because the initial stages of noble metal films grown by ALD generally proceeds via the formation of islands, this technique holds promise for the synthesis

of supported noble metallic nanoparticles for catalysis [52]. Using ALD, King et al [105] demonstrated the deposition of Pt nanoparticles on the inner surface of high surface area carbon aerogels. The Pt-loaded material exhibited high catalytic activity toward CO oxidation with a very low Pt loading of 0.05 mg/cm^2 after two ALD cycles. Inspired by this, single atoms and sub-nanometer clusters of Pt was deposited using ALD on graphene nanosheets [106]. Graphene is an ideal substrate for catalyst support in fuel cells due to its high surface area, high conductivity, and low manufacturing costs. By adjusting the number of ALD cycles, the morphology, size, density and loading of Pt on graphene could be precisely controlled. The deposition of this catalyst showed much higher activity toward methanol oxidation and superior CO tolerance compared to conventional Pt/C catalyst. The unique catalytic activity displayed in this work originates from the low-coordination of Pt atoms to the substrate, as well as is the uniform distribution of catalytic particles imparted by the ALD process.

Although Pt nanoparticles are an effective catalyst in facilitating both hydrogen oxidation and oxygen reduction in fuel cells, the harsh operating conditions of these cells undermine their performance. The acidic environment and high voltage potentials applied in fuel cells cause Pt nanoparticles to agglomerate and lose their catalytic activity [107]. To address this issue Cheng et al [108] demonstrated the stabilization of ALD Pt by depositing ZrO_2 nanocages around Pt particles. This unique study aimed to encapsulate Pt nanoparticles with zirconia nanocages using area-selective ALD. Pt nanoparticles were initially deposited on nitrogen doped carbon nanotubes (NCNT). This Pt-NCNT substrate was then subjected to treatment with oleylamine which would protect and block the surface of Pt nanoparticles. ALD of zirconia was then performed and selectively grew around the Pt NPs. This advanced electrode architecture presented an oxygen reduction activity that was 6.4x greater than commercial Pt/C electrodes. Furthermore, the Pt NPs encapsulated within zirconia nanocages exhibited significantly enhanced thermal resistance and holds promise for future catalyst design by ALD.

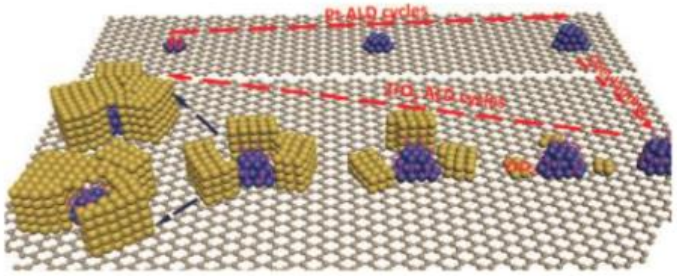


Figure 1.21. *Schematic diagram of platinum encapsulated in zirconia nanocages produced using area-selective ALD* [108].

In addition to the control of particle size and density, control over nanoparticle composition is important for catalysts design. Bimetallic alloyed nanoparticles or core/shell nanoparticles often exhibit improved catalytic performance compared to their monometallic counterparts [109], [110]. For example Pt/Pd, core/shell nanoparticles are important for methanol fuel cells due to their high catalytic activity toward oxygen reduction reactions and methanol electro-oxidation reactions [111]. By carefully turning nucleation behavior, core shell Pt/Pd nanoparticles have been deposited using ALD. These particles were synthesized by first depositing 200 cycles of Pd followed by 50 cycles of Pt. The key characteristic here is the use of low O_2 pressure of to selectively deposit Pt shells over existing Pd nanoparticles [51]. This was further advanced by Lu et al [18] who explored combinations of Pd, Ru and Pt metals to create different core shell nanoparticles. Thermal ALD processing of these noble metals lead to selective growth at 150°C on metal cores without nucleation occurring on the underlying oxide substrate. For example, Pd ALD, using $Pd(hfac)_2$ and formalin, was shown to result in Pd particle growth on oxides. However, Pd ALD using H_2 rather than formalin resulted in the selective growth of Pd on Ru or Pt, but not the underlying substrate oxide. These two examples highlight the capability of ALD in producing metallic core-shell particles as well as advanced alloy structures.

As mentioned earlier, stabilization of catalysts is important for many fuel cell reactions. Additionally, deactivation of catalysts caused by poisoning, coking and fouling, sintering, and attrition must be hindered in order to prolonged catalytic activity and extend catalyst longevity [112]. ALD can be used to deposit a thin over layer to protect catalysts. However, the dense and pin-hole free nature of ALD films may reduce catalytic activity. To address this issue, porous coatings using MLD have been investigated. Liang et al [113] demonstrated this concept by

coating ALD Pt particles with an alucone over layer. The substrate was then subjected to oxidized in air to produce a porous alumina film. Compared to pristine catalyst samples, the oxidized porous alumina over layer significantly reduced the sintering rate of Pt particles. However, the CO oxidation of porous alumina coated Pt particles was found to be less catalytically active. This reduced reactivity of Pt was attributed to the small pore size of 0.6 nm imparted by the oxidized alucone film, which reduced mass transfer and resulted in poor Pt activity.

1.6 References

[1] S. Chu, Y. Cui, and N. Liu, "The path towards sustainable energy," *Nat. Mater.*, vol. 16, no. 1, pp. 16–22, 2016.

[2] H. Wei *et al.*, "Energy conversion technologies towards self-powered electrochemical energy storage systems: the state of the art and perspectives," *J. Mater. Chem. A*, vol. 5, no. 5, pp. 1873–1894, 2017.

[3] J. H. Montoya, L. C. Seitz, P. Chakthranont, A. Vojvodic, T. F. Jaramillo, and J. K. Nørskov, "Materials for solar fuels and chemicals," *Nat. Mater.*, vol. 16, no. 1, pp. 70–81, 2016.

[4] M. Henini, "Handbook of Thin-Film Deposition Processes and Techniques," *Microelectronics J.*, vol. 31, no. 3, p. 219, 2000.

[5] D. Mattox, *Handbook of Physical Vapor Deposition (PVD) Processing*, 2nd ed. Burlington: Elsevier, 2010.

[6] J. Vossen and W. Kern, Eds., *Thin Film Processes II*. San Diego: Academic Press, 1991.

[7] D. Depla and S. Mahieu, *Reactive Sputter Deposition*, vol. 109. 2008.

[8] S. M. Rossnagel, "Thin film deposition with physical vapor deposition and related technologies," *J. Vac. Sci. Technol. A Vacuum, Surfaces, Film.*, vol. 21, no. 5, p. S74, 2003.

[9] W. Heinke, A. Leyland, A. Matthews, G. Berg, C. Friedrich, and E. Broszeit, "Evaluation of PVD nitride coatings, using impact, scratch and Rockwell- C adhesion tests," *Thin Solid Films*, vol. 270, pp. 431–438, 1995.

[10] J.-H. Park and T. S. Sudarshan, *Chemical vapor deposition*, vol. 2. ASM international, 2001.

[11] D. J. H. Emslie, P. Chadha, and J. S. Price, "Metal ALD and pulsed CVD: Fundamental reactions and links with solution chemistry," *Coord. Chem. Rev.*, vol. 257, no. 23–24, pp. 3282–3296, 2013.

[12] J. Y. Zhang, V. Dusastre, and I. W. Boyd, "Characterization of ultraviolet annealed tantalum oxide films deposited by photo-CVD using 172 nm excimer lamp," *Mater. Sci. Semicond. Process.*, vol. 4, no. 1–3, pp. 313–317, 2001.

[13] K. L. Choy, "Chemical vapour deposition of coatings," *Prog. Mater. Sci.*, vol. 48, no. 2, pp. 57–170, 2003.

[14] P. Zanella, G. Rossetto, N. Brianese, F. Ossola, M. Porchia, and J. Williams, "Organometallic Precursors in the Growth of Epitaxial Thin Films of Groups III-V Semiconductors by Metal-Organic Chemical Vapor Deposition," *Chem. Mater.*, vol. 3, no. 2, pp. 225–242, 1991.

[15] K. F. Jensen, E. O. Einset, and D. I. Fotiadis, "Flow Phenomena in Chemical Vapor Deposition of Thin Films," *Annu. Rev. Fluid Mech.*, vol. 23, no. 1, pp. 197–232, 1991.

[16] A. C. Jones and M. L. Hitchman, *Chemical vapour deposition: precursors, processes and applications*. Royal Society of Chemistry, 2009.

[17] D. Version and U. Eindhoven, *Chemical vapor deposition of thin films for 3D lithium-ion microbatteries Chemical Vapor Deposition of Thin Films*. 2016.

[18] J. Lu *et al.*, "Toward atomically-precise synthesis of supported bimetallic nanoparticles using atomic layer deposition.," *Nat. Commun.*, vol. 5, p. 3264, 2014.

[19] P. G. Gordon, "Thin Film Precursors, Properties and Applications: Chemical Vapour Deposition and Atomic Layer Deposition of Group 4, 11 and 13 Elements and Their Oxides," p. 1–173, 2013.

[20] F. Zaera, "The surface chemistry of thin film atomic layer deposition (ALD) processes for electronic device manufacturing," *J. Mater. Chem.*, vol. 18, no. 30, p. 3521, 2008.

[21] R. L. Puurunen, "Surface chemistry of atomic layer deposition: A case study for the trimethylaluminum/water process," *J. Appl. Phys.*, vol. 97, no. 12, 2005.

[22] B. J. O'Neill *et al.*, "Catalyst Design with Atomic Layer Deposition," *ACS Catal.*, vol. 5, no. 3, pp. 1804–1825, 2015.

[23] B. H. Lee, B. Yoon, A. I. Abdulagatov, R. A. Hall, and S. M. George, "Growth and properties of hybrid organic-inorganic metalcone films using molecular layer deposition techniques," *Adv. Funct. Mater.*, vol. 23, no. 5, pp. 532–546, 2013.

[24] Q. Peng, K. Efimenko, J. Genzer, and G. N. Parsons, "Oligomer orientation in vapor-molecular-layer-deposited alkyl-aromatic polyamide films," *Langmuir*, vol. 28, no. 28, pp. 10464–10470, 2012.

[25] T. Bitzer and N. V. Richardson, "Demonstration of an imide coupling reaction on a Si(100)-2??1 surface by molecular layer deposition," *Appl. Phys. Lett.*, vol. 71, no. 5, pp. 662–664, 1997.

[26] C. Prasittichai, H. Zhou, and S. F. Bent, "Area selective molecular layer deposition of polyurea films," *ACS Appl. Mater. Interfaces*, vol. 5, no. 24, pp. 13391–13396, 2013.

[27] A. A. Dameron *et al.*, "Molecular Layer Deposition of Alucone Polymer Films Using Trimethylaluminum and Ethylene Glycol," *Chem. Mater.*, vol. 20, no. 10, pp. 3315–3326, May 2008.

[28] X. Liang, D. M. King, P. Li, S. M. George, and A. W. Weimer, "Nanocoating hybrid polymer films on large quantities of cohesive nanoparticles by molecular layer deposition," *AIChE J.*, vol. 55, no. 4, pp. 1030–1039, 2009.

[29] J. Liu *et al.*, "Ultralow thermal conductivity of atomic/molecular layer-deposited hybrid organic-inorganic zincone thin films," *Nano Lett.*, vol. 13, no. 11, pp. 5594–5599, 2013.

[30] B. H. Lee, B. Yoon, V. R. Anderson, and S. M. George, "Alucone Alloys with Tunable Properties Using Alucone Molecular Layer Deposition and Al 2 O 3 Atomic Layer Deposition," *J. Phys. Chem. C*, vol. 116, no. 5, pp. 3250–3257, 2012.

[31] M. L. Dunn *et al.*, "Thermomechanical properties of aluminum alkoxide (alucone) films created using molecular layer deposition," *Acta Materialia*, vol. 57. pp. 5083–5092, 2009.

[32] P. Sundberg and M. Karppinen, "Organic and inorganic-organic thin film structures by

molecular layer deposition: A review," *Beilstein J. Nanotechnol.*, vol. 5, no. 1, pp. 1104–1136, 2014.

[33] L. D. Salmi, M. J. Heikkilä, E. Puukilainen, T. Sajavaara, D. Grosso, and M. Ritala, "Studies on atomic layer deposition of MOF-5 thin films," *Microporous Mesoporous Mater.*, vol. 182, pp. 147–154, 2013.

[34] M. Nisula, J. Linnera, A. J. Karttunen, and M. Karppinen, "Lithium Aryloxide Thin Films with Guest-Induced Structural Transformation by ALD/MLD," *Chem. - A Eur. J.*, vol. 23, no. 13, pp. 2988–2992, 2017.

[35] N. M. Adamczyk, a. a. Dameron, and S. M. George, "Molecular Layer Deposition of Poly(p -phenylene terephthalamide) Films Using Terephthaloyl Chloride and p -Phenylenediamine," *Langmuir*, vol. 24, no. 5, pp. 2081–2089, 2008.

[36] D. A. King and M. G. Wells, "Reaction Mechanism in Chemisorption Kinetics: Nitrogen on the Plane of Tungsten," *Proc. R. Soc. A Math. Phys. Eng. Sci.*, vol. 339, no. 1617, pp. 245–269, 1974.

[37] T. Suntola and J. Antson, "Method for producing compound thin films." Google Patents, 1977.

[38] A. Rahtu, *Atomic Layer Deposition of High Permittivity Oxides : Film Growth and In Situ Studies*. 2002.

[39] K. Mistry *et al.*, "A 45nm Logic Technology with High-k+Metal Gate Transistors, Strained Silicon, 9 Cu Interconnect Layers, 193nm Dry Patterning, and 100% Pb-free Packaging," in *2007 IEEE International Electron Devices Meeting*, 2007, pp. 247–250.

[40] S. Narasimha *et al.*, "22nm High-performance SOI technology featuring dual-embedded stressors, Epi-Plate High-K deep-trench embedded DRAM and self-aligned Via 15LM BEOL," in *2012 International Electron Devices Meeting*, 2012, no. Fig 6, p. 3.3.1-3.3.4.

[41] F. Koehler, D. H. Triyoso, I. Hussain, S. Mutas, and H. Bernhardt, "Atomic Layer Deposition of SiN for spacer applications in high-end logic devices," *IOP Conf. Ser. Mater. Sci. Eng.*, vol. 41, p. 12006, 2012.

[42] C. H. Tsai *et al.*, "Characteristics of HfZrO x gate stack engineering for reliability improvement on 28nm HK/MG CMOS technology," *Int. Symp. VLSI Technol. Syst. Appl. Proc.*, 2012.

[43] A. U. Mane *et al.*, "An Atomic Layer Deposition Method to Fabricate Economical and Robust Large Area Microchannel Plates for Photodetectors," *Phys. Procedia*, vol. 37, pp. 722–732, 2012.

[44] A. O. Mahony *et al.*, "ALD Functionalization of Alternative Glass Microchannel Plates," no. 1, p. 94720, 2014.

[45] C. D. Ertley *et al.*, "Developments in atomic layer deposited microchannel plates," in *2016 IEEE Nuclear Science Symposium, Medical Imaging Conference and Room-Temperature Semiconductor Detector Workshop (NSS/MIC/RTSD)*, 2016, vol. 60439, pp. 1–7.

[46] J. Hamalainen, M. Ritala, and M. Leskela, “Atomic layer deposition of noble metals and their oxides,” *Chem. Mater.*, vol. 26, pp. 786–801, 2014.

[47] T. Aaltonen, *Atomic Layer Deposition of Noble Metal Thin Films*. 2005.

[48] R. W. Johnson, A. Hultqvist, and S. F. Bent, “A brief review of atomic layer deposition: From fundamentals to applications,” *Mater. Today*, vol. 17, no. 5, pp. 236–246, 2014.

[49] J. A. Singh, N. Yang, and S. F. Bent, “Nanoengineering Heterogeneous Catalysts by Atomic Layer Deposition,” *Annu. Rev. Chem. Biomol. Eng.*, vol. 8, no. 1, pp. 41–62, 2017.

[50] F. Zaera, “New challenges in heterogeneous catalysis for the 21st century,” *Catal. Letters*, vol. 142, no. 5, pp. 501–516, 2012.

[51] M. J. Weber, A. J. M. Mackus, M. A. Verheijen, C. van der Marel, and W. M. M. Kessels, “Supported core/shell bimetallic nanoparticles synthesis by atomic layer deposition,” *Chem. Mater.*, vol. 24, no. 15, pp. 2973–2977, 2012.

[52] A. J. M. Mackus *et al.*, “Atomic layer deposition of Pd and Pt nanoparticles for catalysis: on the mechanisms of nanoparticle formation.,” *Nanotechnology*, vol. 27, no. 3, p. 34001, 2016.

[53] A. J. M. MacKus, M. A. Verheijen, N. Leick, A. A. Bol, and W. M. M. Kessels, “Influence of oxygen exposure on the nucleation of platinum atomic layer deposition: Consequences for film growth, nanopatterning, and nanoparticle synthesis,” *Chem. Mater.*, vol. 25, no. 9, pp. 1905–1911, 2013.

[54] A. J. M. Mackus, A. A. Bol, and W. M. M. Kessels, “The use of atomic layer deposition in advanced nanopatterning,” *Nanoscale*, vol. 6, no. 19, pp. 10941–10960, 2014.

[55] A. J. M. Mackus, S. A. F. Dielissen, J. J. L. Mulders, and W. M. M. Kessels, “Nanopatterning by direct-write atomic layer deposition,” *Nanoscale*, vol. 4, no. 15, p. 4477, 2012.

[56] B. Yoon, J. L. O’Patchen, D. Seghete, A. S. Cavanagh, and S. M. George, “Molecular layer deposition of hybrid organic-inorganic polymer films using diethylzinc and ethylene glycol,” *Chem. Vap. Depos.*, vol. 15, no. 4–6, pp. 112–121, 2009.

[57] Q. Peng, B. Gong, R. M. VanGundy, and G. N. Parsons, “‘Zincone’ zinc oxide - Organic hybrid polymer thin films formed by molecular layer deposition,” *Chem. Mater.*, vol. 21, no. 5, pp. 820–830, 2009.

[58] B. Yoon, B. H. Lee, and S. M. George, “Highly Conductive and Transparent Hybrid Organic–Inorganic Zincone Thin Films Using Atomic and Molecular Layer Deposition,” *J. Phys. Chem. C*, vol. 116, no. 46, pp. 24784–24791, 2012.

[59] B. Yoon, B. H. Lee, and S. M. George, “Molecular Layer Deposition of Conductive Hybrid Organic-Inorganic Thin Films Using Diethylzinc and Hydroquinone,” *ECS Trans.*, vol. 41, no. 2, pp. 271–277, 2011.

[60] B. H. Lee, V. R. Anderson, and S. M. George, “Molecular layer deposition of zircone and ZrO2/zircone alloy films: Growth and properties,” *Chem. Vap. Depos.*, vol. 19, no. 4–6, pp.

204–212, 2013.

[61] R. A. Hall *et al.*, “Growth of zircone on nanoporous alumina using molecular layer deposition,” *Jom*, vol. 66, no. 4, pp. 649–653, 2014.

[62] A. I. Abdulagatov, K. E. Terauds, J. J. Travis, A. S. Cavanagh, R. Raj, and S. M. George, “Pyrolysis of Titanicone Molecular Layer Deposition Films as Precursors for Conducting TiO 2 / Carbon Composite Films,” *J. Phys. Chem. C*, vol. 117, pp. 17442–17450, 2013.

[63] A. I. Abdulagatov, R. A. Hall, J. L. Sutherland, B. H. Lee, A. S. Cavanagh, and S. M. George, “Molecular layer deposition of titanicone films using TiCl 4 and ethylene glycol or glycerol: Growth and properties,” *Chem. Mater.*, vol. 24, no. 15, pp. 2854–2863, 2012.

[64] P. C. Lemaire, C. J. Oldham, and G. N. Parsons, “Rapid visible color change and physical swelling during water exposure in triethanolamine-metalcone films formed by molecular layer deposition,” *J. Vac. Sci. Technol. A Vacuum, Surfaces, Film.*, vol. 34, no. 1, p. 01A134, 2016.

[65] C. Chen *et al.*, “Nanoporous nitrogen-doped titanium dioxide with excellent photocatalytic activity under visible light irradiation produced by molecular layer deposition,” *Angew. Chemie - Int. Ed.*, vol. 52, no. 35, pp. 9196–9200, 2013.

[66] B. H. Lee, V. R. Anderson, and S. M. George, “Growth and Properties of Hafnicone and HfO 2 / Hafnicone Nanolaminate and Alloy Films Using Molecular Layer Deposition Techniques,” *ACS Appl. Mater. Interfaces*, vol. 6, pp. 16880–16887, 2014.

[67] J. B. Goodenough, “Electrochemical energy storage in a sustainable modern society,” *Energy Environ. Sci.*, vol. 7, no. 1, pp. 14–18, 2014.

[68] E. Peled, D. Golodnitsky, and J. Penciner, “The Anode/Electrolyte Interface,” in *Handbook of Battery Materials*, , pp. 419–456, 2007.

[69] J. Liu and X. Sun, “Elegant design of electrode and electrode/electrolyte interface in lithium-ion batteries by atomic layer deposition,” *Nanotechnology*, vol. 26, no. 2, p. 24001, 2015.

[70] J. Vetter *et al.*, “Ageing mechanisms in lithium-ion batteries,” *J. Power Sources*, vol. 147, no. 1–2, pp. 269–281, 2005.

[71] M. Lowe, S. Tokuoka, T. Trigg, and G. Gereffi, “Lithium-ion Batteries for Electric Vehicles :,” *Forecast*, 2010.

[72] X. Meng, X.-Q. Yang, and X. Sun, “Emerging Applications of Atomic Layer Deposition for Lithium-Ion Battery Studies,” *Adv. Mater.*, vol. 24, no. 27, pp. 3589–3615, 2012.

[73] I. D. Scott *et al.*, “Ultrathin coatings on nano-LiCoO2 for Li-ion vehicular applications,” *Nano Lett.*, vol. 11, no. 2, pp. 414–418, 2011.

[74] X. Li *et al.*, “Significant impact on cathode performance of lithium-ion batteries by precisely controlled metal oxide nanocoatings via atomic layer deposition,” *J. Power Sources*, vol. 247, pp. 57–69, 2014.

[75] E. Peled and S. Menkin, “Review—SEI: Past, Present and Future,” *J. Electrochem. Soc.*,

vol. 164, no. 7, pp. A1703–A1719, 2017.

[76] D. Aurbach, E. Zinigrad, Y. Cohen, and H. Teller, "A short review of failure mechanisms of lithium metal and lithiated graphite anodes in liquid electrolyte solutions," *Solid State Ionics*, vol. 148, no. 3–4, pp. 405–416, 2002.

[77] Y. S. Cohen, Y. Cohen, and D. Aurbach, "Micromorphological Studies of Lithium Electrodes in Alkyl Carbonate Solutions Using in Situ Atomic Force Microscopy," *J. Phys. Chem. B*, vol. 104, no. 51, pp. 12282–12291, 2000.

[78] E. Peled, "Advanced Model for Solid Electrolyte Interphase Electrodes in Liquid and Polymer Electrolytes," *J. Electrochem. Soc.*, vol. 144, no. 8, p. L208, 1997.

[79] Y. S. Jung *et al.*, "Unexpected improved performance of ALD coated LiCoO2/graphite li-ion batteries," *Adv. Energy Mater.*, vol. 3, no. 2, pp. 213–219, 2013.

[80] Y. S. Jung *et al.*, "Ultrathin direct atomic layer deposition on composite electrodes for highly durable and safe Li-Ion batteries," *Adv. Mater.*, vol. 22, no. 19, pp. 2172–2176, 2010.

[81] M.-L. Lee *et al.*, "Atomic layer deposition of TiO2 on negative electrode for lithium ion batteries," *J. Power Sources*, vol. 244, pp. 410–416, 2013.

[82] a J. Loebl *et al.*, "Solid Electrolyte Interphase on Lithium-Ion Carbon Nanofiber Electrodes by Atomic and Molecular Layer Deposition," *J. Electrochem. Soc.*, vol. 160, no. 11, pp. A1971–A1978, 2013.

[83] J. Ren *et al.*, "Silicon-Graphene Composite Anodes for High-Energy Lithium Batteries," *Energy Technol.*, vol. 1, no. 1, pp. 77–84, 2013.

[84] H. Zhang and P. V Braun, "Three-dimensional metal scaffold supported bicontinuous silicon battery anodes.," *Nano Lett.*, vol. 12, pp. 2778–83, 2012.

[85] Y. He, X. Yu, Y. Wang, H. Li, and X. Huang, "Alumina-coated patterned amorphous silicon as the anode for a Lithium-Ion battery with high Coulombic efficiency," *Adv. Mater.*, vol. 23, no. 42, pp. 4938–4941, 2011.

[86] D. M. Piper *et al.*, "Reversible High-Capacity Si Nanocomposite Anodes for Lithium-ion Batteries Enabled by Molecular Layer Deposition.," *Adv. Mater.*, pp. 1–6, 2013.

[87] D. M. Piper *et al.*, "Reversible High-Capacity Si Nanocomposite Anodes for Lithium-ion Batteries Enabled by Molecular Layer Deposition.," *Adv. Mater.*, 2013.

[88] R. High, C. Si, N. Anodes, and M. L. Deposition, "Advanced Materials Reversible High Capacity Si Nanocomposite Anodes enabled by Molecular Layer."

[89] Y.-G. Guo, J.-S. Hu, and L.-J. Wan, "Nanostructured Materials for Electrochemical Energy Conversion and Storage Devices," *Adv. Mater.*, vol. 20, no. 15, pp. 2878–2887, Aug. 2008.

[90] W. Xing, "Study of Irreversible Capacities for Li Insertion in Hard and Graphitic Carbons," *Journal of The Electrochemical Society*, vol. 144. p. 1195, 1997.

[91] Y. V. Mikhaylik and J. R. Akridge, "Polysulfide Shuttle Study in the Li/S Battery System," *J. Electrochem. Soc.*, vol. 151, no. 11, p. A1969, 2004.

[92] S. S. Zhang, "Liquid electrolyte lithium/sulfur battery: Fundamental chemistry, problems, and solutions," *J. Power Sources*, vol. 231, pp. 153–162, 2013.

[93] D. Moy, A. Manivannan, and S. R. Narayanan, "Direct Measurement of Polysulfide Shuttle Current: A Window into Understanding the Performance of Lithium-Sulfur Cells," *J. Electrochem. Soc.*, vol. 162, no. 1, pp. A1–A7, 2014.

[94] X. L. Supervisor and A. X. Sun, "Development of Novel Nanomaterials for Li-sulfur Batteries," no. 2013.

[95] Y. Yang *et al.*, "Improving the performance of lithium-sulfur batteries by conductive polymer coating," *ACS Nano*, vol. 5, no. 11, pp. 9187–9193, 2011.

[96] S. Evers and L. F. Nazar, "New approaches for high energy density lithium-sulfur battery cathodes," *Acc. Chem. Res.*, vol. 46, no. 5, pp. 1135–1143, 2013.

[97] Y. J. Choi, Y. D. Chung, C. Y. Baek, K. W. Kim, H. J. Ahn, and J. H. Ahn, "Effects of carbon coating on the electrochemical properties of sulfur cathode for lithium/sulfur cell," *J. Power Sources*, vol. 184, no. 2, pp. 548–552, 2008.

[98] H. Kim, J. T. Lee, D. C. Lee, A. Magasinski, W. Il Cho, and G. Yushin, "Plasma-enhanced atomic layer deposition of ultrathin oxide coatings for stabilized lithium-sulfur batteries," *Adv. Energy Mater.*, vol. 3, no. 10, pp. 1308–1315, 2013.

[99] X. Li *et al.*, "Tailoring interactions of carbon and sulfur in Li–S battery cathodes: significant effects of carbon–heteroatom bonds," *J. Mater. Chem. A*, vol. 2, no. 32, p. 12866, 2014.

[100] X. Li, A. Lushington, J. Liu, R. Li, and X. Sun, "Superior stable sulfur cathodes of Li-S batteries enabled by molecular layer deposition.," *Chem. Commun. (Camb).*, vol. 50, no. 68, pp. 9757–60, 2014.

[101] X. Li *et al.*, "Safe and Durable High-Temperature Lithium-Sulfur Batteries via Molecular Layer Deposited Coating," *Nano Lett.*, 2016.

[102] J. Gao, M. A. Lowe, Y. Kiya, and H. D. Abruña, "Effects of liquid electrolytes on the charge-discharge performance of rechargeable lithium/sulfur batteries: Electrochemical and in-situ X-ray absorption spectroscopic studies," *J. Phys. Chem. C*, vol. 115, no. 50, pp. 25132–25137, 2011.

[103] T. Yim *et al.*, "Effect of chemical reactivity of polysulfide toward carbonate-based electrolyte on the electrochemical performance of Li-S batteries," *Electrochim. Acta*, vol. 107, pp. 454–460, 2013.

[104] P. J. Bouwman, W. Dmowski, J. Stanley, G. B. Cotten, and K. E. Swider-Lyons, "Platinum-Iron Phosphate Electrocatalysts for Oxygen Reduction in PEMFCs," *J. Electrochem. Soc.*, vol. 151, no. 12, p. A1989, 2004.

[105] J. S. King *et al.*, "Ultralow loading Pt nanocatalysts prepared by atomic layer deposition on carbon aerogels," *Nano Lett.*, vol. 8, no. 8, pp. 2405–2409, 2008.

[106] S. Sun *et al.*, "Single-atom Catalysis Using Pt/Graphene Achieved through Atomic Layer Deposition," *Sci. Rep.*, vol. 3, no. 1, p. 1775, 2013.

[107] D. A. Bulushev *et al.*, “Single Atoms of Pt-Group Metals Stabilized by N-Doped Carbon Nanofibers for Efficient Hydrogen Production from Formic Acid,” *ACS Catal.*, vol. 6, no. 6, pp. 3442–3451, 2016.

[108] N. Cheng *et al.*, “Extremely stable platinum nanoparticles encapsulated in a zirconia nanocage by area-selective atomic layer deposition for the oxygen reduction reaction,” *Adv. Mater.*, vol. 27, no. 2, pp. 277–281, 2015.

[109] C. J. Serpell, J. Cookson, D. Ozkaya, and P. D. Beer, “Core@shell bimetallic nanoparticle synthesis via anion coordination,” *Nat. Chem.*, vol. 3, no. 6, pp. 478–483, 2011.

[110] S. Alayoglu, A. U. Nilekar, M. Mavrikakis, and B. Eichhorn, “Ru–Pt core–shell nanoparticles for preferential oxidation of carbon monoxide in hydrogen,” *Nat. Mater.*, vol. 7, no. 4, pp. 333–338, 2008.

[111] X. Zhao *et al.*, “Recent advances in catalysts for direct methanol fuel cells,” *Energy Environ. Sci.*, vol. 4, no. 8, p. 2736, 2011.

[112] P. Forzatti and L. Lietti, “Catalyst deactivation,” *Catal. Today*, vol. 52, pp. 165–181, 1999.

[113] X. Liang and A. W. Weimer, “An overview of highly porous oxide films with tunable thickness prepared by molecular layer deposition,” *Curr. Opin. Solid State Mater. Sci.*, vol. 19, no. 2, pp. 115–125, 2015.

2

Experimental Apparatus and Characterization Techniques

2.1 Experimental Apparatus

This section will explore and discuss the tools used to deposit thin films and nanostructures by ALD and MLD. Two commercially available ALD tools are described herein and the importance of each component will be discussed along with possible ways to prevent tool downtime and maintain consistent results. Advantages and disadvantages of each tool will also be discussed. The aim of this section is to demonstrate the subtle nuances of ALD and MLD as well as the dependence of tool design and how this factors into depositing thin films and nanostructures.

2.1.1 Savannah 100 (Cambridge Nanotech, USA)

The Savannah 100 ALD system (S100), produced by Cambridge Nanotech, is probably one of the most widely used ALD tools in research labs. The S100 system uses a 50 ml precursor bottle made of 316 stainless steel equipped with a ¼" VCR male ball valve or bellows-sealed valve (for high temperature use). The precursor bottles can be heated with a heating jacket provided by Cambridge that can reach a temperature of 175°C. A single manifold design is used in the S100 system and provides attachment for up to 5 different precursors. Carrier gas flow is controlled using a mass flow controller (MFC). The precursor bottle inlet can be attached to the manifold where it is coupled to a 3 way pneumatically actuated ALD diaphragm valve and solenoid. These fast-acting, high-flow solenoid pilot enhanced ALD valves allow for accurate dosing of precursor into the reaction chamber. The actuation time of these solenoid values can be as small as 50 ms. One end of the diaphragm valve is attached to the carrier gas, while the other end is attached to the precursor bottle and the third end of the ALD valve is coupled to the precursor manifold. The entire

manifold assembly is then connected to a pancake style reactor chamber. The manifold assembly is encased in an insulated metal enclosure equipped with a cartridge heater to ensure uniform heating from precursor to reaction chamber. For the S100 ALD tool, a manifold temperature of 190°C can be reached. The pancake style reactor used for this system has a single-inlet single-outlet design and can reach a max temperature of 400°C. To maintain vacuum during the deposition process, a Kalrez O-ring is used. It should be noted that extended exposure to high temperature and long oxidizer pulse times will result in O-ring degradation and eventual loss of vacuum. The outlet of the reactor is connected to an exhaust line assembly which contains a vacuum gauge (Edwards APGX-H NW 16) and stop valve (Norcal solenoid valve) to control pumping exhaust. This assembly can be heated up to 150°C to prevent condensation of excess precursor and reaction by-products. The final component of the exhaust line assembly is a heated trap that is designed to extract and trap excess precursor so that organometallic precursors and reaction by-product do not enter the pump and pump oil. This exhaust line assembly is attached to an Adixen 2021 vacuum pump capable of pumping 14.6 cubic feet per minute (CFM). Using this configuration, an operating pressure of about 0.4-0.5 Torr can be sustained using a flow rate of ~20 sccm. Deposition parameters for ALD experiments are controlled by a custom-made electronics box and a PC LABVIEW program provided by Cambridge.

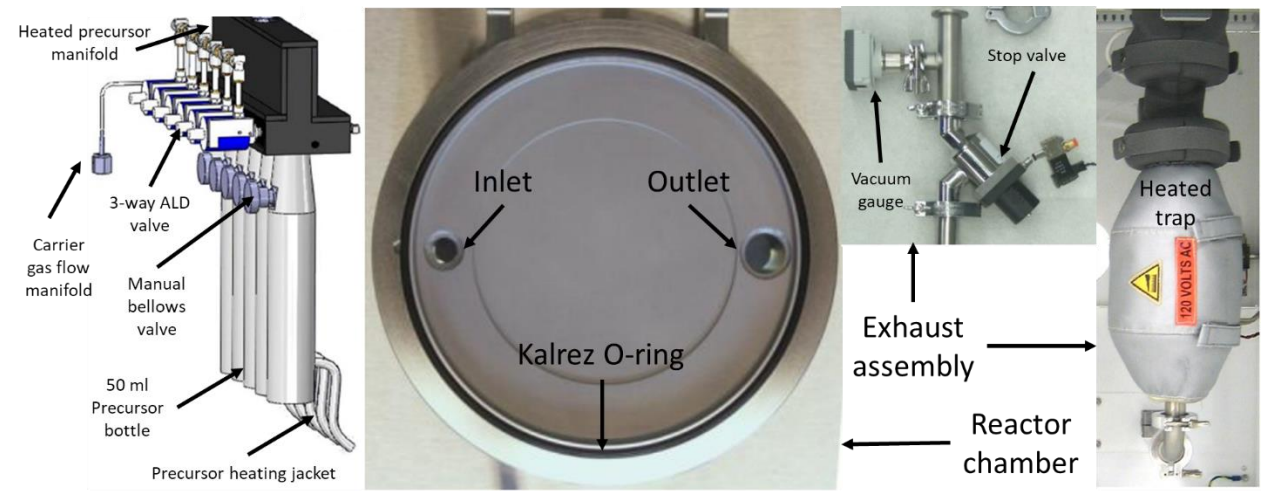


Figure 2.1. *Outline of various components of an ALD S100 Cambridge Savannah tool starting with precursor distribution manifold assembly followed by reactor and exhaust assembly.*

One of the most commonly encountered issues for an ALD system is pump failure. Due to the highly corrosive nature of many ALD precursor, pump oil can quickly become contaminated with corrosive chemicals and begin to corrode internal components of the rotary vane pump. The operation of a rotary vane pump relies on using a vane that is mounted to a cylindrical rotor that rotates inside a cavity. After prolonged exposure to corrosive chemicals, the vanes of the pump, which are typically made of carbon graphite, are eroded and vacuum pressure is quickly lost as the vane no longer sits flush with the cylindrical rotor. Other components inside of the pump may also erode and cause the vacuum pump to seize. Although a heat trap is used to prevent excess precursor for entering the pump, the effectiveness of this system diminishes over time if regular maintenance is not performed. One method to circumvent this issue is to incorporate several in-line traps such as a liquid nitrogen trap or a Posi-trap. Regular oil maintenance is another strategy that was found to work well. It is also possible to use a more chemically resistant oil, such as fomblin. However, this oil is costly and pump issues may still occur as other components in the pump are still susceptible to corrosion.

One issue that is unique to the S100 tool is reaction of precursors prior to entering the reaction chamber. This is due to the single manifold configuration employed in this tool and inherently causes precursor reaction to occur in the manifold as well as in the reaction chamber. Furthermore, this type of design may also result in cross-contamination of precursor which will change precursor properties and result in precursor decomposition and introduction to unwanted reaction products into the reactor. By not spatially separating precursors, prior to introduction into the reaction chamber, unwanted side reactions may take place within the manifold. Eventually a thick film will be deposited within the manifold and impede flow of precursor and carrier gas into the reaction chamber and cause several other issues to appear. Due to this design flaw, MLD was not conducted on this tool. Because MLD uses organic precursor that can be quite sticky, separation of reactants prior to the reaction chamber is crucial, especially when developing new recipes and films. Another common problem with the S100 tool is non-uniform distribution of precursor in the chamber. This is a direct results of the single-inlet single-outlet design employed by this tool. This requires careful and consistent placement of substrate into the reaction chamber in order to achieve reproducible results. The influence of uneven precursor distribution is more obvious for some processes than others, especially ones that employ the use of ozone.

2.1.2 Gemstar-8 (Arradiance, USA)

The Gemstar-8 ALD tool, produced by Arradiance, is a benchtop ALD tool that is quite different from the S100. Rather than utilizing a single precursor manifold design, the Gemstar-8 has two separate manifolds. One manifold is designed for metalorganic precursors while the second manifold is used for oxidizers and reducers. These two manifolds meet a distribution plate which is attached to the reaction chamber. By utilizing a dual manifold design, reactants are kept separate and prevents reaction from occurring prior to the reaction chamber. At each precursor inlet is a three-way ALD valve, like the S100. Interestingly, this ALD tool features a single inert gas vapor pressure assist-line for precursors that have low vapor pressures. This vapor pressure assist-line diverts carrier gas into the precursor bottle and is controlled by a small electronic actuator. A single mass flow controller is also used to control carrier gas flow rate. Unlike the S100 ALD tool, the Gemstar-8 reaction chamber is much larger and has a volume of ~ 2160 cm^3. In comparison the pancake style reaction chamber of the S100 has a volume of ~ 266 cm^3. It is these unique design properties that allows for MLD to be performed on this tool and not the S100. Each manifold in the Gemstar-8 can hold up to four precursors, for a total of 8 precursor attachments. Both manifolds can be heated up to 155°C. 150 ml precursor bottles are used for this ALD tool along with bottle heaters that are capable of reaching a max temperature of 140°C. Precursor bottles are also equipped with a manual 90° bellows seal valve (Fujikin or Ham-let). Precursor distribution into the reaction chamber is governed by 10 holes and a single outlet that allows for uniform precursor exposure to the substrate. The reaction chamber and door can be heated up to 350°C. To ensure a complete seal during vacuum operation, a Kalrez O-ring is used between the door and reaction chamber. Attached to the rear of the reaction chamber is a pressure sensor that is connected to an electronics board. Following the reaction chamber, a stainless-steel tube leading to a CF 2.75 flange is available for metrology use. This exterior port can be used to install a quartz-crystal microbalance (QCM) for in-situ monitoring of deposition and will be covered later. Below this connection is a heated stop valve used to control pumping exhaust, like the S100. A dual stage rotary-vane vacuum pump (E2M18 Edwards) is attached to the system and can provide a vacuum of ~ 0.2 Torr at a carrier gas flow rate of 20 sccm. This system is usually equipped with a liquid nitrogen trap as well as two Posi traps. One Posi trap contains a high surface-area zeolite material while the other Posi trap contains a sodasorb filter to trap and neutralize acidic vapors. This ALD system is controlled by software provided by Arradiance.

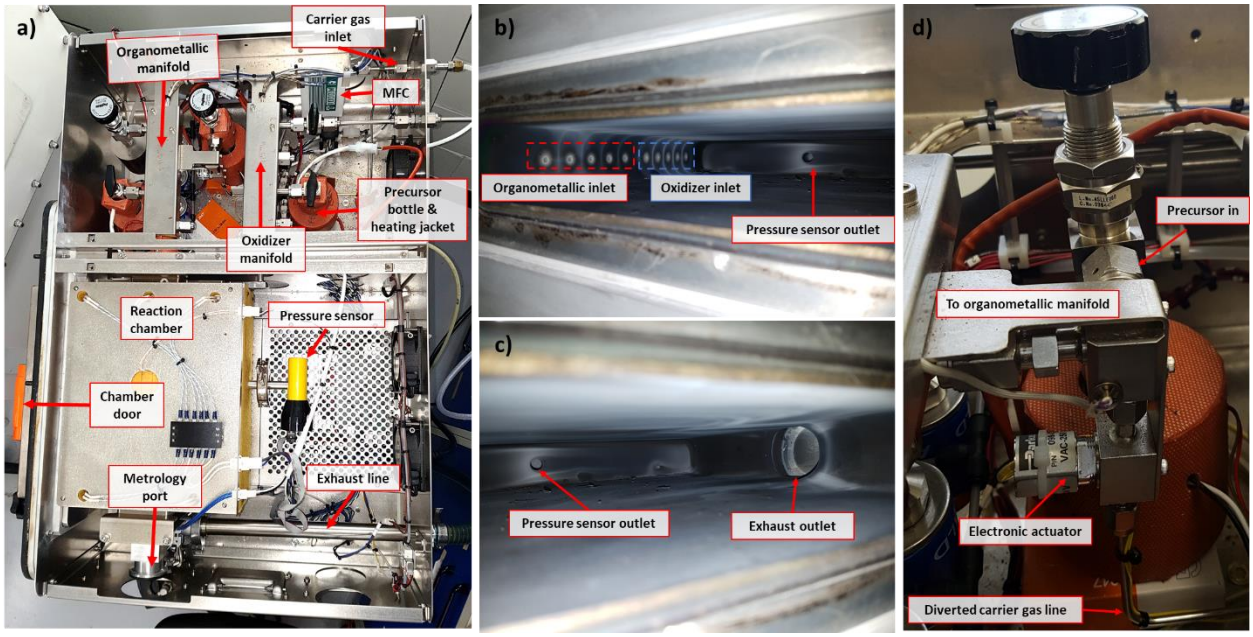


Figure 2.2. *a) Birds eye view of the Gemstar-8 system with labels. b) and c) Interior of ALD reaction chamber demonstrating precursor inlet, outlet, and pressure sensor location. d) Inert gas vapor pressure assist line attached to the organometallic manifold.*

Although there are several unique innovations within the Gemstar-8 ALD system, a number of issues arose during its use. One of primary concern is the pressure sensor used in this system. The original ALD system obtained by our group was outfitted with a CVM211 Stinger pirani gauge. This pressure sensor has a much lower resolution compared to the linear convection gauge employed in the S100 tool. This can be a real issue when trying to deposit materials that require precursors with low vapor pressure, as no signal can be detected during a pulse, even if precursor is entering the chamber. Another issue related to the pressure sensor is its location. Given that the pressure sensor is directly exposed to reaction products and is part of the reaction chamber, deposition will occur within the sensor, especially if using an ALD recipe that requires the exposure valve to be shut so that precursor exposure can be prolonged. Continued deposition at the sensor interface will diminish its lifetime as well as provide erroneous pressure sensor readings as filament material properties are altered due to film deposition. A solution to this issue is to place a nickel foam mesh between the sensor and the chamber. This mesh will absorb some of the reaction products and creates a more tortuous path of incoming precursor molecules. Although this is a band-aid solution, it has prolonged the lifetime of the pressure sensor. A key requirement for ALD is constant and consistent temperature control. To prevent precursor condensation, a

graduation temperature gradient is applied from precursor bottle, to manifold, to reaction chamber. Ideally, the flow of precursor vapor should follow this sequence as well, however, this may not be the case for compounds that have a very high vapor pressure. If a high enough carrier gas flow rate is not used during pulsing of these high vapor pressure compounds, precursor vapor may backstream toward the MFC. In the Gemstar-8 system, no heating is applied or present between the MFC and the two manifolds. If precursor vapor does flow backward, toward the MFC, precursor condensation will occur, causing serious damage to the system and impeding carrier gas flow rate. Probably one of the biggest challenges with using the Gemstar-8 system is its compact design. Engineering a tabletop ALD system results in geometrically constrained areas within the tool. As a result, changing precursor bottles can be cumbersome. Furthermore, such a compact design severely reduces the ability to quickly change components within the machine as well as makes it quite difficult to reach certain parts of the tool.

2.2 Characterization Techniques

This section of the chapter is dedicated to describing the various characterization tools central to this thesis. It will provide the necessary fundamental background for each characterization technique and provide context as to why this technique is important for characterizing films and nanostructures produced by ALD and MLD. The advantages of each technique and the unique information they can provide will be discussed. However, each tool has their limitations and disadvantages. These aspects will also be explored. Specific details for each study outlined in this thesis can be found in the methods section of their respective chapter.

2.2.1 Scanning Electron Microscopy

Provided that films and structures produced by ALD and MLD are in the nanoscale, direct visual observation of surface morphology is difficult to obtain through optical microscopy due to diffraction limit of light. To overcome this issue, scanning electron microscopy (SEM) can be employed. A typical SEM consists of two major parts, the microscope column and the electronics console. The microscope column contains an electron gun, one or two condenser lenses, two pairs of beam deflection coils, an objective lens, and a few aperture lenses. At the bottom of the microscope column is the specimen chamber which houses the specimen stage and detectors for

various signals generated by electron-specimen interaction. The column and chamber are pumped down to create a vacuum and maximize the interaction between the sample and the incoming electron beam. Electrons produced at a cathode are accelerated using a voltage between 0.5-30 kV toward an anode, to form a spot size between 5-10 nm. This beam then passes through a series of lenses and deflection coils toward the sample. Several different detectors are used to analyze sample-electron interaction and provide information pertaining to surface morphology and composition.

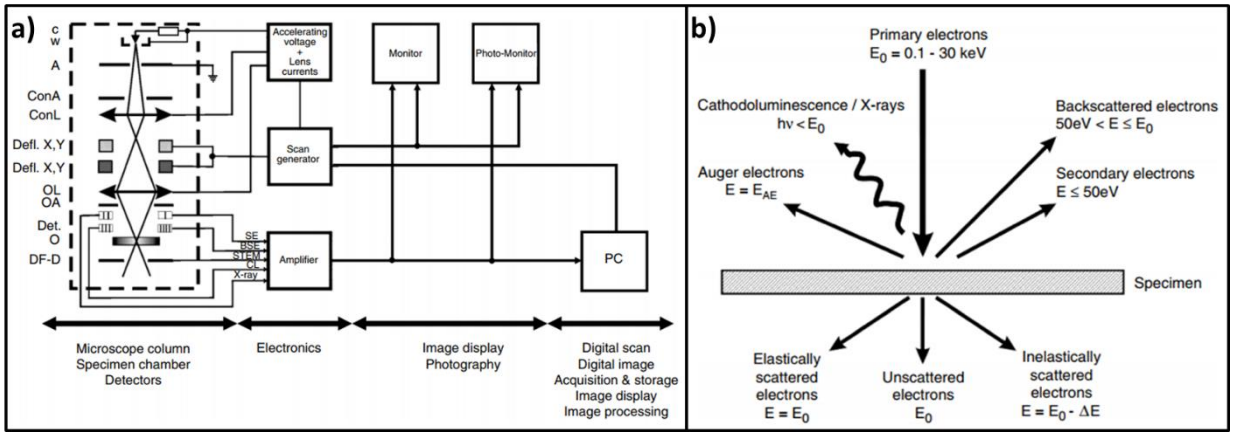


Figure 2.3. a*) Schematic drawing of a conventional SEM. b) Outline of electron beam interaction with sample and the various signals that can be produced by this interaction [1].*

Secondary electrons are typically analyzed for routine imaging of a surface using SEM. These in-elastically scattered electrons have an energy less than 50 eV and allow them to be easily collected and detected close to the substrate surface. Generation of secondary electrons is primarily influenced by surface topography and provides good edge detail and is suitable for observing nanoparticles on surfaces. However, emission of secondary electrons is diminished for non-conductive samples and makes imaging of some films very difficult. Since many ALD and MLD films are non-conductive, obtaining a cross section of films deposited on Si after a few ALD cycles can be problematic, especially if the films tend to trap electron charges. Therefore, thicker films need to be deposited to obtain accurate film thickness measurements. Unfortuently, depositing thicker films by ALD requires a lot of time. This makes SEM not an ideal characterization technique for obtaining film growth rate.

Backscattered electrons are another electron source used to image samples. These electrons are generated by primary incident electrons that are ejected back out of the sample. Backscattered electrons are higher in energy >50 eV and are used to image heavier elements. A higher average atomic number will result in an increased chance for the generation of backscatter electrons. However, images produced using backscattered electrons have decrease spatial resolution and is typically used to collect contrast images to determine average atomic number of a sample. SEM analysis of backscattered electrons is primarily conducted by Nobel metals produced by ALD. Nobel metals have a high atomic number and make them easy to image. Unfortunately, a large enough cluster needs to be present on the surface so that it can be imaged appropriately. Given the low spatial resolution of backscattered electrons, this analysis of these electrons is not always suitable for nanoparticles deposited by ALD.

A Hitachi S-4800 field-emission SEM was used to characterize surface morphology for most samples in this thesis. An accelerating voltage between 5.0 – 10 kV was used to image the surface of materials using a minimum working distance of 5 mm. This configuration can provide a spatial resolution down to ~2 nm, depending on the material. Specimen chamber pressure was maintained at $1x10^{-6}$ Torr. Samples were often attached to a sample holder using either carbon tape or a graphite carbon paste. However, some samples are unsuitable for imaging in the S-4800 due to the high vacuum and accelerating voltage energy used during operation. This is especially the case for imaging the surface of lithium metal. To overcome this issue, an environmental Hitachi 3400N SEM was used instead. This SEM provides a chamber pressure of $7x10^{-3}$ Torr and uses an accelerating voltage of only 5 kV with a probe working distance of 64 mm. However, these imaging conditions come with a severe penalty to image resolution (~ 50 nm).

2.2.2 Fourier Transform Infrared Spectroscopy

Compounds with covalent bonds, whether they be organic or inorganic, absorb electromagnetic radiation in the infrared (IR) region of the electromagnetic spectrum. Like many other energy absorption processes, molecules that are excited by IR radiation jump to a higher energy state as they absorb energy. This quantized process can be used to probe the chemical state of molecules. During IR absorption, IR frequencies that match the natural frequency of the molecule in question are absorbed, and the energy absorbed serves to increase the amplitude of the

vibrational motion of the bonds in the molecule. However, not all bonds in a molecule are capable of absorbing IR energy, even if the frequency of radiation exactly matches that of the bond motion. Only bonds that have a dipole moment that change as a function of time are capable of absorbing IR radiation. For example, symmetric bonds, such as H_2 or Cl_2, do not absorb IR radiation. A bond must have an electrical dipole that varies at the same frequency as the incoming radiation for energy to be successfully transferred. Since each bond has a different natural frequency of vibration, and since two of the same type of bond in two different compounds are in two slightly different environments, no two molecules of different structure have the same IR absorption pattern, or IR spectrum. The instrument used to obtain an absorption spectrum is called an IR spectrometer. These spectrometers use an optical pathway to produce a plot of intensity versus time in a pattern known as an interferogram. To produce an IR interferogram pattern an interferometer is used. In an interferometer, the source energy passes through a beam splitter that separates the beam into an un-deflected beam and another beam oriented at 90°. The beam oriented at 90° traverses to a fixed mirror where it is bounced back to the beam splitter. The un-deflected beam traverses toward a moving mirror and is also returned to the beam splitter. The motion of the mirror causes the pathlength of second beam to vary. When the two beams meet at the beam splitter, they recombine, but the varying pathlength difference between the beams results in a pattern caused by constructive and destructive interferences. The combined beam containing this interference pattern is the interferogram and contains all the radiative energy coming from the source and has a wide range of wavelengths. The generated interferogram, from the combination of the two beams, is oriented toward a sample by the same beam splitter. As it passes through the sample, the sample simultaneously absorbs all wavelengths that are normally found in its infrared spectrum. The altered interferogram pattern then passes through a detector and contains information pertaining to the amount of energy that was absorbed at each wavelength. A final interferogram pattern is produced by comparing the modified interferogram with a reference laser beam. The final interferogram pattern contains information that is in a time domain frequency. A Fourier transform function is then performed to extract individual frequencies that were absorbed, and a plot is reconstructed to provide an IR spectrum. This process is known as Fourier transformed IR (FTIR) spectroscopy [2].

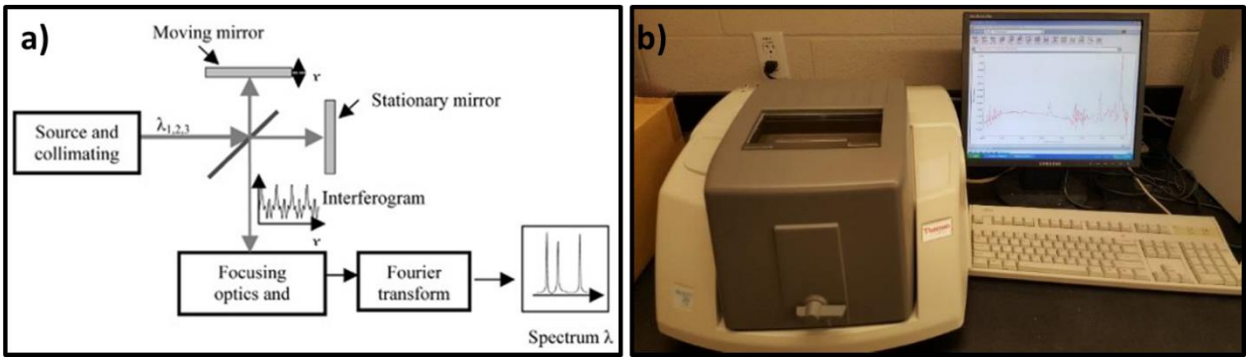


Figure 2.4. a*) Schematic outline for the working principle of FTIR. b) Photo of the Thermo Scientific Nicolet 380 FTIR system used for this thesis.*

For the FTIR spectrums presented in this thesis, a Thermo Scientific Nicolet 280 FTIR system was used. FTIR was used to determine bonding characteristics for as-deposited MLD films and post treated films. This technique is excellent for determining if an MLD process was successful. It is a particularly useful technique for characterization of MLD films as certain polarizable organic bonds, such as C=O, provide strong FTIR signals. MLD was conducted on double polished n-type (100) silicon wafers and an FITR spectrum could be obtained by placing this sample directly into the spectrometer. A blank double wafer was used to provide a background spectrum.

2.2.3 Raman Spectroscopy

Raman spectroscopy is a non-destructive photon-based characterization technique. This technique is based on the inelastic scattering of photons through its interaction with vibrating molecules and probes molecular vibrations. When an incoming photon interacts with a molecule it is excited to a virtual energy state for a short period of time before the photon is emitted back. Inelastic scattering occurs when the energy of the emitted photon is at a different frequency than the incident photon. Raman spectroscopy employs the use of a monochromatic laser beam that is directed to a sample and the light that is scattered is detected perpendicular to the incident beam. Inelastic scattering will cause a portion of the scattered light to have a frequency different from that of the incident light, and this is used to construct a Raman spectrum. Most of the scattered light will have a frequency equal to the frequency of the incident radiation, known as Rayleigh scattering. When the frequency of the scattered radiation is detected to be lower than the frequency

of the incident radiation, Stokes Raman scattering is said to be observed. This is the band that is most commonly observed in Raman spectroscopy. Anti-stokes Raman scattering occurs when a frequency is detected that is higher than the incident radiation. This type of scattering is not typically observed and usually only occurs for fluorescent samples. For a Raman shift to be detected, a change in the polarizability of the molecule must occur. This can be expressed through vibration, rotation, or electronic modes [3].

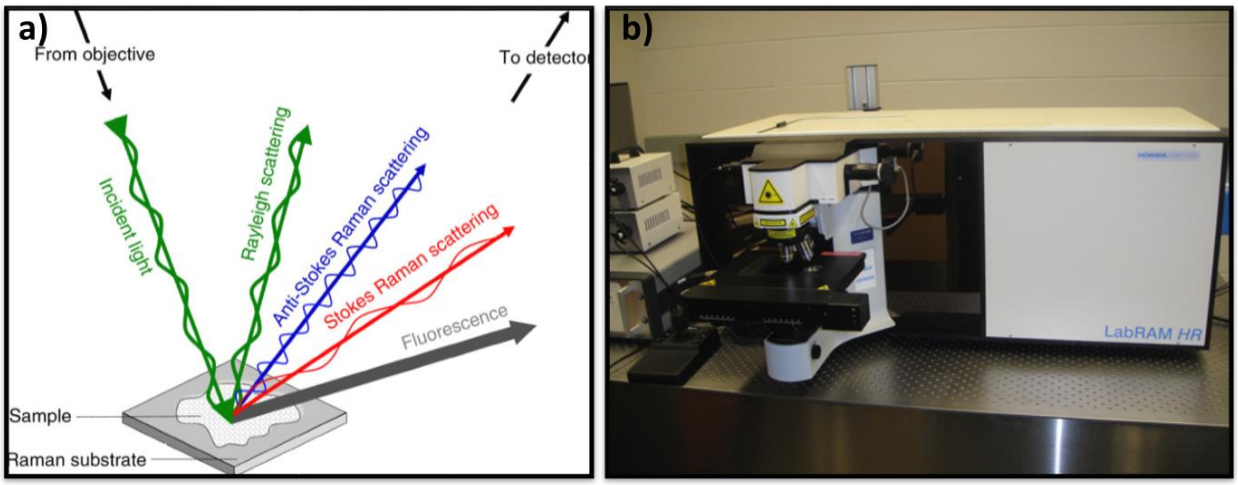


Figure 2.5. *a) Schematic outline of various types of light scatter that can occur following sample irradiation with a laser source [4]. b) Photo of the HORIBA Scientific LabRAM HR Raman spectrometer used.*

Historically, Raman spectroscopy has played an import role in the study and characterization of carbon based materials. It has been used to characterize pyrolytic graphite, carbon fibers, glassy carbon, nanographite ribbons, fullerenes, carbon nanotubes and graphene. Due to the high polarizability of sp^2 and sp^3 type bonds found in carbon based materials, Raman spectroscopy can provide valuable insight about the electronic and geometrical structure of these materials [5]. For this reason, Raman spectroscopy is used to characterize carbon nanotubes and carbon containing films used and developed in this thesis. A HORIBA Scientific LabRAM HR Raman spectrometer, equipped with a 532.4 nm laser and optical microscope, was used for Raman characterization of carbon based materials. This technique provided detailed information about to carbon crystal size domain and defect density of carbon-based materials.

2.2.4 Quartz Crystal Microbalance

Given the excellent piezoelectric properties of quartz, it has been applied to several different applications. One interesting application is the use of quartz as a tool to measure mass changes during film growth, in both liquid and gas environments. This application of quartz is known as a quartz crystal microbalance (QCM). Due to the extremely sensitive nature of quartz's piezoelectric response, QCM is a very powerful technique that can detect the growth of sub-monolayer films. When a certain mass is deposited on a quartz crystal, the resonant frequency of the crystal changes. These changes can be modeled using the following equation:

$$\Delta f = -\frac{2f_0^2 \Delta m}{A\sqrt{\mu\rho}} = -C\Delta m$$

Δf = Change in resonant frequency f_0 =fundamental resonant frequency of the crystal

$\Delta m =$ Change in mass $A =$ Surface area of exposed crystal

$\mu =$ Shear moduls of crystal $\rho =$ density of Quartz

$C =$ Crystal dependent constant

However, the resonant frequency of the quartz crystal is not only dependent on mass change but also gas viscosity, stress in the forming film, pressure, and temperature changes [6]. QCM is an invaluable for process development of ALD and MLD films. The highly sensitive nature of this simple, but yet versatile tool, is well positioned for determining growth rate of ALD and MLD films and can provide valuable mechanistic insight toward growth mechanics. The QCM used in this thesis was provided by Colnatec and uses a Phoenix single sensor crystal head assay mounted on a 2.75" conflat flange. This is coupled with an Eon Lt monitoring tool that is used to record and drive the piezoelectric crystal. A 6 MHz, 14 mm gold coated AT-cut quartz crystals was used in this thesis. The crystal head assay assembly was loaded into the metrology port of the Gemstar-8 system for in-situ monitoring of deposition.

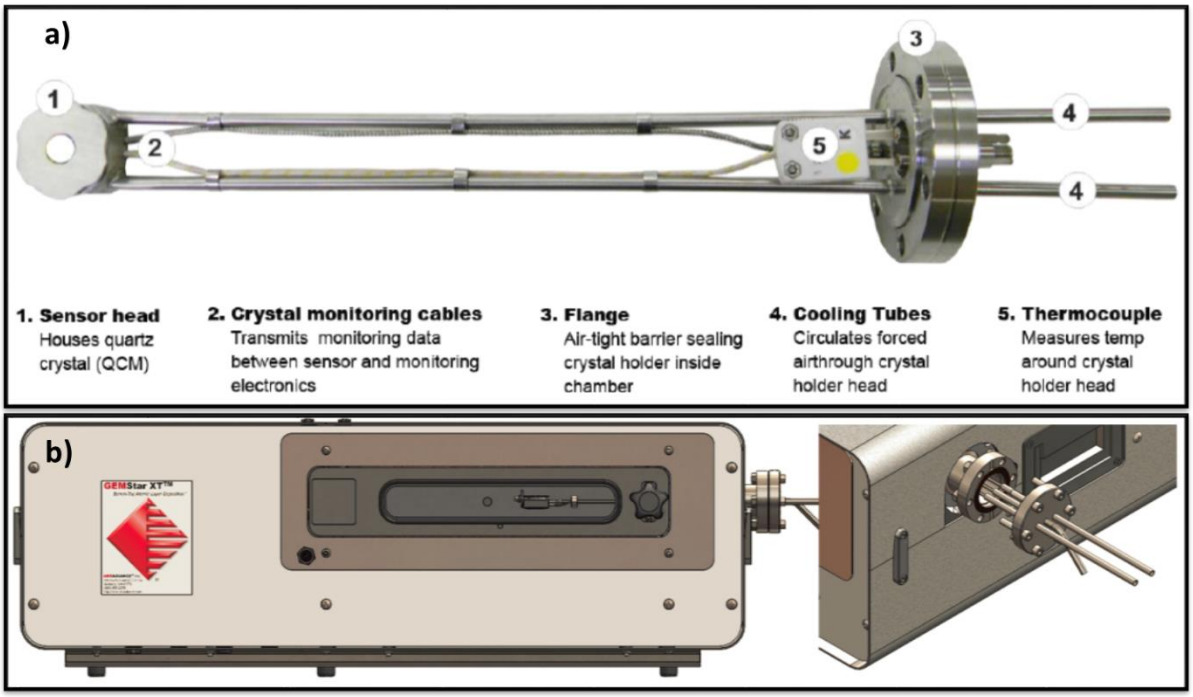


Figure 2.6. a*) Schematic outline of Phoenix QCM crystal head assay provided by Colnatec [7]. b) Use of QCM in Gemstar- 8 ALD system*

2.2.5 X-ray Reflectivity

X-ray reflectivity (XRR) is a non-destructive and non-contact method of determining many important thin film properties. This technique can provide information about film thickness, with precision between 1-3 Å, as well as film density and roughness. Furthermore, it can be used to determine thickness and interface properties of multilayer films. XRR is based on probing electron density at the surface and can be used to characterize polymer coatings, ceramics, or metals, whether they be crystalline or non-crystalline in nature. XRR monitors the intensity of x-ray beams reflected by a sample at very low angles. By measuring the interference of reflected x-rays from the surface due to total external reflection, an interference pattern can be obtained that contains information for the film in question. The reflection at the surface and interfaces is due to a difference in electron density between the two materials. This is also related to the difference in refractive index between materials. For incident angles below some critical angle (θ_c), total external reflection will occur, and this angle can be used to determine film density. Most materials have a critical angle that is less than 0.3° [8]. For incident angles above the critical angle,

reflections from different interfaces will interfere and provide interference fringes. The period of between these interference fringes, known as Kessing fringes, provides information about film thickness. Oscillation amplitude on the other hand provides information on the difference in electron density between the film interface and substrate and provides film roughness measurements. Figure 2.7b presents a typically XRR curve with a very high intensity at low angles, due to complete reflection, and decreased intensity with increasing angle due to interference. Data is typically collected as a function of scattered angle 2θ from the surface. Complex recursion formulas are required to produce theoretical simulation XRR data and requires an estimation of density, thickness, and roughness in order to accurately determine film properties. For XRR experiments conducted in this thesis a Bruker D8 Advance was used. The X-ray diffraction machine used was equipped with a Cu Kα X-ray tube with a wavelength of 1.54 Å. A filament current of 40 mA and a voltage of 40 kV was used for XRR experiments. X-ray reflectivity data was analyzed using the LEPTOS software package to determine film thickness and roughness.

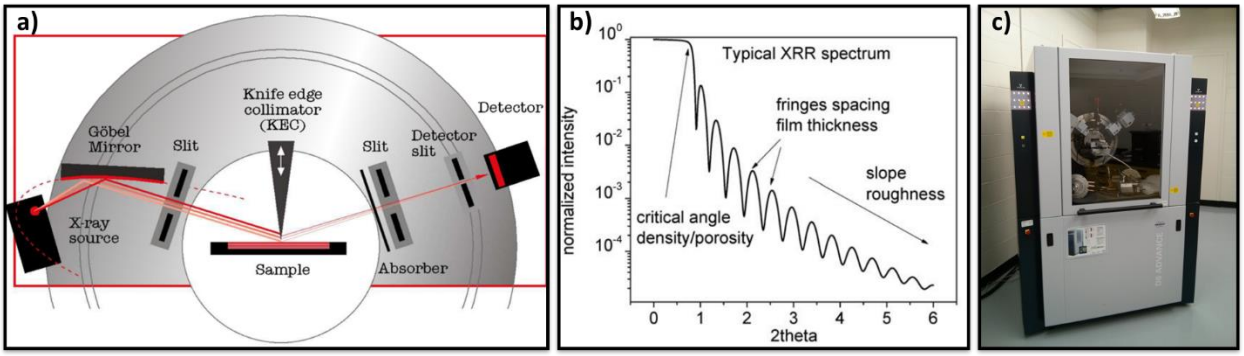


Figure 2.7. a*) Schematic outline of operational setup to perform XRR. b) Typical XRR curve outlining the importance of curve features. c) Photo of the Bruker D8 Advance used for XRR.*

2.2.6 Synchrotron Based Characterization Techniques

Synchrotron radiation sources are a revolutionary tool that can be used to gather structural and chemical properties of materials at the molecular level. These tools produce photons by accelerating charged particle to relativistic speeds and passing them through an insertion device that forces the particle to wiggle or undulate. As the particle changes path, Lorentz forces, acting on the particle, results in the emission of highly brilliant, forward-directed, polarized synchrotron radiation. This radiation is directed toward a beamline end-station where researchers can choose the desired wavelength to study their samples. There are many characterization techniques that

utilize synchrotron radiation, but for the purposes of this thesis three main techniques will be explored, x-ray absorption fine structure (XAFS) spectroscopy, near-edge X-ray absorption fine structure (NEXAFS) spectroscopy and extended x-ray absorption fine structure (EXAFS) spectroscopy. For this thesis several different beamlines are used to characterization of ALD and MLD nanostructures. Specific details can be found within the experimental section of each chapter.

2.2.6.1 Near Edge X-ray Absorption Fine Structure Spectroscopy

XAFS is one of the few spectroscopic techniques that can provide both electronic and structural information of materials. An X-ray absorption signal is generated when an incoming photo has enough energy to excite an electron from a core level to a vacant excited state or to the continuum. This excitation follows dipole selection rules and will appear as a sharp peak at a certain energy, followed by a featureless region beyond which the absorption coefficient decreases with increasing photon energy. The short area, following x-ray absorption, is referred to as the near-edge x-ray absorption fine structure (NEXAFS) region and is sensitive to chemical oxidation state, coordination number, unoccupied densities of states, type of neighboring atoms, and local symmetry [9]. When a material is irradiated with X-rays, the intensity of the incident x-ray beam will decrease after it has passed through the sample. The decrease in x-ray energy is determine by absorption characteristics, defined as $\mu(E)$ of the material, and follows Beer-Lambert's law:

$$I_t = I_0 e^{-\mu(E)x}$$

This transmission based technique requires the material that is analyzed to be thin and is often done using high energy X-rays (>5 keV). It is typically used to measurement and analyze heavier elements such as Pt, Pd and Ru. For NEXAFS of low Z elements, direct transmission measurements are not feasible due to the large absorption cross section for these element, therefore, photoelectrons generated by the x-ray absorption process are detected instead. As an absorbed X-ray excites a core level electron to an empty state above the vacuum or Fermi level, core holes are generated. Auger electron decay then occurs to fill these core holes, resulting in the emission of primary auger electrons. This emission can be directly measured and is referred to as the auger electron yield (AEY). The detection of these electrodes is highly sensitive to the surface and probes a depth of about 1 nm. Furthermore, primary auger electron generated deeper within the sample create scattered secondary electrons and give rise to a total electron yield signal (TEY). The TEY

cascade event involves several scattering events and originates from the electron sampling depth (L) [10]. Due to the high specificity of XAFS, and the level of detail provided by NEXAFS, this technique is used to determine the local chemical state of ALD and MLD materials.

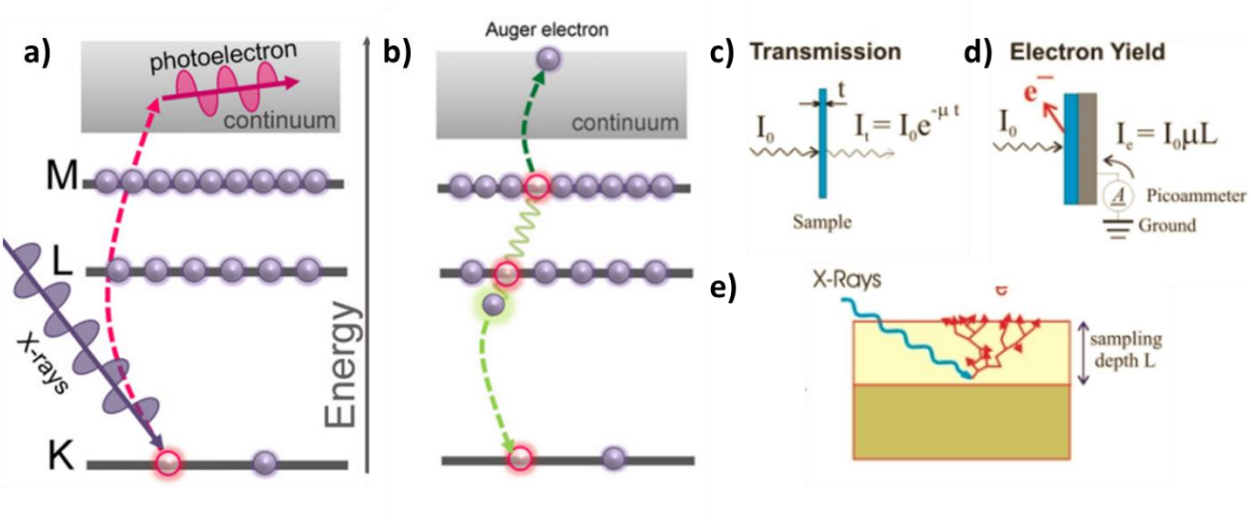


Figure 2.8. a*) Schematic outline of core-hole excitation by X-rays to higher energy levels and b) generation of Auger electrons via Auger decay to fill empty core-hole states [11]. Measurements of X-ray absorption by c) transmission based techniques and d) electron yield techniques. e) depiction of TEY cascade effect caused by Auger electron emission [12].*

2.2.6.2 Extended X-ray Absorption Fine Structure Spectroscopy

Continued x-ray irradiation of a sample, past the absorption edge, results in the generation of an outgoing photoelectron wave generated at the absorbing atom. Quantum mechanically, the outgoing photoelectron can be represented as a spherical wave defined as:

$$\lambda = \frac{2\pi}{k}$$

Where the wave-vector, k, is related to electron mass, m, absorption edge energy, E_{edge}, and zero-point energy or inner potential energy of the core-hole level electron, E_0.

$$k = \sqrt{\left(\frac{8\pi^2 m}{h^2}\right)\left(h\nu + E_0 - E_{edge}\right)}$$

This outgoing spherical wave can scatter off neighboring atoms and will produce a backscattered wave. The outgoing and backscattered waves will interfere and cause an interference pattern to

form that holds information about neighboring atom distance and composition and is based on electron density. Since the absorption coefficient is proportional to the transition probability of the photoelectric event, the total absorption coefficient above the absorption edge can be defined as:

$$\mu_{total} = \mu_0[1 + \chi_{EX}]$$

Where μ_0 represents the atomic background. Since the neighboring atoms surrounds the absorbing atom, χ_{EX} defines the scattering of the outgoing electron against neighboring atoms and appears as subtle oscillations across the total absorption. χ_{EX} is the extended x-ray absorption fine structure (EXAFS) function and contains local structural information surrounding the absorber atom. This function is proportional to the amplitude of the scattered photoelectron wave at the absorbing atom and can provide coordination number. To simplify EXAFS characterization, a single scattering plane-wave approximation is used rather than a spherical one. This assumption is based on the atomic radii of the absorbing atom to be much smaller than the interatomic distances and is only valid when the wave vector generated is greater than 3 Å. Furthermore, a single scattering event is assumed where the electron only scatters once before returning to the absorber atom. Based on this, the χ_{EX} function can be given as a summation over all interference patterns and modeled as sine wave scattering from neighboring atoms:

$$\chi(k) = \sum_{j=1}^{Shells} A_j(k) \sin \Phi_j(k)$$

This equation highlights the fact that X-ray absorption is a bulk technique and probes all atoms of an absorber element equally and gives average coordination around the absorbing element. The $\sin \Phi_j(k)$ term takes into consideration a phase factor and accounts for the time required for the electron to travel to the neighboring atom and return. The amplitude term, $A_j(k)$, contains coordination number (N) information as well as the amount of disorder described by fluctuations in distance between atoms due to thermal motion or structural disorder. This term is commonly referred to as the Debye-Waller factor.

$$A_j(k) = \frac{N_j}{kR_j^2} S_0^2 F_j(k) e^{-2k^2\sigma_j^2} e^{-2\frac{R_j}{\lambda k}}$$

$F_j(k)$ is used to describe the backscattering amplitude and is element specific. An S_0^2 term is introduced to consider amplitude reduction and reflects central atom shake-up and shake off due to relaxation processes following photo-ionization. All these factors taken together provide EXAFS will the ability to probe local atomic environment [13], [14].

2.3 References

[1] M. Amrein *et al.*, *Science of Microscopy*, vol. 1. New York: Springer, 2007.

[2] W. D. Perkins, "Fourier transform-infrared spectroscopy: Part l. Instrumentation," *J. Chem. Educ.*, vol. 63, no. 1, p. A5, 1986.

[3] G. S. Bumbrah and R. M. Sharma, "Raman spectroscopy – Basic principle, instrumentation and selected applications for the characterization of drugs of abuse," *Egypt. J. Forensic Sci.*, vol. 6, no. 3, pp. 209–215, 2016.

[4] H. J. Butler *et al.*, "Using Raman spectroscopy to characterize biological materials," *Nat. Protoc.*, vol. 11, no. 4, pp. 664–687, 2016.

[5] M. S. Dresselhaus, A. Jorio, M. Hofmann, G. Dresselhaus, and R. Saito, "Perspectives on Carbon Nanotubes and Graphene Raman Spectroscopy," *Nano Lett.*, vol. 10, no. 3, pp. 751–758, 2010.

[6] V. M. Mecea, J. O. Carlsson, P. Heszler, and M. Bârtan, "Development and testing of a high temperature quartz crystal microbalance," *Vacuum*, vol. 46, no. 7, pp. 691–694, 1995.

[7] Colnatec, "Quartz Crystal Microbalance," 2017. [Online]. Available: http://colnatec.com/quartz-crystal-microbalance. [Accessed: 11-Nov-2017].

[8] T. Principle, "1 1.1 X-ray-reflectometry (XRR)," pp. 1–5.

[9] X. Sun and T. Sham, "X-Ray Absorption Spectroscopy of Semiconductors," in *X-ray Absorption Spectroscopy of Semiconductors*, vol. 190, New York: Springer, 2015.

[10] J. Stöhr, *NEXAFS Spectroscopy*. Berlin: Springer, 1992.

[11] L. Mino *et al.*, "Low-dimensional systems investigated by x-ray absorption spectroscopy: a selection of 2D, 1D and 0D cases," *J. Phys. D. Appl. Phys.*, vol. 46, no. 42, p. 423001, 2013.

[12] "NEXAFS Spectroscopy." [Online]. Available: https://www-ssrl.slac.stanford.edu/stohr/nexafs.htm. [Accessed: 14-Nov-2017].

[13] D. C. Koningsberger, B. L. Mojet, G. E. Van Dorssen, and D. E. Ramaker, "XAFS spectroscopy ; fundamental principles and data analysis," *Top. Catal.*, vol. 10, pp. 143–155, 2000.

[14] D. C. Koningsberger and R. Prins, *X-ray Absorption*. New York: Wiley, 1988.

3

Surface Modification of Nitrogen Doped Carbon Nanotubes by Ozone via Atomic Layer Deposition*

The use of ozone as an oxidizing agent for atomic layer deposition (ALD) processes is rapidly growing due to its strong oxidizing capabilities. However, the effect of ozone on nanostructured substrates, such as nitrogen-doped multiwalled carbon nanotubes (NCNTs) and pristine multiwalled carbon nanotubes (PCNTs), are not very well understood and may provide an avenue towards functionalizing the carbon nanotube (CNT) surface prior to deposition. The effects of ALD ozone treatment on NCNTs and PCNTs using 10 wt.% ozone at temperatures of 150°C, 250°C and 300°C are studied and presented herein. The effect of ozone pulse time and ALD cycle number on NCNTs and PCNTs was also investigated. Morphological changes to the substrate was observed by scanning electron microscopy (SEM) and high-resolution transmission electron microscopy (HRTEM). BET measurements were also conducted to determine surface area, pore size, and pore size distribution following ozone treatment. The graphitic nature of both NCNTs and PCNTs was determined using Raman analysis while X-ray photoelectron spectroscopy (XPS) was employed to probe the chemical nature of NCNTs. It was found that O_3 attack occurs preferentially to the outermost geometric surface of NCNTs. Our research also revealed that the deleterious effects of ozone are found only on NCNTs while little or no damage occurs on PCNTs. Furthermore, XPS analysis revealed that ALD ozone treatment on NCNTs, at elevated temperatures, results in loss of nitrogen content. Our study demonstrates that ALD ozone treatment is an effective avenue towards creating low nitrogen content, defect rich substrates for use in electrochemical applications and ALD of various metal/metal oxides.

*A version of this chapter has been published in J. Vac. Sci. Tech. A 32 (2014) 01A124

3.1 Introduction

Since the discovery of carbon nanotubes (CNTs) in 1991 [1], their remarkable electronic and mechanical properties have attracted a great deal of attention. The potential applications of CNTs include: sensors, field emission displays, use in hydrogen storage media, and nanosized semiconductor devices, probes, and interconnects [2]. Furthermore, CNTs intrinsically have a high electronic conductivity and large accessible surface area, making them attractive candidates for electrochemical devices [3]. To enhance their performance, broaden their properties and expand their applications, various chemical and physical approaches have been pursued to modify the surface of CNTs. Due to the inert and hydrophobic nature of CNTs, surface modification and functionalization is essential for their application. For example, recent studies have shown that surface modification of CNTs results in the enhancement of lithium storage by allowing access to the inner regions of the tubes via defects and edge formation sites [4].

Many types of surface modification techniques are employed on CNTs including: mechanical grinding [5], electron irradiation [6], covalent bonding of functional groups [7], and non-covalent wrapping or adsorption of mediating molecules onto the CNT surface [8]. Among various surface modification techniques, the bonding of oxygen-containing functional groups to the side walls of CNTs is a popular and versatile approach [9]. Deliberate incorporation of surface oxygen onto CNTs has been achieved through a variety of techniques including chemical oxidation [10], plasma treatment [11], and functionalization using synthetic organic chemistry [12]. Chemical oxidation is widely used due to its uniform contact and even distribution of defect density. However, wet chemical oxidation techniques typically use strong oxidizing chemicals and may lead to tube deterioration and incorporation of impurities [10]. Gas phase oxidation of CNTs can also be used to create defects and functional groups by using oxidizing agents such as ozone. Gas phase ozonolysis of CNTs has been previously shown to enhance the adhesion properties and compatibility of CNTs with polar surfaces as well as improve dispersion and reactivity with polymeric matrices or solvents [13]. Smalley et al [14], reported the oxidation and etching of CNTs using O_3 at room temperature (RT) and demonstrated that the geometrically strained curvature of CNTs resulted in ozone having a high reactivity towards conjugated carbon double bonds. Other studies have also shown that ozonolysis of CNTs results in the shortening of tubes [15].

Another method toward modifying the surface of CNTs is heteroatom doping of elements such as nitrogen [16], phosphorus [17], and boron [18] into the CNT matrix. This method has resulted in improved physical and electrochemical properties of CNTs [19]–[22]. Nitrogen-doped carbon nanotubes (NCNTs) have been shown to be more chemically active than CNTs due to increased surface defects as a result of nitrogen doping [23]. NCNTs have also been shown to have a profound effect on the oxygen reduction reaction (ORR) as well as enhance catalytic splitting of water [24], [25]. Furthermore, NCNTs, with low nitrogen content (< 2%) have displayed decreased charge-transfer resistance and enhanced electrochemical activity, both of which are attributed to the incorporation of graphitic nitrogen atoms [26].

Both CNTs and NCNTs are considered as attractive candidates for atomic layer deposition (ALD) processes that require thin conformal films to be deposited on high surface area substrates. ALD of various metal oxides on functionalized CNTs have shown to greatly improve the performance of supercapacitors [27], transistors [28], and field emission devices [29]. However, due to the chemically inert nature of CNTs, ALD deposition on their surface is often difficult. For this reason, NCNTs, which have a greater number of active sites, are an attractive candidate for ALD processes. Doped-N atoms have the ability to facilitate or promote the adsorption of precursor molecules in order to initiate the deposition process [30]. Furthermore, several studies have shown that NCNTs aid ALD depositions processes of aluminum phosphate [31], iron oxide [30], lithium titanium oxide [32], tin oxide [33], and zirconium oxide [34]. However, the effect of ozone exposure by ALD on these substrates is not very well understood. Jandhyala et al [35], showed that the use of ozone allows for the functionalization of graphene surfaces and provides a non-destructive way for nucleating growth. The study however did not go into detail regarding ozone exposure required to begin graphene functionalization or how ozone aids in the nucleation process. Given the increasing number of ALD processes that utilize ozone as an oxidizing gas, and the attractiveness of CNTs and NCNTs as substrates for ALD, it is imperative to understand the effect ozone may have on these substrates. Furthermore, previous studies have shown that extensive exposure of CNTs to ozone results in significant destruction of the substrate, control over exposure conditions and understanding the consequences of ozone oxidation are important parameters to consider. ALD offers an ideal avenue towards understanding the effect of ozone on these substrates by allowing precise control of ozone exposure in a wide temperature window. In this article, we report the effects of ALD ozone on pristine multiwalled carbon nanotubes (PCNTs)

and multiwalled NCNTs. A systematical study was carried out to investigate the influence of temperature, ALD cycle number and ozone pulse time have on the surface modification of PCNTs and NCNTs. Moreover, the working mechanism of ozone on NCNTs is discussed. To the best of our knowledge, this is the first study to thoroughly determine the effect ALD-ozone has on PCNTs and NCNTs.

3.2 Experimental Details

ALD-Ozone process: PCNTs were purchased from Shenzhen Nanotech Port Co. Ltd. with a diameter range of 30-150 nm. NCNTs with a diameter range of 20-40 nm were prepared by ultrasonic spray pyrolysis as outlined previously [26]. Both PCNTs and NCNTs were ultrasonicated in ethanol for 20 min and dispersed on aluminum foil for ALD-ozone treatment. Ozone experiments were performed in a commercial ALD reactor (Savannah 100, Cambridge Nanotechnology Inc., USA) using 10% ozone (by weight) generated by an OL80F generator. Nitrogen (99.999%) was selected as the carrier gas with a flow rate of 15 sccm. The ALD reactor was evacuated by a vacuum pump (Pascal 2005 I, Adixen), and reached a base pressure of around 0.7 Torr. Ozone treatment was carried out at a temperature range of 150°C to 300°C. One cycle of ALD-ozone treatment consisted of the following three steps: (1) a 2 s or 4 s ozone pulse; (2) a 2 s extended exposure of ozone; (3) and a 10 s nitrogen purge to remove residual ozone and possible by-products.

Characterization of ozone treated PCNTs and NCNTs: A field-emission scanning electron microscope (FE-SEM, Hitachi 4800S) was employed to observe the morphology of ozone treated PCNTs and NCNTs. In addition, the tube walls of ozone treated NCNTs and CNTs was examined by high-resolution transmission electron microscopy (HRTEM, JEOL 2010 FEG). Raman scattering spectra was recorded using a HORIBA Scientific LabRAM HR Raman spectrometer system equipped with a 532.4 nm laser. X-ray photoelectron spectroscopy (XPS) data was obtained using a Kratos Axis Ultra α unit operating at 14 kV. N_2 adsorption-desorption behavior was monitored using a TriStar II 3020 (Micrometrics, USA) at 77K. Isotherms were fitted according to the BJH (Barrett-Joyner-Halenda) theory to give surface area, pore size, and pore size distribution.

3.3 Results and Discussion

SEM images of PCNTs and NCNTs before ozone treatment are shown in Figure 3.1a and 1e respectively. Figure 3.1a displays PCNTs with a wide distribution of diameter between 30-150 nm and are tangled and curved nature with a smooth outer wall surface. Figure 3.1e indicates that the NCNTs are relatively straight and often appear in bundles with a diameter distribution of 20-40 nm.

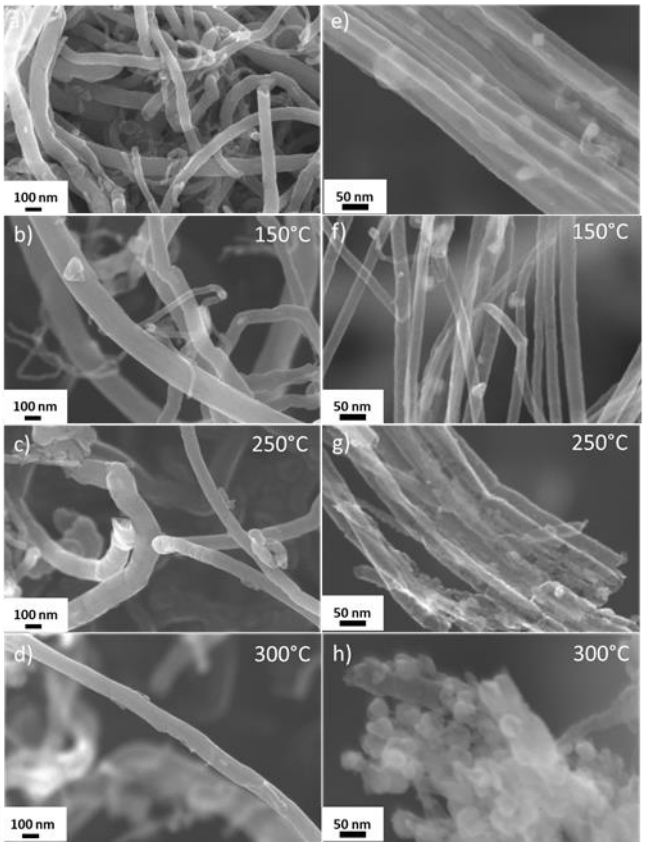


Figure 3.1. *SEM images of a) PCNTs and e) NCNTs before ozone treatment; b-d) PCNTs and f-h) NCNTs after ozone treatment at different temperatures for 500 cycles.*

The reactor temperature was varied from 150°C to 250°C and 300°C, with 500 cycles of ozone. SEM images of PCNTs and NCNTs after ozone exposure at 150°C are shown in Figure 3.1b and 1f respectively. These images demonstrate that no significant morphological changes occur after these treatment parameters. Increasing the reactor temperature to 250°C, results in no visible destruction on PCNTs (Figure 3.1c). However, for NCNTs, jagged holes are seen along the basal plane of the tube, as presented in Figure 3.1g. The holes are unevenly distributed and range

in diameter from a few nanometers up to 30 nm. Furthermore, the number of holes varies from tube to tube. Apart from the visible appearance of surface defects, small agglomeration of material buildup are observed on the outer surface of the NCNTs. Elevating the temperature to 300°C results in PCNTs maintaining their initial morphology (Figure 3.1d) while NCNTs undergo significant destruction and lose the majority of their tubular nature. In addition, there is a substantial increase in agglomerated material found on the surface of NCNTs. Similar to results for ozone treatment of NCNTs at 250°C, the level of destruction is not uniform and varies from one tube to another. From the above results, ozone treatment at 250°C and 300°C results in significant destruction to NCNTs but not to PCNTs. Since nitrogen doping is a major difference between these two materials, it is reasonable to speculate that nitrogen content plays a significant role in the destruction of the NCNT surface.

Armed with the understanding that a reaction between ozone and NCNT surface begins at 250°C, analysis towards the amount of ozone exposure required to cause destruction was undertaken. ALD provides two unique ways to control ozone exposure, one- by varying number of ALD cycles and two- by controlling ozone pulse length. Figure 3.2 displays SEM images of NCNTs after ozone treatment with either 2s or 4s pulses with varying cycle number at a temperature of 250ºC. Using a 2 or 4 second pulse of ozone for 250 cycles fails to create any visible holes or defects, as indicated in figure 3.2a and 3.2d. Increasing the cycles number up to 500, destruction of NCNTs is observed at both 2s and 4s ozone pulse lengths, and can be seen in figure 3.2b and 3.2e respectively. The destruction of NCNTs occurs to a much larger extent using 4s pulse length than a 2s one. Figure 3.2e also indicates that a 4s, 500-cycle ozone treatment results in the removal of large pieces of the NCNT outer wall surface, however, the tubular structure remains intact. Increasing the number of ALD cycles to 1000, results in the formation of large carbon nanoparticles, as shown in Figure 3.2c and 3.2f. The appearance of such large carbon particles is a clear indication that 1000 ALD cycles of ozone has a significant effect on NCNTs.

The above results suggest that ozone exposure time plays an important role in the surface modification of NCNTs.

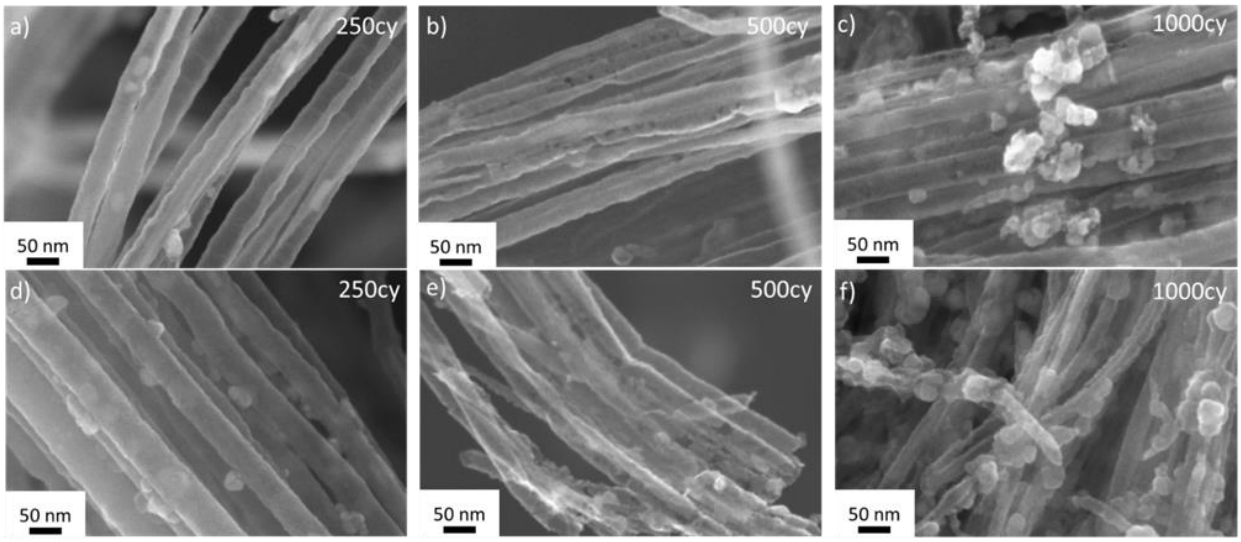


Figure 3.2. *SEM images of NCNTs treated with (a-c) 2s of ozone pulse and (d-f) 4s of ozone pulse using different cycles at 250°C.*

TEM was employed to gain a more detailed picture as to the structure of NCNTs before and after ozone treatment. As shown in Figure 3.3a, the original NCNTs exhibit a bamboo-like structure with a smooth outer wall surface. However, Figure 3.3b shows that following ozone treatment at 150°C a small amount of agglomerated carbonaceous material begins to cover the surface of NCNTs. Increasing the reactor temperature to 250°C leads to the formation of much larger agglomerated carbonaceous material accompanied by partial destruction to the outer wall. Red circles shown in Figure 3.3c highlight the regions where damage to NCNTs occurs. The majority NCNTs retain their tubular nature, but lose their branching bamboo element. Based on SEM and TEM results, it can be concluded that ozone treatment not only creates holes on NCNTs, but also leads to the formation of spherical carbonaceous material and loss of bamboo structure. These results further prove that nitrogen content plays a critical role in the surface modification of CNTs.

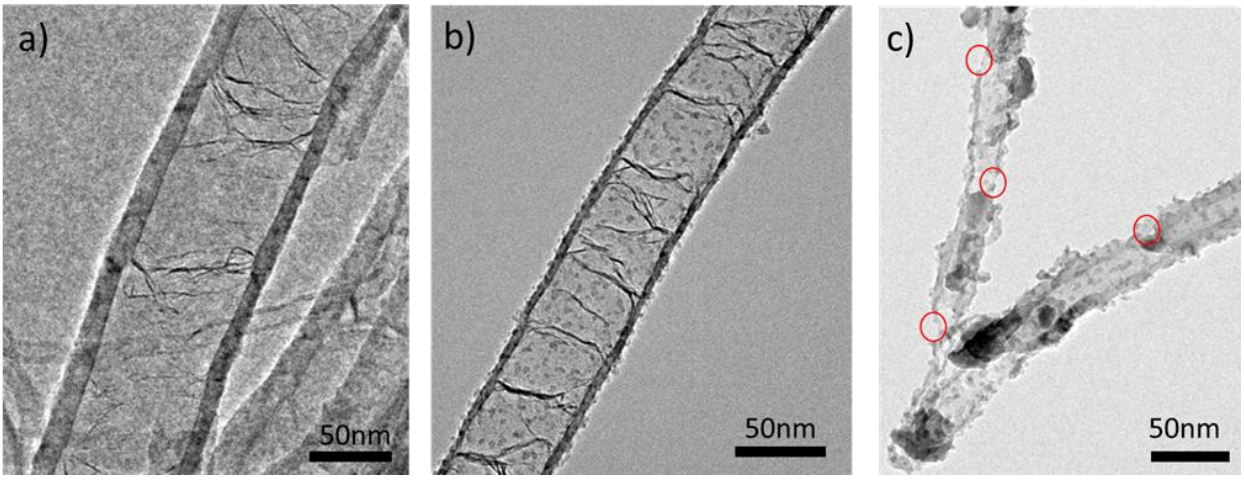


Figure 3.3. *TEM images a) untreated NCNTs, ozone treated NCNTs at b) 150°C, c) 250°C for 500 cycles.*

Raman spectroscopy was employed to determine the effect of ozone treatment on the structural ordering in NCNTs. Figure 3.4a presents raw Raman data collected for NCNTs and displays two prominent peaks at 1350 cm^{-1} and 1580 cm^{-1}. The peak occurring at 1350 cm^{-1} is typically a representation toward the amount of disorder within the graphitic plane, commonly referred to as the D band, while the peak at 1580cm^{-1} reflects well-graphitized carbon in NCNTs, and is referred to as the G band [36]. The data collected indicates an increase in the D-band intensity with elevating reactor temperature while the G band intensity decreases. Similar to SEM results, Raman data collected for ozone treated PCNTs at different temperatures (Supporting information Figure S3.3) indicates that no significant alterations to the graphitic plane occurs. The ratio of intensity between the D band and G band, also know known as I_D/I_G, was used to quantify the graphitic nature of NCNTs [14], [37]. Figure 3.4b shows a plot of I_D/I_G vs. reactor temperature for NCNTs along with cycle number and pulse time. It can be seen that the I_D/I_G ratio increases from 1.52 to 1.72 when the reactor temperature is raised from 150°C to 250°C. One possible reason for this increase is the formation of carbon nanoparticles on the surface of NCNTs, as previously indicated by TEM results in Figures 3.3b and 3.3c. This increase in the D band correlates well with SEM and TEM data and provides further evidence that physical defects are introduced at a reactor temperature of 250°C. Furthermore, the information presented provides strong evidence that an activation barrier may exist between 150°C and 250°C and causes ozone to react with nitrogen doping elements that exist in NCNTs. Raman data indicates that at 250 cycles of ozone exposure

there is a slight increase in the I_D/I_G ratio, and continues to increase with 500 cycles. As expected, the I_D/I_G ratio for 4s ozone pulse times is consistently higher than for 2s exposures of ozone. Interestingly, this is also the case for PCNTs, indicating that a 4s ozone pulse time does causes some interaction to occur on the PCNTs surface, while a 2s ozone pulse does not, regardless of ALD cycle number (Supporting information figure S3.3).

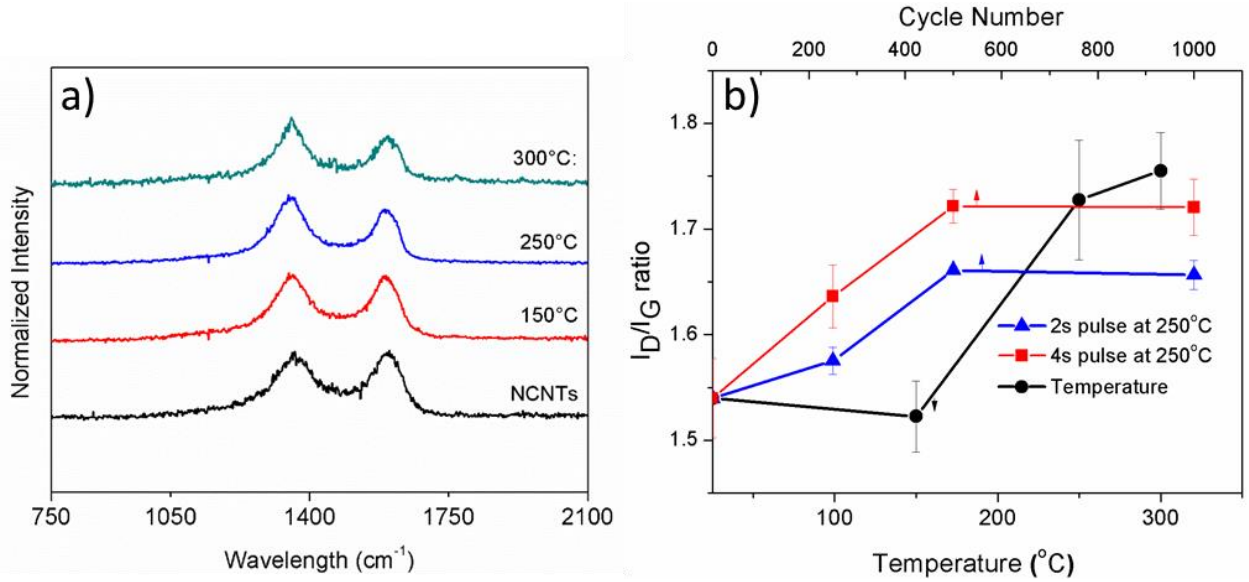


Figure 3.4. *Raman spectra of a) NCNTs and before and after ozone treatment at different temperatures; b) Comparison of I_D/I_G ratio for NCNTs at different temperatures, ALD cycles, and ozone pulse time.*

SEM, TEM and Raman data all provide clear evidence that ozone begins to cause damage to NCNTs at a temperature of 150°C, however, the mechanism of damage remains unclear. HRTEM was employed to gain a better understanding toward the mechanism of destruction. As outlined in Figure 3.5, HRTEM reveals the extent of damage NCNTs undergo at various temperatures.

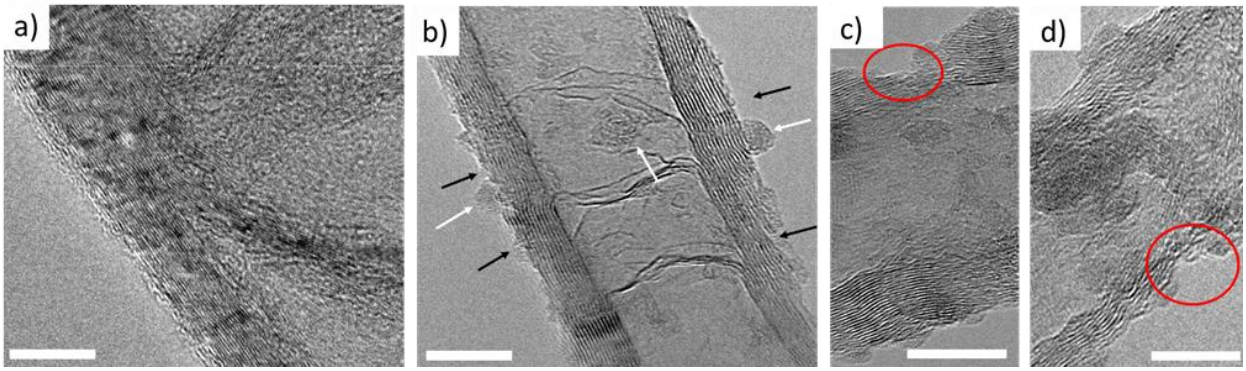


Figure 3.5. *HRTEM image a) untreated NCNTs, and ozone treated NCNTs at b) 150°C, c), d) 250°C. Scale bar in white represents 10 nm.*

Figure 3.5a indicates that untreated NCNTs have an evenly distributed outer wall with branching elements from the inner wall, representing the bamboo structure of NCNTs introduced by nitrogen heteroatom doping. Figure 3.5b shows an HRTEM image of NCNTs treated with ozone at 150°C for 500 cycles. During treatment at this temperature, short tears to the outer wall begin to appear, as indicated by black arrows. Although the tears are miniscule, they appear only for the first few layers. Formation of amorphous carbon nanoparticles can also be seen and is indicated by white arrows in Figure 3.5b. Interestingly, the amorphous carbon nanoparticles appear to be rolled up components of the outer wall. Figure 3.5c and 3.5d are HRTEM images of ozone-treated NCNTs at 250°C for 500 cycles, and indicates that ozone has destroyed the majority of the NCNT wall. Furthermore, this temperature also leads to the exfoliation of NCNT wall. HRTEM images reveals that the number of outer walls for NCNTs treated at 250°C is dramatically reduced and extremely disordered compared to the untreated NCNTs and NCNTs treated at 150°C. Red circles in Figure 3.5c and 3.5d highlight sections that have been completely removed by ALD ozone treatment. Interestingly, the typical inward branching seen for NCNTs is sparsely found in Figure 3.5c and 3.5d. Inward branching of NCNT wall is a result of heteroatom doping, and the loss of this component gives an indication that ozone treatment may result in loss of nitrogen content. This would also explain the non-uniform destruction seen across NCNT surface as nitrogen content varies along the tube. Based on SEM, TEM, Raman and HRTEM results, we can conclude that ozone treatment on NCNTs peel off the outer walls, resulting in the formation of holes. The level of ozone destruction on NCNTs can be controlled by varying reactor temperature, ozone pulse length, and cycle number. However, number of ALD cycles and pulse time also

contribute to NCNT destruction, indicating that exposure is a crucial factor towards the surface modification of NCNTs. Furthermore, ozone destruction of NCNTs works by exfoliating and peeling away the outer walls of the NCNT, resulting in the formation of amorphous carbon nanoparticles and the creation of holes on the NCNT surface.

The pore characteristics of as produced NCNTs and 1000 cycle 300°C ozone treated NCNTs was investigated by nitrogen adsorption isotherms at 77K. The nitrogen adsorption-desorption isotherms (Figure 3.6a) indicate that as produced NCNTs and ozone treated NCNTs are both type IV isotherms with pores in the 1.5-100 nm range. However, ozone treated samples reveal a larger presence of mesopores compared to pristine NCNTs. Ozone treated NCNTs also indicated a higher BET surface area of 183.3 m^2/g compared to pristine NCNTs (92.7 m^2/g). Pore size distribution of both samples was determined by the BJH equation (Figure 3.6b) and indicates that ozone treated samples have a greater volume of pores in the 10-30 nm range. These results correlate well with SEM, TEM and HRTEM results, and indicate that ozone treatment of NCNTs results in the formation of nanosized holes as well as a substantial increase in surface area.

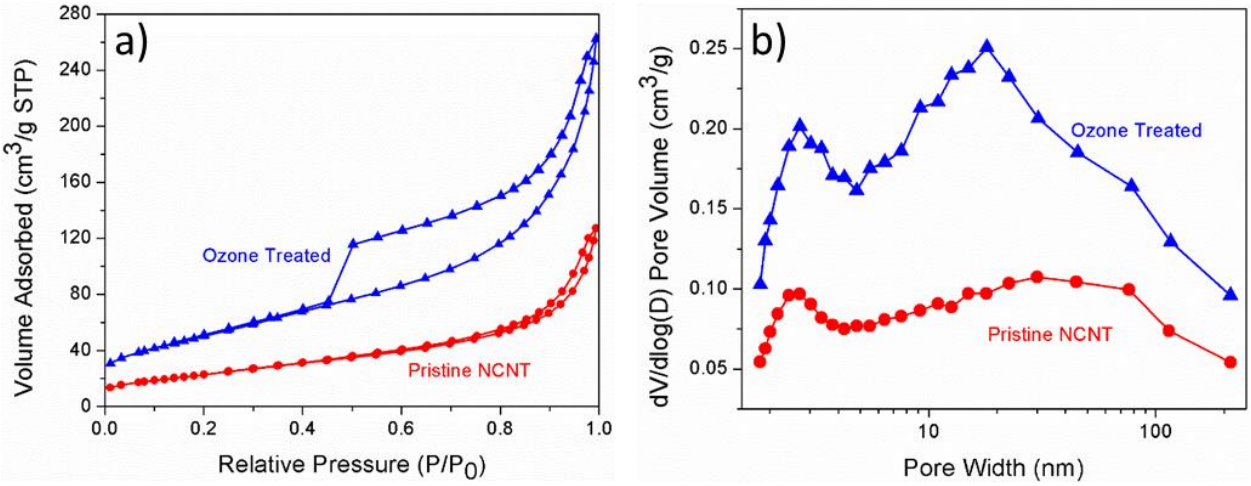


***Figure 3.6**. a) N_2 adsorption-desorption isotherms at 77K and b) pore size distribution of as produced NCNTs and 300°C ozone treated carbon NCNTs.*

XPS analysis was conducted to determine the role of nitrogen doping during ozone treatment of NCNTs. Table 3.1 outlines the atomic percentages obtained from an XPS survey spectra (Figure S3.1 of the Supporting Information) of NCNTs before and after ozone treatment at 300°C for 500 cycles using a 4s pulse.

Table 3.1. *XPS survey analysis comparison between untreated NCNTs and 300°C ozone treated NCNTs.*

Element	Binding Energy (eV)		At% (±0.1%)	
	Untreated	Ozone treated	Untreated	Ozone treated
O1s	531.4	527.9	1.6	14.2
C1s	284.4	280.9	92.7	78.6
N1s	400.6	396.4	5.1	1.8
N1s-Pyridine	398.5	398.8	1.3	0.8
N1s- Graphitic	400.9	400.9	2.0	1.0
N1s- Molecular N_2	403.5	-	0.5	0
N1s- N-oxide	405.1	-	1.3	0

The XPS data reveals that following ozone treatment, NCNTs are comprised of more oxygen and less nitrogen and carbon. This indicates that not only does ozone etch away the NCNTs surface, but it also causes significant changes to its chemical composition. As a result of ozone treatment the increase in oxygen content can be ascribed to the introduction of surface hydroxyl, carbonyl or epoxide functional groups [38]. The decrease in carbon content is due to the removal of carbon layers by ozone treatment as indicated by HRTEM images.

The XPS survey analysis also reveals that binding energies for O1s, N1s and C1s are lower for ozone-treated NCNTs than untreated NCNTs. Typically, nitrogen doping into CNTs results in a charge transfer to occur between the less electronegative carbon to the more electronegative nitrogen [39]. In NCNTs some homopolar C-C bonds are replaced with heteropolar C-N bonds, resulting in a shift to the C1s core level toward higher binding energies [40]. If less heteropolar C-N bonds exist, the C1s core level binding energy should decrease back towards C-C homopolar bonds, as shown by presented XPS data. A negative shift in the C1s peak may also be ascribed to weaker C-C binding and larger interlayer distance between the CNT walls [41]. From Table 3.1, nitrogen content decreases from 5.1 at. % for as produced NCNTs to 1.8 at. % for ozone-treated NCNTs. High resolution XPS of N1s before and after ozone treatment is displayed in Figure 3.7. The N1s peak for untreated NCNTs can be deconvoluted into four peaks located at 398.5 eV, 400.9 eV, 403.5 eV, and 405.1 eV corresponding to pyridinic N, graphitic N, molecular N_2 and chemisorbed N-oxides, respectively [40]. Molecular N_2 has been previously reported to

predominantly exist as an intercalated gas between the graphite layers of NCNTs [42]. Pyridinic nitrogen species are nitrogen atoms that contribute to the π-system with one p-electron, while graphitic N atoms sit in-plane and replaces a graphitic host carbon atom [43]. For ozone-treated NCNTs, only pyridinic N and graphitic N are observed, indicating a loss in diatomic molecular nitrogen and nitrogen oxide species. Furthermore, ozone treated NCNTs display a decrease in graphitic nitrogen, from 2.0% to 1.0% as well as a slight decrease in pyridinic nitrogen, from 1.3% to 0.8%. Clearly, a relationship exists between nitrogen content and the surface modification of NCNTs. It is also important to distinguish between effects induced by thermal treatment and ozone treatment. Kundu et al [44], conducted a series of experiments towards the stability of various nitrogen species that exists within NCNTs with respect to temperature. They noted that at a temperature of 450°C, far above the temperatures used in this study, both molecular nitrogen and chemisorbed nitrogen oxide species remain with NCNTs and are detectable by XPS analysis. Clearly the disappearance of these two peaks is related to ALD ozone treatment.

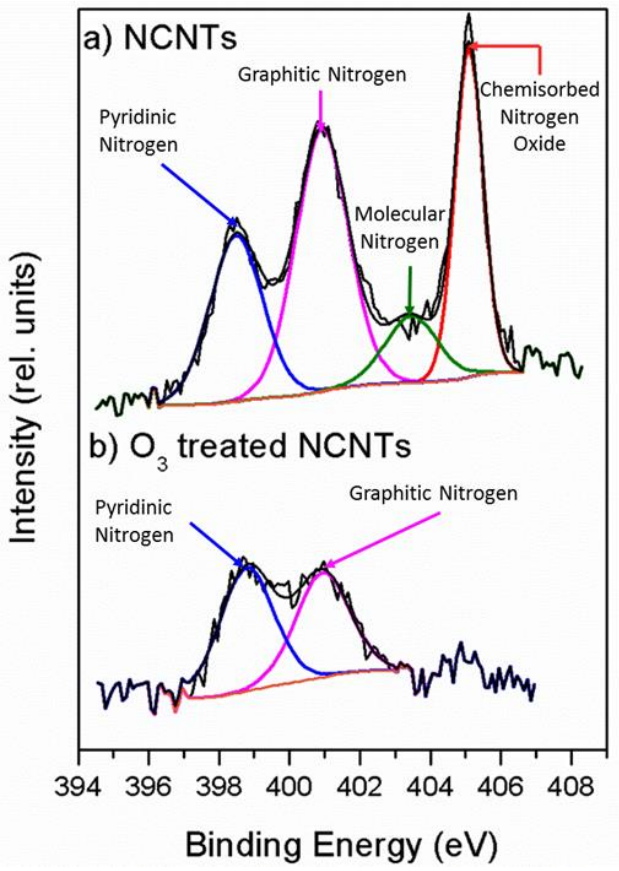


Figure 3.7. *N1s spectra for NCNTs a) before ozone treatment and b) after ozone treatment at 300°C for 500 cycles.*

As mentioned previously, the peak at 403.5 eV is assigned to the incorporation of molecular nitrogen. HRTEM images indicate that following ozone treatment, exfoliation of the graphitic layers occurs. This increase in interlayer distance may result in molecular nitrogen desorbing from between graphitic layers, and resulting in the loss of this peak. Furthermore, the incorporation of holes through the basal plane of the NCNT surface will also allow for adsorbed molecular nitrogen within the tube to escape, especially under the thermal vacuum conditions of ALD. The disappearance of the peak at 405.1 eV (chemisorbed nitrogen oxide groups) is less straight forward and can be related to the decrease in pyridinic and substitution nitrogen also observed. Theoretical calculations have demonstrated that the incorporation of nitrogen atoms into the graphitic framework results in the appearance of localized high charge densities [45]. Nitrogen oxide species have also been shown to contain one negative charge and display nucleophilic ability, resulting in a similar localized charge density [46]. These high charge density sites are preferential locations for initiating oxidation [47]. Furthermore, chemisorbed nitrogen oxide groups are held to the surface by weak dangling bonds and can be easily removed during oxidation.

The use of ozone in an ALD process has been shown to be quite complicated and highly dependent on surface properties. Our results indicate that destruction of NCNTs surface is related to nitrogen content reacting with ozone species. We therefore propose that the uneven destruction seen in SEM, TEM and HRTEM originates from fluctuating nitrogen content from tube to tube. Knoops et al [48], demonstrated that, depending on the surface, ozone undergoes a recombinative surface loss process via ozone decomposition. The mechanism for O_3 surface loss on MnO_2 proposed by Li et al [49], is considered a standard model for the decomposition pathway on other surfaces and occurs via the following mechanism, where * refers to reactive surface sites:

$$O_3\,(g) + * \rightarrow O_2\,(g) + O^* \qquad (1)$$

$$O_3\,(g) + O^* \rightarrow O_2\,(g) + O_2^* \qquad (2)$$

$$O_2^* \rightarrow O_2\,(g) + * \qquad (3)$$

As mentioned previously, nitrogen sites, particularly pyridinic nitrogen and chemisorbed nitrogen sites, are areas of localized charge densities and are prone to ozone attack. Furthermore, p-type oxides have been shown to demonstrate a high activity for ozone decomposition [50]. This correlates well with recent findings that contrary to the expectation of the n-type doping nature of

nitrogen, pyridines like bonding configurations display p-type doping in air [51]. Pyridinic nitrogen sitesn may then act as a catalyst towards ozone decomposition and cause localized oxidation to occur, resulting in the removal of carbon content. As carbon content is etched away, attached graphitic substituted nitrogen will also be lost. This hypothesis is consistent with XPS data, indicating a substantial loss in graphitic, molecular, and chemisorbed nitrogen, but not pyridinic nitrogen due to its catalytic ability.

3.4 Conclusions

We report, for the first time, the effect of ALD ozone on NCNTs and PCNTs. The results indicate that at temperatures of 250°C and above, ozone has a deleterious effect on the surface of NCNTs, but little to no effect on PCNTs. However, HRTEM results indicate that even at lower reactor temperatures, ozone begins to etch away at the outer wall of NCNTs. Raman measurements on ALD ozone temperature experiments indicate that an activation barrier may exist towards the selective destruction of the NCNT outer wall surface. Further experimentation revealed that both pulse time and number of ALD ozone cycles play an important role in the surface modification of NCNTs. Finally, XPS analysis revealed that ALD ozone treatment results in a decrease in pyridinic and graphitic nitrogen species while a complete loss in molecular and physiosorbed nitrogen content is observed. The reaction mechanisms under ALD ozone may be associated with a recombinative process, and depends on ALD conditions as well as reacting surface species. As a result, ALD ozone treatment on NCNT leads to a loss in nitrogen content and deterioration of the NCNT surface. These results pave a way for understanding the use of ozone during ALD deposition on NCNTs and PCNTs while providing a method for controlling surface defects and composition of carbon nanotubes via a simple ALD process.

Acknowledgements: This work was supported by the Natural Sciences and Engineering Research Council of Canada (NSERC), Canada Foundation for Innovation (CFI), Canadian Research Chair's (CRC), and the University of Western Ontario.

3.5 Supporting Information

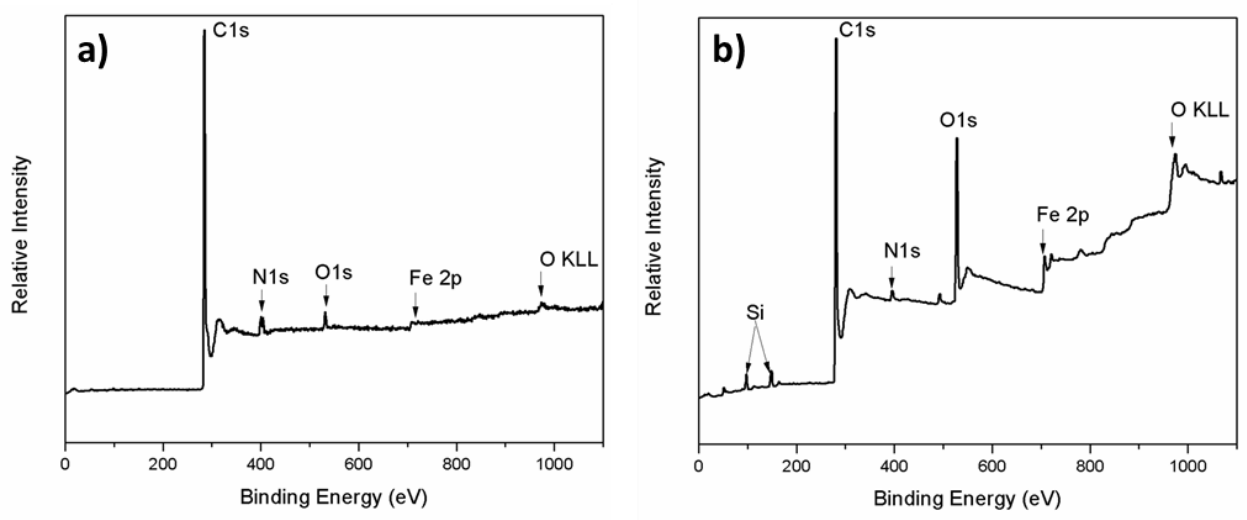


Figure S3.1. *XPS survey spectrum a) before ozone treatment and b) after 300°C ozone treatment.*

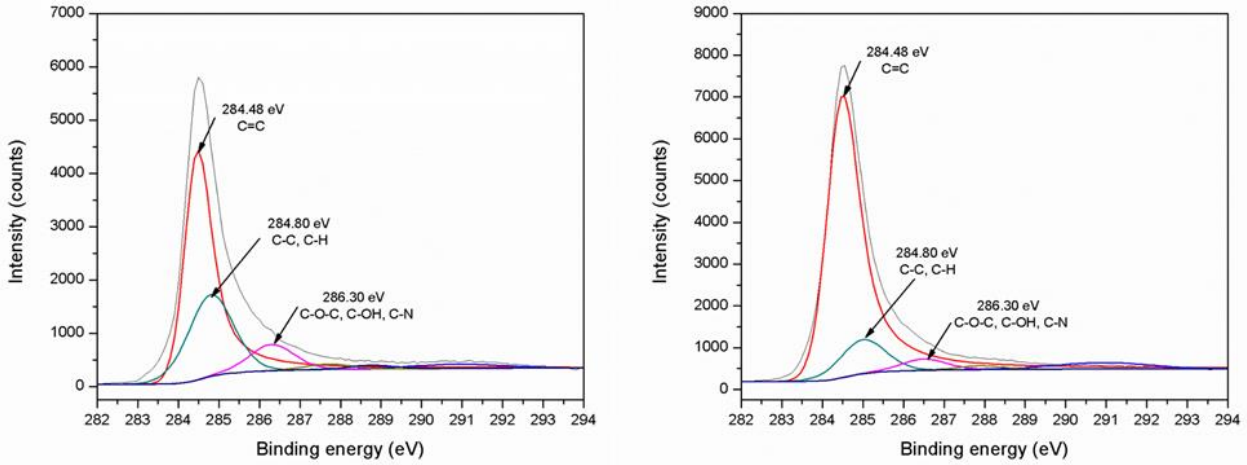


Figure S3.2. *High resolution XPS of C1s spectrum a) before ozone treatment and b) after 300°C ozone treatment.*

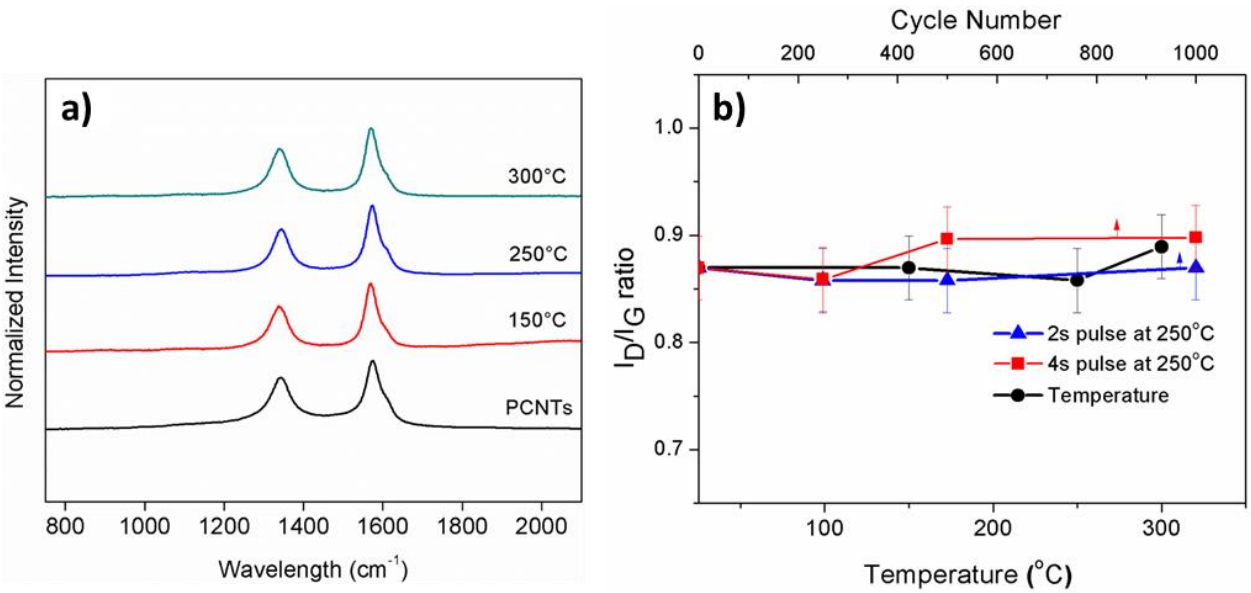


Figure S3.3. *Raman spectra of a) PCNTs and before and after ozone treatment at different temperatures; b) Comparison of I_D/I_G ratio for PCNTs at different temperatures, ALD cycles, and ozone pulse time.*

3.6 References

[1] S. Iijima, "Helical microtubules of graphitic carbon," *Nature*, vol. 354, no. 6348, pp. 56–58, Nov. 1991.

[2] R. H. Baughman, "Carbon Nanotubes--the Route Toward Applications," *Science (80-.).*, vol. 297, no. 5582, pp. 787–792, 2002.

[3] Z. Xiong, Y. Yun, and H.-J. Jin, "Applications of Carbon Nanotubes for Lithium Ion Battery Anodes," *Materials (Basel).*, vol. 6, no. 3, pp. 1138–1158, 2013.

[4] H. S. Oktaviano, K. Yamada, and K. Waki, "Nano-drilled multiwalled carbon nanotubes: characterizations and application for LIB anode materials," *J. Mater. Chem.*, vol. 22, no. 48, p. 25167, 2012.

[5] Á. Kukovecz, T. Kanyó, Z. Kónya, and I. Kiricsi, "Long-time low-impact ball milling of multi-wall carbon nanotubes," *Carbon N. Y.*, vol. 43, no. 5, pp. 994–1000, 2005.

[6] A. V. Krasheninnikov and K. Nordlund, "Ion and electron irradiation-induced effects in nanostructured materials," *J. Appl. Phys.*, vol. 107, no. 7, 2010.

[7] K. Balasubramanian and M. Burghard, "Chemically functionalized carbon nanotubes," *Small*, vol. 1, no. 2, pp. 180–192, 2005.

[8] A. Star *et al.*, "Noncovalent side-wall functionalization of single-walled carbon nanotubes," *Macromolecules*, vol. 36, no. 3, pp. 553–560, 2003.

[9] K. A. Wepasnick, B. A. Smith, J. L. Bitter, and D. Howard Fairbrother, "Chemical and structural characterization of carbon nanotube surfaces," *Anal. Bioanal. Chem.*, vol. 396, no. 3, pp. 1003–1014, 2010.

[10] V. Datsyuk *et al.*, "Chemical oxidation of multiwalled carbon nanotubes," *Carbon N. Y.*, vol. 46, no. 6, pp. 833–840, 2008.

[11] N. P. Zschoerper, V. Katzenmaier, U. Vohrer, M. Haupt, C. Oehr, and T. Hirth, "Analytical investigation of the composition of plasma-induced functional groups on carbon nanotube sheets," *Carbon N. Y.*, vol. 47, no. 9, pp. 2174–2185, 2009.

[12] A. Gromov *et al.*, "Covalent amino-functionalisation of single-wall carbon nanotubes," *J. Mater. Chem.*, vol. 15, no. 32, p. 3334, 2005.

[13] P. X. Hou, C. Liu, and H. M. Cheng, "Purification of carbon nanotubes," *Carbon N. Y.*, vol. 46, no. 15, pp. 2003–2025, 2008.

[14] D. B. Mawhinney, V. Naumenko, A. Kuznetsova, J. T. Yates, J. Liu, and R. E. Smalley, "Infrared spectral evidence for the etching of carbon nanotubes: Ozone oxidation at 298 K [7]," *J. Am. Chem. Soc.*, vol. 122, no. 10, pp. 2383–2384, 2000.

[15] K. J. Ziegler *et al.*, "Cutting single-walled carbon nanotubes," *Nanotechnology*, vol. 16, no. 7, 2005.

[16] J. Liu, Y. Zhang, M. I. Ionescu, R. Li, and X. Sun, "Nitrogen-doped carbon nanotubes with tunable structure and high yield produced by ultrasonic spray pyrolysis," *Appl. Surf. Sci.*, vol. 257, no. 17, pp. 7837–7844, 2011.

[17] J. Liu *et al.*, "Synthesis and characterization of phosphorus-nitrogen doped multiwalled carbon nanotubes," *Carbon N. Y.*, vol. 49, no. 15, pp. 5014–5021, 2011.

[18] L. Yang *et al.*, "Boron-Doped Carbon Nanotubes as Metal-Free Electrocatalysts for the Oxygen Reduction Reaction," *Angew. Chemie*, vol. 123, no. 31, pp. 7270–7273, 2011.

[19] C. W. B. Bezerra *et al.*, "A review of Fe-N/C and Co-N/C catalysts for the oxygen reduction reaction," *Electrochim. Acta*, vol. 53, no. 15, pp. 4937–4951, 2008.

[20] S. Maldonado and K. J. Stevenson, "Influence of nitrogen doping on oxygen reduction electrocatalysis at carbon nanofiber electrodes," *J. Phys. Chem. B*, vol. 109, no. 10, pp. 4707–4716, 2005.

[21] P. H. Matter, E. Wang, M. Arias, E. J. Biddinger, and U. S. Ozkan, "Oxygen reduction reaction activity and surface properties of nanostructured nitrogen-containing carbon," *J. Mol. Catal. A Chem.*, vol. 264, no. 1–2, pp. 73–81, 2007.

[22] F. Charreteur, F. Jaouen, S. Ruggeri, and J. P. Dodelet, "Fe/N/C non-precious catalysts for PEM fuel cells: Influence of the structural parameters of pristine commercial carbon blacks on their activity for oxygen reduction," *Electrochim. Acta*, vol. 53, no. 6, pp. 2925–2938, 2008.

[23] A. H. Nevidomskyy, G. Csányi, and M. C. Payne, "Chemically Active Substitutional Nitrogen Impurity in Carbon Nanotubes," *Phys. Rev. Lett.*, vol. 91, no. 10, p. 105502, 2003.

[24] K. Gong, F. Du, Z. Xia, M. Durstock, and L. Dai, "Nitrogen-Doped Carbon Nanotube Arrays with High Electrocatalytic Activity for Oxygen Reduction," *Science (80-.).*, vol. 323, no. 5915, pp. 760–764, Feb. 2009.

[25] X. Wang *et al.*, "A metal-free polymeric photocatalyst for hydrogen production from water under visible light," *Nat. Mater.*, vol. 8, no. 1, pp. 76–80, 2009.

[26] L. G. Bulusheva *et al.*, "Electrochemical properties of nitrogen-doped carbon nanotube anode in Li-ion batteries," *Carbon N. Y.*, vol. 49, no. 12, pp. 4013–4023, 2011.

[27] S. Boukhalfa, K. Evanoff, and G. Yushin, "Atomic layer deposition of vanadium oxide on carbon nanotubes for high-power supercapacitor electrodes," *Energy Environ. Sci.*, vol. 5, no. 5, p. 6872, 2012.

[28] A. Javey *et al.*, "High-κ dielectrics for advanced carbon-nanotube transistors and logic gates," *Nat. Mater.*, vol. 1, no. 4, pp. 241–246, 2002.

[29] J. M. Green, L. Dong, T. Gutu, J. Jiao, J. F. Conley, and Y. Ono, "ZnO-nanoparticle-coated carbon nanotubes demonstrating enhanced electron field-emission properties," *J. Appl. Phys.*, vol. 99, no. 9, pp. 99–102, 2006.

[30] X. Meng *et al.*, "Heterostructural coaxial nanotubes of CNT@Fe2O3 via atomic layer deposition: Effects of surface functionalization and nitrogen-doping," *J. Nanoparticle Res.*, vol. 13, no. 3, pp. 1207–1218, 2011.

[31] J. Liu, Y. Tang, B. Xiao, T.-K. Sham, R. Li, and X. Sun, "Atomic layer deposited aluminium phosphate thin films on N-doped CNTs," *RSC Adv.*, vol. 3, no. 14, p. 4492, 2013.

[32] X. Meng *et al.*, "Atomic layer deposited Li4Ti5O12 on nitrogen-doped carbon nanotubes," *RSC Adv.*, vol. 3, no. 20, p. 7285, 2013.

[33] X. Meng, Y. Zhong, Y. Sun, M. N. Banis, R. Li, and X. Sun, "Nitrogen-doped carbon nanotubes coated by atomic layer deposited SnO 2 with controlled morphology and phase," *Carbon N. Y.*, vol. 49, no. 4, pp. 1133–1144, 2011.

[34] J. Liu, X. Meng, M. N. Banis, M. Cai, R. Li, and X. Sun, "Crystallinity-Controlled Synthesis of Zirconium Oxide Thin Films on Nitrogen-Doped Carbon Nanotubes by Atomic Layer Deposition," *J. Phys. Chem. C*, vol. 116, pp. 14656–14664, 2012.

[35] S. Jandhyala *et al.*, "Atomic layer deposition of dielectrics on graphene using reversibly physisorbed ozone," *ACS Nano*, vol. 6, no. 3, pp. 2722–2730, 2012.

[36] T. Sharifi *et al.*, "Nitrogen doped multi walled carbon nanotubes produced by CVD-correlating XPS and Raman spectroscopy for the study of nitrogen inclusion," *Carbon N. Y.*, vol. 50, no. 10, pp. 3535–3541, 2012.

[37] S. Osswald, M. Havel, and Y. Gogotsi, "Monitoring oxidation of multiwalled carbon nanotubes by Raman spectroscopy," *J. Raman Spectrosc.*, vol. 38, no. 6, pp. 728–736, 2007.

[38] M. L. Sham and J. K. Kim, "Surface functionalities of multi-wall carbon nanotubes after UV/Ozone and TETA treatments," *Carbon N. Y.*, vol. 44, no. 4, pp. 768–777, 2006.

[39] S. H. Lim *et al.*, "Electronic and optical properties of nitrogen-doped multiwalled carbon nanotubes," *Phys. Rev. B*, vol. 73, no. 4, p. 45402, 2006.

[40] C. Morant, J. Andrey, P. Prieto, D. Mendiola, J. M. Sanz, and E. Elizalde, "XPS characterization of nitrogen-doped carbon nanotubes," *Phys. Status Solidi Appl. Mater. Sci.*, vol. 203, no. 6, pp. 1069–1075, 2006.

[41] and K. L. T. P. Chen, X. Wu, X. Sun, J. Lin, W. Ji, "Electronic Structure and Optical Limiting Behavior of Carbon Nanotubes," *Phys. Rev. Lett.*, vol. 82, 1999.

[42] H. C. Choi *et al.*, "Experimental and theoretical studies on the structure of N-doped carbon nanotubes: Possibility of intercalated molecular N2," *Appl. Phys. Lett.*, vol. 85, no. 23, pp. 5742–5744, 2004.

[43] C. P. Ewels and M. Glerup, “Nitrogen Doping in Carbon Nanotubes,” *J. Nanosci. Nanotechnol.*, vol. 5, no. 9, pp. 1345–1363, 2005.

[44] S. Kundu *et al.*, “Electrocatalytic Activity and Stability of Nitrogen-Containing Carbon Nanotubes in the Oxygen Reduction Reaction,” pp. 14302–14310, 2009.

[45] B. G. Sumpter *et al.*, “Nitrogen-Mediated Carbon Nanotube,” vol. 1, no. 4, pp. 369–375, 2007.

[46] X. Shi *et al.*, “Application of nitrogen-doped carbon powders as low-cost and durable cathodic catalyst to air-cathode microbial fuel cells,” *Bioresour. Technol.*, vol. 108, pp. 89–93, 2012.

[47] R. Cruz-Silva *et al.*, “Formation of nitrogen-doped graphene nanoribbons via chemical unzipping,” *ACS Nano*, vol. 7, no. 3, pp. 2192–2204, 2013.

[48] H. C. M. Knoops, J. W. Elam, J. A. Libera, and W. M. M. Kessels, “Surface loss in ozone-based atomic layer deposition processes,” *Chem. Mater.*, vol. 23, no. 9, pp. 2381–2387, 2011.

[49] W. Li, G. Gibbs, and S. Oyama, “Mechanism of ozone decomposition on a manganese oxide catalyst. 1. In situ Raman spectroscopy and ab initio molecular orbital calculations,” *J. Am. Chem. …*, vol. 7863, no. 7, pp. 9041–9046, 1998.

[50] B. Dhandapani and S. T. Oyama, “Gas phase ozone decomposition catalysts,” *Appl. Catal. B Environ.*, vol. 11, no. 2, pp. 129–166, 1997.

[51] Y. S. Min *et al.*, “Unusual transport characteristics of nitrogen-doped single-walled carbon nanotubes,” *Appl. Phys. Lett.*, vol. 93, no. 4, 2008.

4

Controlling the Conductivity of Thin Films using Molecular Layer Deposition

This chapter presents a novel way of growing aluminum alkoxide films with tunable conductivity using molecular layer deposition (MLD). Alternating exposures of trimethylaluminum (TMA), ethylene glycol (EG), and terephthaloyl chloride (TC) are used to grow aluminum alkoxide films. Control over film composition was accomplished by alternating cycles of EG and TC between cycles of TMA and EG. In this fashion the ratio of aluminum to carbon can be accurately controlled. These films were then pyrolyzed under a reducing atmosphere to yield a conductive Al_2O_3/carbon composite. Raman spectroscopy was used and revealed that nanocrystalline sp^2-graphitic carbon was formed following pyrolysis. Sheet resistance measurements determined that conductivity of the film is directly related to aluminum-carbon ratio. To further elucidate the origin of conductivity within the film, synchrotron based XPS was performed.

*A version of this chapter has been published in App. Surf. Sci 357 (2015) 1319

4.1 Introduction

Inorganic-organic hybrid films have attracted global attention due to their application in solar cells [1], electronics [2], photonics [3], sensors [4], as well as electrochemical processes [5]. Inorganic components of these hybrid films can provide desired mechanical, optical, chemical and electrical properties while the organic component provides increased flexibility and reduced material density [6]. There are a number of methods for preparing inorganic-organic hybrid materials including sol-gel processes [7], use of siloquinoxanes [8], hydrothermal synthesis [9], self-assembling procedures [10], integrative synthesis [11], langmuir-blodget method [12], and electrodeposition [13]. Although these methods are quite versatile, they lack the ability to grow films over high aspect ratio substrates with atomic precision. An alternative method for growing hybrid inorganic-organic materials is to utilize the gas phase deposition technique of atomic layer deposition (ALD) and molecular layer deposition (MLD). ALD and MLD are thin-film deposition techniques based on sequential, self-limiting surface reactions. These two techniques that can conformally coat high aspect ratio structures while providing angstrom level control over film growth. ALD processes typically focus on inorganic materials [14], whereas MLD processes are designed to use organic reactants [15]. By mixing the process of ALD and MLD together, binary surface reactions between a metal-ligand reactant and an organic reactant can yield a hybrid inorganic-organic film. Many inorganic-organic hybrid materials have been grown using this technique including alucone [16], zincones [17], and titanicones [18]. This family of "metalcones", is prepared using an organic alcohol precursor along with an organometallic precursor to deposit metal alkoxide polymeric films. The number of possible combinations using inorganic ALD and organic MLD reactants is extensive due to the large number of organic moieties available. However, the mixed deposition of ALD and MLD is challenging, and appropriate reactions between inorganic and organic components need to be determined.

Hybrid films are useful for a number of applications in their as-deposited state, however, they can also be used as precursors for metal oxide/carbon composites or porous metal oxide films [19]. Pyrolyzing hybrid films under inert atmospheres can produce metal oxide/carbon composite films [5]. Being able to deposit thin conformal conductive films on high surface area materials has several key applications, especially for electrochemical devices. Furthermore, pyrolysis of hybrid ALD/MLD films containing nitrogen has been shown to produced N-doped metal oxides [20].

Abdulagatov et al [5], showed that the pyrolysis of titanicone films can produce conductive substrates. The conductivity of these pyrolyzed film can be attributed to the formation of sp^2-graphitic carbon. However, the control of conductivity for hybrid inorganic-organic films is still limited. Furthermore, the effect of carbon on the metal oxide during pyrolysis was not determined.

In this chapter, we describe a new MLD strategy to deposit aluminum alkoxide films with tunable carbon content. MLD films are grown using trimethylaluminum (TMA), ethylene glycol (EG), and terephthaloyl chloride (TC). These films are pyrolyzed at various temperatures under an inert atmosphere. The effect of carbon on the metal oxide is studied by Raman analysis as well as synchrotron based XPS. To the best of our knowledge, this is the first reported process of a metalcone with tunable carbon content.

4.2 Experimental Details

Deposition conditions: hybrid inorganic-organic films were deposited in a commercial cross flow-type hot-wall Gemsta-8 ALD reactor (Arradiance) using $Al(CH_3)_3$ (trimethylaluminum, TMA; Strem, 98%), $C_2H_6O_2$ (ethylene glycol, EG; Sigma-Aldrich, 99.8%), and $C_8H_4Cl_2O_2$ (terephthaloyl chloride, TC; Sigma-Aldrich, 99%). All precursors were evaporated in an external reservoir. TMA was held at room temperature (RT) While EG and TC were heated up to 90ºC to provide sufficient vapor pressure. Nitrogen (99.999%, Praxair) was used as both a carrier and purge gas. All depositions were conducted at 150ºC on double polished Si (100) and high purity SiO_2 glass substrate. Precursor manifolds were heated to 120ºC to ensure precursor volatility before entering the deposition chamber. An aluminum oxide seed layer of 10 nm was deposited on the substrate using TMA and H_2O. Inorganic-organic hybrid films with increased carbon content were deposited using a 50 ms pulse of TMA and EG and a 500 ms pulse of TC. Following each pulse, carrier gas flow rate was increased to 100 sccm for 15 seconds to ensure complete removal of precursor from the manifold. Following this, the flow rate was then dropped to 10 sccm for 15 seconds to remove by-products produced during the reaction. Relatively long purge times were used to guarantee removal of excess precursor and reaction by-products.

Annealing treatment: pyrolysis of MLD films was performed at temperatures ranging from 600-1000ºC in a high temperature furnace (Lindberg/Blue M tube furnace). Silicon samples with MLD films were placed on ceramic boats which were then inserted into a quartz tube. Prior to pyrolysis,

high purity Ar was introduced into the quartz tube for 30 min to ensure an inert atmosphere was present. Samples were held at the pyrolysis temperature for 1 hour as is typically done for treatment of MLD films [5].

Physical Characterization: film thickness and surface morphology were determined by a field emission scanning electron microscope (FE-SEM, Hitachi S4800). Raman spectroscopy was obtained using a HORIBA Scientific LabRAM HR Raman spectrometer system with a 532.4 nm laser and optical microscope operating at RT. Fourier transform infrared spectroscopy (FTIR) was obtained with a Nicolet 6700 FTIR spectrometer. Aluminum 2p X-ray photoelectron spectroscopy (XPS) measurements were collected at the variable line spacing plane grating monochromator (VLS-PGM) beamline equipped with a Scientia 100 analyzer at the Canadian Light Source (CLS) in Saskatoon, Saskatchewan, Canada. The CLS is a third-generation synchrotron light source operating at 2.9 GeV. Electrical measurements were performed on pyrolyzed MLD films deposited on high purity SiO_2 glass. Sheet resistance measurements were carried out using a home-built four-point probe equipped with a Keithley 2400 source meter.

4.3 Results and Discussion

Carbon content in aluminum alkoxide films was controlled by altering the number of ethylene glycol (EG) and terephthaloyl chloride (TC) cycles prior to a pulse of trimethylaluminum (TMA). As outlined in Figure 4.1, step "A" consists of a TMA pulse, while steps B and C are pulses of EG and TC, respectively. Each step is followed by an N_2 purge to remove reaction by-products. Steps "B" and "C" can be cycled to increase carbon content in the MLD film. 1 MLD cycle for a 1:1 film would consist of steps "ABCB", whereas 1 MLD cycle for a 1:3 film would consist of, "ABCBCBCB." In this manner, the amount of carbon in the film can be precisely controlled. In order to insure a homogenous distribution of hydroxyl groups on the surface, a 10 nm Al_2O_3 seed layer was deposited prior to the deposition of the inorganic-organic hybrid films. Cross section SEM of silicon wafers was used to determine film thickness. As shown in Figure 4.2, the produced 1:1 polymer film uniformly coats the Si substrate with negligible roughness.

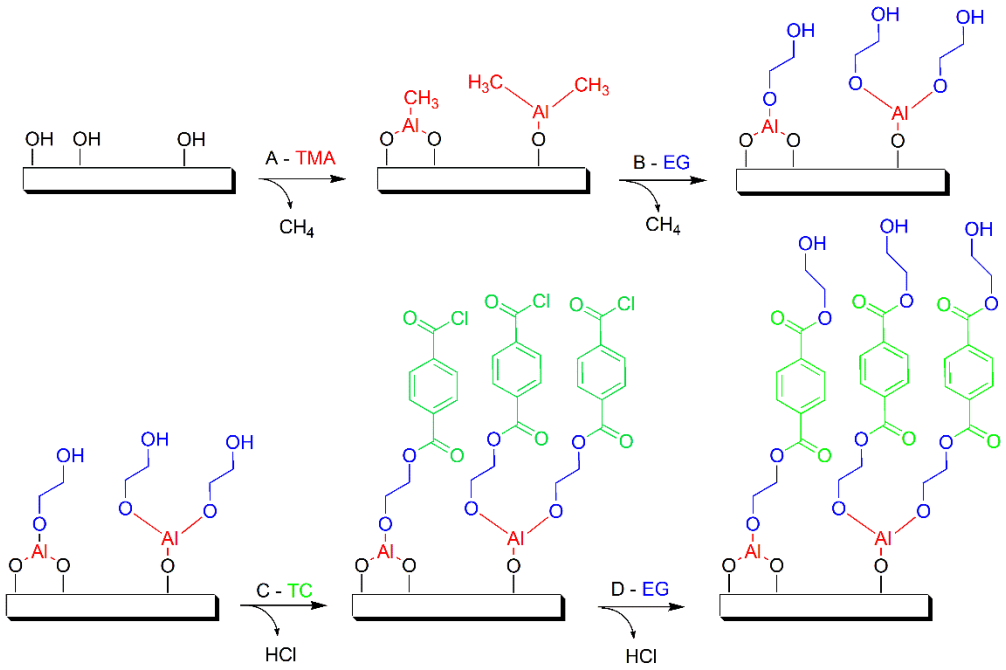


Figure 4.1. *Mechanism of MLD reaction between TMA, EG and TC.*

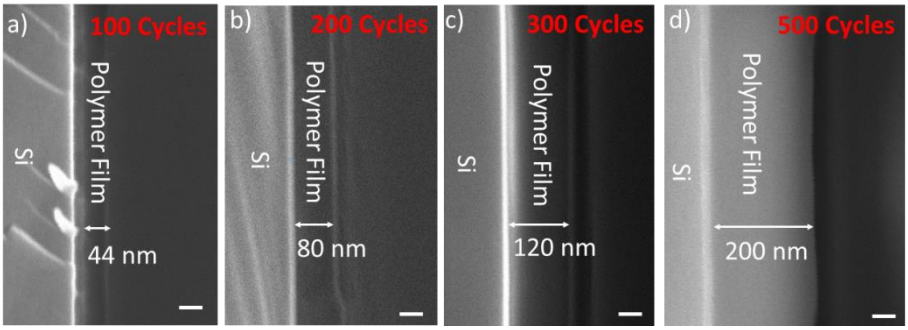


Figure 4.2. *SEM cross section view of MLD films deposited using a sequence of 1:1 with increasing cycling number. Scale bar represents 50 nm.*

Figure 4.3 shows the cycle dependence of the deposited MLD films. Clearly, the 1:1 and 1:3 films increase in thickness linearly with number of cycles. By fitting the data in Figure 4.3 linearly, the growth per cycle of the MLD films is calculated to be 0.4 nm/sequence and 0.6 nm/sequence for 1:1 and 1:3 films, respectively. For comparison, cycles of TMA-EG were also deposited on Si with a growth rate of 0.15 nm/sequence. This value correlates well with previous results [21].

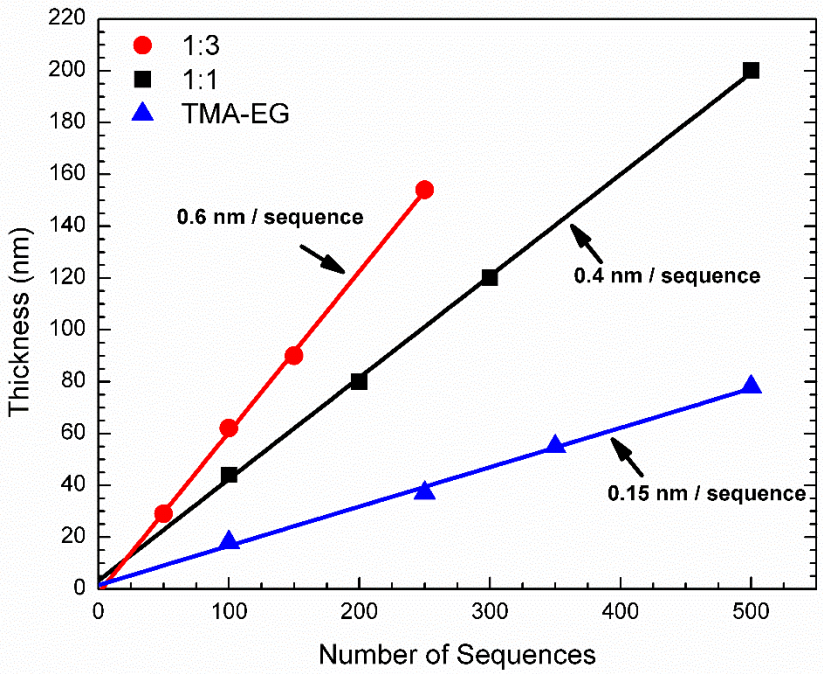


Figure 4.3. *Thickness of 1:1, 1:3 and TMA-EG MLD films verses number of deposition cycles at 150°C.*

Figure 4.4 presents FTIR data for TMA-EG, 1:1 and 1:3 films. All spectra demonstrate a prominent peak at 610 cm^{-1} and 905 cm^{-1} which can be attributed to Si-O and Al-O bonds respectively [22], [23] . In addition, C-O stretching vibrations are observed at 1100 cm^{-1} for all spectra, and originate from EG. As expected, additional peaks can be found for the 1:1 and 1:3 film due the inclusion of TC. Typically, a strong, C=O absorption band is seen between 1750-1735 cm^{-1} for saturated aliphatic esters. However, the C=O stretch for 1:1 and 1:3 films appears at 1729 cm^{-1}. This stretching vibration is shifted to lower frequency due to its conjugation with an aromatic group [24]. The higher carbon content films also display a weak skeletal vibration stemming from C-C stretching within the ring with absorptions appearing between 1450-1550 cm^{-1} region [25]. Importantly, a signature peak for chlorinated C=O and C-Cl are not present in the obtained FTIR spectra, indicating that all TC has been successfully removed from the substrate along with its reaction by-products [26].

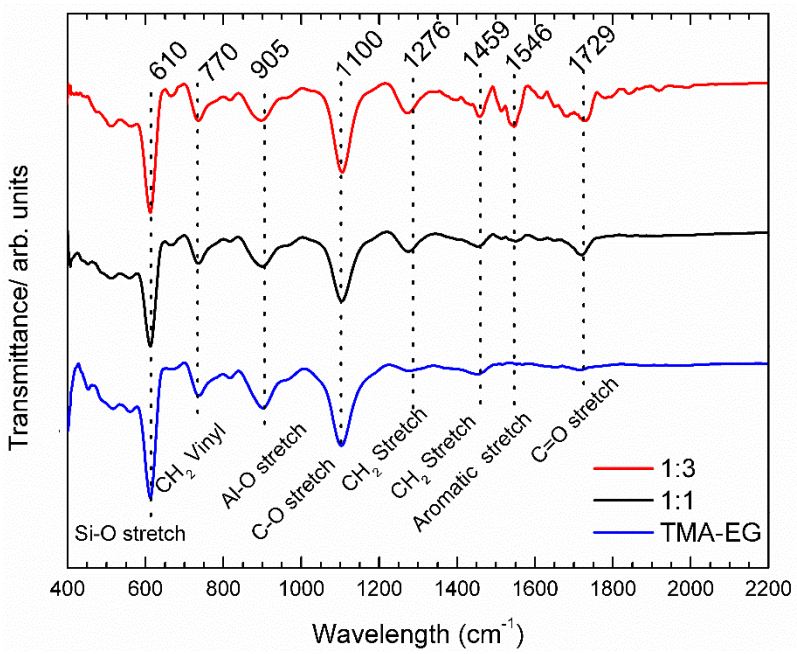


Figure 4.4. *FTIR spectra for 100nm thick TMA-EG, 1:1 and 1:3 MLD films deposited on double polished Si at 150°C.*

Raman spectroscopy was employed to determine the state of carbon following pyrolysis. Pyrolysis was conducted at 1 atm under 5% H_2/Ar gas at various temperatures (600°C, 700°C, 800°C and 900°C). Figure 4.5a and 4.5b presents the Raman spectra for pyrolyzed 1:1 and 1:3 MLD films at various temperatures. Two peaks located at ~ 1350 cm^{-1} and 1590 cm^{-1} appear because of pyrolysis and vary in intensity for each sample set. Raman intensities at 1590 cm^{-1} and 1350 cm^{-1} are usually designated as G (graphitic sp^2 phase carbon) and D (disordered sp^2/sp^3 phase carbon), respectively [27]. Obtained Raman spectra for 1:3 MLD films display a narrowing of the G band as well as a slight shift to 1600 cm^{-1} with increasing pyrolysis temperature. This is can be attributed to the growth of nanographitic crystals [28]. This structural change can be attributed to the material becoming increasingly polycrystalline as well as a reduction in the number of sp^3 sites [29]. Ferrari et al [30] established that the full width at half maximum (FWHM) of the G peak can be used to measure the amount of graphitic disorder for carbon substrates. Figure 4.5b indicates that with increasing temperature, the G peak of the 1:3 film increases in intensity while simultaneously becoming narrower. This is a strong indication that the graphitic planes within the film are increasing in order and size. However, the spectrum for 1:1 MLD films is starkly different. There is a dramatic decrease in both D and G band intensity along with a peak broadening with increasing pyrolysis temperature. This broadening indicates that phonon lifetimes are being

significantly reduced, implying that defect density of the sp^2 carbon is increasing [31]. Dillion et al [28] determined that a decrease in D and G band linewidth is consistent with the removal of bond-angle disorder and increasing dominance of crystallites [28], [31], [32]. This would suggest that for the 1:1 MLD films, as pyrolysis temperatures increase, bond-angle disorder also increases, resulting in an increased linewidth to appear in the Raman spectra. Furthermore, a reduction in phonon lifetime may also be attributed to the formation of Al_2O_3.

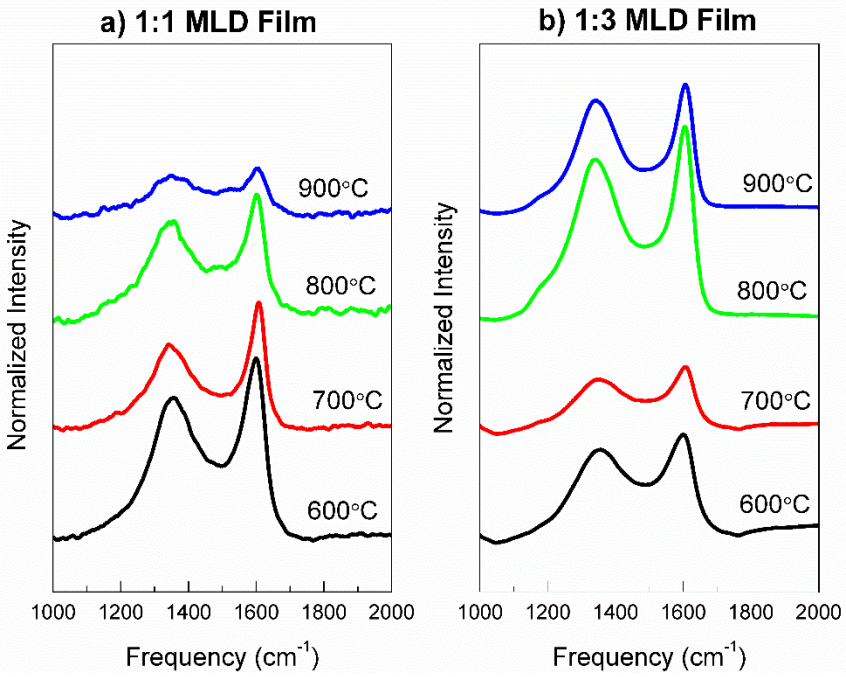


Figure 4.5. *Raman spectra for a) 1:1 and b) 1:3 MLD films with initial thickness of 200nm annealed with 5% H_2/Ar at 600, 700, 800 and 900°C for 1 hour.*

Sheet resistance of 1:1 and 1:3 MLD deposited films was plotted as a function of heat treatment temperature, as shown in Figure 4.6. The films were grown on high purity SiO_2 glass slides and heat treated under a mixture of 5% H_2/Ar gas at temperatures from 500 to 1000°C for 1h. Sheet resistance was obtained using a four-point probe. As shown in Figure 4.6, sheet resistance rapidly declines until 900ºC. This dramatic decrease in sheet resistance is attributed to the formation of nanocrystalline graphite, as indicated by Raman spectroscopy. Similar evolution in electrical resistance has been observed for the pyrolysis of pure organic polymers [33]. Interestingly, the 1:3 MLD film demonstrates a sheet resistance of 4.6 x 10^4 Ω/□ compared to 3.5 x 10^5 Ω/□ for the 1:1 MLD films pyrolyzed at 900ºC. this demonstrates that increasing the carbon content of the MLD film, results in a decrease in sheet resistance. This decrease in sheet resistance

is attributed to changes in the film composition as a result of decreasing carbon to aluminum ratio [34]. Furthermore, the significant decrease in sheet resistance for a higher carbon film may also be due to larger domains of nanocrystalline graphite and less disordered carbon. As indicated by Raman spectroscopy, the 1:3 film pyrolyzed at 900ºC presents sharp D and G bands, whereas the 1:1 film pyrolyzed at the same temperature presents very broad D and G bands. This indicates increased carbon disorder and decreased graphitic nanocrystalline size. Another possibility for the large difference in sheet resistance between the 1:1 and 1:3 film is presence of carbothermally reduced aluminum oxide. Typically, carbothermal reduction of alumina occurs at temperatures > 1400ºC. However, previous studies have determined that the formation of Al_4O_4C and Al_4C_3 can occur at much lower temperatures but is highly dependent on Al_2O_3 grain size and reducing environment [35]. Interestingly at temperature greater than 900°C, the sheet resistance for both films increases. A similar behavior is also observed in the pyrolysis of other hybrid MLD films [5]. The large increase in sheet resistance at 1000°C may be attributed to the chemical attack of basic groups in the film by aluminum species. A previous paper published by Bou et al [36] established that aluminum preferentially attacks basic sites and leads to compounds with increased resistance. Another possibility for the occurrence of this phenomenon is the change in film morphology. Increased heating temperatures will result in film shrinkage and a loss in film uniformity. This may also result in higher sheet resistant measurements taken by a four-point probe. A better understanding of this phenomenon can be determined by using current sensing atomic force microscopy along with XPS measurements of the film following annealing.

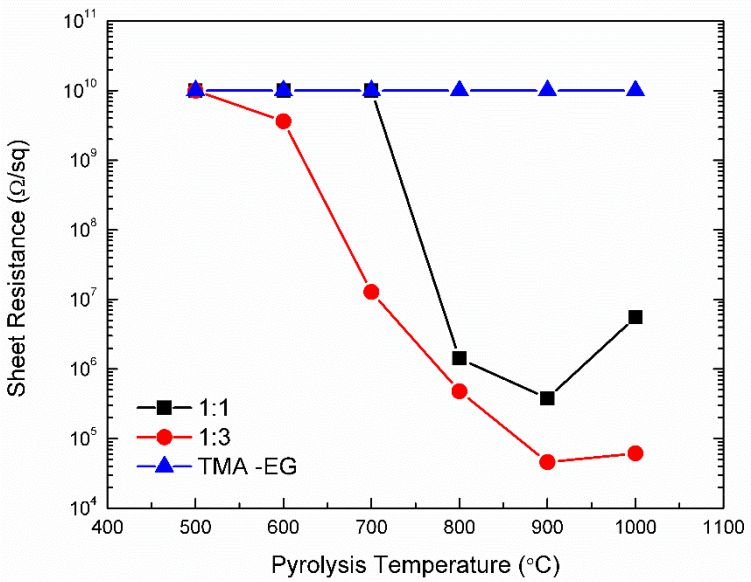


Figure 4.6. *Sheet resistance measurements for 100 nm thick TMA-EG, 1:1, and 1:3 MLD films pyrolyzed at various temperatures*

The structure of amorphous materials is difficult to determine with diffraction-based techniques due to the lack of long-range order. To overcome this difficulty, X-ray spectroscopy is employed as it can provide information pertaining to the local environment of the element being examined. Furthermore, synchrotron XPS is highly surface sensitive and can provide a stronger signal to noise ratio due to the use of a high intensity light source. As shown in Figure 4.7a, the as deposited films display a binding energy of 74.7 eV, 75.0 eV, and 75.6 eV for the 1:3, 1:1 and TMA-EG films respectively. Al-O bonds are typically seen at 74.6 eV and shift to higher binding energy in higher oxidized forms such as Al-O-C [37]–[39]. This indicates that the aluminum in the TMA-EG films exist at a higher oxidation state than in the 1:1 and 1:3 MLD films. Interestingly, pyrolysis of TMA-EG films results in the aluminum peak shifting to higher binding energies, while the aluminum in 1:1 and 1:3 MLD films shift to lower binding energy. The increased binding energy for pyrolyzed TMA-EG films, from 75.6 eV to 76.0 eV, is strong evidence that Al_2O_3 is formed. The decrease in binding energy seen for 1:1 and 1:3 films, down to 74.2 eV and 74.0 eV, respectively, is a clear indication that the higher carbon content in these film results in reduction of aluminum. This may also be linked to the decrease seen in sheet resistance observed for pyrolyzed MLD films. The increase in the aluminum 2p peak for TMA-EG films can be attributed to a low carbon to aluminum ratio. However, because the carbon to aluminum ratio is much higher in the 1:1, and even more so in 1:3 MLD films, carbothermal reduction is likely to occur.

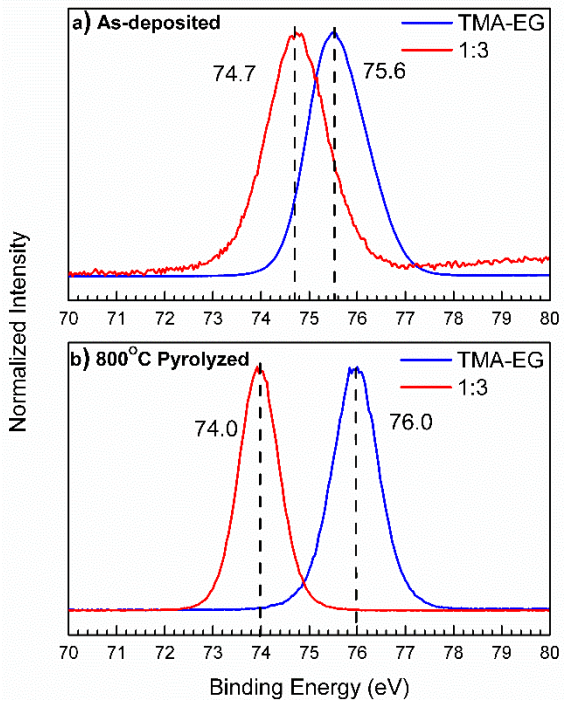


Figure 4.7. *Synchrotron based XPS of a) as deposited and b) 800°C pyrolyzed TMA-EG and 1:3 MLD films*

4.4 Conclusions

Aluminum alkoxide hybrid inorganic-organic films with tunable carbon content were grown using sequential exposure of TMA, EG and TC. Pure alucone, 1:1 and 1:3 films were then pyrolyzed under a reducing atmosphere to produce a conductive Al_2O_3/carbon composite film. Raman spectra of the pyrolyzed films indicate that carbon content in the film leads to nanocrystalline graphite. The amount of nanocrystalline graphite in the film is related to the amount of carbon deposited in the initial MLD film. Sheet resistance of pyrolyzed films dramatically decreases with increasing pyrolysis temperature. Furthermore, films produced with higher carbon content resulted in a greater decrease in sheet resistance due increased sp^2 carbon formation. Synchrotron XPS revealed that following pyrolysis, increasing carbon content in aluminum alkoxide films leads to carbothermal reduction of aluminum. This work demonstrates the powerful capabilities of MLD in creating hybrid inorganic-organic films with tunable composition. Using this novel MLD approach, thin hybrid films with tunable amorphous polymeric regions and dense inorganic regions can be made. This type of film has many applications and can be used in solid polymer electrolytes for lithium ion batteries which require

regions of highly amorphous carbon for elevated lithium ion mobility. Furthermore, using this approach increased control over pore size for MLD films annealed in air is achievabale. By tuning the amount of carbon to aluminum in the film, porous aluminum oxide with various pore sizes can be fabricated.

4.5 References

[1] J. H. Noh, S. H. Im, J. H. Heo, T. N. Mandal, and S. Il Seok, "Chemical Management for Colorful, Efficient, and Stable Inorganic–Organic Hybrid Nanostructured Solar Cells," *Nano Lett.*, vol. 13, no. 4, pp. 1764–1769, 2013.

[2] L. Wang, M.-H. Yoon, G. Lu, Y. Yang, A. Facchetti, and T. J. Marks, "High-performance transparent inorganic–organic hybrid thin-film n-type transistors," *Nat. Mater.*, vol. 5, no. 11, pp. 893–900, 2006.

[3] Y. Zou *et al.*, "Solution Processing and Resist-Free Nanoimprint Fabrication of Thin Film Chalcogenide Glass Devices: Inorganic-Organic Hybrid Photonic Integration," *Adv. Opt. Mater.*, vol. 2, no. 8, pp. 759–764, 2014.

[4] H. Ma, R. Gao, D. Yan, J. Zhao, and M. Wei, "Organic–inorganic hybrid fluorescent ultrathin films and their sensor application for nitroaromatic explosives," *J. Mater. Chem. C*, vol. 1, no. 26, p. 4128, 2013.

[5] A. I. Abdulagatov, K. E. Terauds, J. J. Travis, A. S. Cavanagh, R. Raj, and S. M. George, "Pyrolysis of titanicone molecular layer deposition films as precursors for conducting TiO2/carbon composite films," *J. Phys. Chem. C*, vol. 117, no. 34, pp. 17442–17450, 2013.

[6] B. H. Lee, B. Yoon, A. I. Abdulagatov, R. A. Hall, and S. M. George, "Growth and properties of hybrid organic-inorganic metalcone films using molecular layer deposition techniques," *Adv. Funct. Mater.*, vol. 23, no. 5, pp. 532–546, 2013.

[7] G. Larsen, R. Velarde-Ortiz, K. Minchow, A. Barrero, and I. G. Loscertales, "A method for making inorganic and hybrid (organic/inorganic) fibers and vesicles with diameters in the submicrometer and micrometer range via sol-gel chemistry and electrically forced liquid jets," *J. Am. Chem. Soc.*, vol. 125, no. 5, pp. 1154–1155, 2003.

[8] X. Wang *et al.*, "Organic–inorganic hybrid liquid crystals derived from octameric silsesquioxanes. Effect of the peripheral groups in mesogens on the formation of liquid crystals," *J. Mater. Chem.*, vol. 21, no. 14, p. 5248, 2011.

[9] V. Singh *et al.*, "Hydrothermal synthesis of inorganic-organic hybrid gadolinium hydroxide nanoclusters with controlled size and morphology.," *Dalton Trans.*, vol. 42, no. 45, pp. 16176–84, 2013.

[10] P. R. L. Malenfant, J. Wan, S. T. Taylor, and M. Manoharan, "Self-assembly of an organic-inorganic block copolymer for nano-ordered ceramics.," *Nature nanotechnology*, vol. 2, no. 1. pp. 43–46, 2007.

[11] T. Kimura and K. Kato, "Synthesis of ordered mesoporous aluminium alkylenediphosphonates with integrated inorganic?organic hybrid frameworks," *Journal of Materials Chemistry*, vol. 17, no. 6. p. 559, 2007.

[12] H. Tachibana, Y. Yamanaka, H. Sakai, M. Abe, and M. Matsumoto, "Highly conductive inorganic-organic hybrid Langmuir-Blodgett films based on MoS2," *Chem. Mater.*, vol. 12, no. 3, pp. 854–856, 2000.

[13] T. Yoshida *et al.*, "Electrodeposition of inorganic/organic hybrid thin films," *Adv. Funct. Mater.*, vol. 19, no. 1, pp. 17–43, 2009.

[14] R. L. Puurunen, "Surface chemistry of atomic layer deposition: A case study for the trimethylaluminum/water process," *J. Appl. Phys.*, vol. 97, no. 12, 2005.

[15] B. Yoon, D. Seghete, A. S. Cavanagh, and S. M. George, "Molecular layer deposition of hybrid organic - Inorganic alucone polymer films using a three-step abc reaction sequence," *Chem. Mater.*, vol. 21, no. 22, pp. 5365–5374, 2009.

[16] M. L. Dunn *et al.*, "Thermomechanical properties of aluminum alkoxide (alucone) films created using molecular layer deposition," *Acta Materialia*, vol. 57. pp. 5083–5092, 2009.

[17] J. Liu *et al.*, "Ultralow thermal conductivity of atomic/molecular layer-deposited hybrid organic-inorganic zincone thin films," *Nano Lett.*, vol. 13, no. 11, pp. 5594–5599, 2013.

[18] J. J. Brown, R. A. Hall, P. E. Kladitis, S. M. George, and V. M. Bright, "Molecular Layer Deposition on Carbon Nanotubes," no. 9, pp. 7812–7823, 2013.

[19] X. Liang and A. W. Weimer, "An overview of highly porous oxide films with tunable thickness prepared by molecular layer deposition," *Curr. Opin. Solid State Mater. Sci.*, vol. 19, no. 2, pp. 115–125, 2015.

[20] C. Chen *et al.*, "Nanoporous nitrogen-doped titanium dioxide with excellent photocatalytic activity under visible light irradiation produced by molecular layer deposition," *Angew. Chemie - Int. Ed.*, vol. 52, no. 35, pp. 9196–9200, 2013.

[21] A. A. Dameron *et al.*, "Molecular Layer Deposition of Alucone Polymer Films Using Trimethylaluminum and Ethylene Glycol," *Chem. Mater.*, vol. 20, no. 10, pp. 3315–3326, 2008.

[22] G. L. Fisher *et al.*, "Bond insertion, complexation, and penetration pathways of vapor-deposited aluminum atoms with HO- and CH3O-terminated organic monolayers," *J. Am. Chem. Soc.*, vol. 124, no. 19, pp. 5528–5541, 2002.

[23] M. Nakamura, Y. Mochizuki, K. Usami, Y. Itoh, and T. Nozaki, "Infrared absorption spectra and compositions of evaporated silicon oxides (SiOx)," *Solid State Commun.*, vol. 50, no. 12, pp. 1079–1081, 1984.

[24] D. Pavia, G. Lampman, G. Kris, and J. Vyvyan, "Introduction to Spectroscopy," 4th ed., Belmont: Brooks/Cole, 2009, pp. 66–69, 2009.

[25] T. V. Ivanova, P. S. Maydannik, and D. C. Cameron, "Molecular layer deposition of polyethylene terephthalate thin films," *J. Vac. Sci. Technol. A Vacuum, Surfaces, Film.*, vol. 30, no. 1, p. 01A121, 2012.

[26] N. M. Adamczyk, a. a. Dameron, and S. M. George, "Molecular layer deposition of poly(p-phenylene terephthalamide) films using terephthaloyl chloride and p-phenylenediamine," *Langmuir*, vol. 24, no. 5, pp. 2081–2089, 2008.

[27] M. A. Tamor and W. C. Vassell, "Raman 'fingerprinting' of amorphous carbon films," *J. Appl. Phys.*, vol. 76, no. 6, pp. 3823–3830, 1994.

[28] R. O. Dillon, J. A. Woollam, and V. Katkanant, "Use of Raman scattering to investigate disorder and crystallite formation in as-deposited and annealed carbon films," *Phys. Rev. B*, vol. 29, no. 6, pp. 3482–3489, 1984.

[29] A. C. Ferrari and J. Robertson, "Interpretation of Raman spectra of disordered and amorphous carbon," *Phys. Rev. B*, vol. 61, no. 20, pp. 14095–14107, 2000.

[30] a. Ferrari, S. Rodil, and J. Robertson, "Interpretation of infrared and Raman spectra of amorphous carbon nitrides," *Phys. Rev. B*, vol. 67, no. 15, pp. 1–20, 2003.

[31] R. G. Buckley, T. D. Moustakas, L. Ye, and J. Varon, "Characterization of filament-assisted chemical vapor deposition diamond films using Raman spectroscopy," *J. Appl. Phys.*, vol. 66, no. 8, pp. 3595–3599, 1989.

[32] J. Gonzalez-Hernandez, G. H. Azarbayejani, R. Tsu, and F. H. Pollak, "Raman, transmission electron microscopy, and conductivity measurements in molecular beam deposited microcrystalline Si and Ge: A comparative study," *Appl. Phys. Lett.*, vol. 47, no. 12, pp. 1350–1352, 1985.

[33] Z. Sun, X. Shi, X. Wang, and Y. Sun, "Structure and properties of hard carbon films depending on heat treatment temperatures via polymer precursor," *Diam. Relat. Mater.*, vol. 8, pp. 1107–1113, 1999.

[34] R. Kostecki, B. Schnyder, D. Alliata, X. Song, K. Kinoshita, and R. Kötz, "Surface studies of carbon films from pyrolyzed photoresist," *Thin Solid Films*, vol. 396, no. 1–2, pp. 36–43, 2001.

[35] I. Ahmad *et al.*, "Multi-walled carbon nanotubes reinforced Al2O3 nanocomposites: Mechanical properties and interfacial investigations," *Compos. Sci. Technol.*, vol. 70, no. 8, pp. 1199–1206, 2010.

[36] M. Bou, J. M. Martin, T. Le Mogne, and L. Vovelle, "Chemistry of the interface between aluminium and polyethyleneterephthalate by XPS," *Appl. Surf. Sci.*, vol. 47, no. 2, pp. 149–161, 1991.

[37] R. Cueff, G. Baud, M. Benmalek, J. . Besse, J. . Butruille, and M. Jacquet, "X-ray photoelectron spectroscopy studies of plasma-modified PET surface and alumina/PET interface," *Appl. Surf. Sci.*, vol. 115, no. 96, pp. 292–298, 1997.

[38] R. Cueff, G. Baud, M. Benmalek, J. P. Besse, J. R. Butruille, and M. Jacquet, "Alumina coatings on polyethylene terephthalate: Characterisation and X-ray photoelectron spectroscopy study," *Surf. Coatings Technol.*, vol. 80, no. 1–2, pp. 96–99, 1996.

[39] B. Maruyama, F. S. Ohuchi, and L. Rabenberg, "Catalytic carbide formation at aluminium-carbon interfaces," *J. Mater. Sci. Lett.*, vol. 9, no. 7, pp. 864–866, 1990.

5

Orientation and Ordering of Organic and Hybrid Inorganic-Organic Polyurea Films using Molecular Layer Deposition*

The molecular orientation and ordering of films produced by a vapor-phase deposition technique, known as molecular layer deposition (MLD), is investigated. Specifically, the influence of incorporating an inorganic component into MLD films is determined. Film growth properties and surface saturating conditions of a purely organic polyurea film (PDIC-ED) and a mixed inorganic-organic polyurea film (TMA-ED-PDIC) is investigated by *in-situ* quartz crystal microbalance. Polarization-dependent X-ray absorption spectroscopy (XAS) was employed to determine the orientation and ordering of these films. Both films demonstrate preferential orientation parallel to the substrate surface. However, the degree of ordering between the films was found to be starkly different. In-depth analysis revealed that the hybrid inorganic-organic films display a high degree of ordering compared to purely organic polyurea films. This study sheds light on the ability of MLD to finely tune oligomer packing density, growth rate, molecular orientation, and film ordering.

*A version of this chapter has been published in J. Phys. Chem. C 121 (2017) 11757

5.1 Introduction

Many emerging technologies rely on the production of thin films with tailored composition and architectures. As a result, manufacturers have turned to atomic layer deposition (ALD) for producing high-quality, nanometer-scale films as this process enables control over film thickness, density, conformity and uniformity [1]. Due to these attractive features, ALD has been utilized in a wide variety of fields including microelectronics [2], catalyst preparation [3], dye-sensitized solar cells [4], and lithium-ion batteries [5]. Although ALD is typically used for the deposition of inorganic materials (such as metals, metal oxides, nitrides, and sulfides) [6] there is a growing need for well-controlled fabrication of organic thin films (such as oligomers and polymers) on various substrates. This requirement can be met by molecular layer deposition (MLD), an analogue of the ALD technique. MLD follows the same cyclic surface-limited reaction route employed by ALD to produce highly conformal polymeric films [7]–[9]. Furthermore, binary surface reactions occurring between metal-ligands and organic reactants can produce hybrid inorganic-organic films [10]–[12]. To date, there have been a number of reports hybridizing the properties of inorganic and organic films by MLD [11], [13]–[15]. By precisely controlling deposition parameters and the inorganic-organic content within these films, researchers have been able to accurately tune film properties such as electronic conductivity [15], [16], thermal conductivity [12], mechanical strength [17], and magnetic ordering [18].

Of different organic films prepared by MLD, polyurea films are of particular interest due to their low deposition temperature and lack of by-product formation. Polyurea-based composites are a type of elastomer typically synthesized by reacting an isocyanate with a diamine [19]. Due to the great elasticity, high strength, and good thermal stability of polyurea composites, these polymers have been widely adopted as a protective coating for textiles [20], metal plates [21], and drug delivery systems [22]. Furthermore, the high degree of hydrogen bonding interactions typically found in polyurea polymers has led to their use in self-healing applications [23]. The strong hydrogen bonding characteristics imparted by the polyurea functional groups have been found to produce a self-healing effect when applied to battery materials that undergo large volume change during electrochemical cycling [24]. This type of self-healing behavior, along with mechanical and thermal stability, make polyurea polymers and their blends, an interesting system

for investigation, especially at the nanoscale. There have been a number of reports demonstrating the deposition of both aliphatic and aromatic polyurea's by MLD [7], [19], [25]–[27]. Compared to polyurea films, mixed inorganic-organic polyurea films would allow for increased flexibility by introducing chemically reactive metal species and allowing tuning of mechanical, optical, and magnetic properties and hold promise for many applications. Unfortunately, no mixed inorganic-organic polyurea films have been fabricated to date.

Another interesting phenomenon observed for the growth of MLD films is their significantly lower growth rate compared to the ideal repeat unit length [7], [8], [27], [28]. This phenomenon is thought to stem from double side reactions taking place during the deposition process. Organic molecules tend to bend and react multiple times with the surface, thereby reducing the number of reactive sites available. Furthermore, organic precursors are often bulky and may cause steric hindrance issues during the deposition process, resulting in a reduced number of reactive sites. Interestingly, all polyurea films produced by MLD demonstrate lower than expected growth rates, suggesting a high degree of tilt occurring within the film. Although a handful of studies have been dedicated to analyzing the growth characteristics of MLD films [29]–[31], many of these studies do not address the interactions that may between oligomer chains. This is an important consideration when attempting to understand the mechanical properties of polymeric films as well as film growth characteristics. Furthermore, the difference in growth rate seen between pure organic MLD films and mixed inorganic-organic films has yet to be determined. One technique that can provide information pertaining to the alignment of polymer chains is polarization dependent Near-Edge X-ray Absorption Fine Structure (NEXAFS) spectroscopy. This technique has been proven to be a powerful tool for studying molecular orientation of materials produced from a number of methods including Langmuir-Blodgett films [32], block co-polymers [33], and single stranded DNA [34]. This tool can probe structures at the surface and in the bulk of the material at the same time, while maintaining high sensitivity to orientation of chemical bonds. Although techniques such as polarized absorption spectroscopy, polarized microscopy, and X-ray scattering have been used to determine the degree of order or alignment of polymers, these methods lack the sensitivity to monitor both electronic structure and structural modification of the polymers at the molecular level.

In this study, the effect of inorganic species on the molecular structure of MLD films is investigated. This is achieved by comparing the growth of purely organic polyurea MLD films to hybrid inorganic-organic polyurea films. Growth behavior and surface-limited reaction studies are carried out by using *in-situ* quartz crystal microbalance (QCM) while polarization dependent NEXAFS spectra is obtained to determine the orientation and ordering difference between organic polyurea films and mixed inorganic-organic polyurea films. Given the interesting hydrogen bonding properties of polyurea films, as well as their widespread application as a mechanically robust coating material, determining the intra and inter molecular interaction as a result of orientation and ordering is important for future film design and application.

5.2 Experimental Details

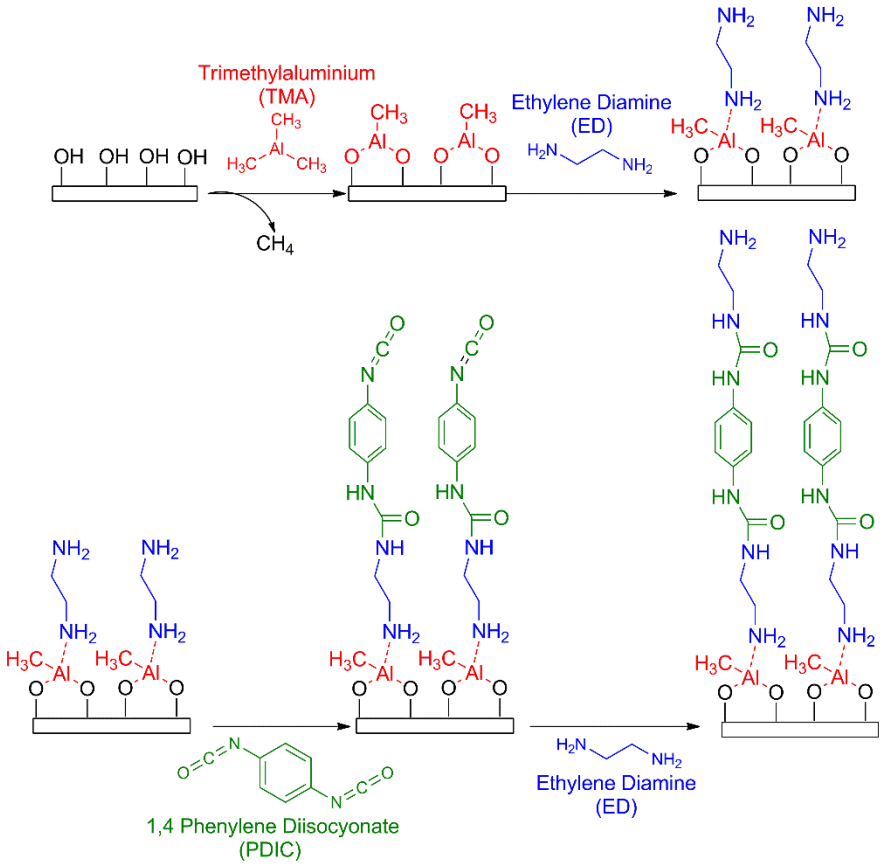
Deposition conditions: MLD films were deposited in an GEMstar-8 ALD system (Arradiance) using ethylenediamine (ED), 1,4 phenylene diisocyonate (PDIC), and trimethylaluminum (TMA) purchased from Sigma-Aldrich and used as received. TMA and ED were held in external reservoirs at room temperature (RT) while PDIC was heated to 90°C to provide sufficient vapor pressure. Manifold temperature was held at 100°C to maintain precursor volatility. 99.999% Nitrogen (Praxair) was used as both carrier and purge gas with a flow rate of 50 sccm. Unless otherwise stated, MLD films were deposited at 50°C at a processing pressure of ~0.8 Torr. For deposition of pure polyurea films (PDIC-ED), a 1 s dose of PDIC and a 100 ms dose of ED was used. For growth of hybrid inorganic-organic films of aluminum and polyurea (TMA-ED-PDIC), a 100 ms pulse of TMA followed by a 100 ms and 1 s dose of ED and PDIC, respectively followed by a 100 ms pulse of ED was used. A 60 s N_2 purge was employed between each pulse to remove unreacted precursors. Films were grown on single and double polished silicon (100) wafers, which were sonicated in acetone for 30 min followed by sonication in ethanol for another 30 min and subsequently dried in air.

Characterization Techniques: MLD and ALD reactions were monitored using *in-situ* QCM experiments with an RC-cut quartz crystal (gold coated and polished, 6 MHz, Colnatec) supplemented by an Eon-Lt processing system (Colnatec). An aluminum oxide seed layer of 1 nm was deposited using TMA and water on each substrate prior to deposition to ensure a homogeneous distribution of nucleation sites.

NEXAFS spectroscopy was performed at the Advanced Light Source, Lawrence Berkeley National Laboratory. N K-edge and C K-edge measurements were collected at the beamline (BL) 6.3.1.2 ISAAC end station. The bending magnet at BL 6.3.1.2 provides a photon source with an energy range of 250-2000 eV with a spot size of 100 x 500 μm^2. Nitrogen and carbon K-edge absorption spectra was calibrated using boron nitride (BN) and highly orientated pyrolytic graphite (HOPG), respectively, at an angle of 55° to the surface normal to eliminate any effects related to molecular orientation. Angle dependent NEXAFS calibration data for BN and HOPG was also collected using an X-ray incidence angle ranging between 15° to 85°. Fourier transform infrared spectroscopy (FTIR) was obtained using a Nicolet 6700 FTIR spectrometer in transmission mode. All samples used for FTIR measurements had a film thickness of 30 nm. Film thickness and surface roughness was acquired using X-ray reflectivity (XRR) on a Bruker D8 Advance and analyzed using the LEPTOS software package. The X-ray source was a Cu Kα X-ray tube with a wavelength of 1.54 Å with a filament current of 40 mA and a voltage of 40 kV.

5.3 Results and Discussion

Scheme 5.1 outlines the reactions sequence used to grow hybrid inorganic-organic polyurea films using MLD. Starting with a thin 1 nm Al_2O_3, TMA is pulsed to react with surface hydroxyl groups. This is followed by a pulse of ED, producing a dative Al-N bond. Theoretical calculations conducted by Xu et al [35], determined that the ligand exchange barrier between TMA and amine groups is large. However, their calculations also revealed that the outcome of this reaction is a dative Al-N bond. This theoretical calculation is verified by experimental data obtained by Räupke et al [36], who also established that TMA datively binds to NH_2. This datively coordinated TMA-ED complex is then exposed to PDIC followed by another pulse of ED to regenerate amine groups for the next cycle of TMA. This film is referred to as TMA-ED-PDIC.



Scheme 5.1. *Schematic representation for preparation of hybrid inorganic-organic polyurea MLD films using trimethylaluminum (TMA), ethylene diamine (ED) and 1,4 phenylene diisocyonate (PDIC).*

Pure organic polyurea films (PDIC-ED) were grown following the procedure reported by Loscutoff et al [26]. Film thickness and roughness was determine using XRR analysis [37]. Figure 5.1a demonstrates the linear relationship between cycle number and film thickness for PDIC-ED (0.38 nm/cycle) and TMA-ED-PDIC (0.82 nm/cycle) on Si (100) wafers at 50°C. Loscutoff et al. found a growth rate of 0.41 nm/cycle for PDIC- ED at a deposition temperature of 35°C. This is far lower than the theoretical growth rate of 1.26 nm/cycle predicted by DFT calculation. The researchers attributed this lower than expected growth rate to a 71° chain tilt from the surface normal, a behavior typically observed for MLD films [8], [12], [28]. Furthermore, given the bifunctional nature of the precursor employed, PDIC may react twice with adjacent ED, in a double side reaction. These reactions result in lower than expected growth rates as well as films with increased porosity and surface roughness. The slightly diminished growth rate observed herein may be attributed to the higher deposition temperature employed. Interestingly, the addition of

TMA and ED into these films results in a significantly higher growth rate. The pure organic films of PDIC-ED have a surface roughness of 0.42 nm and were stable in air for 2 weeks with negligible change in film thickness or film roughness. Conversely, the as-deposited hybrid films of TMA-ED-PDIC had a very low surface roughness of 0.05 nm but a 14% increase in film thickness was observed following exposure to ambient air for two weeks. This film thickness increase was accompanied by an increase to surface roughness up to 1.0 nm. This dramatic change in the film can be attributed to moisture absorption into the film. This is likely driven by conversion of dative Al-N bonded species into Al-O. Previous studies have also displayed a similar increase to film thickness and instability for hybrid MLD films left exposed to air [38], [39].

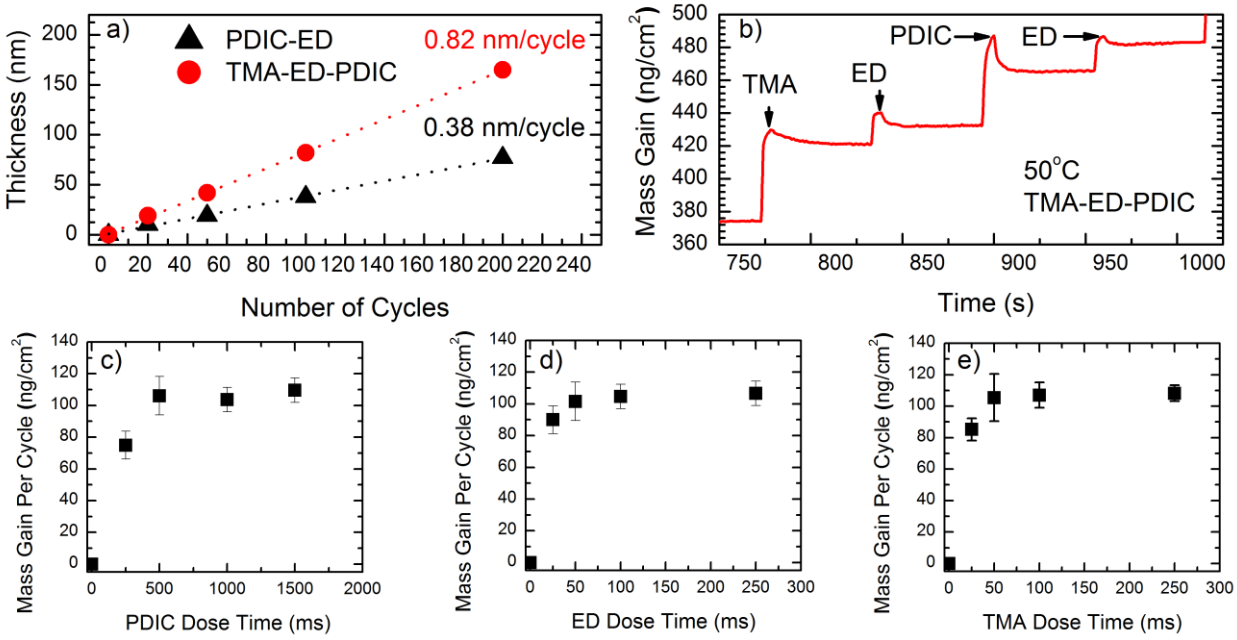


Figure 5.1. *a) Growth rate comparison between PDIC-ED (triangle) and TMA-ED-PDIC (circle) and b) QCM data for one cycle of TMA-ED-PDIC. Saturation conditions for c) PDIC, d) ED, e) TMA.*

To verify MLD growth behavior for TMA-ED-PDIC films, *in-situ* QCM experiments were conducted. As shown in Figure 5.1b, the growth for hybrid polyurea films occurs in a digital, step wise fashion, with a mass gain of ~ 110 ng/cm^2/cycle. A pulse of TMA provides a mass gain of 45 ng/cm^2 while ED and PDIC doses yielded a mass gain of 17 ng/cm^2 and 28 ng/cm^2, respectively. A linear growth rate however does not necessarily imply true MLD characteristics. A key requirement for MLD films is that the precursors react at the surface in a self-limiting fashion.

Furthermore, it is important to consider that hybrid inorganic-organic films grown using TMA by MLD in a three-step ABC reaction have been shown to have a strong dependence on TMA dose and purge times [40]. If too much TMA is left within the growing polymer, film growth characteristics would be significantly affected, resulting in films with increased density and alternate polymeric structures. To test saturation conditions for the hybrid polyurea films, dose times of TMA, ED and PDIC were evaluated. As shown in Figures 5.1c-e, saturation conditions for PDIC, ED and TMA are found after 1 s, 100 ms, and 50 ms, respectively.

FTIR spectroscopy was conducted using 30 nm films deposited on double polished Si (100) wafers. Key peaks are highlighted in Figure 5.2. In particular, characteristic carbonyl urea peaks are observed at 1651 cm^{-1} (amide I) and 1513 cm^{-1} (amide II). Furthermore, free carbonyl groups of the amide I stretch for polyurea blends appear at 1690 cm^{-1} while hydrogen bonded carbonyl groups appear at a slightly lower frequency, somewhere between 1630-1665 cm^{-1} [41]. Similar to findings reported by Loscutoff et al [26], the polyurea films deposited here display well-ordered hydrogen bonding characteristics. Furthermore, the amide I and amide II carbonyl stretching vibrations for TMA-ED-PDIC films is slightly red-shifted compared to peaks presented by PDIC-ED films, suggesting that inter-chain hydrogen bonding is more pronounced in the hybrid polyurea film [41].

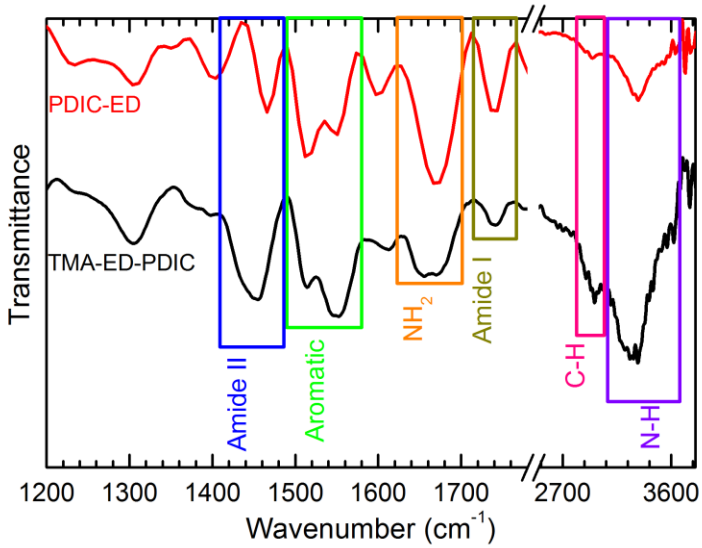


Figure 5.2. *FTIR spectra of PDIC-ED (black) and TMA-ED-PDIC (red) films grown on double polished Si. Characteristic polyurea bonds are outlined.*

In general, the MLD deposition of the pure organic polyurea and mixed inorganic-organic polyurea follow MLD growth characteristics. Interestingly, large growth differences are seen between the hybrid film and the pure organic one. Furthermore, FTIR data indicates that both films display the presence of inter-chain hydrogen bonding, with the hybrid film demonstrating this to a greater degree.

Carbon and nitrogen 1s core level NEXAFS spectra were obtained for both TMA-ED-PDIC and PDIC-ED films, and is presented in Figure 5.3a and 5.3b. The films show a sharp peak at 285.0 eV corresponding to the C1s $\rightarrow 1\pi^*_{C=C}$ transition, originating from the C-H bond in the phenyl group. A weaker peak, centered at 286.2 eV, matches with C1s $\rightarrow 1\pi^*_{C=C}$ transitions, stemming from the ring carbon, bonded to an amide group.[42] This transition is shifted due to electron-withdrawing properties of the amide group, causing the C 1s binding energy of this carbon to be red shifted. This phenomenon is commonly referred to as the "C-R shift" [43]. The peak found at 289.2 eV is attributed to C 1s $\rightarrow 1\pi^*_{C=O}$ transition, while the broad peak at 294.5 eV is assigned to 1s$\rightarrow\sigma^*_{C-C}$ transitions [30]. A weak shoulder can be found at approximately 289 eV, in the region of the C 1s$\rightarrow 1\pi^*_{C=O}$, and corresponds to C 1s$\rightarrow 2\pi^*_{C=C}$ originating from the $b_{2g}\pi^*$ aromatic benzene orbital [42]. This shoulder is slightly more pronounced for PDIC-ED films and may originate from inter-chain oligomer bonding characteristics.

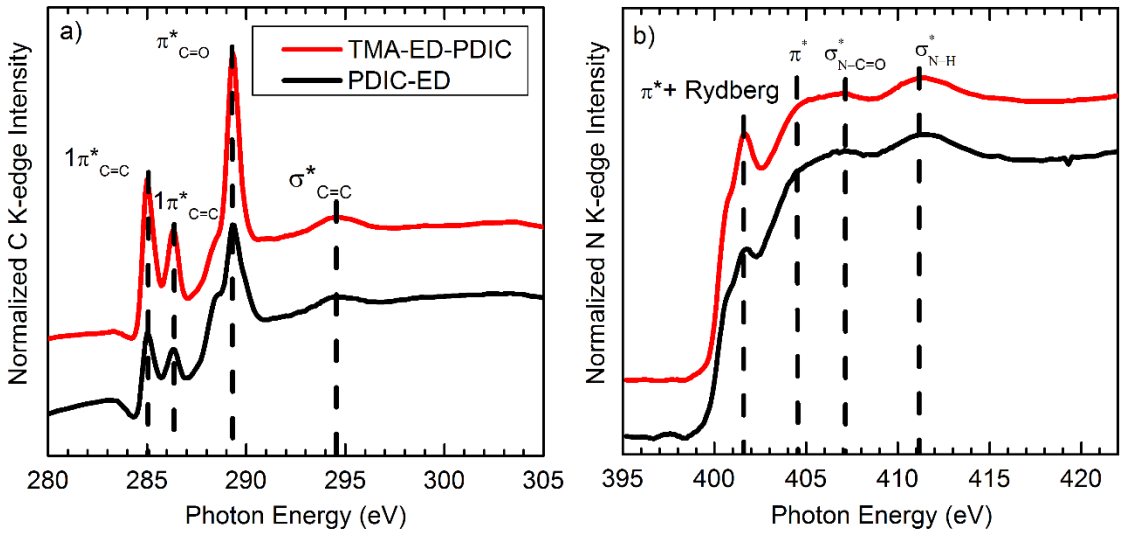


Figure 5.3. *a) C 1s and b) N1s NEXAFS spectra of 25 nm TMA-ED-PDIC and PDIC-ED polymers grown at 50°C acquired using total electron yield.*

Compared to the C 1s spectra, N 1s NEXAFS data can be quite complicated as both Rydberg and orbital transitions are expected to overlap. As pointed out by Urquhart et al [42], the bonding nature of the nitrogen atom is problematical to interrupt due to the high degree of delocalization surrounding the $\pi^*_{C=O}$ orbital. The spectra obtained for PDIC-ED and TMA-ED-PDIC films display a peak at 401.5 eV and is assigned as a mixture of N 1s → π^* and N 1s → 3s Rydberg transition states due to significant delocalization surrounding the $\pi^*_{C=O}$ orbital. [42], [44], [45] This transition from the *s* orbital to an antibonding π one is often characterized as a zwitterionic/ hydroxyimine representations of the structure [46], [47]. The broad band at 411 eV in both spectra is assigned to the 1s → σ^* transition for both σ^*_{C-N} and σ^*_{N-H} orbitals [48]. Based on Extended Huckle Molecular Orbital (EHMO) calculations previously conducted for polyurethanes [42], the shoulder at 404.5 eV is thought to be a high energy π^* orbital located on the phenyl rings. These calculations also predict a strong peak occurring at 408 eV for transitions to $\sigma^*_{N-C=O}$ and/or σ^*_{N-Ph} orbitals, where Ph denotes the phenyl ring. From the results obtained here, it seems that this peak is shifted slightly lower to 407 eV as a result of nonplanar conformations around the nitrogen atom bonded to the phenyl ring, thereby yielding a broad band and high twist angle [42].

Polarization dependent NEXAFS was employed in order to evaluate the molecular orientation of TMA-ED-PDIC and PDIC-ED films. Using this method, developed by Stöhr and Outka [49], the molecular orientation of MLD films can be determined by obtaining total electron yield X-ray absorption data at various incident photon angles. As shown in Figure 5.4a and 5.4b, the two films display very different spectra when comparing their peak intensity with varying angles of X-ray incidence. The purely organic polyurea films (Figure 5.4a) appear to show a slight increase in peak intensity with decreasing incident X-ray angle. NEXAFS polarization data indicates that at a low angle of incidence, the intensity of the π^* transitions reaches a maximum while at higher angles a slight increase to the intensity of σ^*_{N-H} and σ^*_{C-H} transitions occur. This suggests that the PDIC-ED films are oriented parallel with the surface and provides a possible explanation for the lower than expected growth rate obtained for these films. Interestingly, the mixed inorganic-organic films of TMA-ED-PDIC display a pronounced effect with varying angles of X-ray incidence. As shown in Figure 5.4b, a definitive maximum can be observed for the N 1s → π^* and N 1s → 3s Rydberg transition at 401.5 eV at an angle of 15°. An inflection point can

also be observed at approximately 406 eV, where the incoming X-ray energy is high enough to allow transitions of the σ^* orbitals to occur. This also signifies that the TMA-ED-PDIC films are lying parallel to the substrate surface. The data clearly shows that the both films demonstrate angular dependence.

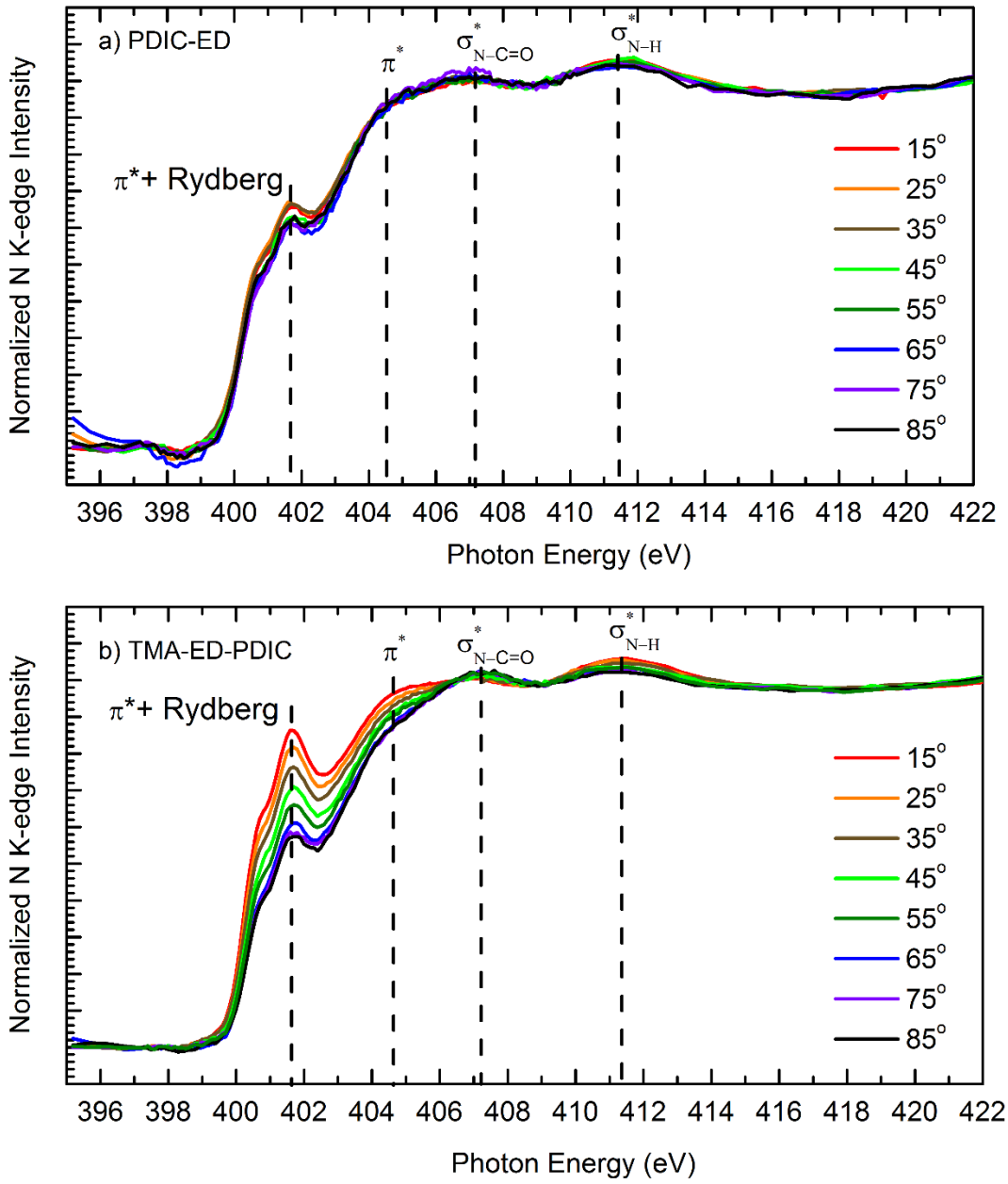


***Figure 5.4**. Polarization dependent NEXAFS data taken at for a) PDIC-ED b) TMA-ED-PDIC.*

Orientation ordering of the MLD films can be derived from the polarization dependent NEXAFS spectra. Given that the experimental cross-section for an orbital transition is proportional to the square of the dot-product of the polarization vector of the incident beam and the orbital vector of the π^* orbital, a statistical average of the contributions toward this excitation from alternate orbital orientations can be calculated. Petrovykh et al [34], established that molecules have a range of tilt angles that can be described by a Gaussian distribution rather than a fixed angle. By assuming that the orbital vectors have a random azimuthal angle (ϕ) in the surface plane, one can then assign a particular tilt to the orbital vector with respect to the surface normal. This preferred tilt angle is given by τ with a distribution of likely tilt angles given by the width, δ. Using this method, the NEXAFS intensity from an orbital transition by an incoming photon source at an incidence angle of θ_i can be modeled as follows:

$$I(\theta_i, \tau, \delta) = \int_0^{2\pi} d\phi \int_0^{\pi} d\omega \, sin(\omega) P(\omega, \tau, \delta) I(\theta_i, \omega, \phi).$$

Where $P(\omega, \tau, \delta)$ is a normalized Gaussian distribution with respect to the unit sphere and $I(\theta_i, \omega, \phi)$ is the cross-section of the orbital intensity given by Stöhr et al [49]:

$$I(\theta_i, \omega, \phi) \propto \left\{\hat{\varepsilon}(\theta_i) \cdot \hat{O}(\omega, \phi)\right\}^2$$

The polarization vector of the photon source is denoted as $\hat{\varepsilon}$ and is a function of the incident angle, θ_i. $\hat{O}$ is defined as the orbital vector given by polar angle ω and azimuthal angle ϕ. Finally, a normalized model using $G(x) = 16^{-x^2}$ as the Gaussian distribution parameter, can be written as:

$$N(\tau, \delta) = \int_0^{2\pi} d\phi \int_0^{\pi} dx \, sin(x) G\left(\frac{x - \tau}{\delta}\right).$$

Using the experimental polarization dependent NEXAFS data obtained, an intensity modulation amplitude value, A_π, can be determined by calculating the intensity difference between the resonance at a grazing incidence angle and normal incidence angle, $I\left(\frac{\pi}{2}, \omega, \phi\right) - I(0, \omega, \phi)$. This value reflects the molecular orientation order as opposed to a set tilt angle [34], [50], [51]. Intensity of the N 1s → π^* and N 1s → 3s Rydberg transition at 401.5 eV as a function of incidence angle is given in Figure 5.5a. This analysis reveals that the degree of ordering between the two

films is vastly different. Solutions for τ and δ at the calculated A_π for TMA-ED-PDIC and PDIC-ED films are given in Figure 5.5b and a schematic representation of this analysis is shown in Figure 5.5c. Clearly the range of possible tilt angles for the purely organic film is much larger than the hybrid inorganic-organic film, indicating that the hybrid film is well ordered in nature. "The lower than expected growth rate for pure polyurea films may be attributed to a larger average angle of orientation. This conclusion can be drawn by looking at the range of solution possible for each system, which is given in Figure 5.5b. Given the large number of possible solution for the PDIC-ED system, the chance of double side reactions is increased. Furthermore, the decreased A_π value found for the pure organic system is indicative of decreased long-range order, thus providing increased probability for double side reactions to occur, and therefore decreasing the growth rate of the film.

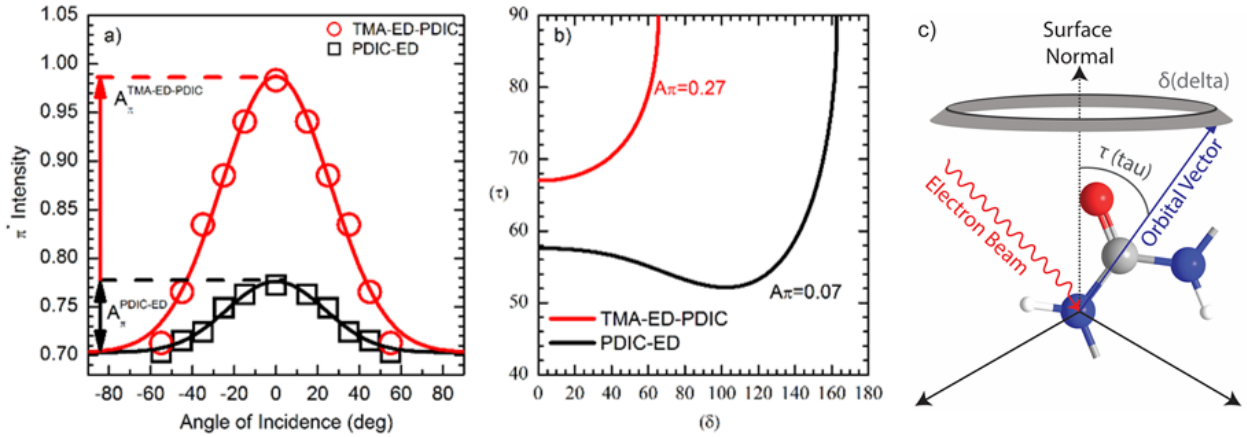


Figure 5.5. *Interpretation of NEXAFS orientation signatures for disordered films. (a) Polarization dependence of the π* bond with fits using the model with fixed tilt angle. Using a model assuming that π* orbitals have random azimuthal orientation and Gaussian distribution of tilt angles with an average tilt τ. The width of this distribution, serves as an orientation disorder parameter. The smaller δ is the more ordered the system is. (b) Solutions to τ and δ using A_π values for TMA-ED-PDIC and ED-PDIC. (c) Schematic diagram outlining the significance of τ and δ values.*

Additionally, the maximum possible value of δ, δ_{max}, is independent of tilt angle and a reflection of the range of δ, thus providing a degree of disorder in the system [50]. The larger the value of δ_{max} the more disordered the system. Organic polyurea films of PDIC-ED displays a δ_{max} value of 160° while the mixed inorganic-organic polyurea TMA-ED-PDIC MLD film shows a δ_{max} value of only 64°, representing a high degree of ordering within the film.

Figure 5.6 illustrates the proposed film characteristics of hybrid polyurea films and organic polyurea films. The figure depicts how organic polyurea films have a large degree of variation with increasing number of polyurea chains but the hybrid polyurea films grow in an ordered manner. This increased amount of ordering must be a related to the addition of TMA into the matrix of the polymer film. Furthermore, a higher degree of ordering may be present due to an increased amount of hydrogen bonding occurring within polymer chains, as observed by FTIR data. Film growth data obtained by XRR also indicates a growth rate nearly double for the mixed inorganic-organic film versus the organic one. This high degree of ordering may be a contributing factor for the higher than expected growth rate. It is also possible that the datively bonded complex formed by TMA and ED locks the addition of PDIC-ED into a fixed configuration, thereby significantly reducing the range of tilt angles possible and reducing the chance of double side reactions occurring. This radical change in geometry suggests that the interaction between polymer chains (hydrogen bonding) and within the polymer chain (dative bonding complexes) can significantly influence the degree of ordering in MLD films. Many other MLD films suffer from double side reactions resulting in consumption of reactive sites as well as blocking, thereby resulting in low packing density and increased porosity [10], [11], [40], [52]. Given the high degree of ordering found in the inorganic-organic TMA-ED-PDIC film, a high packing density is predominant and suggests a decrease in the number of double side reactions occurring.

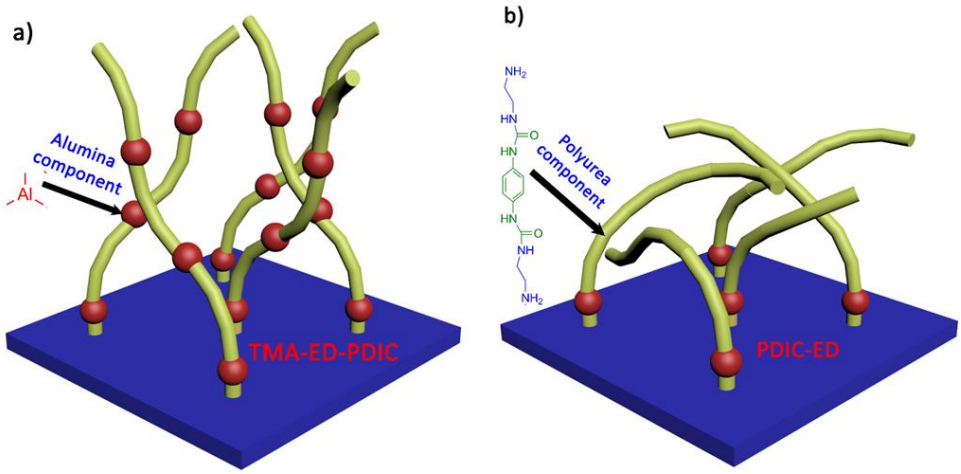


Figure 5.6. *Depiction of structural morphology of (a) hybrid inorganic-organic polyurea films and (b) pure organic polyurea films.*

5.4 Conclusions

A novel inorganic-organic polyurea film was synthesized by MLD and its growth characteristics were investigated by *in-situ* QCM. Polarization dependent NEXAFS spectroscopy was employed to determine the difference in alignment of the pure organic polyurea molecular chains and mixed inorganic-organic polyurea chains. Both films demonstrated significant tilting away from the surface normal. However, an in-depth analysis revealed that the mixed inorganic-organic films display a much higher degree of molecular ordering compared to the purely organic polyurea films. This work demonstrates that the molecular orientation of polymer films can be tailored by controlling the precursors used in the MLD process. Given the wide application of polyurea films, the hybrid film produced here may find advantageous application where flexibility and strength must be carefully balanced. These include coatings for materials that experience large volume expansion such as silicon or lithium metal in lithium ion batteries. Furthermore, such coatings may be used to functionalize the surface of nanocarbon materials, imparting enhanced mechanical strength and the ability to graft additional constituents. The findings outlined here pave a platform toward designing organic and inorganic/organic films with desirable properties, such as packing density, film orientation, and thin film ordering.

Acknowledgments: This research was supported by the Natural Science and Engineering Research Council of Canada (NSERC), Canada Research Chair Program (CRC), Canada Foundations for Innovation (CFI), Ontario Research Fund, and the University of Western Ontario. The Advanced Lights Source (ALS) is supported by the Office of Basic Energy Sciences under U.S. Department of Energy Contract DEAC02-05CH11231. Financial support for Andrew Lushington was also provided by the Michael Smith Foreign Study supplement as well as NSERC's Canada Graduate Scholarship program. Dr. Jian Liu is grateful for the funding support from NSERC Postdoctoral Fellowship (PDF) program.

5.5 References

[1] R. L. Puurunen, "Surface chemistry of atomic layer deposition: A case study for the trimethylaluminum/water process," *J. Appl. Phys.*, vol. 97, no. 12, 2005.

[2] F. Zaera, "The surface chemistry of thin film atomic layer deposition (ALD) processes for electronic device manufacturing," *J. Mater. Chem.*, vol. 18, no. 30, p. 3521, 2008.

[3] S. Sun *et al.*, "Single-atom Catalysis Using Pt/Graphene Achieved through Atomic Layer Deposition," *Sci. Rep.*, vol. 3, no. 1, p. 1775, 2013.

[4] K. Park, Q. Zhang, B. B. Garcia, X. Zhou, Y. H. Jeong, and C. Cao, "Effect of an ultrathin TiO2 layer coated on submicrometer-sized ZnO nanocrystallite aggregates by atomic layer deposition on the performance of dye-sensitized solar cells," *Adv. Mater.*, vol. 22, no. 21, pp. 2329–2332, 2010.

[5] J. Liu and X. Sun, "Elegant design of electrode and electrode/electrolyte interface in lithium-ion batteries by atomic layer deposition," *Nanotechnology*, vol. 26, no. 2, p. 24001, 2015.

[6] V. Miikkulainen, M. Leskelä, M. Ritala, and R. L. Puurunen, "Crystallinity of inorganic films grown by atomic layer deposition: Overview and general trends," *J. Appl. Phys.*, vol. 113, no. 2, 2013.

[7] H. Zhou, M. F. Toney, and S. F. Bent, "Cross-linked ultrathin polyurea films via molecular layer deposition," *Macromolecules*, vol. 46, no. 14, pp. 5638–5643, 2013.

[8] Y. Du and S. M. George, "Molecular Layer Deposition of Nylon 66 Films Examined Using in Situ FTIR Spectroscopy," *J. Phys. Chem. C*, vol. 111, no. 24, pp. 8509–8517, 2007.

[9] N. M. Adamczyk, a. a. Dameron, and S. M. George, "Molecular Layer Deposition of Poly(p -phenylene terephthalamide) Films Using Terephthaloyl Chloride and p - Phenylenediamine," *Langmuir*, vol. 24, no. 5, pp. 2081–2089, 2008.

[10] B. Gong, Q. Peng, and G. N. Parsons, "Conformal organic-inorganic hybrid network polymer thin films by molecular layer deposition using trimethylaluminum and glycidol," *J. Phys. Chem. B*, vol. 115, no. 19, pp. 5930–5938, 2011.

[11] Q. Peng, B. Gong, R. M. VanGundy, and G. N. Parsons, "'Zincone' zinc oxide - Organic hybrid polymer thin films formed by molecular layer deposition," *Chem. Mater.*, vol. 21, no. 5, pp. 820–830, 2009.

[12] J. Liu *et al.*, "Ultralow thermal conductivity of atomic/molecular layer-deposited hybrid organic-inorganic zincone thin films," *Nano Lett.*, vol. 13, no. 11, pp. 5594–5599, 2013.

[13] B. Yoon, D. Seghete, A. S. Cavanagh, and S. M. George, "Molecular layer deposition of hybrid organic - Inorganic alucone polymer films using a three-step abc reaction sequence," *Chem. Mater.*, vol. 21, no. 22, pp. 5365–5374, 2009.

[14] A. I. Abdulagatov, R. A. Hall, J. L. Sutherland, B. H. Lee, A. S. Cavanagh, and S. M. George, "Molecular layer deposition of titanicone films using TiCl 4 and ethylene glycol or

glycerol: Growth and properties," *Chem. Mater.*, vol. 24, no. 15, pp. 2854–2863, 2012.

[15] A. I. Abdulagatov, K. E. Terauds, J. J. Travis, A. S. Cavanagh, R. Raj, and S. M. George, "Pyrolysis of Titanicone Molecular Layer Deposition Films as Precursors for Conducting TiO 2 / Carbon Composite Films," *J. Phys. Chem. C*, vol. 117, pp. 17442–17450, 2013.

[16] A. Lushington *et al.*, "A novel approach in controlling the conductivity of thin films using molecular layer deposition," *Appl. Surf. Sci.*, vol. 357, pp. 1319–1324, 2015.

[17] B. H. Lee, B. Yoon, V. R. Anderson, and S. M. George, "Alucone Alloys with Tunable Properties Using Alucone Molecular Layer Deposition and Al2O3 Atomic Layer Deposition," *J. Phys. Chem. C*, vol. 116, no. 5, pp. 3250–3257, 2012.

[18] C. Kao, B. Li, Y. Lu, J. Yoo, and A. J. Epstein, "Thin films of organic-based magnetic materials of vanadium and cobalt tetracyanoethylene by molecular layer deposition," *J. Mater. Chem. C*, vol. 2, no. 30, p. 6171, 2014.

[19] C. Prasittichai, H. Zhou, and S. F. Bent, "Area selective molecular layer deposition of polyurea films," *ACS Appl. Mater. Interfaces*, vol. 5, no. 24, pp. 13391–13396, 2013.

[20] S. Giraud *et al.*, "Flame retarded polyurea with microencapsulated ammonium phosphate for textile coating," *Polym. Degrad. Stab.*, vol. 88, no. 1, pp. 106–113, 2005.

[21] D. Mohotti, T. Ngo, S. N. Raman, M. Ali, and P. Mendis, "Plastic deformation of polyurea coated composite aluminium plates subjected to low velocity impact," *Mater. Des.*, vol. 56, pp. 696–713, 2014.

[22] N. Agnihotri, R. Mishra, C. Goda, and M. Arora, "Microencapsulation – A Novel Approach in Drug Delivery : A Review," *J. Pharm. Sci.*, vol. 2, no. 1, pp. 1–20, 2012.

[23] A. Rekondo, R. Martin, A. Ruiz de Luzuriaga, G. Cabañero, H. J. Grande, and I. Odriozola, "Catalyst-free room-temperature self-healing elastomers based on aromatic disulfide metathesis," *Mater. Horizons*, vol. 1, no. 2, pp. 237–240, 2014.

[24] C. Wang, H. Wu, Z. Chen, M. T. McDowell, Y. Cui, and Z. Bao, "Self-healing chemistry enables the stable operation of silicon microparticle anodes for high-energy lithium-ion batteries," *Nat. Chem.*, vol. 5, no. 12, pp. 1042–1048, 2013.

[25] A. Kim, M. A. Filler, S. Kim, and S. F. Bent, "Layer-by-layer growth on Ge(100) via spontaneous urea coupling reactions," *J. Am. Chem. Soc.*, vol. 127, no. 16, pp. 6123–6132, 2005.

[26] P. W. Loscutoff, H. Zhou, S. B. Clendenning, and S. F. Bent, "Formation of Organic Nanoscale Layer Deposition," *ACS Nano*, vol. 4, no. 1, pp. 331–341, 2010.

[27] H. Zhou and S. F. Bent, "Molecular layer deposition of functional thin films for advanced lithographic patterning," *ACS Appl. Mater. Interfaces*, vol. 3, no. 2, pp. 505–511, 2011.

[28] P. Sundberg and M. Karppinen, "Organic and inorganic-organic thin film structures by molecular layer deposition: A review," *Beilstein J. Nanotechnol.*, vol. 5, no. 1, pp. 1104–1136, 2014.

[29] S. E. Atanasov *et al.*, "Highly conductive and conformal poly(3,4-ethylenedioxythiophene)

(PEDOT) thin films via oxidative molecular layer deposition," *Chem. Mater.*, vol. 26, no. 11, pp. 3471–3478, 2014.

[30] Q. Peng, K. Efimenko, J. Genzer, and G. N. Parsons, "Oligomer orientation in vapor-molecular-layer-deposited alkyl-aromatic polyamide films," *Langmuir*, vol. 28, no. 28, pp. 10464–10470, 2012.

[31] P. W. Loscutoff, H. B. R. Lee, and S. F. Bent, "Deposition of ultrathin polythiourea films by molecular layer deposition," *Chem. Mater.*, vol. 22, no. 19, pp. 5563–5569, 2010.

[32] J. Weber, A. Beier, E. Hasselbrink, and T. Balgar, "Thermally induced conformational changes of Ca-arachidate Langmuir-Blodgett Films at different compression," *J. Chem. Phys.*, vol. 141, no. 4, p. 44912, 2014.

[33] J. Genzer *et al.*, "Orientation of semifluorinated alkanes attached to polymers at the surface of polymer films," *Macromolecules*, vol. 33, no. 5, pp. 1882–1887, 2000.

[34] D. Y. Petrovykh *et al.*, "Nucleobase orientation and ordering in films of single-stranded DNA on gold," *J. Am. Chem. Soc.*, vol. 128, no. 1, pp. 2–3, 2006.

[35] Y. Xu and C. B. Musgrave, "A DFT Study of the Al2O3 Atomic Layer Deposition on SAMs: Effect of SAM Termination," *Chem. Mater.*, vol. 16, no. 4, pp. 646–653, 2004.

[36] A. Räupke *et al.*, "Conformal and highly luminescent monolayers of Alq3 prepared by gas-phase molecular layer deposition," *ACS Appl. Mater. Interfaces*, vol. 6, pp. 1193–1199, 2014.

[37] V. Holy, T. Baumbach, and M. Bessiere, "Interface roughness in surface-sensitive X-ray methods," *J. Phys. D. Appl. Phys.*, vol. 28, no. 1945, pp. A220–A226, 1995.

[38] P. Sundberg, A. Sood, X. Liu, L.-S. Johansson, and M. Karppinen, "Atomic/molecular layer deposited thin-film alloys of Ti-4,4′-oxydianiline hybrid–TiO2 with tunable properties," *Dalton Trans.*, vol. 41, pp. 10731–10739, 2012.

[39] W. Zhou, J. Leem, I. Park, Y. Li, Z. Jin, and Y.-S. Min, "Charge trapping behavior in organic–inorganic alloy films grown by molecular layer deposition from trimethylaluminum, p-phenylenediamine and water," *J. Mater. Chem.*, vol. 22, no. 45, p. 23935, 2012.

[40] D. Seghete, R. A. Hall, B. Yoon, and S. M. George, "Importance of trimethylaluminum diffusion in three-step ABC molecular layer deposition using trimethylaluminum, ethanolamine, and maleic anhydride," *Langmuir*, vol. 26, no. 24, pp. 19045–19051, 2010.

[41] J. Mattia and P. Painter, "A comparison of hydrogen bonding and order in a polyurethane and poly(urethane-urea) and their blends with poly(ethylene glycol)," *Macromolecules*, vol. 40, pp. 1546–1554, 2007.

[42] S. G. Urquhart, A. P. Hitchcock, R. D. Priester, and E. G. Rightor, "Analysis of polyurethanes using core excitation spectroscopy. Part II: Inner shell spectra of ether, urea and carbamate model compounds," *J. Polym. Sci. Part B Polym. Phys.*, vol. 33, no. 11, pp. 1603–1620, 1995.

[43] R. R. Cooney and S. G. Urquhart, “Chemical Trends in the Near-Edge X-ray Absorption Fine Structure of Monosubstituted and Para-Bisubstituted Benzenes,” *J. Phys. Chem. B*, vol. 108, no. 47, pp. 18185–18191, 2004.

[44] I. Ishii and a. P. Hitchcock, “A quantitative experimental study of the core excited electronic states of formamide, formic acid, and formyl fluoride,” *J. Chem. Phys.*, vol. 87, no. 2, p. 830, 1987.

[45] P. Leinweber *et al.*, “Nitrogen K-edge XANES - An overview of reference compounds used to identify ‘unknown’ organic nitrogen in environmental samples,” *J. Synchrotron Radiat.*, vol. 14, no. 6, pp. 500–511, 2007.

[46] K. Oichi *et al.*, “No Title,” *Phot. Fact. Rep.*, p. 282, 1992.

[47] E. Otero and S. G. Urquhart, “Nitrogen 1s near-edge X-ray absorption fine structure spectroscopy of amino acids: Resolving zwitterionic effects,” *J. Phys. Chem. A*, vol. 110, no. 44, pp. 12121–12128, 2006.

[48] S. G. Urquhart *et al.*, “NEXAFS spectromicroscopy of polymers: overview and quantitative analysis of polyurethane polymers,” *J. Electron Spectros. Relat. Phenomena*, vol. 100, no. 1–3, pp. 119–135, 1999.

[49] J. Stöhr and D. A. Outka, “Determination of molecular orientations on surfaces from the angular dependence of near-edge x-ray-absorption fine-structure spectra,” *Phys. Rev. B*, vol. 36, no. 15, pp. 7891–7905, 1987.

[50] L. Wang, D. Qi, L. Liu, S. Chen, X. Gao, and A. T. S. Wee, “Molecular Orientation and Ordering during Initial Growth of Copper Phthalocyanine on Si(111),” *J. Phys. Chem. C*, vol. 111, no. 8, pp. 3454–3458, 2007.

[51] N. Ballav, P. Koelsch, and M. Zharnlkov, “Orientation and ordering in monomolecular films of sulfur-modified homo-oligonucleotides on gold,” *J. Phys. Chem. C*, vol. 113, no. 42, pp. 18312–18320, 2009.

[52] B. H. Lee, B. Yoon, A. I. Abdulagatov, R. A. Hall, and S. M. George, “Growth and properties of hybrid organic-inorganic metalcone films using molecular layer deposition techniques,” *Adv. Funct. Mater.*, vol. 23, no. 5, pp. 532–546, 2013.

6

Single-Atom and Clusters to Nanoparticles: Controlling the Nucleation of Pt Through Regulated Gas Phase Chemisorption*

To reduce the usage of expensive noble metals, research into the development and application of single-atom catalysts has recently gained much attention. In this study, we investigate the ability to deposit Pt as single-atoms and clusters on nitrogen doped carbon nanotubes (NCNTs) and pristine carbon nanotubes (PCNTs) through the use of atomic layer deposition (ALD). Our unique approach here, is to expose NCNTs and PCNTs to varying exposures of trimethyl(methylcyclopentadienyl)-platinum without the use of an oxidizing pulse, at various temperatures, to determine the self-limiting characteristics of this precursor. By omitting an oxidizing step, we aim to stabilize single-atoms of Pt on the substrates' surface by using the existing precursor ligands. Through a 1-minute exposure of the Pt precursor at 250°C, we were able to primarily obtain single-atoms and ultra-small clusters of Pt on NCNTs. However, the same conditions yielded very different results for PCNTs. Our investigation demonstrates the conditions necessary to deposit single-atoms and ultra-small clusters of Pt on a NCNT substrate, and outlines the parameters that influence this process.

*A version of this chapter is currently being written for publication

6.1 Introduction

Supported nanocatalysts have been widely studied due to their high activity for various chemical reactions. An important aspect that dictates the catalytic performance of nanocatalysts is their size [1]. To achieve favorable catalytic activity, controlling particle size is highly important. Noble metals, such as Pt, Pd, Ru, Rh, and Ir, are catalysts that are ubiquitously used across several different industries. However, due to the high price and low natural abundance of these noble metals, their use must be limited and carefully engineered. Minimizing the use of such expensive catalysts, while retaining their desired catalytic activity, has been a research topic of interest for several decades [2]–[4]. Downsizing of noble metals to clusters, or even single-atoms, is one effective method in maximizing atom efficiency. The unique catalytic properties of single-atom catalysts have attracted a great deal of attention due to their distinct behavior from metal nanoparticles (NPs) [5]–[7]. At this small scale, the characteristics of single-atoms – such as low coordination environment, quantum size effects, and metal-support interaction - are starkly different from their nanometer or sub-nanometer counterparts. This enables single-atom catalysts to possess extraordinary catalytic activity and selectivity [8]–[11]. However, the stability of single-atom catalysts is an important aspect that has not yet been fully realized and research into this issue remains in its infancy. Nobel metal atoms tend to aggregate and form clusters. This behavior undermines the potential catalytic application of single-atom particles. Furthermore, the electronic structural differences between single-atom Pt and clusters is an issue that still needs to be addressed.

Pt-based catalysts are of great importance in the field of fuel cells and are generally considered to be the most effective electrocatalysts for the hydrogen evolution reaction (HER) [11], [12]. However, Pt is expensive and scarce, thereby limiting its commercial potential. Therefore, it is very important to decrease the loading of Pt while simultaneously increasing utilization efficiency. Reducing the size of Pt NPs to clusters, or even single-atoms, could significantly decrease noble metal usage and provides a promising avenue toward developing cheap and efficient fuel cell electrodes. Previous reports have demonstrated that single Pt atoms dispersed on an FeO_x surface have enhanced catalytic activity for CO oxidation compared to their larger Pt NP counterparts [13]. Furthermore, single-atom catalysts of Pt have also been shown to

significantly improve the catalytic activity of methanol oxidation compared to commercial carbon-supported Pt catalysts [14].

Atomic layer deposition (ALD) is a thin film deposition technique that is gaining increasing attention for the growth of noble metals due to its ability to deposit very small particles uniformly over high aspect ratio structures [15]. Our group demonstrated the deposition of single-atom Pt by ALD on graphene; however, this investigation yielded a mixture of single-atoms, clusters and NPs [14]. Here we report the deposition conditions necessary to primarily achieve single-atom Pt catalysts. Typically, deposition of noble metals by ALD consists of exposing the substrate to an organometallic precursor, in this case trimethyl(methylcyclopentadienyl)-platinum (IV) ($MeCpPtMe_3$), followed by an oxidizing pulse. This process is dependent on two events occurring: (1) the adsorption of $MeCpPtMe_3$, and (2) the removal of the precursor ligands by either oxygen, ozone, hydrogen, or plasma treatment [16]–[19]. However, this seemingly simple process encompasses numerous intricate reaction mechanisms such as combustion and hydrogenation/dehydrogenation [20]. As a result, experimental probing techniques have been employed to provide clarification toward the underlying ALD mechanism. These techniques include Fourier transform infrared spectroscopy [21], photoemission spectroscopy [22], X-ray absorption near edge spectroscopy (XANES) [23], and quadrupole mass spectrometry [24], to name a few. Although there exists a great deal of literature on the deposition of Pt NPs by ALD, the results vary drastically, with radial growth rates of Pt NPs ranging from 0.20 nm/cycle to 0.85nm/cycle [25], [26]. A detailed comparison of the published results reveals a complicated range of interactions that influence Pt NP nucleation and growth, such as substrate dopant species, Pt precursor dosing times, and decomposition rates. Additionally, mechanistic studies have indicated that the combustion of the remaining organic ligands attached to adsorbed $MeCpPtMe_3$ is dependent on temperature, as well as the partial pressure of the oxidizers [20], [27]–[29].

Our unique approach here is to utilize the existing ligands attached to the Pt precursor to stabilize and anchor single Pt atoms to the surface. It has been suggested in literature, that long Pt deposition times could lead to steric hinderance between the adsorbed Pt molecules, thus preventing agglomeration and promoting a decreased growth rate [30]. To achieve this, we omit any oxidizing pulse following the initial exposure of $MeCpPtMe_3$. Rather, we perform a single exposure of the organometallic precursor for varying lengths of time to determine the self-limiting

surface saturation conditions. To highlight the importance of substrate, we perform and compare the deposition of Pt on both nitrogen doped multiwalled carbon nanotubes (NCNTs) and pristine multiwalled carbon nanotubes (PCNTs). Both substrates are ideal for potential use in fuel cell application due to their high surface area and excellent conductivity as well as the π and surface defect states that interact with Pt. By exposing the substrates to deposition conditions that vary in dosing time and temperature, we demonstrate the ability to control the Pt particle size through self-limiting reactions, from single-atoms and small clusters to NPs. We will also discuss influential factors that provide an avenue toward controlling the self-limiting decomposition of $MeCpPtMe_3$ on NCNT and PCNT surfaces.

6.2 Experimental Details

Substrate preparation: PCNTs (MRCMW10) were purchased from MER Corporation and used as received. Synthesis of NCNTs was performed by using spray pyrolysis chemical vapor deposition (SPCVD) method. A quartz tube, with an aluminum crucible, was placed in the middle of the tube and purged with Ar (500 sccm) for 15 min to produce an inert atmosphere and placed in a tube furnace heated up to 850°C. A solution containing 2 g of imidazole and 0.2 g of ferrocene in 10 mL of acetonitrile was introduced into the tube with the aid of an ultrasonic probe sonicator at a flow rate of 250 uL/min for 10 min. The tube was then allowed to cool to room temperature and NCNTs are removed from the aluminum crucible. Obtained NCNTs were then refluxed in nitric acid (HNO_3) (70%) for 12 h at 90°C to remove any leftover catalyst. Following this, NCNTs were placed back in an inert quartz tube in a tube furnace set to 800°C to re-graphitize the surface. For ALD deposition, both PCNTs and NCNTs were well-dispersed in ethanol, and the mixture solution was dropped onto aluminum foil. Evaporation of ethanol resulted in a porous carbon nanotube network to allow for maximum exposure of precursor during the ALD process.

Deposition conditions and loading analysis: Pt was deposited on PCNT and NCNT substrate by ALD (Savannah 100, Cambridge nanotechnology Inc., USA) using trimethyl(methylcyclopentadienyl)-platinum (IV) ($MeCpPtMe_3$) as a precursor. High purity N_2 (99.999%) was used as both a purging and carrier gas. $MeCpPtMe_3$ was held in an external reservoir kept at 65°C to provide a steady exposure of Pt precursor. Gas lines were held at 100°C to avoid precursor condensation. Since ALD valves can only be opened for 30 s at a time, a 1-

minute exposure of Pt precursor consisted of two 30s pulses separated by a 10s purge. The same routine was applied for 30 minutes and 60 minute exposures of $MeCpPtMe_3$. Pt loading was analyzed using an inductively coupled plasma optical emission spectrometer (ICP-AES) with samples dissolved in hot fresh aqua regia overnight and filtered.

Transmission electron microscopy: TEM samples were prepared by drop casting an ultrasonicated solution of dilute high-performance liquid chromatography grade methanol solution with the sample of interest onto a lacey carbon grid. Generally, two samples were prepared, in which one was baked at 100°C overnight and the other was left to dry in air. Whenever possible, the non-baked sample was used, and only in cases of high beam contamination that prevented the ability to image the Pt atoms was the baked sample used for imaging. High resolution images were acquired using an FEI Titan 80-300 Cubed TEM. Aberration correction was tuned to minimize spherical aberration in the probe forming lens and the acceleration voltage was set to 80 kV. STEM imaging was performed using HAADF (detector semi-angles of 63.8 mrad to 200 mrad) conditions with a C2 aperture of 50 μm. Varying exposure times were used for each given sample with a beam current of approximately 50 pA. EELS spectra were acquired to examine the quality of the NCNTs and were acquired in an energy filtered STEM (EFSTEM) mode with a dispersion of 0.4 eV/pixel and a convergence and collection semi-angle of 19 mrad and 55 mrad, respectively. Relatively fast acquisition times are preferred to decrease the amount of sample drift and beam interaction with the Pt atoms. The Pt spectrum image was acquired using an exposure time of 0.1 s/pixel.

Auger spectroscopy: Auger spectroscopy was also utilized to quantify the elemental content in the NCNTs. The spectroscopy was completed using a JEOL JAMP-9500F field emission-Auger microprobe with an energy of 10 kV, a current of 40 nA, a tilt of 30°, and used in M4 mode. The reported values from the quantification were normalized with respect to the total elemental content; however, beam contamination was an issue, therefore the concentrations of all elements, with exception of carbon, may be slightly underestimated. Quantification was completed using an in-house standard sample of highly oriented pyrolytic graphic from a freshly cleaved surface. Cr_2N, SiO_2, NaCl, ZnS, CaF_2 JEOL supplied standards for the C-KLL, N-KLL, O-KLL, Cl-LVV, S-LLV, Ca-LMM Auger electrons, respectively. The values reported are averages acquired from a minimum of nine measurements on NCNT bundles, and the reported error is the sample standard

deviation. Samples were prepared by drop casting suspended samples in HPLC methanol onto an SiO_2 wafer with an Au sputter coated surface.

X-ray Absorption Spectroscopy: XANES measurements of the Pt L3- edge were conducted on the 061D superconducting wiggler at the hard X-ray microanalysis beamline at the Canadian Light Source. Each sample spectra was collected using fluorescence yield mode with a solid-state detector. High purity Pt and PtO_2 metal foil was collected in transmission mode for comparison and monochromatic energy calibration. Analysis of XANES and EXAFS data was performed using the ATEHNA and ARTEMIS software package, respectively.

6.3 Results and Discussion

Figure 6.1 (a-c) displays high angle annular dark field scanning transmission electron microscopy (HAADF-STEM) images of NCNTs exposed to $MeCpPtMe_3$ for varying dosing times at 250°C. Based on the approximate Z^2 image contrast of the HAADF technique, a distribution of bright spots, corresponding to Pt atoms, can be found on the surface of the NCNTs. Particle size distribution (PSD) histograms for varying dosing times are shown in Figure 6.1 (d) (measurement and calculation details can be found in the supporting information). Interestingly, all pulse times, from 1 minute to 60 minutes, demonstrate some fraction of Pt particles in the single-atom and small cluster region, as seen in bins assigned to 0.2 and 0.4 nm. However, increasing the dosing time resulted in a PSD that is right-skewed compared to the relatively narrow distribution observed for the 1 minute sample. Furthermore, as expected, increased dosing time was accompanied with an increase in Pt loading (Table 6.1, ICP analysis). Current published literature, suggests that Pt NP growth during ALD occurs via combustion of organic ligands during exposure to an oxidant [27], [28]. Contrarily, our results suggest that NP growth can occur without an oxygen step, insinuating a more complicated self-limiting growth mechanism. Ideally in ALD, a self-limiting reaction is described as a gas-solid reaction where atoms, which are included in ALD growth, are adsorbed on the surface and those that are not are removed as by-products. Furthermore, it also describes a reaction in which saturation of surface sites can be reached and excess precursor does not further react with products on the surface or in the gas phase. However, the parameters that influence whether a reaction is self-limiting or self-terminating are numerous. It is a process that is dependent on adsorption kinetics, mechanisms related to precursor chemisorption, surface chemistry, temperature and film growth mode [31]. As pointed out by Takakusagi et al [32],

decomposition of $MeCpPtMe_3$ may occur on a chemically active surface that contains coordinatively unsaturated adatoms. Furthermore, once a small Pt cluster is formed on the surface, further decomposition of supplied $MeCpPtMe_3$ precursor may occur readily [33]. The narrow PSD observed for the 1 minute dosing time suggests that the Pt precursor is initially pinned to a surface site. Prolonged dosing times result in larger NP sizes (Table 6.1), suggesting the removal of precursor ligands and NP growth through means other than combustion via oxygen. The formation of numerous larger Pt clusters and NPs, observed in the HAADF-STEM images presented in Figure 6.1, suggests that the Pt particles are mobile during deposition with an abundance of nucleation sites on the substrate. Interestingly, Pt exposure times of 30 minutes and 60 minutes result in a similar PSD, suggesting saturation of adsorption sites prior to or following the 30 minute Pt precursor dosing. Pt densities were calculated from the processed images and are presented in the supporting information. Particle density was acquired from Pt located in the center of the NCNTs (see supporting information for measurement details). It should be noted that these values should be interpreted as approximations, since the number of images analyzed varied from two to five for each individual sample and are based on the images acquired using HAADF. Nevertheless, the densities provide complimentary information to the PSD histograms. It can be noted from Table 6.1 that the 60 minute dosing time resulted in a lower density of Pt when considering the counts/nm^2 with respect to the 30 minute exposure, but a higher density when examining the area/nm^2. This further supports the observation of Pt growth observed in the PSD when comparing the 60 minute to 30 minute samples. Essentially the number of nucleation sites remains the same, or decreases (when considering the error), when the exposure time was prolonged, but the relative size of the particles increased. Considering the Pt density and loading (ICP data in Table 6.1), and the increase in the fractional frequency for larger sized particles with increasing dosing time, suggests that after the adsorption sites are saturated, continued growth of Pt occurs through coalesce, adatom diffusion, or reactions with gaseous precursor. These results are confirmed when examining Pt deposited at 250°C on PCNTs and Pt deposited at 100°C on NCNTs for dosing times of 1 minute and 30 minutes. In each case, a right-skewed shift in the PSD (Figure 6.3 (d) and

Figure S6.5) was observed with an increase in particle size, Pt loading, and density (Table 6.1) as the dosing time increased.

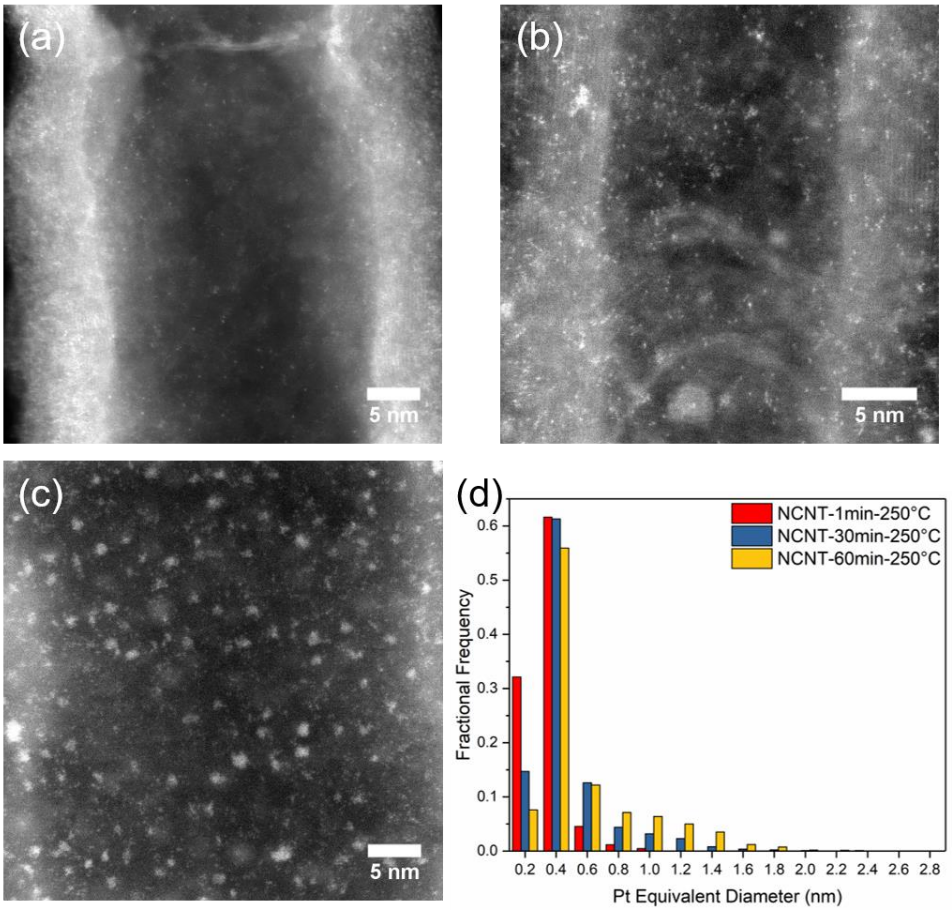


Figure 6.1. *HAADF-STEM images of ALD Pt deposition on NCNTs at 250°C using a dosing time of (a) 1 minute, (b) 30 minutes, and (c) 60 minutes. Experimental (d) PSD histograms were acquired from six different NCNTs for each sample. Image quantification steps and raw/processed images can be found in the supporting information.*

To determine the influence of temperature on the deposition conditions required to deposit single Pt atoms, a 1 minute dosing time was introduced to the chamber at 100°C, 175°C, and 250°C. The PSD for this experiment is shown in Figure 6.2 (a). Regardless of temperature, a 1 minute dosing time on the NCNTs produced a very narrow PSD with approximately equivalent average particle sizes (Table 6.1). Typically, growth of Pt by ALD is temperature dependent with significantly inhibited growth for substrate temperatures lower than 150°C. However, for our system, temperature does not seem to be have a significant effect on particle size and demonstrates nucleation at temperatures as low as 100°C. Additionally, as shown in Table 6.1, Pt NP density

(counts/nm^2 and area/nm^2) remains approximately constant (within error) regardless of temperature when employing a dosing time of 1 minute. To ensure the effect of temperature was not an anomaly for a dosing time of 1 minute, a dosing time of 30 minutes was examined at deposition temperatures of 100°C and 250°C. As shown in Figure 6.2 (b) and Table 6.1, a nearly identical right-skewed PSD, and average particle size, is obtained for a 30 minute dosing time at 100°C and 250°C, respectively, thus further exemplifying the non-self-limiting nature of this process. According to literature, as the temperature is decreased it can be expected that the particle size will decrease, and a narrower size distribution will ensue, due to a decreased Pt diffusion rate [28], [34]. In situations where temperature had little effect on the particle size, it was theorized that the diffusion of the Pt was not limited by the temperature, but the substrate [29]. This suggests that surface contaminants, ligand steric hinderance, or ligand decomposition from the dehydrogenation reaction could be limiting diffusion of Pt [29], [30]. Interestingly, there is a marked increase in particle density (both counts/nm^2 and area/nm^2) at 250°C in comparison to 100°C at a dosing time of 30 minutes. This trend is also visible in the ICP analysis and correlates well with data obtained from HAADF-STEM measurements. The context for this phenomenon will become more evident when comparing deposition results between NCNTs and PCNTs.

Table 6.1. *Comparison of density and diameter data obtained from HAADF-STEM for NCNTs and PCNTs exposed to $MeCpPtMe_3$ at different temperatures and dosing times. ICP analysis was performed to determine the atomic weight percent of Pt on each sample analyzed in HAADF-STEM.*

Dose Time (min)	Temperature (°C)	Density (counts /nm²)	Density (area/nm²)	Average Equivalent Diameter (nm)	ICP analysis (atomic weight %)
1	250	0.084 ± 0.03	0.0050 ± 0.001	0.25 ± 0.1	0.42%
		0.050 ± 0.02 (PCNT)	0.012 ± 0.01 (PCNT)	0.37 ± 0.2 (PCNT)	too low for detection
	175	0.089 ± 0.02	0.0054 ± 0.0006	0.31 ± 0.1	0.39%
	100	0.084 ± 0.02	0.0062 ± 0.002	0.28 ± 0.1	0.25%
30	250	0.37 ± 0.2	0.046 ± 0.02	0.36 ± 0.2	0.89%
		0.19 ± 0.01 (PCNT)	0.052 ± 0.02	0.44 ± 0.4 (PCNT)	0.32%
	100	0.13 ± 0.1	0.015 ± 0.004	0.38 ± 0.2	0.28%
60	250	0.30 ± 0.2	0.074 ± 0.02	0.48 ± 0.3	0.93%

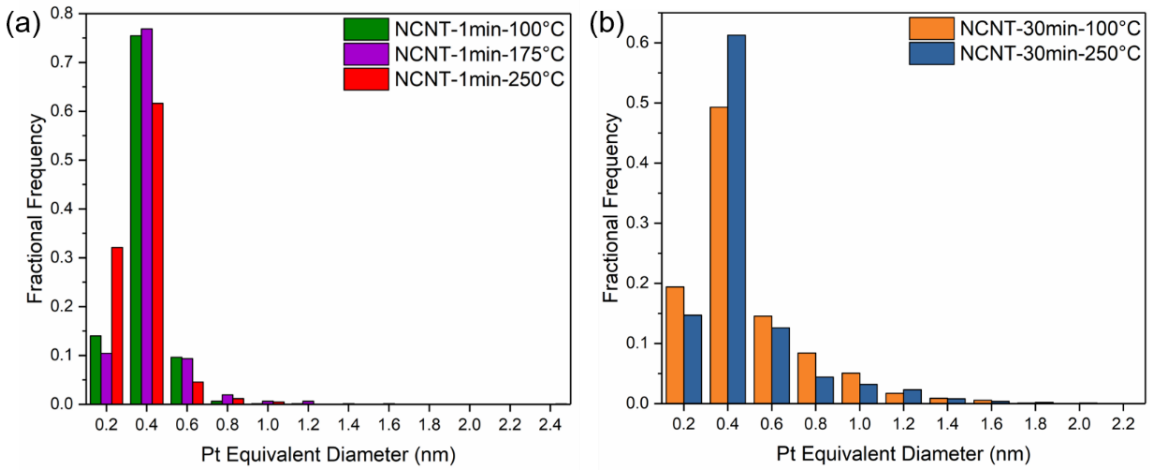


Figure 6.2. *PSD comparison for (a) a 1 minute exposure of Pt to NCNTs at a temperature of 100°C, 175°C, and 250°C, and (b) a 30 minute exposure of Pt to NCNTs at a temperature of 100°C and 250°C.*

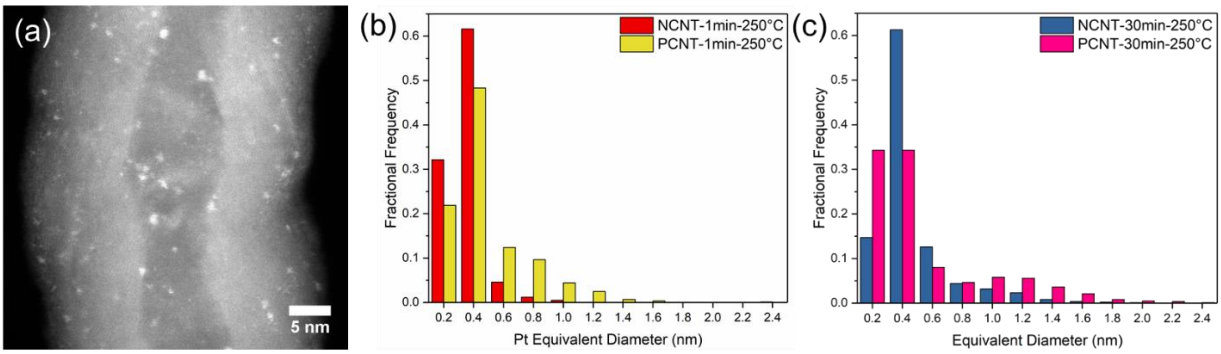
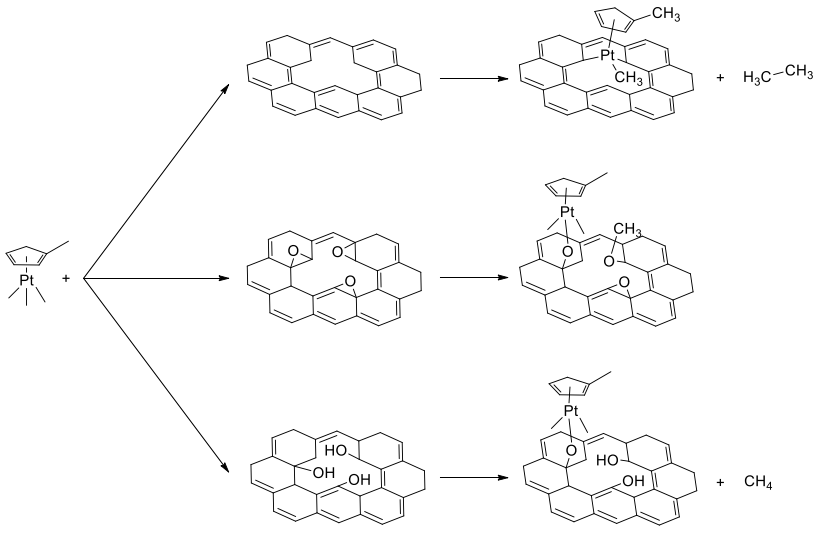


Figure 6.3. *HAADF-STEM images of single pulsed Pt deposited at 250°C on a (a) NCNT and (b) PCNT for a 1 minute exposure. PSD comparison of (c) a 1 minute exposure on NCNTs and PCNTs and (d) a 1 minute and 30 minute exposure on PCNTs.*

Figure 6.3 demonstrates the stark difference in deposition of Pt on NCNTs (Figure 6.1 (a)) and PCNTs (Figure 6.3 (a)) dosed for 1 minute at 250°C. The PSD for PCNTs with dosing times of 1 minute (Figure 6.3 (b)) and 30 minutes (Figure 6.3 (c)) indicate a much broader Pt size distribution on the PCNTs compared to NCNTs. As shown in Table 6.1, the density (counts/nm^2) of particles deposited on the PCNT surface is significantly less than that observed for NCNTs, thus suggesting a decrease in the number of nucleation sites. Alternatively, the area/nm^2 is equivalent or greater on the PCNTs versus the NCNTs for both dosing times. This also suggests that less Pt nucleation sites are present on the surface of PCNTs, resulting in an increased growth regime on the PCNTs compared due the NCNTs, as evidenced by the increased average equivalent diameter (Table 6.1) and broader PSD on the PCNTs. This was also observed by Setthapan et al [23], on metal oxide surfaces, such that higher surface area substrates resulted in higher Pt loadings and smaller nanoparticles. Interestingly, the loading of Pt on the NCNTs is significantly higher than the PCNTs, thus suggesting the potential for reduced nucleation sites and preferred desorption mechanisms on the PCNTs.

We believe the discrepancy in particle size and density observed between the NCNTs and PCNTs can be related to three mechanisms taking place concurrently. The first is related to the density of surface functionality and surface defects. Several publications have demonstrated the richness and high density of defects, as well as surface functionality, that exists for NCNTs [35]–[37]. Chen et al [38], reported a similar observation of decreased Pt NP size, as well as increased density of NPs on an NCNT surface, compared to PCNTs via reduction of $H_2PtCl_6{\cdot}6H_2O$ by ethylene glycol. They attributed this phenomenon to localized areas of increased electron density

on the NCNT surface, due to the incorporation of the N-dopant which resulted in improved chemical activity. As a result, an increased number of reductive sites are available on the NCNT surface, leading to increased particle density. Comparatively, the surface of PCNTs are relatively pristine and defect free and provide only a limited number of sites for Pt nucleation, therefore significantly decreasing Pt particle density. Additionally, Karasulu et al [39], preformed a detailed computational analysis on the adsorption kinetics of $MeCpPtMe_3$ toward graphene and graphene oxide substrates. Their study indicated kinetically favorable reaction energies for $MeCpPtMe_3$ bonding at epoxy, hydroxyl, carbon defect sites, and hydrogen groups on graphene oxide in comparison to pristine graphene. Depending on the surface reaction site, the process is hypothesized to proceed as outlined in Scheme 6.1. The second concurrent mechanism is related to steric hindrance and obstruction of functional sites by liberated gaseous ligands. Several publications have suggested that adsorbed organic material remains on the surface following $MeCpPtMe_3$ chemisorption [21], [27], [28]. This organic material serves two purposes, one is to obstructively limit the growth of Pt NPs, while the second purpose is to suppress the aggregation of Pt by hindering its mobility. The third and final mechanism governing the self-limiting properties of $MeCpPtMe_3$ is its electronic interaction with the surface. The catalytic ability of Pt, and the extent to which ligand decomposition occurs, is related to the oxidation state of Pt, especially its unoccupied d states as well as its size which affects the densities of states of Pt relevant to its catalytic behavior [1], [40], [41].



Scheme 6.1. *Representation of the chemisorption of $MeCpPtMe_3$ species on defective graphene and graphene oxide.*

With these three mechanisms in mind, we can begin to form a basis for the observations reported herein. Given that the surface of the NCNTs are defect rich and contain many different functional groups as, shown by the Auger spectroscopy analysis in the supporting information, chemisorption of $MeCpPtMe_3$ is relatively easy with surface saturation occurring after 30 minutes of dosing. As surface saturation of the chemisorbed Pt precursor occurs, liberated ligands are either removed through the gas phase or are reabsorbed back on the surface and sterically hinder the growth of Pt NPs while simultaneously suppressing Pt mobility. This phenomenon is best observed when comparing particle densities for 30 minute dose times on NCNTs at 250°C and 100°C. Deposition at 100°C contains about half as many particles (counts/nm^2 and loading in Table 6.1) compared to experiments conducted at 250°C. This decrease in particle density can be related to the difficulty of removing carbonaceous material left behind following precursor chemisorption when operating at a lower temperature, as the kinetic barrier for this process is decreased at elevated temperatures. Furthermore, at lower temperatures, the initial chemisorption process is more difficult due to decreased kinetic energy. Finally, the large discrepancy observed between the NCNTs and PCNTs can be explained by a reduced number of defect and functional sites on the PCNTs, resulting in the decreased particle density (counts/nm^2) and loading. The larger particle sizes observed for PCNTs, even after 1 minute of dosing, can be attributed to facile adatom mobility as the surface of PCNTs are relatively pristine. Additionally, a lack of surface functionality decreases the chance of liberated ligand from reabsorbing on the surface, thus providing ample room for NP growth. Furthermore, the bonding sites for chemisorption of $MeCpPtMe_3$ are likely to be different for PCNTs compared to NCNTs, with nucleation occurring at defect sites for PCNTs, and adsorbed hydrocarbons. Finally, the reaction site of the $MeCpPtMe_3$ will undoubtedly influence the oxidation state of the absorbed precursor, thus resulting in alternative catalytic activities and precursor decomposition routes.

To elucidate the local coordination environment of single Pt atoms on NCNTs, XANES and EXAFS analysis was conducted. Figure 6.4 (a) presents Pt L_3 absorption edges for NCNTs exposed to $MeCpPtMe_3$ for 1 minute and 30 minutes, and PCNTs exposed for 30 minutes, alongside standard Pt and PtO_2. It should be noted that the intensity of the whiteline is related to the unoccupied densities of 5d states just above the Fermi level. Careful examination of the energy position and whiteline intensity reveals that increasing the dosing time results in an edge jump that shifts toward a more oxidized state of Pt. It is important to remember that XANES provides an

average of the X-ray absorption process occurring for all Pt atoms within the beam spot size. Given the large increase in particle loading from the 1 minute to 30 minute sample, the XANES spectra for the 30 minute sample is a good representation of the oxidation state of single Pt atoms and small clusters. These observations suggest that Pt exists in an oxidized form but with an alternate stoichiometry from bulk PtO_2. It is well known that O_2 adsorbed on the surface of single crystal Pt possess elongated O-O bonds that can be easily activated [42]. The increased shift in oxidation for the 30 minute sample, compared to the 1 minute sample, can be attributed to increased saturation of surface sites, therefore resulting in Pt appearing in a more oxidized state. In actuality, there are a mixture of particles that are in a wide range of oxidation states depending on where they are bonded to on the NCNT surface. Interestingly, the PCNT sample displays a whiteline intensity that is closer to metallic Pt than PtO_2 and exists in some form that is in-between these two standards.

To provide further information pertaining to structural details of adsorbed Pt, EXAFS was performed. Figure 6.4 (b) displays the Fourier transformed (FT) $k^2\chi(k)$ data in real-space for the same samples shown in Figure 6.4 (a). Both NCNT samples of 1 minute and 30 minutes show similar EXAFS FT profiles that are starkly different from the PtO standard and 30 minute PCNT sample. All samples display an initial peak between 1.54 Å to 2.01 Å, which correspond to Pt-O. It is possible that this first peak is associated with either Pt-C or Pt-N, but this is difficult to discern the bonding differences due to the similar Z factor for these elements. It is therefore difficult to determine if the Pt atoms are stabilized by the precursor ligands or simply by the attachment to the NCNT surface sites. Interestingly, this first peak shifts from 1.54 Å for the 1 minute dosing time on the NCNT substrate to 1.85 Å for 30 minute dosing time. Furthermore, a shift of 2.01 Å is observed for the 30 minute PCNT sample, thus demonstrating elongating radial distance with increasing exposure. Additionally, the 30 minute NCNT and PCNT samples exclusively show a peak associated with the Pt-Pt interaction, at approximately 3 Å. All samples demonstrate absorption occurring through two interface O atoms or perhaps one O atom and another species that may be associated with attached ligands. A more detailed analysis involving in-situ

experiments is required to determine if ligands are still attached following substrate exposure to $MeCpPtMe_3$.

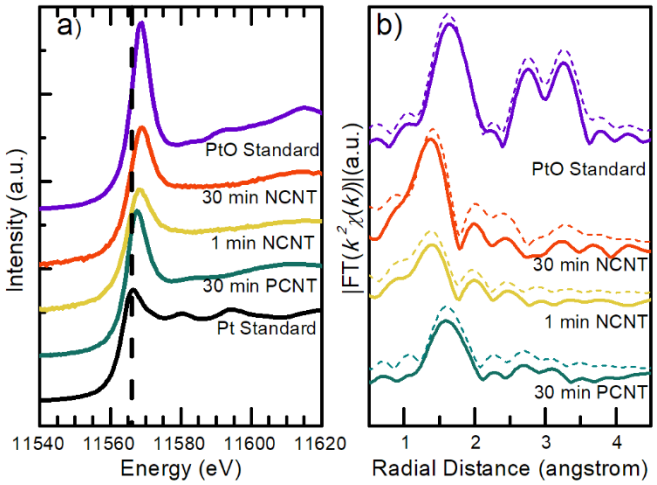


Figure 6.4. *(a) Pt L_3-edge XANES of samples prepared using varying dosing times of $MeCpPtMe_3$ on NCNTs and PCNTs at 250°C along with standard Pt and PtO_2. (b) Pt L_3 edge k^2-weighted FT-EXAFS spectra of samples presented in (a) in solid lines and their corresponding best fits as dotted lines.*

6.4 Conclusion

In conclusion, we demonstrate the feasibility of achieving single Pt atoms and clusters on a NCNT substrate using ALD by controlling the exposure of the Pt precursor to the substrate. The self-limiting characteristics of the $MeCpPtMe_3$ precursor was used to control the size of the Pt particles from single-atoms, sub-nanometer clusters, to NPs through a single pulse of the Pt precursor during the ALD process without any oxidizing step. This unique approach allows for the stabilization of Pt particles on the surface by leaving the remaining ligands attached to the absorbed Pt particle. Furthermore, our results demonstrate the importance of substrate interaction in controlling the Pt particle size, with NCNTs demonstrating much finer control over smaller particles compared to a PCNT substrate. This phenomenon is hypothesized to stem from the multitude of interactions available on the NCNT surface compared to the PCNT surface, and therefore allows for facile Pt particle nucleation. Furthermore, the relatively more complicated surface of the NCNTs which contain an abundance of nucleation sites as well as a l layer of carbonaceous decomposition material, which prevents adatom diffusion and coalescence, allows

for the stabilization of much smaller particles. Our work provides a promising approach for the design of single Pt atom catalysts and presents the potential to reduce the high cost of industrial commercial noble-metal catalysts.

Acknowledgements: This research was supported by the Natural Science and Engineering Research Council of Canada (NSERC), Canadian Light Source (CLS), Canada Research Chair (CRC) Program, Canada Foundation for innovation (CFI), Ontario Research Fund (ORF), Automotive Partnership of Canada (APC) and the University of Western Ontario. The outstanding electron microscopy presented herein was conducted at the Canadian Center for Electron Microscopy, a national facility supported by CFI under the MSI program, NSERC and McMaster University.

6.5 Supporting Information

6.5.1 Data Processing

Image quantification: To examine the effect of ALD conditions on Pt particle size, the acquired HAADF images required quantification. For each sample, the Pt size was examined for six individual CNTs. Selection of the CNTs was random based on size (diameter); however, CNTs that appeared to be the cleanest were preferred. Generally, the CNTs appeared to have a layer of residue surrounding them, which added background contrast, making the CNTs more difficult to image. Furthermore, some tubes were filled with either a liquid or gas (as to be discussed later) that would move when imaged and cause the tube to become more easily damaged. Therefore, to ensure better quality images, tubes that were highly covered in residue or seemed to be filled were avoided. Additionally, when possible, during quantification, images that showed signs of beam damage to the CNTs and/or beam contamination were avoided. Based on the nature of knock-on damage to CNTs and beam contamination issues when using solvents, it was not always possible to avoid these effects, as these images occasionally offered the best resolution, such that the Pt was in focus, thus in these cases the images were selected [43], [44]. For openness and clarity to the reader, all raw and processed images used for quantification have been included at the end of this chapter.

The steps used for image quantification are as follows. First, each HAADF image was calibrated using a MAG*I*CAL® reference standard from Electron Microscopy Sciences© (Figure S6.6 (a)). Second, ImageJ was utilized to perform a background subtraction using the "subtract background" built-in function with the smoothing function enabled (Figure S6.6 (b) and (c)) [45]. Third, using the polygon selection tool and consulting the original image, the Pt atoms and particles that appeared to be in focus were manually encircled and deleted from the image (Figure S6.6 (d)). Fourth, the "Simple Math" built-in function in GATAN Digital Micrograph software was used to subtract the image with the deleted Pt particles (Figure S6.6 (d)) from the original image (Figure S6.6 (a)) to produce an image wherein the particles were of varying greyscale and all other areas in the image were black (Figure S6.6 (e)). Fifth, the threshold of the subtracted image was adjusted using ImageJ to accept all grey levels except pure black (background) (Figure S6.6 (f)).

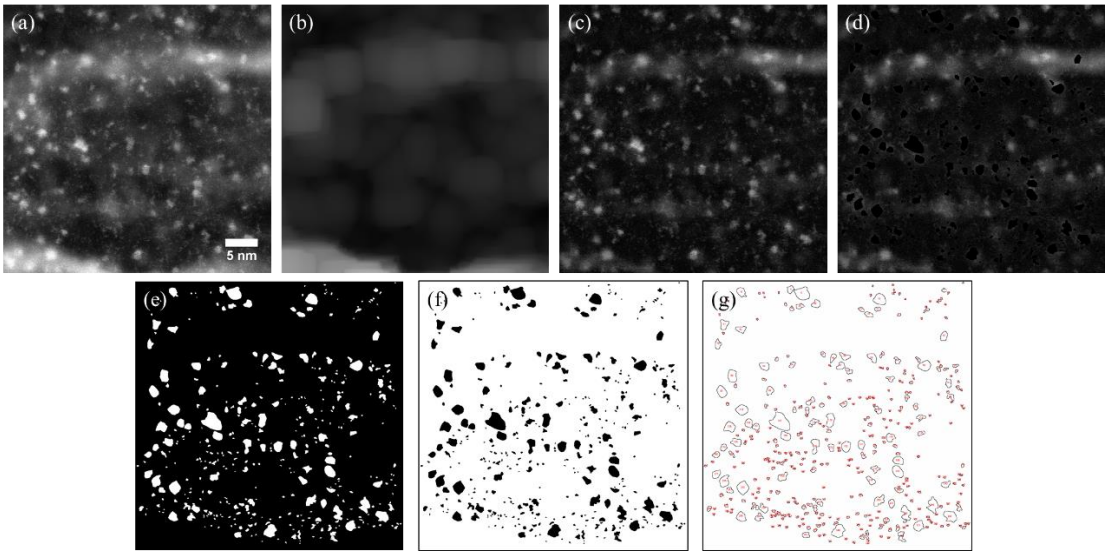


Figure S6.6. Experimental steps used for the quantification of the Pt equivalent diameter. *60 minute Pt dosing time at 250°C (a) calibrated raw HAADF image. ImageJ was used to subtract the (b) background from (a), thus forming the (c) background subtracted image. Pt was then manually removed using the polygon selection tool in ImageJ. Digital Micrograph software was used to subtract image (d) from (a) to produce image (e), wherein the (f) threshold was adjusted, and the image was (g) analyzed with ImageJ.*

The particles from Figure S6.6 (f) were then analyzed in ImageJ using the "Analyze Particles" function with the particles on the edge excluded. Specifically, the "Analyze Particles" function was used to determine the area of each individual particle, the number of particles, and the total area of the particles (Figure S6.6 (g)). Prior to constructing the histograms shown in this chapter, the measurements were analyzed and particles of one-pixel area were removed, which likely originated from noise in the image. ImageJ provided a value of the area (A) measured for each particle based on the number of pixels encircled per particle and the calibrated scale. This value was then converted into an equivalent diameter (d_{eq}) by assuming that Pt particles have a spherical shape or a circular shape when projected in the two-dimensional image $\left(d_{eq} = 2 \times \sqrt{\frac{A}{\pi}}\right)$.

Error analysis and histogram formation: Error was introduced into the measurements through intrinsic mechanisms related to the image collection process from STEM and from manual error during data processing. According to Browning et al [46], the resolution of STEM images can be affected by the object under investigation, probe size, vibrations experienced at the sample and from the scanning coils, and the image being out of focus. Other effects may also include sample

drift, atom movement from beam excitation, and beam damage. Following error analysis completed for manual measurements of biological samples, an error analysis was completed using a single image in which the Pt size was measured on five separate days [47]. This information was used to determine the binning width and the error associated with each bin. The image was selected based on its magnification and range of particle size. The images analyzed for this investigation commonly had a magnification of 1.8 Mx or 2.55 Mx (with the exception of one image with a magnification of 1.3 Mx and two images with a magnification of 3.6 Mx). The selected image for the error analysis was acquired at 1.8 Mx, which would be more susceptible to error based on the image resolution. Furthermore, the selected image had the broadest range of particle sizes based on the original data analysis, thus allowing for the error characterization over more Pt sizes. After performing the image quantification process, described in Figure S6.6 for the same image on five separate days, the total error and intra-observer error was then estimated.

The data was compiled for the five days, and a histogram was created wherein each bin represents a single pixel, and the counts per bin were acquired based on the number of pixels measured in each particle. The bins were then summed over the five days to compile the total number of counts for each bin into a single histogram, as shown in Figure S6.7 (a). Two peaks were observed in a low and high pixel number regime (Figure S6.7 (a)), at approximately 25 and 650 pixels, respectively). The error associated with Pt particles containing a lower number of pixels will be greater, as the deviation of one pixel will have a greater effect on the total area of the Pt particle examined. Following this rationale, a Gaussian fit was performed on the peak in the low pixel number regime from 0 to 174 pixels using OriginPro software (Figure S6.7 (b)). While the model did not entirely fit the data, likely due to the high noise, the FWHM (w) was used to estimate the total error of the measurement. Therefore, with a w equal to 20 pixels, the error equates to an area of 0.032 nm^2 (image calibration of 24.8412 pixels/nm) and an equivalent diameter of 0.20 nm.

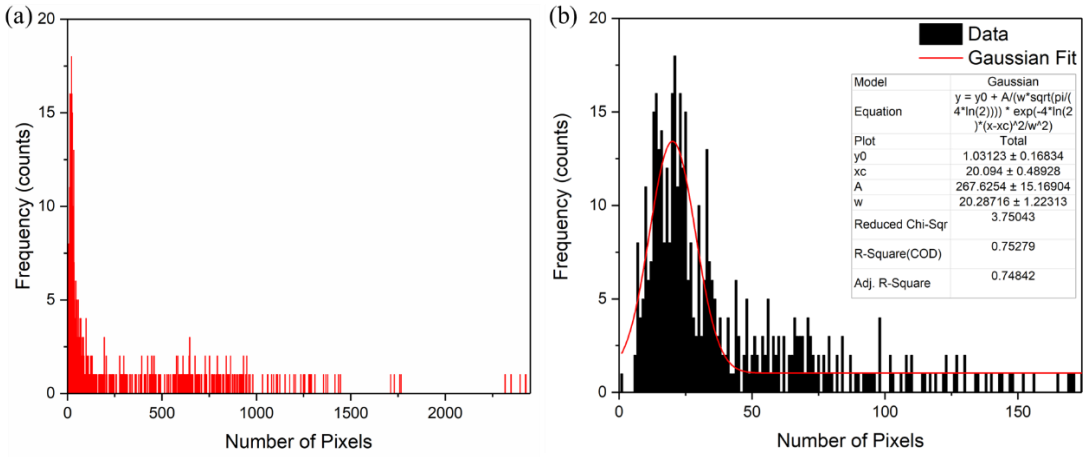


Figure S6.7 *Error analysis for the Pt quantification process. Histogram showing the (a) total counts for the Pt entities as a function of the number of pixels, summed from a five day data analysis of a single image. (b) Fitted Gaussian model and parameters from the low range peak in (a).*

Using the error as the bin width, the data collected over the five days is presented in Figure S6.3 (a) as individual components, and (b) as the mean value per bin with the error bars calculated by the standard deviation for each bin. These error bars represent the error introduced by the manual measurement (intra-observer error) and are individually calculated for each bin. The data presented in the remaining histograms has been normalized to the total number of Pt particles for each individual CNT, such that over a single measurement the frequency of all bins sums to 1.

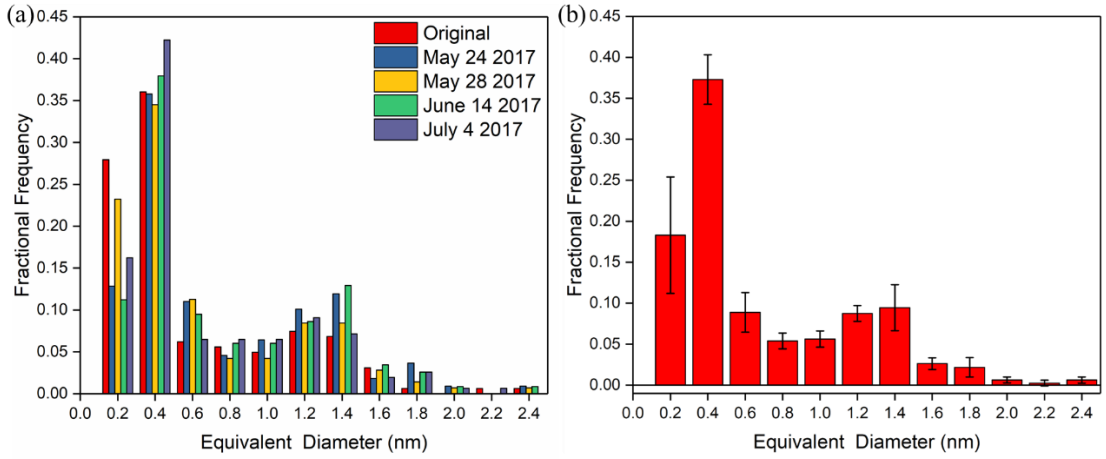


Figure S6.8 *Error analysis results from a five day study of a single HAADF image with bins showing the experimental error. Data analysis from a single image showing (a) each individual analysis over five days and (b) the mean and standard deviation for each bin from the five day measurement. The errors in (b) represent the error introduced into the measurement from the manual process.*

Following the error analysis, all histograms were produced with a bin width of 0.2 nm. The histograms were constructed by examining the size of the Pt entities on six different tubes, in which a minimum of 59 atoms were counted per nanotube. If a single image did not contain 59 atoms, multiple images of the same tube were analyzed from different areas along the tube (Table S6.3). It should be noted that in a single location, only one side of the tube was examined to limit the CNT to electron exposure and hence decrease possible damage induced by the electron beam. In some cases, out of curiosity, both sides of the tubes were imaged, and it was found that a higher loading was preferentially deposited on one side of the tube. This was not further examined for the extent of this investigation, but could be a future area of research, possibly using electron tomography to get a better representation of the Pt homogeneity on a single tube.

Table S6.3 *Number of images analyzed, and the number of Pt entities counted per image.*

Time (min)	Temp (°C)/Substrate	Number of Images Analyzed	Number of Pt Entities
1	250/NCNT	12	1034
	250/PCNT	15	613
	175/NCNT	8	825
	100/NCNT	10	934
30	250/NCNT	6	3534
	250/PCNT	11	863
	100/NCNT	9	927
60	250/NCNT	6	2490

Using the threshold images produced from the quantification routine, Pt density was measured. In order to perform the measurement, it was necessary to have the Pt in focus across the entire area examined. Due to the curvature of CNTs, it is difficult to maintain the focus over the entire surface area from the depth of focus of the imaging lens. Therefore, images from the center most region of the tubes (one quarter of the inner diameter of the tube) were analyzed. These values should be considered as strict approximations, as not all tubes could be analyzed, due to the fact that some images were acquired at the edge on the CNT. For cases in which the edge of the tubes could not be seen in the image, it was assumed that the image was centered on the CNT, and those images were used for density quantification. All errors presented in the measurements were acquired from

the sample standard deviation of all the measurements acquired for each individual experimental condition.

6.5.2 Elemental Quantification

Auger spectroscopy: Using auger spectroscopy, the surface of the NCNTs were examined for their elemental content prior to Pt deposition. Table S6.4 indicates that the N content of these nanotubes was 3.2 ± 0.4 at. % and the O content was approximately 5.4 ± 0.8 at. %. Trace amounts of contaminants (Cl and S) were found on the NCNTs during a full spectrum acquisition; however, the concentration for these elements was low, thus they are expected to have little effect on the surface sites of the NCNTs. The O content may originate from a few potential sources: hydrocarbon contamination, and O or N-oxide adsorbents. Through examination of the Au substrate the contamination caused by the methanol solvent and beam contamination is evident by the 30 at. % C content, suggesting that the values acquired from the NCNTs were also affected by the C contamination, which could lead to the underestimation of the doping levels. Commonly, an *in situ* Ar^+ plasma source is used to remove this contamination; however, due to the low knock-on damage threshold of the NCNTs, this procedure was not completed to ensure the nanotubes were not damaged prior to Auger analysis. Upon EELS analysis and further auger quantification trace amounts of Ca (0.5 ± 0.1 at. %) were locally found on the NCNTs.

Table S6.4. *Auger Spectroscopy elemental quantification of NCNTs. Reported at. % were acquired from the average value of nine measurements with the error calculated by the sample standard deviation.*

C (%)	N (%)	O (%)	Cl (%)	S (%)
90 ± 1.7	3.2 ± 0.4	5.4 ± 0.8	0.81 ± 0.7	0.51 ± 0.2

EELS: EELS showed local variations on individual NCNTs at low magnifications (<1.3 Mx), which included large FeOx catalysts, and Ca oxide particles. These are expected to arise from the remaining growth catalysts, and the contaminants observed by Auger spectroscopy. Because the larger particles in these low magnification images were determined to be growth catalysts and contaminants, during image quantification low magnification images were excluded, such that only the Pt atoms and NPs were examined. EELS further revealed local variations of contaminants on the NCNTs, such as N_2 gas, a potential O-containing liquid within the NCNTs, and a thick polymeric-like substance. While the contamination sources are unknown, these contributed to a

bright contrast of the NCNTs (with exception to the N2 gas), due to the increased nuclear charge and thickness, thus they were avoided during NCNT selection, as to ensure a more reliable image quantification could be performed.

Examination of high magnification ADF images acquired in GATAN Digital Micrograph (Figure S6.6 (a) and (b)) shows many bright spots decorating the NCNT. It is expected through the Z-contrast, that the bright spots are related to Pt. For confirmation, EELS was used to determine the origin of the bright spots. Through consultation of the ADF image (Figure S6.6 (c)) and the spectrum image (Figure S6.6 (d)) a Pt-M edge at 2122 eV (Figure S6.6 (e)) is evident from the region of interest (ROI) in red, over the bright contrast found in the ADF image, thus confirming that the origin of the bright spots in the HAADF images used for quantification are the ALD deposited Pt catalysts. The beam effects on the Pt atoms are observed when comparing the ROI (green box) in the ADF image before (Figure S6.6 (a)) and after (Figure S6.6 (b)) the EELS acquisition. Due to beam excitation, the atoms tend to migrate on the surface of the NCNT, thus acting as a source of error on the size of the Pt atoms (as mentioned in the image quantification section).

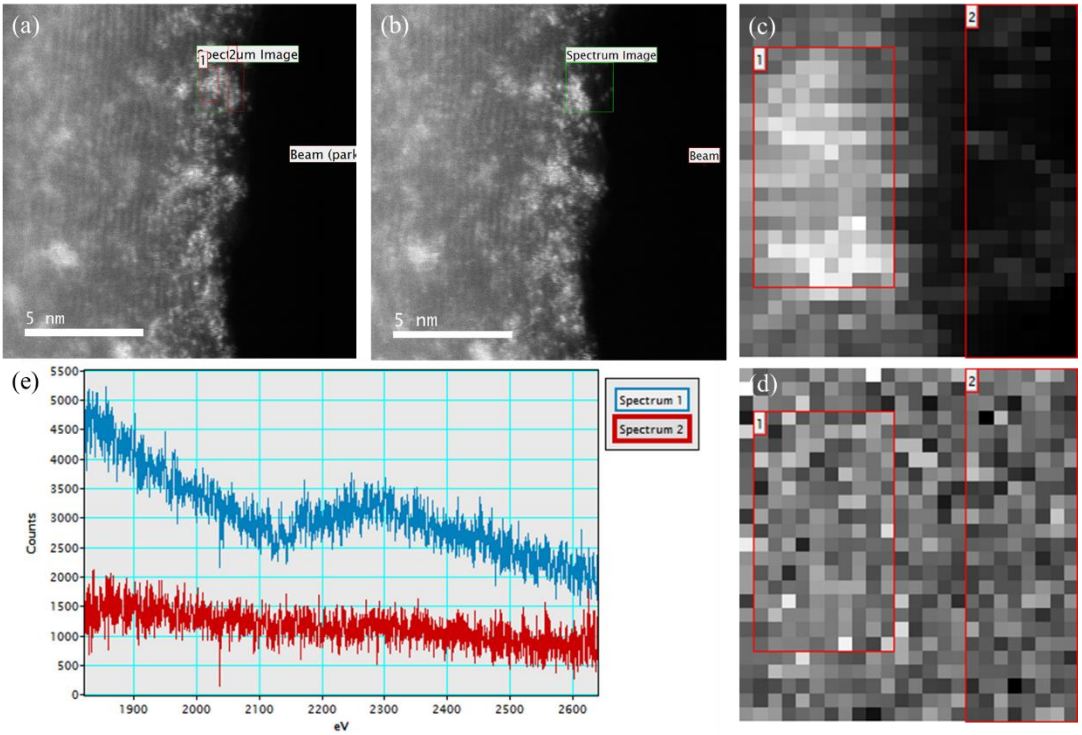


Figure S6.9. *High energy EELS analysis of Pt deposited on NCNTs for 60 minutes at a temperature of 250°C was imaged using ADF (a) before and (b) after the EELS acquisition. The (c) ADF image corresponding to the (d) spectrum image shows that the bright spots correlate to a Pt-L edge, as shown in the (e) extracted spectra from the areas outlined in (c) and (d).*

6.5.3 Additional Histograms

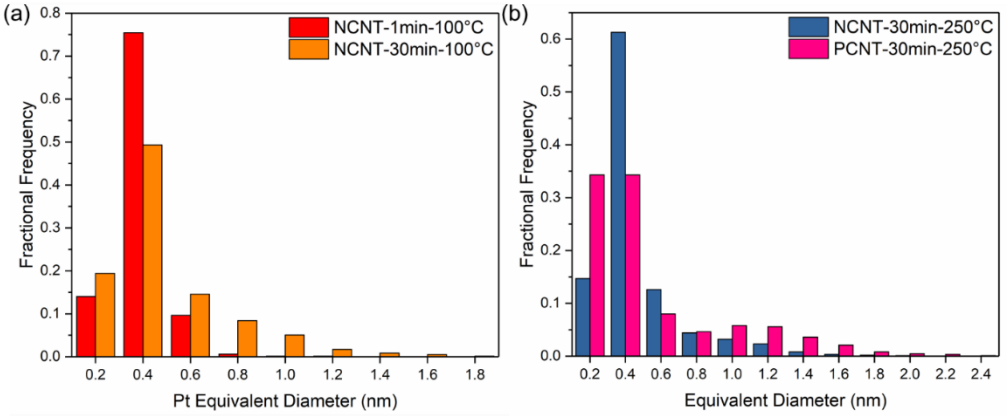


Figure S6.10. *PSD histograms from (a) NCNTs at 100°C using a dosing time of 1 minute, and 30 minutes, and (b) NCNTs and PCNTs at 250°C using a dosing time 30 minutes.*

6.6 References.

[1] B. R. Cuenya, "Synthesis and catalytic properties of metal nanoparticles: Size, shape, support, composition, and oxidation state effects," *Thin Solid Films*, vol. 518, no. 12, pp. 3127–3150, 2010.

[2] E. A. Ticianelli, C. R. Derouin, and S. Srinivasan, "Localization of platinum in low catalyst loading electrodes to to attain high power densities in SPE fuel cells," *J. Electroanal. Chem. Interfacial Electrochem.*, vol. 251, no. 2, pp. 275–295, 1988.

[3] M. S. Wilson and S. Gottesfeld, "Thin-film catalyst layers for polymer electrolyte fuel cell electrodes," *J. Appl. Electrochem.*, vol. 22, no. 1, pp. 1–7, 1992.

[4] V. Mehta and J. S. Cooper, "Review and analysis of PEM fuel cell design and manufacturing," *J. Power Sources*, vol. 114, no. 1, pp. 32–53, 2003.

[5] C. Zhu, S. Fu, Q. Shi, D. Du, and Y. Lin, "Single-Atom Electrocatalysts," *Angew. Chemie Int. Ed.*, pp. 2–19, 2017.

[6] J. Liu, "Catalysis by Supported Single Metal Atoms," *ACS Catal.*, vol. 7, no. 1, pp. 34–59, 2017.

[7] X. F. Yang, A. Wang, B. Qiao, J. Li, J. Liu, and T. Zhang, "Single-atom catalysts: A new frontier in heterogeneous catalysis," *Acc. Chem. Res.*, vol. 46, no. 8, pp. 1740–1748, 2013.

[8] S. Yang, Y. J. Tak, J. Kim, A. Soon, and H. Lee, "Support Effects in Single-Atom Platinum Catalysts for Electrochemical Oxygen Reduction," *ACS Catal.*, vol. 7, no. 2, pp. 1301–1307, 2017.

[9] J. Lin *et al.*, "Remarkable Performance of Ir 1 /FeO x Single-Atom Catalyst in Water Gas Shift Reaction," *J. Am. Chem. Soc.*, vol. 135, no. 41, pp. 15314–15317, 2013.

[10] Z. Zhang *et al.*, "Thermally stable single atom Pt/m-Al2O3 for selective hydrogenation and CO oxidation," *Nat. Commun.*, vol. 8, p. 16100, 2017.

[11] N. Cheng *et al.*, "Platinum single-atom and cluster catalysis of the hydrogen evolution reaction," *Nat. Commun.*, vol. 7, p. 13638, 2016.

[12] J. K. Nørskov *et al.*, "Trends in the Exchange Current for Hydrogen Evolution," *J. Electrochem. Soc.*, vol. 152, no. 3, p. J23, 2005.

[13] B. Qiao *et al.*, "Single-atom catalysis of CO oxidation using Pt1/FeOx," *Nat. Chem.*, vol. 3, no. 8, pp. 634–641, 2011.

[14] S. Sun *et al.*, "Single-atom Catalysis Using Pt/Graphene Achieved through Atomic Layer Deposition," *Sci. Rep.*, vol. 3, no. 1, p. 1775, 2013.

[15] A. Mackus, "Atomic layer deposition of platinum from surface reactions to nanopatterning," Eindhoven: Technische Universiteit Eindhoven, 2013.

[16] T. Aaltonen, M. Ritala, T. Sajavaara, J. Keinonen, and M. Leskelä, "Atomic layer deposition of platinum thin films," *Chem. Mater.*, vol. 15, no. 9, pp. 1924–1928, 2003.

[17] J. Hamalainen, M. Ritala, and M. Leskela, "Atomic layer deposition of noble metals and their oxides," *Chem. Mater.*, vol. 26, pp. 786–801, 2014.

[18] J. Lu *et al.*, "Toward atomically-precise synthesis of supported bimetallic nanoparticles using atomic layer deposition.," *Nat. Commun.*, vol. 5, p. 3264, 2014.

[19] L. Baker *et al.*, "Nucleation and growth of Pt atomic layer deposition on Al2O 3 substrates using (methylcyclopentadienyl)-trimethyl platinum and O2 plasma," *J. Appl. Phys.*, vol. 109, no. 8, 2011.

[20] A. J. M. MacKus, N. Leick, L. Baker, and W. M. M. Kessels, "Catalytic combustion and dehydrogenation reactions during atomic layer deposition of platinum," *Chem. Mater.*, vol. 24, no. 10, pp. 1752–1761, 2012.

[21] W. M. M. Kessels, H. C. M. Knoops, S. A. F. Dielissen, A. J. M. Mackus, and M. C. M. van de Sanden, "Surface reactions during atomic layer deposition of Pt derived from gas phase infrared spectroscopy," *Appl. Phys. Lett.*, vol. 95, no. 1, p. 13114, 2009.

[22] S. M. Geyer, R. Methaapanon, B. Shong, P. A. Pianetta, and S. F. Bent, "In Vacuo Photoemission Studies of Platinum Atomic Layer Deposition Using Synchrotron Radiation," *J. Phys. Chem. Lett.*, vol. 4, no. 1, pp. 176–179, 2013.

[23] W. Setthapun *et al.*, "Genesis and evolution of surface species during Pt atomic layer deposition on oxide supports characterized by in situ XAFS analysis and water-gas shift reaction," *J. Phys. Chem. C*, vol. 114, no. 21, pp. 9758–9771, 2010.

[24] T. Aaltonen, O. Nilsen, A. Magrasó, and H. Fjellvåg, "Atomic Layer Deposition of Li 2 O–Al 2 O 3 Thin Films," *Chem. Mater.*, vol. 23, no. 21, pp. 4669–4675, 2011.

[25] J. Li, X. Liang, D. M. King, Y. B. Jiang, and A. W. Weimer, "Highly dispersed Pt nanoparticle catalyst prepared by atomic layer deposition," *Appl. Catal. B Environ.*, vol. 97, no. 1–2, pp. 220–226, 2010.

[26] J. A. Enterkin *et al.*, "Propane Oxidation over Pt / SrTiO 3 Nanocuboids," *ACS Catal.*, vol. 1, p. 629, 2011.

[27] A. J. M. MacKus, M. A. Verheijen, N. Leick, A. A. Bol, and W. M. M. Kessels, "Influence of oxygen exposure on the nucleation of platinum atomic layer deposition: Consequences for film growth, nanopatterning, and nanoparticle synthesis," *Chem. Mater.*, vol. 25, no. 9, pp. 1905–1911, 2013.

[28] F. Grillo, H. Van Bui, J. A. Moulijn, M. T. Kreutzer, and J. R. Van Ommen, "Understanding and Controlling the Aggregative Growth of Platinum Nanoparticles in Atomic Layer Deposition: An Avenue to Size Selection," *J. Phys. Chem. Lett.*, vol. 8, no. 5, pp. 975–983, 2017.

[29] A. J. M. Mackus *et al.*, "Atomic layer deposition of Pd and Pt nanoparticles for catalysis: on the mechanisms of nanoparticle formation.," *Nanotechnology*, vol. 27, no. 3, p. 34001, 2016.

[30] H. Van Bui, F. Grillo, and J. R. van Ommen, "Atomic and molecular layer deposition: off the beaten track," *Chem. Commun.*, vol. 53, no. 1, pp. 45–71, 2017.

[31] R. L. Puurunen, “Surface chemistry of atomic layer deposition: A case study for the trimethylaluminum/water process,” *J. Appl. Phys.*, vol. 97, no. 12, 2005.

[32] S. Takakusagi, K. Fukui, R. Tero, F. Nariyuki, and Y. Iwasawa, “Self-Limiting Growth of Pt Nanoparticles from from MeCpPt3 Adsorbed on TiO2(110) Studied by Scanning Tunneling Microscopy,” *Phys. Rev. Lett.*, vol. 91, no. 6, p. 66102, 2003.

[33] M. Hiratani, T. Nabatame, Y. Matsui, K. Imagawa, and S. Kimura, “Platinum Film Growth by Chemical Vapor Deposition Based on Autocatalytic Oxidative Decomposition,” *J. Electrochem. Soc.*, vol. 148, no. 8, p. C524, 2001.

[34] H. Feng, J. A. Libera, P. C. Stair, J. T. Miller, and J. W. Elam, “Subnanometer palladium particles synthesized by atomic layer deposition,” *ACS Catal.*, vol. 1, no. 6, pp. 665–673, 2011.

[35] A.-C. Johansson, R. B. Yang, K. B. Haugshøj, J. V. Larsen, L. H. Christensen, and E. V. Thomsen, “Ru-decorated Pt nanoparticles on N-doped multi-walled carbon nanotubes by atomic layer deposition for direct methanol fuel cells,” *Int. J. Hydrogen Energy*, vol. 38, no. 26, pp. 11406–11414, 2013.

[36] D. C. Higgins, D. Meza, and Z. Chen, “Nitrogen-Doped Carbon Nanotubes as Platinum Catalyst Supports for Oxygen Reduction Reaction in Proton Exchange Membrane Fuel Cells,” *J. Phys. Chem. C*, vol. 114, no. 50, pp. 21982–21988, 2010.

[37] L.-M. Zhang, X.-L. Sui, L. Zhao, J.-J. Zhang, D.-M. Gu, and Z.-B. Wang, “Nitrogen-doped carbon nanotubes for high-performance platinum-based catalysts in methanol oxidation reaction,” *Carbon N. Y.*, vol. 108, pp. 561–567, 2016.

[38] Y. Chen *et al.*, “Nitrogen doping effects on carbon nanotubes and the origin of the enhanced electrocatalytic activity of supported pt for proton-exchange membrane fuel Cells,” *J. Phys. Chem. C*, vol. 115, no. 9, pp. 3769–3776, 2011.

[39] B. Karasulu, R. H. J. Vervuurt, W. M. M. Kessels, and A. A. Bol, “Continuous and ultrathin platinum films on graphene using atomic layer deposition: a combined computational and experimental study,” *Nanoscale*, vol. 8, no. 47, pp. 19829–19845, 2016.

[40] B. Roldan Cuenya and F. Behafarid, “Nanocatalysis: Size- and shape-dependent chemisorption and catalytic reactivity,” *Surf. Sci. Rep.*, vol. 70, no. 2, pp. 135–187, 2015.

[41] Y. G. Guo, J. S. Hu, and L. J. Wan, “Nanostructured materials for electrochemical energy conversion and storage devices,” *Adv. Mater.*, vol. 20, no. 15, pp. 2878–2887, 2008.

[42] J. Zhang, *PEM fuel cell electrocatalysts and catalyst layers: Fundamentals and applications*. 2008.

[43] R. F. Egerton, R. McLeod, F. Wang, and M. Malac, “Basic questions related to electron-induced sputtering in the TEM,” *Ultramicroscopy*, vol. 110, no. 8, pp. 991–997, 2010.

[44] B. W. Smith and D. E. Luzzi, “Electron irradiation effects in single wall carbon nanotubes,” *J. Appl. Phys.*, vol. 90, no. 7, pp. 3509–3515, 2001.

[45] C. A. Schneider, W. S. Rasband, and K. W. Eliceiri, “NIH Image to ImageJ: 25 years of

image analysis," *Nat. Methods*, vol. 9, no. 7, pp. 671–675, 2012.

[46] N. L. Okamoto *et al.*, "Determination of nanocluster sizes from dark-field scanning transmission electron microscopy images," *J. Phys. Chem. C*, vol. 112, no. 6, pp. 1759–1763, 2008.

[47] C. Söderman *et al.*, "Evaluation of Accuracy and Precision of Manual Size Measurements in Chest Tomosynthesis using Simulated Pulmonary Nodules," *Acad. Radiol.*, vol. 22, no. 4, pp. 496–504, 2015.

7

Deconvoluting the Effects of Stripping and Plating of Li Coated Using Atomic and Molecular Layer Deposition*

The use of metallic Li anode is being reevaluated due to an increasing demand for energy storage devices with high gravimetric and volumetric energy density. The Li metal anode has an extremely high theoretical capacity and is a necessary component for next-generation batteries such as Li-S, Li-air, and all solid-state Li batteries. However, Li metal is highly reactive and unfortunately suffers from un-controllable dendrite growth and volume expansion during cycling, resulting in rapid electrolyte consumption and numerous safety concerns. Some of these issues can be mitigated by using advanced coating techniques such as atomic layer deposition (ALD) and molecular layer deposition (MLD). Herein we compare the stripping and plating behavior of Li coated using 50 cycles of either trimethylaluminum (TMA)-water (H_2O), TMA-ethylene glycol (EG) or TMA–glycerol (GLY). Galvanostatic cycling of Li symmetric cells using a current density of 3mA cm^{-2} and capacity of 2 mAh cm^{-2} determined that TMA-GLY coated Li electrodes can be cycled for much longer than either TMA-H_2O or TMA-EG coated electrodes. To unravel the reason for this, gravimetric intermission titration technique (GITT) is conducted on coated electrodes to deconvolute the effects of stripping and plating of Li. Additionally, following cycling, electrode morphology was examined using SEM while Rutherford backscattering spectroscopy is used to reveal the compositing of the solid electrolyte interphase. Our results reveal that an MLD coating contributes positively to the formation of a stable SEI layer. This study sheds light on the role of ALD and MLD coatings in generating a stable SEI layer with continued cycling.

*A version of this chapter is being prepared for publication.

7.1 Introduction

The use of metallic Li as an anode has tremendous potential in significantly increasing the gravimetric and volumetric energy density of Li-based batteries. Li metal anodes have a theoretical capacity of 3860 mA h g^{-1}, a low redox potential of -3.040 V vs standard hydrogen electrode (SHE) and a low density of 0.59 g cm^{-3}. Thus, the successful incorporation of this material as an anode, would impart energy storage devices with high energy density [1], [2]. The use of metallic Li anode has been under investigation since its initial proposal in 1976 [3]. However, due to several critical safety issues, commercialization of Li metal batteries was hindered and the use of graphite as an anode for Li-ion batteries was realized instead. Although graphite based batteries have attained commercial success in the field of portable electronics, and recently in electric vehicles, the increasing need for high energy density storage devices cannot be quenched by this material. This necessity has revitalized research and development of metallic Li electrodes. Furthermore, next-generation batteries, such as Li-S, Li-air, and solid-state Li batteries, require the use of Li metal as an anode. Before these promising systems can attain commercial success, several issues surrounding the use of Li metal must be addressed. The first, and one of primary concern, is the uncontrolled growth of the solid electrolyte interphase (SEI). Li metal is highly reductive and reaction with electrolyte is inevitable, especially at low voltage potentials. This results in the accumulation of mossy-like reaction products on the surface at the interface between the electrode and electrolyte. The uncontrolled SEI formation rapidly consumes electrolyte and causes low columbic efficiency. This issue is exacerbated by the continual growth of Li dendrites which expose fresh Li to electrolyte and causes further side reactions to occur. Additionally, Li dendrites can growth and penetrate the separate, resulting in short-circuiting [4]–[6]. Given that the electrolyte employed in these battery systems have low flash points, and are extremely volatile, the occurrence of short circuits poses a significant threat to device safety.

It has been proven that the stabilization of the SEI layer is a key factor toward improving the lifetime and reducing the growth of dendrites for Li metal anode. Several different strategies have been explored to try and mitigate these issues. The use of electrolyte additives has seen some promising results in suppressing dendrite growth and reinforcing the surface of Li in terms of in-situ formation of a strong SEI layer on the surface of Li metal. These additives include vinylene carbonate [7], Li polysulfides [8], various Li salts as well as ionic liquids [9]–[12]. A particularly

interesting study conducted by Ding et al [13] demonstrated the use of a self-healing electrostatic shield to influence the plating of Li. This method introduces electrolyte additives with a metal cation that have an effective reduction potential lower than Li^+. As a result, during Li deposition, the deposited cations will repel incoming Li^+ ions and force them to be deposited in a more uniform manner. However, the use of electrolyte additives is limited. After a certain number of cycles, additive components will eventually be consumed into the solid electrolyte interface (SEI), rendering them inactive [14], [15]. Coating strategies have also been investigated in preventing direct contact between Li and the electrolyte. Both chemical and physically stable barriers have been investigated to control reactions at the interface between Li metal and the electrolyte. These coating materials include polymer membranes [16], [17], ceramic electrolytes [18], [19], two-dimensional boron nitride [20], graphene [21], [22], and carbon nanospheres [23]. However, many approaches are performed on the different substrates and have not been directly applied to Li foil. Meanwhile, the low ionic conductivity and large interfacial resistance of these materials limit their use. Furthermore, these strategies fail to address the issue of uneven Li electrodeposition.

Atomic layer deposition (ALD) is a thin film deposition technique that has been widely applied to the field of Li batteries. This technique is based on self-limiting chemical reactions between gaseous precursors and a substrate, allowing for angstrom level control over film thickness and composition over high aspect ratio substrates. Furthermore, compared to other gas phase deposition techniques, ALD materials can be deposited at relatively low temperatures with accurate thicknesses. Due to these unique characteristics, ALD has been used to modify the surface of cathode electrodes for Li ion batteries with various metal oxides such as Al_2O_3, TiO_2, and ZrO_2 as well the solid-state electrolytes, like $LiTaO_3$.[24]–[28] Recently, ALD has been applied to protecting the surface of Li metal for Li ion and Li sulfur batteries. Kozen et al [29], firstly demonstrated the protection of Li metal using plasma enhanced ALD to form a thin film of Al_2O_3 by using trimethylaluminum (TMA) and oxygen plasma. Using this method, enhanced capacity retention for Li sulfur batteries was demonstrated. Shortly after, Kazyak et al [30], also presented studies for the protection of Li using ALD Al_2O_3. Their investigation used H_2O to oxidize surface bound TMA rather than oxygen plasma. Based on their analysis, Li coated with 20 cycles of TMA-H_2O could double the lifetime of Li cycled at a current density and capacity of 1 mA cm^{-2} and 0.25 mAh cm^{-2}, respectively. Their study verified that Al was still present on the surface following electrochemical cycling, insinuating that the ALD film remains intact and that Li can diffuse

through Al_2O_3. However, with continued cycling, the amount of Al present at the surface, confirmed by XPS analysis, was less than 1%. Interestingly, the authors noted that simple thermal treatment and exposure of Li metal to the ALD reaction chamber, without any chemical constituents, enhanced the cyclability of Li. This observation implies that coating on Li metal is complex and involves numerous reactions occurring simultaneously. Following this work, Chen et al [31], addressed some very important questions surrounding the influence of Al_2O_3 on the stripping and plating kinetics of Li. Similar to previous ALD studies on Li metal, this research team also established that ALD Al_2O_3 using 20 cycles of TMA-H_2O can prolong the lifetime to metallic Li. Furthermore, this team was able to confirm that Li ions can diffuse through the coating and deposit on the underlying Li. They also provided important insight on the influence of electrolyte volume on Li cyclability. Based on these studies we expand the protection of Li by using molecular layer deposition (MLD). Unlike ALD, which involves the deposition of inorganic materials, MLD is conducted to deposit organic polymeric materials. This technique is similar to ALD and is also based on sequentially pulsing in gaseous precursors with self-limiting characteristics with a purge step introduced between each precursor dose. Furthermore, ALD and MLD can be conducted concurrently to produce mixed inorganic-organic hybrid materials with unique properties. Dameron et al [32], first presented the possibility of depositing metal alkoxide films by reacting TMA with ethylene glycol (EG) to produce an "alucone" film. Since then several other inorganic-organic materials have been produced using MLD [33]–[37]. These materials have been shown to demonstrate several unique properties such as increased flexibility [38], variable electronic [34] and thermal conductivity [37], and tunable hardness [39]. Inspired by this, our group reported the use of MLD alucone (EG) as a coating for Li metal foil in both ether and carbonate based electrolyte, in which the MLD film shows better performances than ALD coated Li or bare Li foil. Furthermore, Zhao et al [40], first demonstrated the use of MLD for protecting sodium metal during electrochemical cycling. These promising results demonstrate that using a thin layer of TMA-EG can effectively suppress dendrite formation and significantly improve the longevity of sodium. However, alucone films made with TMA-EG are typically porous and have low growth rates due to bifunctional nature of EG and results in double side reactions occurring and blocking of reactive sites [41], [42]. To overcome the issue of blocked reactive sites, alucone films can be made using TMA with glycerol (GLY). Unlike EG, GLY has three possible sites for reaction, resulting in decreased film porosity and increased film density. Additionally, the

crosslinking nature imparted by GLY results in increased film robustness [35]. Based on this, Piper et al [43], used TMA-GLY films to improve the cyclability of nano-Si in Li-ion batteries. Si is a promising anode material for Li ion batteries, however, similar to Li metal anodes, uncontrollable SEI formation and large volume expansion render commercialization of Si difficult. By employing the use of a robust MLD film, this group demonstrated that TMA-GLY films can prolong the cyclability of Si. The same group then used in-situ TEM to discover that the MLD coating process itself alters the surface if Si and allows for the formation of a more favorable and stable SEI layer [44]. The MLD TMA-GLY coating was found to effectively facilitate fast and thorough reversible lithiation compared to the native film found on Si.

Based on these studies, we firstly apply the MLD film of TMA-GLY as protective layer for Li metal anode and evaluate the galvanostatic stripping and plating performance of TMA-GLY coated Li electrodes and compare the results to Li electrodes coated with TMA-EG and TMA-H_2O. Galvanostatic intermission titration technique (GITT) is used for the first time to characterize and deconvolute the effects of stripping and plating of Li on these films. We use this technique in a unique half-cell configuration to determine the influence of plating on ALD and MLD films vs stripping from them. By conducting this type of experiment, the effects of stripping and plating can be deconvoluted and the strength and weaknesses of each ALD and MLD film can be identified. Finally, RBS and SEM measurements are conducted to provide insight as to how these thin films influence deposition characteristics and the state of the deposited film following electrochemical cycling.

7.2 Experimental

Electrode preparation: Pre-cut Li foil with a diameter of 12 mm and a thickness of 0.4 mm was used for all experiments and was stored inside an argon-filled glovebox. Atomic and molecular layer deposition was conducted using a commercially available Gemstar-8 ALD system (Arradiance, USA) that is interfaced with an argon-filled glovebox. Li foil was pressed and brushed prior to deposition. The electrodes were placed into the chamber and pumped down to a pressure of ~ 800 mTorr at a flow rate of 25 sccm using 99.999% Ar (Praxair) as a carrier gas. All depositions were conducted at 150°C. TMA-H_2O films were produced by alternating doses of trimethylaluminum (TMA) and water (H_2O) using a pulse-purge-pulse-purge program of 0.01s/40s/0.01s/40s. TMA-EG films are produced using the same program with ethylene glycol

(EG) as an oxidizing agent to produce alucone films. EG was kept in an external reservoir set to 90°C while the oxidizing manifold was held at 120°C. TMA-GLY films were produced by sequentially introducing TMA and glycerol (GLY) into the chamber using a program of 0.01s/40s/0.5s/60s. GLY was kept in an external reservoir set to 140°C while the oxidizing manifold was heated to 150°C.

Electrochemical measurements: Electrochemical analysis was performed using CR2032 coin-type cells. Cells were assembled in an argon-filled glovebox using a symmetrical Li/electrolyte-separator/Li configuration with a polypropylene separator (Celgard 2400). The electrolyte used in this study was 1M $LiPF_6$ dissolved in ethylene carbonate (EC), diethyl carbonate (DEC) and dimethyl carbonate (DMC) in a 1:1:1 volume ratio. Li stripping and plating studies were carried out using an Land 2001 (Wuhan, China) battery testing station. Galvanostatic cycling was applied to electrodes while potential was recorded over time. Gravimetric intermission titration experiments were conducted using the same battery testing station. For these experiments a current density of 5 mA cm^{-2} was applied for 15 s followed by a 3-minute rest period until a capacity of 5 mAh cm^{-2} was attained.

Characterization: SEM images were taken using a Hitachi 3400N environmental Scanning Electron Microscope (SEM) operating at an acceleration voltage of 5 kV. Prior to imaging, cells were disassembled in an argon filled glovebox using plyers. Electrodes were then thoroughly washed with ethyl methyl carbonate (EMC) to remove residual salt left on the surface. Samples were loaded into containers and wrapped with parafilm to prevent air exposure and transferred into the SEM chamber. Rutherford backscattering spectroscopy measurements were conducing using 2.5 MeV He^+ beams (Western Tandetron Facility) at several locations on the surface to confirm uniformity. All samples were transferred in an Ar-filled glove bag. An Sb-implanted amorphous Si sample with a known concentration of Sb atoms (4.82×10^{15} atoms cm^{-2}) was used for calibration.

7.3 Results and Discussion

7.3.1 Galvanostatic cycling of Li-Li symmetric cells

Galvanostatic Li-Li symmetrical cell testing was performed to determine the extent of protection imparted by three different ALD and MLD coatings. All films employ the use of TMA with different co-reactant molecules, water (H_2O), ethylene glycol (EG), and glycerol (GLY). All

films were deposited at a temperature of 150°C. In our previous work, we determined that 50 cycles of TMA-EG on Li metal was sufficient in extending the cyclability of Li in carbonate-based electrolyte at the current density of 1 mA cm^{-2} with the capacity of 1 mAh cm^{-2}. However, the performance of TMA-EG coated Li under high current density with high capacity was still unsatisfactory. Based on this, all cells tested had 50 cycles of either TMA-H_2O, TMA-EG, or TMA-GLY deposited on the surface of Li. Although the growth rate for these films may be slightly different, the role of film thickness is not the primary property under investigation. Rather, the primary research question is the effect of film composition on prolonging the cyclability of Li in carbonate-based electrolyte systems.

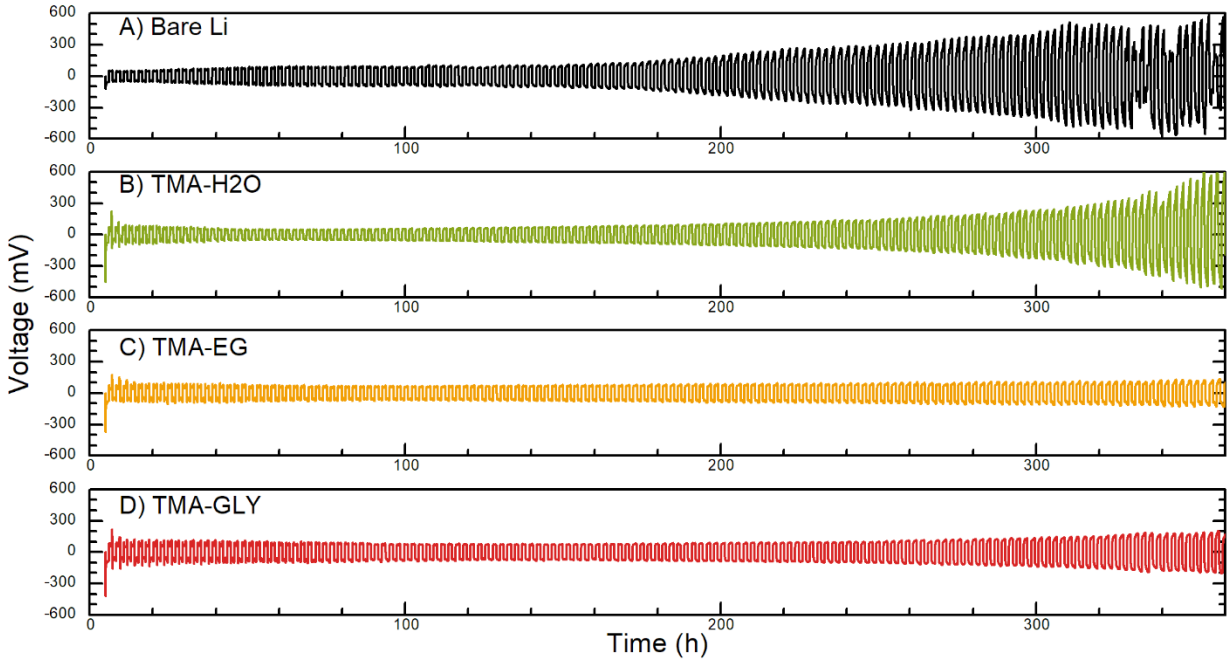


Figure 7.1. *Galvanostatic cycling of Li-Li symmetric cells at a current density of 1mA cm^{-2} until a capacity of 1mAh cm^{-2} is reached. Cells are cycled in EC/DEC/DMC electrolyte with 1M $LiPF_6$*

Figure 7.1 presents Li-Li symmetrical cell cycling data for protected Li foil (TMA-H_2O, TMA-EG and TMA-GLY) along with bare Li at a current density of 1 mA cm^{-2} and a capacity of 1 mAh cm^{-2}. After about 200 hours of cycling, voltage curves for bare Li cells begin to demonstrate an “arching” behavior, rather than the “peaking” behavior observed at the start of galvanostatic cycling (Figure 7.1a). Chen et al [45], identified that the root cause for arching voltage hysteresis is accumulation of dead Li on the surface. This thick layer of non-active material results in Li ions venturing through a tortuous path to reach the surface, giving rise to increasing overpotential.

Characteristically, bare Li cells display increasing overpotential until about 320 h, after which erratic and fluctuating voltage potential curves begin to appear. This behavior has been typically assigned to dendrite-induced soft circuits occurring within the cell [46]. Furthermore, as inactive material accumulates on the surface, electrolyte is consumed and causes rapid battery failure. Several reports have indicated that a lack of available electrolyte ultimately causes cell death [47]–[49]. The highly porous nature of the accumulated inactive material on the surface of Li results in rapid electrolyte decomposition, eventually causing the cell to become dry and leads to facile soft short circuiting to occur as well as the appearance of rapid voltage fluctuations during galvanostatic cycling. By prolonging the onset of this type of behavior, the cyclability of metallic Li can be enhanced. Interestingly, using a coating of either TMA-H_2O, TMA-EG or TMA-GLY, the lifetime of Li electrodes can be improved with a lower overpotential and decreased resistance during cycling. Among them, TMA-GLY and TMA-EG coated electrodes displaying the most stable performance. Close observation of the first discharge potential for coated electrodes reveals an increased overpotential compared to bare Li. Given that the cells tested are symmetrical, any overpotential observed originates from plating and stripping behavior of Li. This increased overpotential during the initial discharge stems from stripping and plating kinetics of the deposited ALD of MLD film. Similar to studies presented by Kozen et al [29], the increased initial energy requirement is due to preliminary lithiation of the film and only occurs during the first cycle. Additional galvanostatic cycling tests can be found in the supporting information (Figure.S7.1 and Figure.S7.2) where cells are cycled at 3 mA cm^{-2} and 5 mA cm^{-2} using a capacity of 1 mAh cm^{-2}. With increased current densities, the TMA-GLY coated Li electrodes still demonstrate the best performance and longest lifetime compared to TMA-EG, TMA-H_2O and bare Li foil. Briefly, the inorganic-organic hybrid MLD coatings (TMA-GLY and TMA-EG) indicate better performance and enhanced lifetime compared with ALD coating (TMA-H_2O and bare Li), which can be attributed to the highly flexibility and robust structure of the MLD film. More promisingly, with organic linker of GLY demonstrate much better performance than EG, which can be explained by the increased crosslinking structure from the TMA-GLY film.

To further evaluate the performance of coated Li electrodes, galvanostatic symmetrical testing using increased capacity and current density was conducted. Figure 7.2 presents symmetrical cell testing data for bare and coated Li using a higher current density of 3 mA cm^{-2} and capacity of 2 mAh cm^{-2}. These harsh conditions result in rapid failure for bare Li metal, with

signs of soft short-circuiting occurring after 50 h of cycling. In comparison, the stable cycling time of the TMA-H_2O and TMA-EG coated Li electrodes can be extended into 65 h and 80 h, respectively. Promisingly, TMA-GLY coated electrodes, on the other hand, do not start displaying arching behavior until about 80 h into cycling. Furthermore, although a slight decrease in overpotential is observed around the 100 h mark, signs of fluctuating voltage are not observed for the entire duration of 120 h of cycling. In this case, our new design of TMA-GLY can employ very stable performances under high current density with high capacity, which will be very promising for the future practical applications.

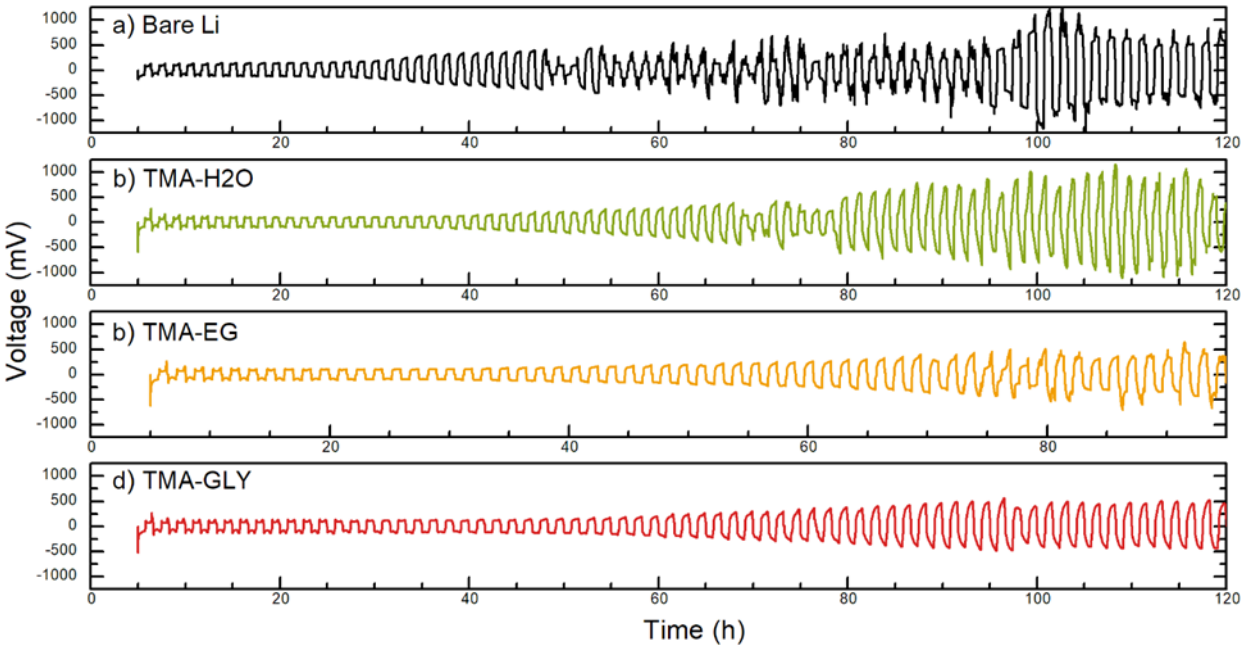


Figure 7.2. *Galvanostatic cycling of Li-Li symmetric cells at a current density of 3 mA cm^{-2} until a capacity of 2 mAh cm^{-2} is reached. Cells are cycled in EC/DEC/DMC electrolyte with 1M $LiPF_6$*

Clearly the TMA-GLY coated Li electrodes display the lowest overpotential, posing the question, why can TMA-GLY films display such stable performance compared to TMA-EG and TMA-H_2O films? Furthermore, an area of contention in this field of research is whether the ALD/MLD film remains on the surface following electrochemical cycling. Although Chen et al [45], used in-situ TEM and XPS to determine the nature of the ALD film following electrochemical cycling, both techniques can only investigate very small areas of the electrode. Furthermore, their study was limited to using a current density of 1 mA cm^{-2} and capacity of 1 mAh cm^{-2}, which is quite low

and equates to about ~5 μm of Li deposition [31]. Given that ALD films are in the nanometer regime and Li deposition growth occurs in microns, it is unlikely that the film remains intact following stripping and plating of Li. Additionally, this 5 μm of Li deposition during plating is unlikely to occur evenly across the surface. Several reports have indicated that the growth of Li dendrites is a result of surface inhomogeneities and a buildup of local current, leading to uneven Li plating [50]–[53]. As a result, both stripping and plating will occur unevenly across the surface of Li and both TEM and XPS are unsuitable for tracking this type of behavior.

7.3.2 Galvanostatic Intermission Titration Technique

Galvanostatic intermission titration technique (GITT) is employed to provide insight as to why TMA-GLY films outperform TMA-H_2O and TMA-EG films. GITT is performed by applying a current for a short amount of time and then allowing for a period of rest. This galvanostatic pulsing of current is continued until the desired capacity is achieved. By performing GITT, a quasi-steady-state concentration gradient can be established. Depositing a small amount of Li after long periods of relaxation allows for each Li ion to be platted at near static equilibrium conditions. This means that each ion will experience reduce effects from depletion of ions in the electrolyte at the interphase.[45], [54], [55] By performing GITT, an envelope voltage shape can be formed by connecting the maximum voltages during each current pulse. This voltage shape is similar to the one found during galvanostatic cycling, but is representative of reaction kinetics rather than mass transport effects during cycling. Using GITT, effects related to reaction kinects of lithium electrodissolution or electrodeposition can be extracted rather than the mixture of reaction kinects and mass transport effects. Given that cycling performance at elevated current densities is similar between TMA-H_2O and TMA-EG films, GITT comparison between TMA-GLY and TMA-H_2O films are conducted. For this investigation, GITT experiments were performed using a current density of 5 mA cm^{-2} for 15 s pulse of followed by a 3-minute rest period until a capacity of 5 mAh cm^{-2} was reached.

Prior to tackling the experimental results of GITT, some discussion pertaining to the information provided by voltage hysteresis in Li-Li symmetric cells is required. Figure 7.3 presents the first few cycles of GITT data for bare Li, demonstrating several characteristic voltage peaks. Wood et al [56] provide an excellent description for this behavior and demonstrate that the origin

of this behavior is related to stripping and plating kinetics occurring at both the anode and cathode. During the very first cycle a large initial overpotential is observed (section 0-a in red, Figure 7.3). This can be attributed to the overpotential required to remove Li from electrode b (E-b) and plate it to electrode a (E-a). The extent of this initial peak can be linked to the energy required to plate Li on the native surface layer of E-a. This native surface layer may be formed during manufacturing and storage as well as exposure to electrolyte [6], [57]. The overpotential required for this first half cycle is then a mixture of creating pits at E-b as well as nucleation and growth of Li at E-a. Upon reversal of cell polarization, a sharp increase in voltage is observed, highlighted in green in Figure 7.3 and labeled as 1-b. This is caused by electrodissolution of Li from dendrites formed on E-a. However, much of the energy required here is associated with plating characteristics at E-b. Following this, cell voltage decreases as energy required for dendrite nucleation on E-b decreases and the surface becomes easier to plate on, this is marked as region 2-b in Figure 7.3. The length of time for this region is characterized by the amount of time required to completely strip Li from dendrites produced at E-a during the first half cycle, section 0-a. Once Li has been stripped from previously deposited Li on E-a, another sharp increase in overpotential is observed and is labelled as 3-b. This increase in overpotential is attributed to the energy required to switch from stripping from deposited Li to stripping from the surface of E-a, resulting in the generation of pits. Although the reactions occurring during 3-b are quite complicated, the overpotential here can simplistically thought of as the energy barrier that exists between stripping from the SEI to surface Li, at E-a. It is also during section 3-b that dead and inactive material is formed on the surface of E-a. Once the desired capacity has been achieved, cell polarization will reverse, and the entire process is repeated on the opposite electrode. This behavior is repeatable and three distinct sections can be seen in the envelope of the GITT data. However, as shown in Figure 7.3c, distinguishing between section 2 and 3 becomes increasingly difficult with prolonged cycling. Due to an accumulation of inactive material on the surface, the overpotential required to switch from previously deposited Li to bulk Li becomes less dependent on reaction kinetics and more dependent on mass transfer effects [45], [58]. Furthermore, with increasing cycling, overpotential required also increases. This insinuates that a thick layer of material is being deposited on each side of the cell and requires a large amount of energy for equilibrium to be reached during each current pulse.

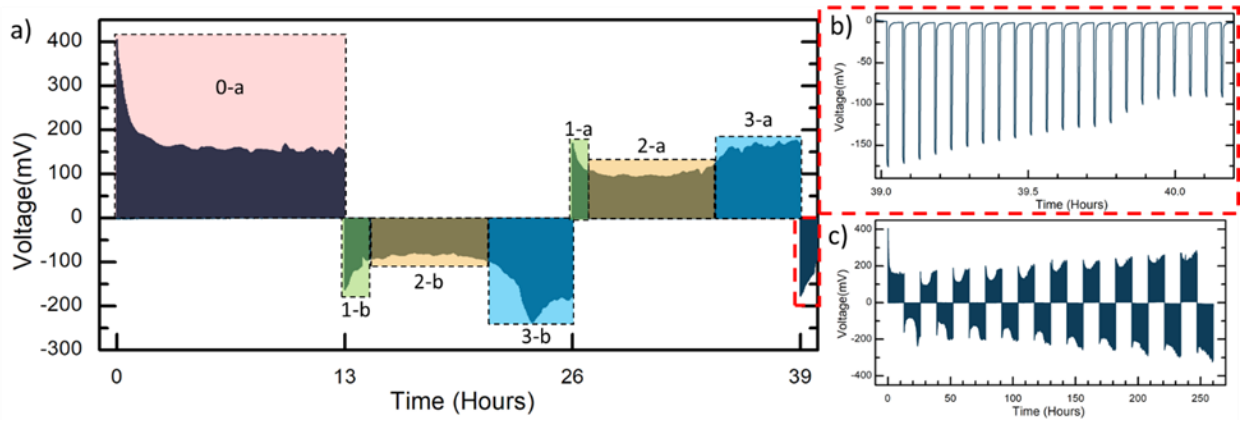


Figure 7.3. *a) First few cycles of GITT data for bare Li outlining an envelope voltage pattern. b) Cells are cycled using a 15 s current pulse at a density of 5 mA cm^{-2} followed by a rest period of 3-minutes until a capacity of 5 mAh cm^{-2} is attained. C) 10 GITT cycles for bare Li cells.*

Based on this understanding, GITT experiments were conducted using TMA-H_2O and TMA-GLY coated Li electrodes. However, instead of using a symmetrical configuration, a half-cell configuration was used with one electrode being coated while the other electrode is bare, untreated Li. By using this configuration, insights can be gained regarding the roll of ALD or MLD coating. For example, TMA-GLY: anode would denote a cell where an MLD coated electrode is placed on the negative end of the coin cell and a bare Li electrode is used as the cathode. Performing GITT on this cell, and observing the voltage behavior in comparison to a symmetrical bare Li cells under the same conditions, details regarding the stripping kinects from MLD films and its influence on plating on bare Li can be obtained. Concurrently, a cell in the configuration denoted as TMA-GLY: cathode will provide insights regarding the plating of Li on MLD films. In this manner, the effects of stripping and plating can be deconvoluted. Furthermore, some insight regarding the nature of reaction products can be attained. Figure 7.4 presents 10 full cycles of GITT data for TMA-GLY (red and yellow) and TMA-H_2O (green and purple) coated electrodes acting as either anode or cathode, against bare Li (dark blue).

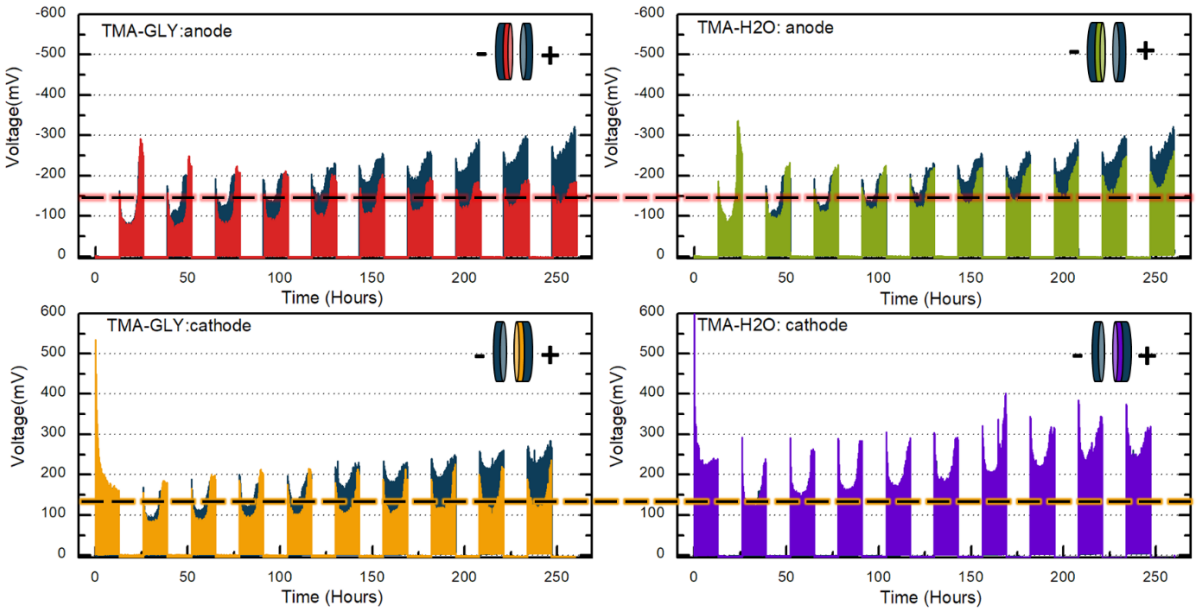


Figure 7.4. *GITT experiments for half-cell configurations of TMA-GLY or TMA-H2O as either anode and cathode against bare Li. Schematic outline for configuration employed can be found at the top right corner of each graph.*

This experiment provides some very interesting information and really highlights the difference in reaction kinetics occurring for these two films. Starting with TMA-GLY: anode, compared to bare Li, the overpotential in the second half-cycle, for section 1-b and 2-b, is virtually identical, meaning that plating in the pits formed under TMA-GLY is not a kinetically difficult process. However, TMA-GLY electrodes demonstrate an increased overpotential for section 3-b compared to bare Li. As mentioned earlier, this voltage increase is correlated with the energy barrier required to switch from dissolution of Li from dendrites to pits. It is interesting that an increase in overpotential is seen here since the contribution to overpotential here should predominantly originate from the bare Li surface and not the coated one. Furthermore, this behavior is observed for the TMA-H_2O: anode cell as well. Continued GITT cycling of TMA-GLY: anode reveals that a more stable SEI layer is formed compared to bare Li. By the fourth half cycle, region 2-b has a lower overpotential and the onset of region 3-b occurs later compared to bare Li. Furthermore, this behavior is continued with cycling. Additionally, the overpotential for region 1-b of TMA-GLY: anode remains consistent and stays between 150-200 mV (Li^+ vs Li). This is in stark contrast to bare Li, where all three regions demonstrate increasing overpotential with increased GITT cycling. This is also seen for TMA: H_2O: anode cells and is characterized by decreasing length of time for

region 2-b as well as a blurring of region 2-b and 3-b into a single increasing sloping overpotential. As pointed out by Bieker et al [58], this behavior stems from Li electrodissolution taking place on a rough Li surface that is covered by a thick layer of electrically isolated Li. Furthermore, the initial distinct nature between region 2-b and 3-b is rooted in deposition occurring on smooth, low surface area Li substrate [59]. This implies that for TMA-GLY: anode, a smooth Li surface remains following repeated plating and stripping compared to bare Li and TMA-H_2O: anode. The difference between the two coated electrodes in this anode configuration is highlighted by the glowing red black dashed line.

Moving on to the cathode configuration, a dramatic difference in voltage characteristics can be observed. Region 0-a for TMA-GLY and TMA-H_2O cathode cells display an overpotential requirement that is greater than bare Li. This is to be expected as both films are inherently electronically and ionically insulating. This overpotential can be thought of as the energy required to lithiate the deposited film. Interestingly, plating on TMA-H_2O seems to require more energy compared to TMA-GLY. Furthermore, the overpotential required to plate on TMA-GLY decreases quickly from 530 mV to 170 mV. This contrasts with TMA-H_2O which requires an initial overpotential of 620 mV and plateaus at 225 mV. This observation is a strong indicator that lithiation of aluminum oxide s is more difficult than TMA-GLY films and is in accordance with results presented by previous research [40], [44], [60]. Subsequent cycling reveals that plating on aluminum oxide requires more energy than bare Li. This is a strong signal that nucleation of dendrites is difficult on ALD Al_2O_3. In the third half cycle, TMA-H_2O: cathode requires an overpotential of 300 mV for initial dendrite nucleation (region 1a), whereas bare Li requires an overpotential of only 170 mV and is similar to TMA-GLY: cathode. This trend continues for TMA-H_2O coated Li and consistently demonstrates a requirement of increased overpotential for all regions of Li plating compared to bare Li. TMA-GLY: cathode electrodes on the other hand demonstrate reversible stripping and plating behavior with an overpotential requirement that is lower than bare Li. Following the 11^{th} half cycle, a dramatic difference in region 2-a and 3-a can be seen between TMA-GLY cathode and bare Li. To highlight this a glowing yellow black dashed line is added to Figure 7.4. This behavior is consistent with observations seen for TMA-GLY: anode electrodes and implies that both Li plating and stripping of this film results in a kinetically favorable surface layer that is relatively smooth and uniform. These observations also imply that plating on TMA-H_2O is a kinetically difficult process that results in the formation of an SEI film

that is rough in morphology and is both electrically and ionically insulating. By using GITT we can see the big difference in using ALD or MLD films in either an anode or cathode configuration. This technique provides valuable insight toward the reaction kinetics of lithium electrodissolution and electroplating. From these experiments is can be seen that both stripping and plating is a facile process on TMA-GLY coated Li. For TMA-H2O coated Li, however, a strong difference between stripping and plating can be seen. From our observation it seems that plating on TMA-H2O coated Li is more difficult and requires an increased overpotential compared to stripping. This increase in overpotential is result in rapid decomposition of electrolyte as well as changes to the composition of the SEI.

7.3.3 Morphology Analysis by Scanning Electron Microscopy

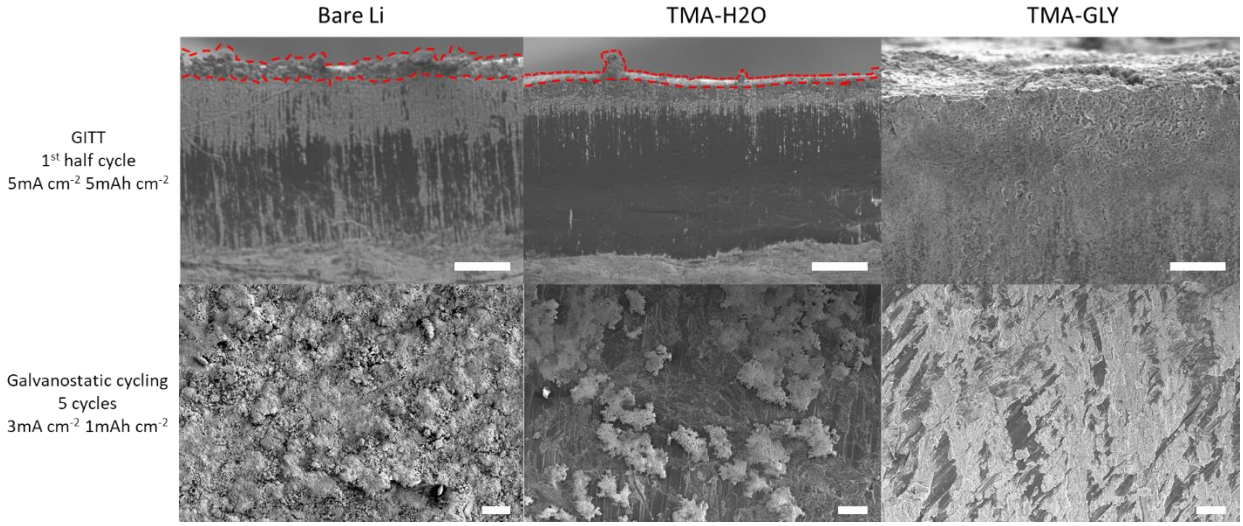


Figure 7.5. *Cross section SEM images of Li surface following 1st half cycle (0-a) using GITT (top row) and top view SEM images of the same electrodes after 5 galvanostatic cycles. Scale bar in white represents 100 μm. Red dashed line outlines the thickness of the SEI layer*

To better understand the improved performance of TMA-GLY coated Li electrodes compared to bare Li, morphology changes of electrodes following cycling was analyzed using SEM. Figure 7.5 compares the SEM images of bare Li, TMA-H_2O coated Li and TMA-GLY coated Li. The top row shows morphological differences under the cross-section views after the first half cycle using GITT. From the images presented above, bare Li shows the growth of a mossy, dendritic surface that has high surface roughness and is characteristic of porous SEI

material. This is also seen in the row below after 5 cycles of galvanostatic cycling at 3 mA cm^{-2} using a capacity of 1 mAh cm^{-2}. This type of mossy/dendritic Li leads to the formation of dead Li during the plating/stripping process and consumes Li. Furthermore, the high surface area of this SEI will also result in rapid consumption of electrolyte, leading to low coulombic efficiency. Compared to bare Li, both coated electrodes show a decrease in the amount of mossy, porous material and is highlighted by a red dashed line. Although the TMA-H_2O coated Li electrodes present some mossy, dendrite material, it is to a lower extent than to bare Li. Interestingly, with an MLD coating, the surface morphology of electrochemically cycled Li is relatively smooth and does not appear to have a buildup of mossy material. Furthermore, cross section images show that virtually no gap exists between plated Li and bulk Li, indicating a uniform electrochemical deposition process. Additionally, top view images of galvanostatically cycled TMA-GLY coated Li, indicates uniform Li plating and stripping. These results further confirm that plating and stripping on MLD films occurs in a uniform and consistent manner compared to ALD films. Based on GITT data, lithiation of MLD films occurs readily to form a more stable SEI layer that is conducive to large volume changes.

7.3.4 Rutherford Backscattering Spectroscopy

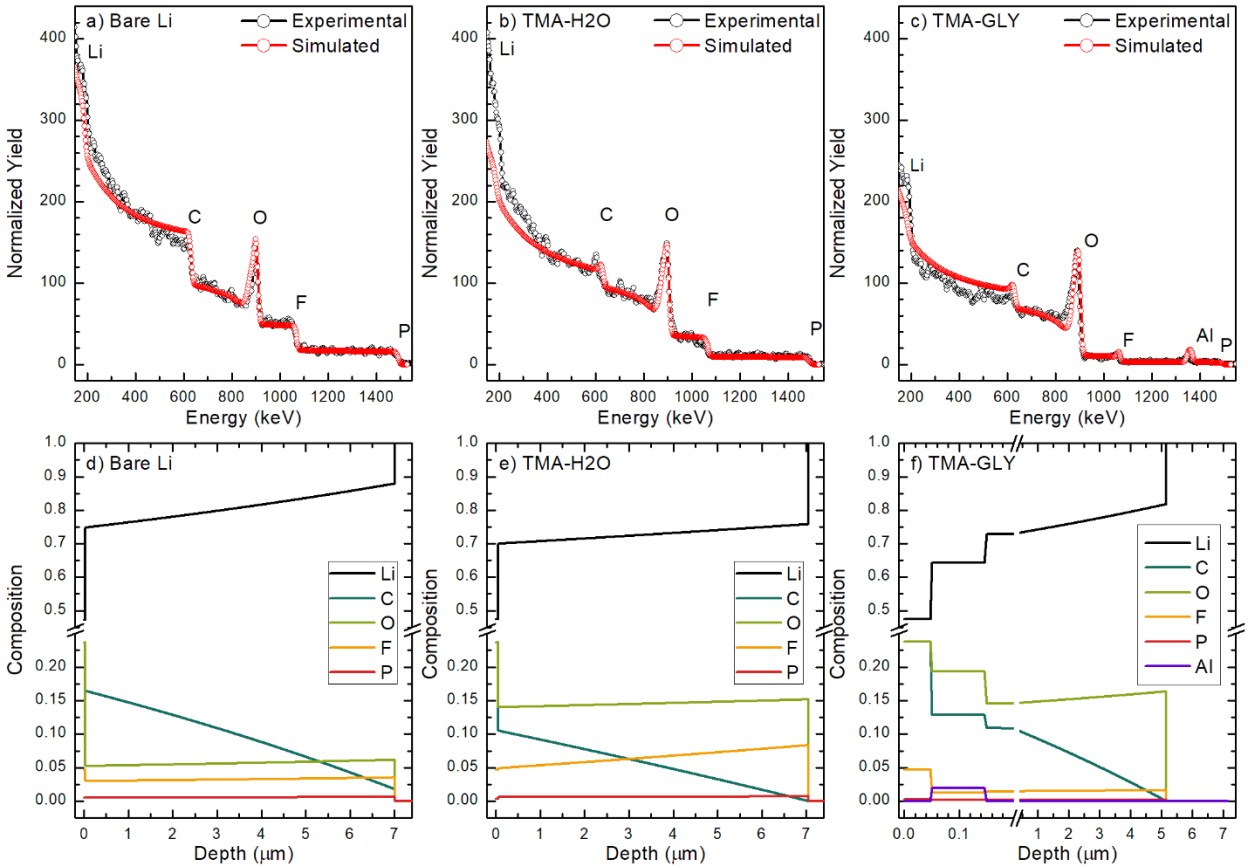


Figure 7.6. *RBS spectra and calculated depth profile for bare Li (a, d), TMA-H_2O coated Li (b, e), and TMA-GLY coated Li (c, f) following 60 cycles of plating and stripping at 3 mA cm^{-2} using a capacity of 2 mAh cm^{-2}.*

Rutherford backscattering spectroscopy (RBS) was carried out to determine the surface chemistry of the SEI layer following galvanostatic cycling in carbonate based electrolyte. Since we wanted to determine the robustness of the coating layer, extended cycling using high current density and capacity was performed. Following 60 cycles of Li stripping/plating process at 3 mA cm^{-2} using a capacity of 2 mAh cm^{-2}, cells were disassembled and washed with EMC to remove residual salt left on the surface. RBS testing was then carried out and the results are presented in Figure 7.6. RBS data for all samples indicate the presence of Li, C, O, F, and P as expected since a carbonate based electrolyte is used and $LiPF_6$ is used as a salt [61]. All electrodes show an increase in carbon content at the SEI-electrolyte interface. As you approach the SEI-Li electrode interface, the amount of carbon gradually decreases. This is consistent with reports in literature of

a polyhetero microphase SEI with an porous organic layer consisting of polyolefin and semi-carbonate species that covers most of the surface of the compact SEI which is composed of inorganic compounds [62]–[65]. Interestingly, only the TMA-GLY coated Li electrode presents evidence of Al buried within the SEI layer following galvanostatic cycling. Although no Al can be found in the TMA-H_2O coated Li electrode, the composition of the SEI for this sample is quite different than bare Li. This observation provides evidence that although the ALD film may no longer be intact, a significant contribution is made to the composition and formation of the SEI layer. The appearance of fluoride based species likely stems from LiF caused by the reduction of $LiPF_6$ salt and has been shown to play a key role in the Li passivation mechanism. LiF is a thermodynamically stable compound that is a good cationic conductor and having this species in the SEI promotes uniform Li deposition and electrodissolution [64]. Provided that the electronic and ionic conductivity on aluminum oxide is quite low, a large overpotential is required to lithiate the film. This large overpotential may result in rapid reduction of $LiPF_6$ salt and therefore an increase in the appearance of fluorine close to the SEI/electrode interface. Even more interesting are the results observed for TMA-GLY coated Li electrodes. The MLD coated electrodes display an SEI layer that is 2 μm thinner than either bare Li or TMA-H_2O coated Li. Furthermore, an Al signal is detected near the surface of the SEI layer, about 40 nm below an inorganic layer of Li, F, and O. This is consistent with results presented previously demonstrating that Li can pass through the aluminum MLD layer [66]–[68]. RBS analysis indicates that the thickness of this MLD aluminum layer is ~ 110 nm. This is much thicker than the original layer and is consistent with observations made by other researchers demonstrating successful lithiation of alucone MLD. Given the great mechanical flexibility and Li conductivity of TMA-GLY films a stable SEI layer can be created on the surface of Li that remains intact with large volume changes [44]. Furthermore, the MLD process alters the composition of the SEI layer and creates a surface that allows for uniform Li electrodeposition and electrodissolution.

7.4 Conclusions

In conclusion, we demonstrate the first comparison of Li coated with TMA-H_2O, TMA-EG and TMA-GLY. Galvanostatic cycling of Li-Li symmetric cells at various current densities with different capacity identified that TMA-GLY films significantly improve the lifetime of Li

compared to TMA-H_2O or TMA-EG films. By using half-cell configurations of coated Li vs bare Li, GITT was able to identify that plating on TMA-H_2O films requires a much higher overpotential compared to TMA-GLY films. Furthermore, we were able to identify that stripping from TMA-GLY films is an easier process than for ALD TMA-H_2O films. Meanwhile, morphologies of the Li surface was observed via SEM following electrochemical cycling and indicated that the TMA-GLY coating results in uniform deposition of Li and a thinner SEI layer. Furthermore, RBS analysis concluded that aluminum remains on the surface of Li after long cycling for TMA-GLY coated Li, but was not observed for TMA-H_2O coated electrodes. This observation leads to be conclude that TMA-GLY is a robust film that allows for the formation of a stable SEI layer and is more conducive toward uniform electro-deposition and electro-dissolution of Li metal. These results indicate that MLD is a promising strategy to stabilize Li anodes for next-generation Li-based batteries such as Li-S, Li-air, and all solid-state Li batteries.

7.5 Supporting Information

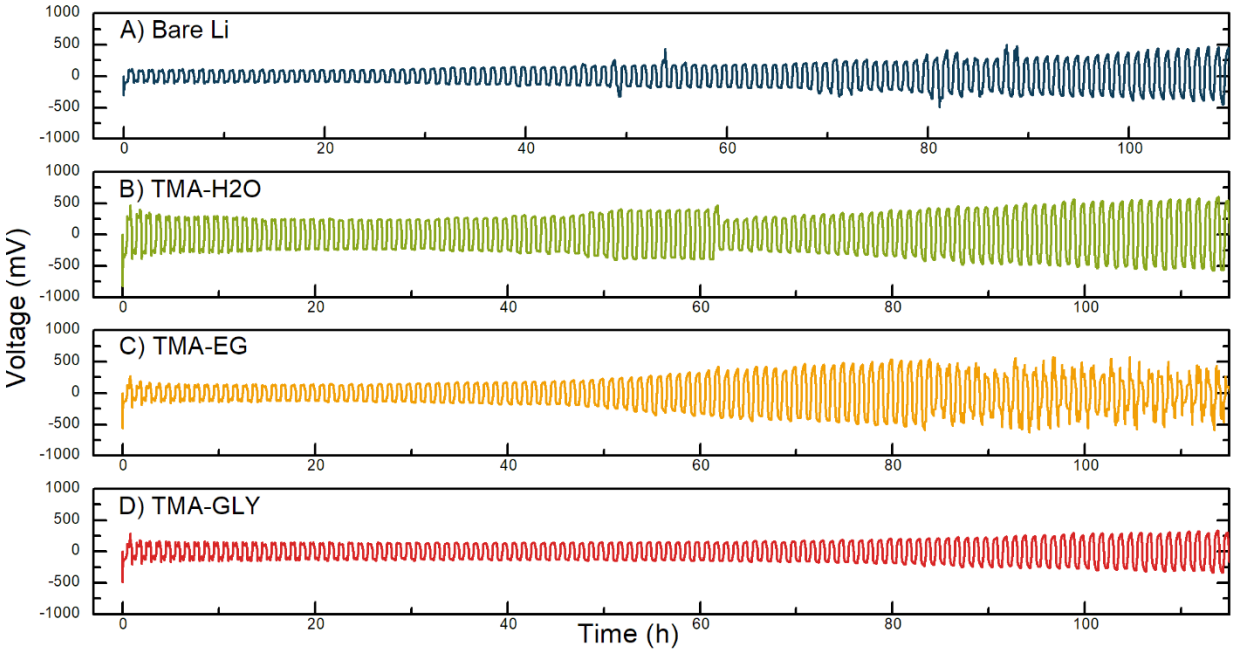


Figure S7.1. *Galvanostatic cycling of Li-Li symmetric cells at a current density of 3mA cm^{-2} until a capacity of 1mAh cm^{-2} is reached.*

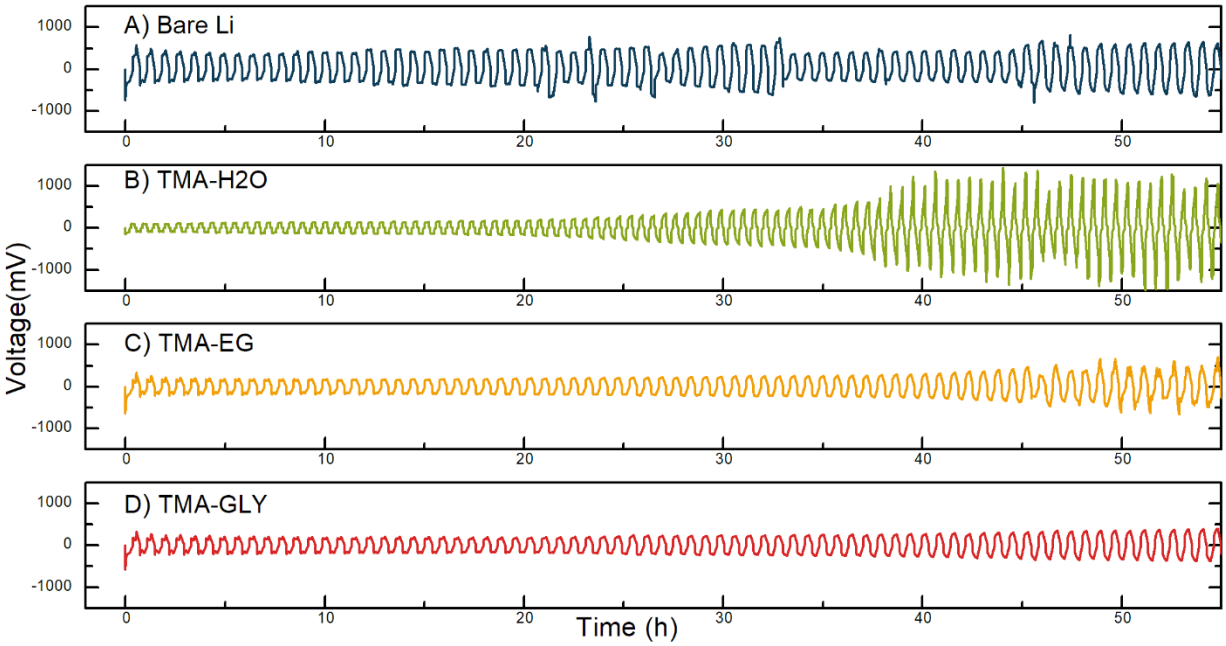


Figure S7.2. *Galvanostatic cycling of Li-Li symmetric cells at a current density of 5mA cm^{-2} until a capacity of 1mAh cm^{-2} is reached.*

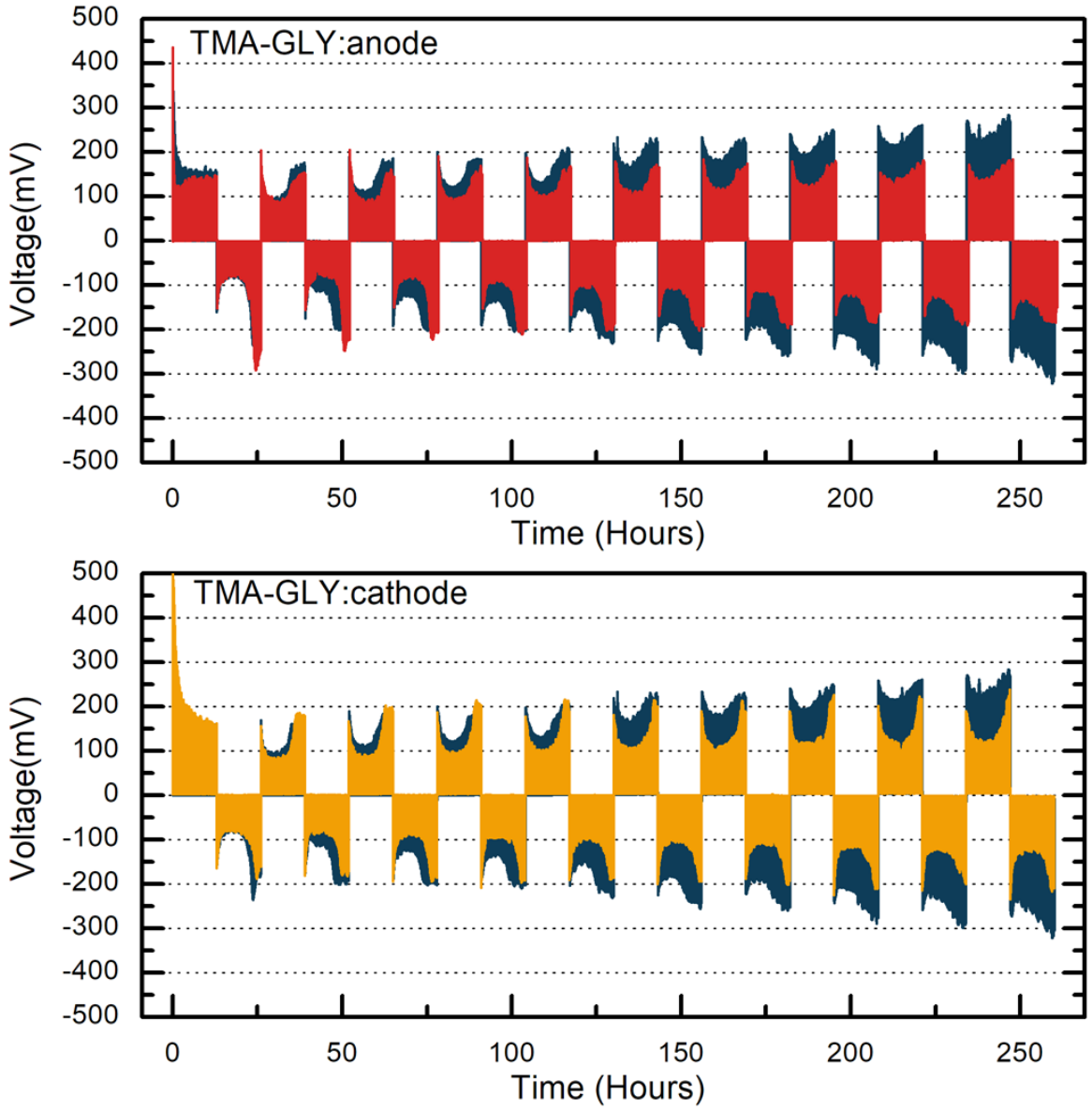


Figure S7.3. *GITT experiments for half-cell configurations of TMA-GLY anode and cathode against bare Li.*

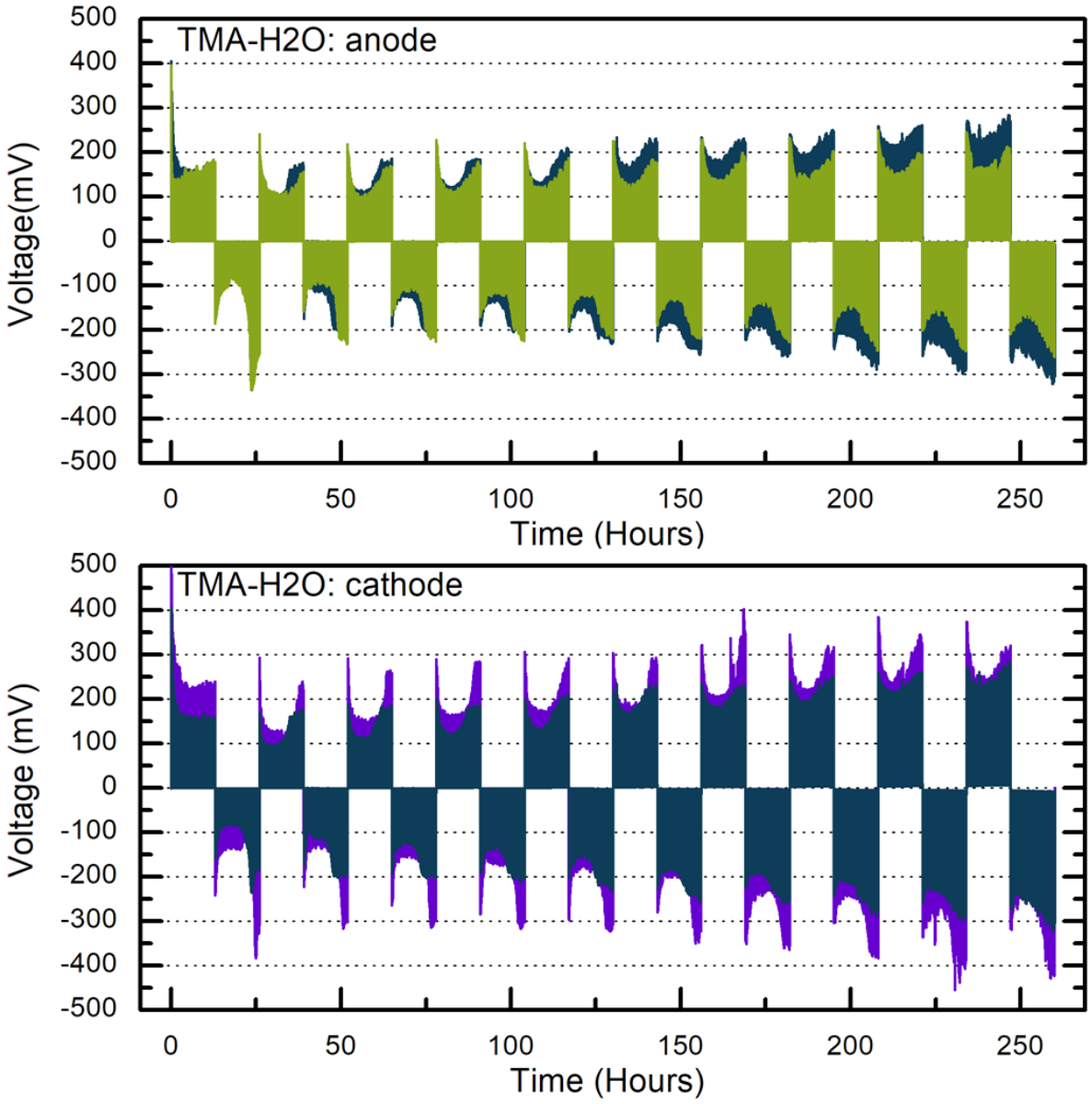


Figure S7.4. *GITT experiments for half-cell configurations of TMA-H2O anode and cathode against bare Li.*

7.6 References

[1] W. Xu *et al.*, "Lithium metal anodes for rechargeable batteries," *Energy Environ. Sci.*, vol. 7, no. 2, pp. 513–537, 2014.

[2] L. Ji, Z. Lin, M. Alcoutlabi, and X. Zhang, "Recent developments in nanostructured anode materials for rechargeable lithium-ion batteries," *Energy Environ. Sci.*, vol. 4, no. 8, p. 2682, 2011.

[3] M. S. Whittingham, "Electrical Energy Storage and Intercalation Chemistry," *Science (80-.).*, vol. 192, no. 4244, pp. 1126–1127, 1976.

[4] J. N. Chazalviel, "Electrochemical aspects of the generation of ramified metallic electrodeposits," *Phys. Rev. A*, vol. 42, no. 12, pp. 7355–7367, 1990.

[5] C. Yang, K. Fu, Y. Zhang, E. Hitz, and L. Hu, "Protected Lithium-Metal Anodes in Batteries: From Liquid to Solid," *Adv. Mater.*, vol. 1701169, pp. 1–28, 2017.

[6] X. B. Cheng, R. Zhang, C. Z. Zhao, F. Wei, J. G. Zhang, and Q. Zhang, "A review of solid electrolyte interphases on lithium metal anode," *Adv. Sci.*, vol. 3, no. 3, pp. 1–20, 2015.

[7] H. Ota, Y. Sakata, Y. Otake, K. Shima, M. Ue, and J. Yamaki, "Structural and Functional Analysis of Surface Film on Li Anode in Vinylene Carbonate-Containing Electrolyte," *J. Electrochem. Soc.*, vol. 151, no. 11, p. A1778, 2004.

[8] C. Yan, X. B. Cheng, C. Z. Zhao, J. Q. Huang, S. T. Yang, and Q. Zhang, "Lithium metal protection through in-situ formed solid electrolyte interphase in lithium-sulfur batteries: The role of polysulfides on lithium anode," *J. Power Sources*, vol. 327, pp. 212–220, 2016.

[9] L. Suo, Y. S. Hu, H. Li, M. Armand, and L. Chen, "A new class of Solvent-in-Salt electrolyte for high-energy rechargeable metallic lithium batteries," *Nat. Commun.*, vol. 4, no. February, pp. 1–9, 2013.

[10] R. Miao, J. Yang, X. Feng, H. Jia, J. Wang, and Y. Nuli, "Novel dual-salts electrolyte solution for dendrite-free lithium-metal based rechargeable batteries with high cycle reversibility," *J. Power Sources*, vol. 271, pp. 291–297, 2014.

[11] J. Qian *et al.*, "High rate and stable cycling of lithium metal anode," *Nat. Commun.*, vol. 6, 2015.

[12] A. Basile, A. I. Bhatt, and A. P. O'Mullane, "Stabilizing lithium metal using ionic liquids for long-lived batteries," *Nat. Commun.*, vol. 7, p. ncomms11794, 2016.

[13] F. Ding *et al.*, "Dendrite-free lithium deposition via self-healing electrostatic shield mechanism," *J. Am. Chem. Soc.*, vol. 135, no. 11, pp. 4450–4456, 2013.

[14] H. Haruna, S. Takahashi, and Y. Tanaka, "Accurate Consumption Analysis of Vinylene Carbonate as an Electrolyte Additive in an 18650 Lithium-Ion Battery at the First Charge-Discharge Cycle," *J. Electrochem. Soc.*, vol. 164, no. 1, pp. A6278–A6280, 2017.

[15] A. L. Michan *et al.*, "Fluoroethylene carbonate and vinylene carbonate reduction: Understanding lithium-ion battery electrolyte additives and solid electrolyte interphase

formation," *Chem. Mater.*, vol. 28, no. 22, pp. 8149–8159, 2016.

[16] R. Khurana, J. L. Schaefer, L. A. Archer, and G. W. Coates, "Suppression of lithium dendrite growth using cross-linked polyethylene/poly(ethylene oxide) electrolytes: A new approach for practical lithium-metal polymer batteries," *J. Am. Chem. Soc.*, vol. 136, no. 20, pp. 7395–7402, 2014.

[17] Q. Lu *et al.*, "Dendrite-Free, High-Rate, Long-Life Lithium Metal Batteries with a 3D Cross-Linked Network Polymer Electrolyte," *Adv. Mater.*, vol. 29, no. 13, 2017.

[18] W. Zhou, S. Wang, Y. Li, S. Xin, A. Manthiram, and J. B. Goodenough, "Plating a Dendrite-Free Lithium Anode with a Polymer/Ceramic/Polymer Sandwich Electrolyte," *J. Am. Chem. Soc.*, vol. 138, no. 30, pp. 9385–9388, 2016.

[19] Z. Tu, Y. Kambe, Y. Lu, and L. A. Archer, "Nanoporous polymer-ceramic composite electrolytes for lithium metal batteries," *Adv. Energy Mater.*, vol. 4, no. 2, pp. 2–7, 2014.

[20] K. Yan *et al.*, "Ultrathin two-dimensional atomic crystals as stable interfacial layer for improvement of lithium metal anode," *Nano Lett.*, vol. 14, no. 10, pp. 6016–6022, 2014.

[21] J. S. Kim, D. W. Kim, H. T. Jung, and J. W. Choi, "Controlled Lithium Dendrite Growth by a Synergistic Effect of Multilayered Graphene Coating and an Electrolyte Additive," *Chem. Mater.*, vol. 27, no. 8, pp. 2780–2787, 2015.

[22] R. Mukherjee *et al.*, "Defect-induced plating of lithium metal within porous graphene networks," *Nat. Commun.*, vol. 5, pp. 1–10, 2014.

[23] G. Zheng *et al.*, "Interconnected hollow carbon nanospheres for stable lithium metal anodes," *Nat. Nanotechnol.*, vol. 9, no. 8, pp. 618–623, 2014.

[24] X. Li *et al.*, "Significant impact on cathode performance of lithium-ion batteries by precisely controlled metal oxide nanocoatings via atomic layer deposition," *J. Power Sources*, vol. 247, pp. 57–69, 2014.

[25] H.-M. Cheng, F.-M. Wang, J. P. Chu, R. Santhanam, J. Rick, and S.-C. Lo, "Enhanced cycleabity in lithium ion batteries: Resulting from atomic layer depostion of Al2O3 or TiO2 on LiCoO2 electrodes," *The Journal of Physical Chemistry C*, vol. 116. pp. 7629–7637, 2012.

[26] D. Guan and Y. Wang, "Ultrathin surface coatings to enhance cycling stability of LiMn2O4 cathode in lithium-ion batteries," *Ionics (Kiel).*, vol. 19, no. 1, pp. 1–8, 2013.

[27] J. S. Park *et al.*, "Ultrathin lithium-ion conducting coatings for increased interfacial stability in high voltage lithium-ion batteries," *Chem. Mater.*, vol. 26, no. 10, pp. 3128–3134, 2014.

[28] Y. Zhao *et al.*, "Superior Stable and Long Life Sodium Metal Anodes Achieved by Atomic Layer Deposition," *Adv. Mater.*, 2017.

[29] A. C. Kozen *et al.*, "Next-Generation Lithium Metal Anode Engineering *via* Atomic Layer Deposition," *ACS Nano*, vol. 9, no. 6, pp. 5884–5892, 2015.

[30] E. Kazyak, K. N. Wood, and N. P. Dasgupta, "Improved Cycle Life and Stability of Lithium Metal Anodes through Ultrathin Atomic Layer Deposition Surface Treatments," *Chem.*

Mater., vol. 27, no. 18, pp. 6457–6462, 2015.

[31] L. Chen *et al.*, "Lithium metal protected by atomic layer deposition metal oxide for high performance anodes," *J. Mater. Chem. A*, vol. 5, no. 24, pp. 12297–12309, 2017.

[32] A. A. Dameron *et al.*, "Molecular Layer Deposition of Alucone Polymer Films Using Trimethylaluminum and Ethylene Glycol," *Chem. Mater.*, vol. 20, no. 10, pp. 3315–3326, May 2008.

[33] Q. Peng, B. Gong, R. M. VanGundy, and G. N. Parsons, "'Zincone' zinc oxide - Organic hybrid polymer thin films formed by molecular layer deposition," *Chem. Mater.*, vol. 21, no. 5, pp. 820–830, 2009.

[34] A. Lushington *et al.*, "A novel approach in controlling the conductivity of thin films using molecular layer deposition," *Appl. Surf. Sci.*, 2015.

[35] B. H. Lee, B. Yoon, A. I. Abdulagatov, R. A. Hall, and S. M. George, "Growth and properties of hybrid organic-inorganic metalcone films using molecular layer deposition techniques," *Adv. Funct. Mater.*, vol. 23, no. 5, pp. 532–546, 2013.

[36] A. Lushington *et al.*, "Orientation and Ordering of Organic and Hybrid Inorganic?Organic Polyurea Films Using Molecular Layer Deposition," *J. Phys. Chem. C*, vol. 121, no. 21, pp. 11757–11764, 2017.

[37] J. Liu *et al.*, "Ultralow thermal conductivity of atomic/molecular layer-deposited hybrid organic-inorganic zincone thin films," *Nano Lett.*, vol. 13, no. 11, pp. 5594–5599, 2013.

[38] B. H. Lee, B. Yoon, V. R. Anderson, and S. M. George, "Alucone Alloys with Tunable Properties Using Alucone Molecular Layer Deposition and Al2O3 Atomic Layer Deposition," *J. Phys. Chem. C*, vol. 116, no. 5, pp. 3250–3257, 2012.

[39] B. H. Lee, V. R. Anderson, and S. M. George, "Growth and Properties of Hafnicone and HfO 2 /Hafnicone Nanolaminate and Alloy Films Using Molecular Layer Deposition Techniques," *ACS Appl. Mater. Interfaces*, vol. 6, no. 19, pp. 16880–16887, Oct. 2014.

[40] Y. Zhao *et al.*, "Inorganic-Organic Coating via Molecular Layer Deposition Enables Long Life Sodium Metal Anode," *Nano Lett.*, vol. 17, no. 9, pp. 5653–5659, 2017.

[41] B. Yoon, J. L. O'Patchen, D. Seghete, A. S. Cavanagh, and S. M. George, "Molecular layer deposition of hybrid organic-inorganic polymer films using diethylzinc and ethylene glycol," *Chem. Vap. Depos.*, vol. 15, no. 4–6, pp. 112–121, 2009.

[42] C. L. Langford, "Application of Molecular Layer Deposition for Graphite Anodes in Lithium-ion Batteries and Porous Thin-film Materials," University of Western Ontario, 2016.

[43] D. M. Piper *et al.*, "Reversible high-capacity Si nanocomposite anodes for lithium-ion batteries enabled by molecular layer deposition," *Adv. Mater.*, vol. 26, no. 10, pp. 1596–1601, 2014.

[44] Y. He *et al.*, "*In Situ* Transmission Electron Microscopy Probing of Native Oxide and Artificial Layers on Silicon Nanoparticles for Lithium Ion Batteries," *ACS Nano*, vol. 8, no.

11, pp. 11816–11823, 2014.

[45] K.-H. Chen *et al.*, “Dead lithium: mass transport effects on voltage, capacity, and failure of lithium metal anodes,” *J. Mater. Chem. A*, vol. 5, no. 23, pp. 11671–11681, 2017.

[46] Y. Liu, D. Lin, Z. Liang, J. Zhao, K. Yan, and Y. Cui, “Lithium-coated polymeric matrix as a minimum volume-change and dendrite-free lithium metal anode,” *Nat. Commun.*, vol. 7, p. 10992, 2016.

[47] M. R. Palacin and A. de Guibert, “Why do batteries fail?,” *Science (80-.).*, vol. 351, no. 6273, pp. 1253292–1253292, 2016.

[48] J. Zheng *et al.*, “Highly Stable Operation of Lithium Metal Batteries Enabled by the Formation of a Transient High-Concentration Electrolyte Layer,” *Adv. Energy Mater.*, vol. 6, no. 8, pp. 1–10, 2016.

[49] P. Arora, “Capacity Fade Mechanisms and Side Reactions in Lithium-Ion Batteries,” *J. Electrochem. Soc.*, vol. 145, no. 10, p. 3647, 1998.

[50] J. Park, J. Jeong, Y. Lee, M. Oh, M. H. Ryou, and Y. M. Lee, “Micro-Patterned Lithium Metal Anodes with Suppressed Dendrite Formation for Post Lithium-Ion Batteries,” *Adv. Mater. Interfaces*, vol. 3, no. 11, pp. 1–9, 2016.

[51] Y. Li, J. Jiao, J. Bi, X. Wang, Z. Wang, and L. Chen, “Controlled deposition of Li metal,” *Nano Energy*, vol. 32, no. July 2016, pp. 241–246, 2017.

[52] Q. Li, S. Tan, L. Li, Y. Lu, and Y. He, “Understanding the molecular mechanism of pulse current charging for stable lithium-metal batteries,” *Sci. Adv.*, vol. 3, no. 7, p. e1701246, 2017.

[53] W. Liu, D. Lin, A. Pei, and Y. Cui, “Stabilizing Lithium Metal Anodes by Uniform Li-Ion Flux Distribution in Nanochannel Confinement,” *J. Am. Chem. Soc.*, vol. 138, no. 47, pp. 15443–15450, 2016.

[54] M. D. Levi and D. Aurbach, “Potentiostatic and Galvanostatic Intermittent Titration Techniques,” *Charact. Mater.*, 2012.

[55] C. Wang, I. Kakwan, A. J. Appleby, and F. E. Little, “In situ investigation of electrochemical lithium intercalation into graphite powder,” *J. Electroanal. Chem.*, vol. 489, no. 1, pp. 55–67, 2000.

[56] K. N. Wood *et al.*, “Dendrites and pits: Untangling the complex behavior of lithium metal anodes through operando video microscopy,” *ACS Cent. Sci.*, vol. 2, no. 11, pp. 790–801, 2016.

[57] R. L. Sacci, J. M. Black, N. Balke, N. J. Dudney, K. L. More, and R. R. Unocic, “Nanoscale imaging of fundamental Li battery chemistry: Solid-electrolyte interphase formation and preferential growth of lithium metal nanoclusters,” *Nano Lett.*, vol. 15, no. 3, pp. 2011–2018, 2015.

[58] G. Bieker, M. Winter, and P. Bieker, “Electrochemical in situ investigations of SEI and dendrite formation on the lithium metal anode,” *Phys. Chem. Chem. Phys.*, vol. 17, no. 14,

pp. 8670–8679, 2015.

[59] Y. S. Cohen, Y. Cohen, and D. Aurbach, "Micromorphological Studies of Lithium Electrodes in Alkyl Carbonate Solutions Using in Situ Atomic Force Microscopy," *J. Phys. Chem. B*, vol. 104, no. 51, pp. 12282–12291, 2000.

[60] D. M. Piper *et al.*, "Reversible High-Capacity Si Nanocomposite Anodes for Lithium-ion Batteries Enabled by Molecular Layer Deposition.," *Adv. Mater.*, 2013.

[61] D. Aurbach, I. Weissman, A. Zaban, and O. Chusid, "Correlation between surface chemistry, morphology, cycling efficiency and interfacial properties of Li electrodes in solutions containing different Li salts," *Electrochim. Acta*, vol. 39, no. 1, pp. 51–71, 1994.

[62] K. Edström, M. Herstedt, and D. P. Abraham, "A new look at the solid electrolyte interphase on graphite anodes in Li-ion batteries," *J. Power Sources*, vol. 153, no. 2, pp. 380–384, 2006.

[63] P. Verma, P. Maire, and P. Nov??k, "A review of the features and analyses of the solid electrolyte interphase in Li-ion batteries," *Electrochim. Acta*, vol. 55, no. 22, pp. 6332–6341, 2010.

[64] E. Peled, D. Golodnitsky, and J. Penciner, "The Anode/Electrolyte Interface," in *Handbook of Battery Materials*, pp. 419–456 2007.

[65] E. Peled and S. Menkin, "Review—SEI: Past, Present and Future," *J. Electrochem. Soc.*, vol. 164, no. 7, pp. A1703–A1719, 2017.

[66] D. Molina Piper *et al.*, "Mitigating irreversible capacity losses from carbon agents via surface modification," *J. Power Sources*, vol. 275, pp. 605–611, 2015.

[67] Y. He *et al.*, "In Situ Transmission Electron Microscopy Probing of Native Oxide and Arti fi cial Layers on Silicon Nanoparticles for Lithium Ion Batteries," pp. 11816–11823, 2014.

[68] a J. Loebl *et al.*, "Solid Electrolyte Interphase on Lithium-Ion Carbon Nanofiber Electrodes by Atomic and Molecular Layer Deposition," *J. Electrochem. Soc.*, vol. 160, no. 11, pp. A1971–A1978, 2013.

8

Conclusions and Future Prospective

This chapter will summarize the work presented in this thesis. The highlights of each experimental chapter will be examined and discussed. A focus of this chapter is to analyze the work conducted and presented herein and its contributions to the field of ALD/MLD. The enabling properties of ALD in the context of materials engineering is a central tenant of this thesis and will be discussed. In addition, the novelties presented in this thesis are summarized. Finally, a short discussion is given about the future application of ALD and MLD.

8.1 Conclusions

Atomic layer deposition (ALD) has long been considered as an enabling technique. It's ability to deposit films in a conformal, uniform manner on geometrically complex surfaces gives it a competitive advantage over other deposition techniques. The primary advantages of ALD are derived from the sequential, self-saturating, gas-surface reactions that take place during the deposition process. Conformality of deposition on three dimensionally-structured materials is made possible by self-terminating characteristics, which restricts the reaction at the surface to no more than one layer of precursor. With sufficient precursor pulse time, organometallic precursors can be uniformly exposed into deep trenches, allowing for complete reaction with the entire surface. Other gas phase deposition techniques, such as CVD and PVD, suffer from non-uniformity due to faster surface reactions and shadowing effects. The unique capabilities of ALD have allowed this technique reach commercial success and has ushered in a new way for chipset manufacturers to design advanced semiconductors. Since then ALD has been applied to many different fields, allowing researchers to finely tune the characteristics of materials by changing surface properties. The intersection of ALD and nanotechnology has been an especially fruitful one and has enabled the application of novel nanomaterials. While ALD is limited to depositing metals and inorganic material, molecular layer deposition (MLD) can be used to deposit polymeric materials. These two techniques can be combined to produce a new class of inorganic-organic materials with tunable film composition and yield materials with unique properties. Both ALD and MLD can be used to enhance the properties of nanomaterials.

This thesis work is mainly focused on applying the techniques of ALD and MLD to various nanomaterials and nanostructures. A series of experiments were carried out to change the surface properties of nanomaterials as well as produce new types of ALD and MLD films. Several different characterization techniques were conducted to determine ALD/MLD film and nanostructure properties. This insight was then used and applied to materials used in energy storage and conversion. In summary, this study is focused on the different ways ALD and MLD can be used to alter and enhance the properties of nanomaterials. The detailed study presented herein provides a context for the range of applications these two techniques can be used for. This work also highlights how ALD and MLD can be used in more non-traditional ways to enhance material

properties. This work paves a path for the future use of ALD and MLD in two very promising and important fields of technology, fuel cells and energy storage.

The third chapter examined the influence of ozone on nitrogen-doped multiwalled carbon nanotubes (NCNTs) and pristine multiwalled carbon nanotubes (PCNTs). An ALD tool was used to control experimental parameters such as temperature and ozone exposure time. The effect of ALD ozone pulse time, cycle number and temperature was investigated. Morphological changes to both substrates were examined using SEM and TEM. BET measurements were also conducted to determine surface area, pore size and pore size distribution while XPS was using to probe the chemical nature of NCNTs and PCNTs following ALD ozone treatment. This investigation determined that the deleterious effects of ozone are limited to NCNTs and have little to no effect on PCNTs. Furthermore, this work establishes that these effects are only observed above a certain temperature threshold. This published experiment demonstrates how ALD ozone treatment is an avenue toward creating defect rich substrates. It also highlights the importance of understanding precursor-substrate interaction, especially for ALD recipes that involve strong oxidizing agents.

The fourth chapter describes the growth of a novel aluminum alkoxide film that has tunable conductivity with annealing treatment by using MLD. Alternating exposures of trimethylaluminum (TMA), ethylene glycol (EG) and terephthaloyl chloride (TC) are used to grow the aluminum alkoxide films. In the first study of its kind, aluminum to carbon ratio was accurately controlled by using sub-cycles of EG and TC. Pyrolysis of these films in a reducing atmosphere yielded a conductive Al_2O_3/carbon composite. Raman spectroscopy was then used to determine the nature of carbon in these films following annealing treatment. Furthermore, the origin of film conductivity was determined along with oxidation state of aluminum following pyrolysis using synchrotron based XPS.

The fifth chapter outlined in this thesis investigates the molecular orientation and ordering of films produced by ALD and MLD. Pure organic polyurea films and a novel mixed inorganic-organic polyurea film is grown and the depositions conditions necessary for MLD growth are presented. The influence of incorporating an inorganic component in the MLD film was the primary research question of this study. Polarization-dependent X-ray absorption spectroscopy was employed to determine the orientation and ordering of these films. It was found that both films exhibit a tendency to oriented themselves parallel to the substrate surface. Interestingly,

however, the degree of ordering between the films was found to be vastly different. Inorganic-organic polyurea films were found to have a much higher degree of ordering compared to pure organic polyurea.

Following this, research on the development of single atom Pt by ALD is presented in chapter six. The ability to deposit Pt as single atoms and clusters on NCNTs and PCNTs was investigated. By varying the exposure time of trimethyl(methylcyclopentadienyl)-platinum to the substrate surface, precursor saturating conditions were determined. In this experiment an oxidizing step was omitted so that single-atoms of Pt can be stabilized on the surface. It was found that using a 1 minute exposure of Pt precursor at 250°C, single-atoms and ultra-small clusters of Pt can be deposited on NCNTs. Interestingly, the same treatment yielded very different results for PCNTS. This study highlights the importance of understanding precursor-substrate interaction and the parameters that influence conditions for precursor self-saturation. This chapter demonstrates the potential application of ALD single-atom Pt for use in fuel cells.

Finally, chapter seven describes the use of ALD and MLD for the protection of lithium metal for use as an anode in lithium-based batteries. The stripping and plating behavior of Li coated with either TMA-H_2O, TMA-EG or TMA-GLY are examined. The study determined that TMA-GLY coated Li can be cycled much longer than the other coated electrodes. To determine the reason for this unique behavior, gravimetric intermission titration technique was conducted. This unique experimental design allowed for the effects of stripping and plating to be deconvoluted. It was determined that TMA-GLY films produce a more uniform solid electrolyte interphase (SEI) layer compared to TMA-H_2O and TMA-EG. Furthermore, through RBS, TMA-GLY coated Li electrodes had a significantly different solid electrolyte interphase composition compared to Li coated with TMA-EG and TMA-H_2O. This study highlights how ALD and MLD can be used to change surface properties. Furthermore, it demonstrates that although the coating layer maybe destroyed after electrochemical cycling, it still influences the composition of the solid electrolyte layer and plays an important role in electrode passivation.

8.2 Thesis Novelties

This thesis presents some of the available avenues that ALD and MLD can be used to alter or enhance the properties of nanomaterials. A key part of this thesis is demonstrating the importance of precursor-substrate interaction. The first chapter presents some of the subtle nuances that may be present when using strong oxidizing agents on substrates that may have an inherent reactivity of their own. Many ALD processes require the use of ozone to oxidize organic ligands. However, as this study demonstrates, it is important to understand how each precursor that is being introduced into the reaction chamber interacts with its surroundings. This aspect is again highlighted in chapter six where the saturation conditions of an ALD Pt precursor are explored. The novelty produced here is the demonstration that growth of noble metals by ALD is highly influenced by substrate and that an ALD recipe that may work on one substrate will not necessarily produce the same results for a different substrate. This chapter also is the first to demonstrate the growth of single-atoms and ultra-small clusters of Pt by ALD and presents the potential application of this technology for fuel cells. However, this is only achievable by carefully controlling several deposition conditions as well as appropriate choice of substrate.

Chapters four and five present the deposition of two novel ALD/MLD films. The first novel inorganic-organic film presented in this thesis is the growth of a polyethylene terephthalate film that also includes aluminum. By using subcycles of EG and TC the length of the polyethene terephthalate component can be controlled and subsequently capped off by introducing an inorganic component in the form of TMA. This was the first study of its kind using this method to control the ratio between organic and inorganic in an ALD/MLD film. By using this novel methodology, the conductivity of the annealed film could be accurately controlled. Furthermore, this film can also be used to control pore size of annealed films. But increasing the amount of carbon content in the film and annealing the substrate in air, larger pores can be formed as the carbon is burned out. The second novel inorganic-organic film presented in this thesis is the growth of a polyurea film with aluminum. However, this study presents the importance the polymer orientation on film growth properties. This was the first study of its kind to demonstrate how introducing an inorganic component into the deposition of an organic polymer influences the packing density and structural ordering of ALD/MLD films. Both studies are one of the few

publications available that use synchrotron radiation to analyze ALD/MLD films and demonstrates the power of this technique in providing important information about material properties.

The final novelty presented in this thesis the protection of lithium by MLD. There have been a few papers reporting the successful protection of Li using ALD Al_2O_3, but to date, there have been no reports published on the protection of Li by MLD. Furthermore, this investigation demonstrates the different properties imparted toward Li protection by ALD and MLD. It also is the first of its kind to separate the effects of electroplating and electrodissolution of Li on ALD and MLD films using GITT. This technique has only been reported in one other publications for the protection of Li.

8.3 Future Perspective

There is tremendous future potential for the use of ALD and MLD in the field of energy storage and conversion. This is further augmented by the fact that these two techniques can be easily scaled-up to meet the demands of industrial production. Additionally, recent developments have demonstrated the feasibility of roll-to-roll ALD tools. Below are several strategies where ALD and MLD can be potentially used for the field of energy storage and conversion:

(1) Currently, there are several safety issues that plague the commercialization and use of lithium-based batteries. Many of these issues are related to the use of organic electrolytes that have low flash points and are extremely volatile. Given that the cathode of these batteries is a strong oxidizing environment, the occurrence of a thermal even may release oxidants at the cathode and ignite the electrolyte. The only appropriate way to entirely mitigate this issue, is to shift toward non-combustible electrolytes. Unfortunately, to date, the only electrolytes that are non-combustible and are currently available are solid-state inorganic ones. Recently there have been great technological strides in producing fast lithium-ion conducting solid-state electrolytes, such as $Li_{10}GeP_2S_{12}$. However, the incorporation of these solid-state electrolytes into industrial battery production is severely hindered by several issues and requires a complete overhaul of current manufacturing practices. Presently, batteries are primarily fabricated using coating technologies, lamination, and calendaring. The only way to successfully integrate materials such as $Li_{10}GeP_2S_{12}$ into the production of battery electrodes is by using a solid

deposition technique. ALD is uniquely suited to addressing this issue, especially with the emergence of roll-to-roll ALD tools.

(2) ALD is also poised to be an enabling technology for the future of all-solid-state 3D batteries. As a technology that produces conformal, uniform pin-hole free films with facile control over thickness and composition, ALD can be used to deposit thin films onto complicated spatially demanding structures and increase the volumetric energy density of solid-state batteries. Unfortunately, the deposition of lithium containing materials by ALD is quite complicated and currently available precursors do not always behave in a self-terminating fashion. The field of ALD is quiet heavily dependent on inorganic chemists who can develop novel precursors that suit material requirements. Hopefully, in the near future, new, custom tailored lithium containing precursors can be synthesized that exhibit better self-terminating characteristics and are able to produce lithium containing films at lower deposition temperatures. Currently, Li containing ALD films needs to be deposited at temperatures higher than 200°C. This temperature is above the melting point or glass transition temperature of many binders used in electrodes and must be avoided. Furthermore, high temperature depositions results in delamination of electrode materials and reduces the structural integrity of the electrode.

(3) Although ALD has been extensively studied for its use in lithium batteries, the use of MLD in this is field remains in its nascent stages. However, the possibilities of MLD use in battery research is extensive. Given that MLD can be used to deposit thin polymeric materials, the development of MLD-based polymer electrolytes is very promising. This opportunity is also enticing given that ALD inorganic materials can be incorporated into the MLD film to give tunable properties. Much of this work can be done through superlattice structures with highly specialized functionality. Although this may be a difficult optimization problem, the increasing use of supercomputers to determine material properties will aid in the development of these types of films. Furthermore, post-treatment of MLD/ALD films can enhance film properties. One example of this is producing crosslinking films via UV exposure either during or after deposition. These cross-linked films are very suitable for materials that undergo large volume expansion during lithiation and delithiation, such as Si, Sn and Li.

(4) Apart from using MLD as a coating technique, there is also an opportunity to deposit organic electrode materials using this technique. Organic compounds offer a possibility to produce

cost-effective, environmentally friendly rechargeable batteries. The type of compounds that can be used as electrodes in lithium-based batteries include organosulfur compounds, organic free radical compounds, organic carbonyl compounds, conducting polymers, non-conjugated redox polymers, and layer organic compounds. However, many of these compounds are electronic insulators and therefore a large amount of conductive carbon needs to be used for these electrodes. Furthermore, a major issue for organic electrodes is rapid capacity fading due to dissolution of active materials into the electrolyte solution. MLD can uniquely solve both this problems by depositing electroactive materials on highly conductive nanomaterial substrates, such as graphene, carbon nanotubes, or MoS_2. Additionally, MLD is a surface mediated technique that is based on molecules being chemically bonded to the surface. This provides an avenue to anchoring organic compounds to the surface and prevent issues related to dissolution. ALD can also be incorporated into this process to engineer surface bonding characteristics and further improve longevity of organic electrodes produced by MLD.

(5) Another very interesting field that has recently emerged from the ALD community is atomic layer etching (ALE). Considered as a next-generation etch technology, ALE selectively removes targeted materials at the atomic scale without damaging other parts of the material. For example, ALE can be used to remove materials in a structure to form trenches with gaps on the order of 1-1.5 nm. It is essentially the reverse of ALD and uses sequential, self-limiting processes to remove materials layer-by-layer at the atomic scale. ALE comes in two different configurations, thermal ALE and plasma ALE. However, these can be combined to create a hybrid ALE process. Plasma ALE offers the ability to directionally etch materials while thermal ALE is targeted toward isotropic etching. These two techniques can be used to develop novel nanostructures on nanomaterials and further increase the available surface area for electrochemical reaction. For examples, ALE can be used to selectively etch away at a surface and create a pattern that can later be utilized in an ALD process. This could be one possible direction for the development of fuel cell catalysts with highly tunable selectivity, catalyst particle size, and catalyst loading. This type of technology can also be used to create unique, three-dimensional nanoscaled host structures for lithium metal. By providing a large specific surface area, low current density and uniform distribution of positive charges can be obtained. Furthermore, specifically designed structures can be fabricated using ALE so that ample space can be engineering into the material to accommodate Li. Another possibility is to directly

create 3D structures on the surface of lithium by ALE and thus create a surface that is more conducive to providing uniform current distribution. This can be coupled with ALD or MLD to produce a favorable SEI layer.

The unparalleled resolution imparted by ALD and MLD will continue to significantly impact many different fields. Both these technologies have a bright future in enabling the use of various nanomaterials and will undoubtedly be a central technique for use in the field of nanotechnology.

Appendices

Appendix A: Permission from AIP for Published Article

Published article:

Surface Modification of Nitrogen-Doped Carbon Nanotubes by Ozone via Atomic Layer Deposition. **J. Vac. Sci. Tech. A.**, 2014, 32, 01A124-1 – 01A124-8.

AIP PUBLISHING LLC LICENSE TERMS AND CONDITIONS

Dec 19, 2017

This Agreement between Mr. Andrew Lushington ("You") and AIP Publishing LLC ("AIP Publishing LLC") consists of your license details and the terms and conditions provided by AIP Publishing LLC and Copyright Clearance Center.

License Number	4252660219784
License date	Dec 19, 2017
Licensed Content Publisher	AIP Publishing LLC
Licensed Content Publication	Journal of Vacuum Science & Technology A
Licensed Content Title	Surface modification of nitrogen-doped carbon nanotubes by ozone via atomic layer deposition
Licensed Content Author	Andrew Lushington, Jian Liu, Yongji Tang, et al
Licensed Content Date	Jan 1, 2014
Licensed Content Volume	32
Licensed Content Issue	1
Type of Use	Thesis/Dissertation
Requestor type	Author (original article)
Format	Print and electronic
Portion	Excerpt (> 800 words)
Will you be translating?	No
Title of your thesis / dissertation	DEVELOPMENT OF NANOSTRUCTURES BY ATOMIC AND MOLECULAR LAYER DEPOSITION FOR SURFACE MODIFICATION OF NANOMATERIALS FOR ENERGY STORAGE AND CONVERSION APPLICATIONS
Expected completion date	Dec 2017
Estimated size (number of pages)	205

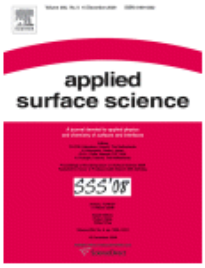
Appendix B: Permission from Elsevier for Published Article

Published article:

A Novel Approach in Controlling the Conductivity of Thin Films using Molecular Layer Deposition. **App. Surf. Sci.**, 2015, 357, 1319-1324

Copyright Clearance Center RightsLink®

Home | Create Account | Help



Title: A novel approach in controlling the conductivity of thin films using molecular layer deposition
Author: Andrew Lushington,Jian Liu,Mohammad N. Bannis,Biwei Xiao,Stephen Lawes,Ruying Li,Xueliang Sun
Publication: Applied Surface Science
Publisher: Elsevier
Date: 1 December 2015
Copyright © 2015 Elsevier B.V. All rights reserved.

LOGIN
If you're a copyright.com user, you can login to RightsLink using your copyright.com credentials. Already a RightsLink user or want to learn more?

Please note that, as the author of this Elsevier article, you retain the right to include it in a thesis or dissertation, provided it is not published commercially. Permission is not required, but please ensure that you reference the journal as the original source. For more information on this and on your other retained rights, please visit: https://www.elsevier.com/about/our-business/policies/copyright#Author-rights

BACK | CLOSE WINDOW

Copyright © 2017 Copyright Clearance Center, Inc. All Rights Reserved. Privacy statement. Terms and Conditions.
Comments? We would like to hear from you. E-mail us at customercare@copyright.com

Appendix C: Permission from ACS for Published Article

Published Article:

Orientation and Ordering of Organic and Hybrid Inorganic-Organic Polyurea Films Using Molecular Layer Deposition. **J. Phys. Chem. C** 121 (2017) 11757-11764.

Copyright Clearance Center RightsLink®

Home | Account Info | Help

ACS Publications
Most Trusted. Most Cited. Most Read.

Title: Orientation and Ordering of Organic and Hybrid Inorganic–Organic Polyurea Films Using Molecular Layer Deposition
Author: Andrew Lushington, Craig Langford, Jian Liu, et al
Publication: The Journal of Physical Chemistry C
Publisher: American Chemical Society
Date: Jun 1, 2017
Copyright © 2017, American Chemical Society

Logged in as:
Andrew Lushington
LOGOUT

PERMISSION/LICENSE IS GRANTED FOR YOUR ORDER AT NO CHARGE

This type of permission/license, instead of the standard Terms & Conditions, is sent to you because no fee is being charged for your order. Please note the following:

- Permission is granted for your request in both print and electronic formats, and translations.
- If figures and/or tables were requested, they may be adapted or used in part.
- Please print this page for your records and send a copy of it to your publisher/graduate school.
- Appropriate credit for the requested material should be given as follows: "Reprinted (adapted) with permission from (COMPLETE REFERENCE CITATION). Copyright (YEAR) American Chemical Society." Insert appropriate information in place of the capitalized words.
- One-time permission is granted only for the use specified in your request. No additional uses are granted (such as derivative works or other editions). For any other uses, please submit a new request.

Curriculum Vitae

Name:	Andrew Lushington
Post-secondary Education and Degrees:	The University of Western Ontario London, Ontario, Canada 2013-2017 Ph. D. Carleton University Ottawa, Ontario, Canada 2006-2012 B.Sc. Chemistry
Honors and Awards:	Nelson Canada Chemistry Award 2012 Alexander Graham Bell Canada Graduate Scholarship 2014-2017 Michael Smiths Foreign Study Supplement 2015 The Electrochemical Society: Montreal Student Chapter 2015 American Vacuum Society: Michigan Chapter 2017
Related Work Experience:	Teaching and Research Assistant The University of Western Ontario 2013-2016

Thermal Hazard Researcher

Canadian Explosives Research Lab: Natural Resources Canada

Jan 2011 – Apr 2011

Nanomaterials Analyst

Environment Canada

May 2010 – Dec 2010

Publications:

(A) *Peer-reviewed Journal Papers Based on This Thesis (**First author**)*

1. **A. Lushington**, J. Liu, Y. Tang, R. Li, and X. Sun, *Surface Modification of Nitrogen-Doped Carbon Nanotubes by Ozone via Atomic Layer Deposition.* **J. Vac. Sci. Tech. A** 32 (2014) 01A124
2. **A. Lushington**, J. Liu, M.N. Banis, B. Xiao, S. Lawes, R. Li, and X. Sun, *A Novel Approach in Controlling the Conductivity of Thin Films Using Molecular Layer Deposition.* **App. Surf. Sci** 357 (2015) 1319
3. **A. Lushington**, C. Langford, J. Liu, K. Nie, R. Li, X. Sun, J. Guo, and X. Sun, *Orientation and Ordering of Organic and Hybrid Inorganic-Organic Polyurea Films Using Molecular Layer Deposition.* **J. Phys. Chem. C** 121 (2017) 11757

(B) *Peer-reviewed Journal Papers to be Submitted (**First author**)*

4. **A. Lushington**, S. Stambula, M.N. Banis, N. Cheng, Y. Zhou, R. Li, T.K. Sham, G. Botton, and X. Sun, *Single-Atom, and Clusters to Nanoparticles: Controlling the Nucleation of Pt Through Regulated Gas Phase Chemisorption.* **To be submitted**.
5. **A. Lushington**, Y. Zhao, L.V. Goncharova, Q. Sun, R. Li, and X. Sun, *Deconvoluting the Effects of Stripping and Plating of Lithium Coated using ALD and MLD.* **To be submitted**.

(C) *Peer-reviewed Journal Papers Based on This Thesis (**Co-author)***

6. X. Li, Y. Hu, J. Liu, **A. Lushington**, R. Li, and X. Sun, *Structurally Tailored Graphene Nanosheets as Lithium Ion Battery Anodes: An Insight to Yield Exceptionally High Lithium Storage Performance.* **Nanoscale** 5 (2013) 12607

7. J. Liu, M.N. Banis, X. Li, **A. Lushington**, M. Cai, R. Li, T.K. Sham, and X. Sun, *Atomic Layer Deposition of Lithium Tantalate Solid-State Electrolytes.* **J. Phys. Chem. C** 117 (2013) 20260

8. M. Guo, D. Li, M. Zhao, Y. Zhang, D. Geng, **A. Lushington**, and X. Sun, *Nitrogen ion Implanted Graphene as Thrombo-protective Safer and Cytoprotective Alternative for Biomedical Applications.* **Carbon** 61 (2013) 321

9. X. Li, J. Liu, M.N. Banis, **A. Lushington**, R. Li, M. Cai, and X. Sun, *Atomic Layer Deposition of Solid-State Electrolyte Coated Cathode Materials with Superior High-Voltage Cycling Behavior for Lithium Ion Battery Application.* **Energy Environ. Sci.** 7 (2014) 768

10. X. Li, **A. Lushington**, J. Liu, R. Li, and X. Sun, *Superior Stable Sulfur Cathodes of Li-S Batteries Enabled by Molecular Layer Deposition.* **Chem. Comm.** 50 (2014) 9757

11. X. Li, X. Li, M.N. Banis, B. Wang, **A. Lushington**, X. Cui, R. Li, T.K. Sham, and X. Sun, *Tailoring Interaction of Carbon, and Sulfur in Li-S Battery Cathodes: Significant Effects of Carbon-Heteroatom Bonds.* **J. Mater. Chem. A** 2 (2014) 12866

12. J. Liu, M.N. Banis, Q. Sun, **A. Lushington**, R. Li, T.K. Sham, and X. Sun, *Rational Design of Atomic-Layer-Deposited LiFePO4 as a High-Performance Cathode for Lithium Ion Batteries.* **Adv. Mater.** 26 (2014) 6472

13. J. Zeng, M. Li, X. Li, C. Chen, D. Xiong, L. Dong, D. Li, **A. Lushington**, and X. Sun, *A Novel Coating onto LiMn2O4 Cathode with Increasing Lithium Ion Battery Performance.* **App. Surf. Sci.** 317 (2014) 884

14. J. Liu, M.N. Banis, B. Xiao, Q. Sun, **A. Lushington**, R. Li, J. Guo, T.K. Sham, and X. Sun, *Atomically precise Growth of Sodium Titanates as Anode Materials for High-Rate, and Ultralong Cycle-Life Sodium-Ion Batteries.* **J. Mater. Chem. A** 3 (2015) 24821

15. H. Yadegari, M.N. Banis, B. Xiao, Q. Sun, X. Li, **A. Lushington**, B. Wang, R. Li, T.K. Sham, X. Cui, and X. Sun, *Three-Dimensional Nanostructured Air Electrodes for Sodium-Oxygen Batteries: A Mechanism Toward the cyclability of the Cell.* **Chem. Mater.** 27 (2015) 3040

16. K. Kaliyappan, J. Liu, **A. Lushington**, R. Li, and X. Sun, *Highly Stable Na2/3 (Mn0.54 Ni0.13, Co0.13) O2 cathode Modified by Atomic Layer Deposition for Sodium-Ion Batteries.* **Chem. Sus. Chem.** 8 (2015) 2537

17. X. Li, **A. Lushington**, Q. Sun, W. Xiao, J. Liu, B. Wang, Y. He, K. Nie, Y. Hu, Q. Xiao, R. Li, J. Guo, T.-K. Sham, and X. Sun, *Safe and Durable High-Temperature Lithium-Sulfur Batteries via Molecular Layer Deposited Coating.* **Nano Lett.** 16 (2016) 3545

18. H. Shan, X. Li, Y. Cui, D. Xiong, B. Yan, D. Li, **A. Lushington**, and X. Sun, *Sulfur/Nitrogen Dual-Doped Porous Graphene Aerogels Enhancing Anode Performance of Lithium Ion Batteries.* **Electro. Acta** 205 (2016) 188

19. Z. Song, N. Cheng, **A. Lushington**, and X. Sun, *Recent Progress on MOF-Derived Nanomaterials as Advanced Electrocatalysts in Fuel Cells.* **Catalysis** 6 (2016) 116

20. J. Wang, C. Liu, **A. Lushington**, N. Cheng, M.N. Banis, A. Riese, and X. Sun, *Pd on Carbon Nanotubes-Supported Ag for Formate Oxidation: The Effects of Ag on Anti-Poisoning Performance.* **Electro. Acta** 210 (2016) 285

21. H. Yadegari, M.N. Banis, **A. Lushington**, Q. Sun, R. Li, T.K. Sham, X. Sun, *A Bifunctional Solid State Catalyst with Enhanced Cycling Stability for Na, and Li-O2 Cells: Revealing the Role of Solid State Catalysts.* **Energy Environ. Sci.** 10 (2017) 286

22. Q. Sun, J. Liu, X. Li, B. Wang, H. Yadegari, **A. Lushington**, M.N. Banis, Y. Zhao, W. Xiao, N. Chen, J. Wang, T.K. Sham, and X. Sun, *Atomic Layer Deposited Non-Noble Metal Oxide Catalyst for Sodium-Air Batteries: Tuning the Morphologies and Composition of Discharge Product.* **Adv. Func. Mater.** 27 (2017) 160662

23. Y. Zhao, L.V. Goncharova, **A. Lushington**, Q. Sun, H. Yadegari, B. Wang, W. Xiao, R. Li, X. Sun, *Superior Stable, and Long Life Sodium Metal Anodes Achieved by Atomic Layer Deposition.* **Adv. Mater.** 29 (2017) 160663

24. S. Lawes, Q. Sun, **A. Lushington**, B. Xiao, Y. Liu, X. Sun, *Inkjet-Printed Silicon as High-Performance Anodes for Li-Ion Batteries.* **Nano Energy** 36 (2017) 313

25. S. Deng, B. Xiao, B. Wang, X. Li, K. Kaliyappan, Y. Zhao, **A. Lushington**, R. Li, T.K. Sham, H. Wang, and X. Sun, *New Insight into Atomic-Scale Engineering of Electrode Surface for Long-Life and Safe High Voltage Lithium Ion Cathodes.* **Nano Energy** 38 (2017) 19

26. K. Kaliyappan, J. Liu, B. Xiao, **A. Lushington**, R. Li, T.K. Sham, and X. Sun, *Enhanced Performance of P2-Na0.66 (Mn0.54, Co0.13, Ni0.13) O2 Cathode for Sodium-Ion Batteries by Ultrathin Metal Oxide Coatings via Atomic Layer Deposition.* **Adv. Func. Mater.** 27 (2017) 160664